Multiple Sulfur Isotope Applications in Diagenetic Models and Geochemical Proxy Records

Multiple Sulfur Isotope Applications in Diagenetic Models and Geochemical Proxy Records

A dissertation presented

by

Andrew Laurence Masterson

to

The Department of earth and Planetary Sciences

in partial fulfillment of the requirements

for the degree of

Doctor of Philosophy

in the subject of

Earth and Planetary Sciences

Harvard University

Cambridge, Massachusetts

August 2016

Dissertation Advisor
David T. Johnston

Author
Andrew Laurence Masterson

MULTIPLE SULFUR ISOTOPE APPLICATIONS IN DIAGENETIC MODELS AND GEOCHEMICAL PROXY RECORDS

ABSTRACT

Many of the long-term geochemical fluxes influencing the surface sulfur cycle are microbially catalyzed and a substantial portion of active S cycling occurs in organic-rich continental margin sediments. Stable S isotopes historically provide the most powerful analytical tool for understanding these small and large scale fluxes and for relating them back to laboratory characterizations of microbial metabolisms—particularly that of dissimilatory sulfate reduction. A more recent expansion of stable S isotope geochemistry to include the minor isotopes (^{33}S and ^{36}S) has demonstrated the capacity to diagnose the presence of additional S metabolic processes and to further characterize the response of microbial sulfate reduction to environmental forcing. In particular, emerging work suggests that multiple S isotope signatures in laboratory experiments are dictated by the physiological rate of a metabolic process. This is especially true for sulfate reduction. In this thesis we expand the scope of minor S isotope geochemistry to include early diagenetic processes, exploring the fidelity of laboratory calibrations and how they translate both to the modern marine sediments as well as an S isotope proxy records of seawater sulfate through the Cretaceous and Cenozoic.

Early diagenesis of organic carbon in marine sediments via sulfate reduction is a dominant microbial process, and leaves a characteristic isotopic imprint in pore water and solid phase S-bearing species. To place those S isotope signatures into a physical context, we construct reactive transport models that take sulfur, carbon, and in one case, iron cycling into account for two geochemically well-characterized sedimentary environments: Alfonso basin and Aarhus bay. Alfonso basin is an anoxic-silled marginal basin in the Gulf of California and Aarhus bay is a well-oxygenated, shallow coastal system. We demonstrate in both cases that large S isotope fractionations during microbial sulfate reduction ($^{34}\varepsilon_{SR}$ = 70‰) are required to explain the pore water isotope signatures, and there is no need

for a depth or rate-dependent fractionation relationship. Furthermore, in the case of Aarhus Bay, it is clear that that isotopic contribution from oxidative S processes is negligible. Both these results – an apparent fixed $^{34}\varepsilon_{SR}$ in sediments and little to no isotopic sensitivity to oxidative reactions – should hold true across similar, common shallow water marginal sediments.

In parallel to work targeting the behavior of modern marine sediments, we revisit a well-known $\delta^{34}S$ proxy record for Cretaceous and Cenozoic seawater sulfate. Using minor isotope techniques, we demonstrate that $\Delta^{33}S$ and $\Delta^{36}S$ values are isotopically homogeneous ($\Delta^{33}S_{SO4}$ = 0.043±0.016‰ and $\Delta^{36}S_{SO4}$ = -0.39±0.15‰) despite $\delta^{34}S$ variability. These observations, the first of their kind, place upper limits on pyrite burial and evaporite dissolution over the last 120 million years.

Together, this thesis highlights analytical advances in stable isotope geochemistry and complements those measurements with reactive transport environmental modeling. To date much attention has focused on the laboratory scale generation and controls on the production of microbial isotope signature. Using high-precision minor isotope measurements, paired with the construction of the models incorporating multiple S isotope systematics, allows for the placement of quantitative constraints on sedimentary S cycling and for understanding the global scale consequences for seawater sulfate S isotope proxy records. More succinctly, this furthers our understanding of the imprint that microbial processes have on the multiple S isotope record.

Contents

Abstract . . . iii

Contents . . . vii
List of Figures . . . viii
List of Tables . . . ix
List of Equations . . . x

Acknowledgements . . . xii

Dedication . . . xiv

1 Introduction . . . 1
1.1 Earth's surface S cycle . . . 2
1.2 Sulfur isotope systematics . . . 3
1.2.1 Multiple S isotope nomenclature . . . 4
1.2.2 Multiple S isotope Insights into Microbial Metabolisms . . . 6
1.2.3 Analytical Methods for Multiple S Isotope Geochemistry . . . 8
1.3 Role of Sulfur in Early Diagenesis of Marine Sediments . . . 9
1.3.1 Sedimentary S/C cycling . . . 10
1.3.2 Reactive Transport modeling of Sedimentary Systems . . . 11
1.4 Isotope Records of the Global Biogeochemical S Cycle . . . 13
1.5 Summary of Thesis Chapters . . . 14
1.6 References . . . 15

2 A Multiple Sulfur Isotope Diagenetic Model for Anoxic Sediments of the California-Mexico Margin . . . 20
2.1 Introduction . . . 21
2.2 Alfonso Basin Sampling and Analytical Methods . . . 25
2.2.1 Coring and Pore Water Sampling . . . 25
2.2.2 Sulfur Isotope Analyses . . . 26
2.3 Model Construction . . . 27
2.3.1 Model Architecture and Operation . . . 27
2.3.2 Bulk Pore water Geochemical Model . . . 27
2.3.2.1 Porosity . . . 27
2.3.2.2 Pore water Boundary conditions . . . 27
2.3.2.3 Physical Parameters and Diffusion Coefficients . . . 29
2.3.2.4 Organic Carbon Degradation . . . 30
2.3.2.5 SRR, Methanogenesis, and CH_4 Oxidation . . . 31
2.3.2.6 DIC Production and $CaCO_3$ Precipitation . . . 32
2.3.2.7 Baseline Model Outputs . . . 32
2.3.3 Triple isotop(ologu)e model for SO_4^{2-} ($^{32}SO_4^{2-}$, $^{33}SO_4^{2-}$, $^{34}SO_4^{2-}$) . . . 33
2.3.3.1 Fractionation factors—$^{34}\alpha_{SR}$ and $^{33}\alpha_{SR}$ via $^{33}\lambda_{SR}$ . . . 33
2.3.3.2 Model output . . . 34
2.4 Results and Discussion . . . 35
2.4.1 Alfonso basin sediment geochemistry, Organic Carbon (POC), and model fits . . . 35
2.4.2 Pore water SO_4^{2-}, [CH_4], and DIC . . . 36
2.4.3 Modeled rate profiles: GRR and SRR . . . 37
2.4.4 Sulfate $\delta^{34}S$ and $\Delta^{33}S$ profiles . . . 39
2.4.5 Fractionation factors ($^{34}\alpha_{SR}$ and $^{33}\lambda_{SR}$) and open-system modeling . . . 40
2.4.6 Environmental expression of S isotope effects and implications . . . 43
2.4.7 The Uniqueness of Alfonso Basin Sediments . . . 47

2.5 Conclusions . . . 49
2.6 Acknowledgements . . . 50
2.7 References . . . 51
2.8 Appendix . . . 56
2.8.1 Derivation of GRR and SRR in the Bulk Geochemical Model . . . 56
2.8.2 Derivation of upper boundary conditions for $[^{32}SO_4^{2-}]$, $[^{33}SO_4^{2-}]$, and $[^{34}SO_4^{2-}]$ from $\delta^{34}S_{SO4}$, and $\Delta^{33}S_{SO4}$ values of seawater SO_4 . . . 58
2.8.3 Lower boundary conditions for $[^{32}SO_4^{2-}]$, $[^{33}SO_4^{2-}]$, and $[^{34}SO_4^{2-}]$ . . . 60
2.8.4 Derivation of isotope (^{32}S, ^{33}S, and ^{34}S) specific rate terms ^{32}SRR, ^{33}SRR, and ^{34}SRR, and construction of the steady-state diagenetic equations . . . 60

3 A Multiple Sulfur isotope diagenetic model of Aarhus Bay Sediments: Reconciling Measurements with Reactive Transport . . . 68
3.1 Introduction . . . 69
3.1.1 Isotope Notation . . . 72
3.2 Aarhus Bay Sampling and Analytical Methods . . . 73
3.2.1 Site Characteristics and Geochemistry . . . 73
3.2.2 Coring and Porewater Chemistry . . . 73
3.2.3 Sulfur Isotope Analyses . . . 74
3.3 Model Construction . . . 75
3.3.1 Model Architecture and Operation . . . 75
3.3.2 Geochemical (POC, CH_4, SO_4^{2-}, H_2S, S^0, FeS, FeS_2, DIC) model . . . 76
3.3.2.1 Porosity . . . 76
3.3.2.2 Boundary conditions for pore water (CH_4, SO_4^{2-}, H_2S, Fe^{2+}) Species . . . 76
3.3.2.3 Solid phase (POC,'G', Fe^{3+}, S^0, FeS, FeS_2) Boundary conditions . . . 77
3.3.2.4 Physical Parameters and Diffusion Coefficients . . . 78
3.3.2.5 POC degradation Kinetics . . . 79
3.3.2.6 Bulk Geochemical Rates and Kinetics . . . 80
3.4 Results and Discussion . . . 85
3.4.1 Sediment and Pore water Geochemistry . . . 85
3.4.2 Depth—Rate and Depth—Concentration Profiles . . . 86
3.4.3 Isotope Dynamics—$^{34}\varepsilon_{SR}$ and $\delta^{34}S$ Model fits . . . 89
3.4.4 Influence of Methane Oxidation, Sulfide oxidation and disproportionation on S isotope geochemistry of Aarhus Bay Sediments . . . 92
3.4.5 Triple isotope (^{32}S, ^{33}S, ^{34}S) signatures . . . 94
3.4.6 Fe and oxidation chemistry . . . 97
3.4.7 Environmental implications of $^{34}\varepsilon_{SR}$ . . . 97
3.5 Conclusions . . . 100
3.6 Acknowledgements . . . 102
3.7 References . . . 102
3.8 Appendix . . . 105

4 The Minor Sulfur Isotope Composition of Cretaceous and Cenozoic Seawater Sulfate . . . 106
4.1 Introduction . . . 107
4.2 Materials and methods . . . 109
4.3 Results . . . 110
4.4 Discussion . . . 112
4.4.1 The Fidelity of Barite Records . . . 114

4.4.2 A 125 Million year Record of Seawater Sulfate 115
4.5 Conclusions 122
4.6 Acknowledgements 122
4.7 References 123
5 Conclusions & Future Directions 126

Appendix A1: Calibration of multiple Sulfur Isotope Measurements at Harvard University 131

Appendix A2: Minor S Isotope Signatures of Pore Water Sulfate Within Amazon Delta Sediments 143

Appendix A3: Placing an Upper limit on Cryptic sulfur cycling 148

List of Figures

Figure 2.1: Location and bathymetric map of Alfonso Basin 24
Figure 2.2: Porosity and POC models of Alfonso sediment core 37
Figure 2.3: Organic carbon remineralization and sulfate reduction rate models 38
Figure 2.4: Pore water SO_4, CH_4, DIC, Ca concentrations and model fits 39
Figure 2.5: Pore water $\delta^{34}S$ data and model fit 40
Figure 2.6: Pore water sulfate $\Delta^{33}S$ data and model fit 42
Figure 2.7: Triple isotope plot ($\delta^{34}S/\Delta^{33}S$) of pore water SO_4 data and model fits 42
Figure 2.8: Triple isotope plot of all CalMex basins measured:
Alfonso, Mazatlan, San Blas, and Santa Monica 48
Figure 2.9: Rate-fractionation relationship tests for Alfonso Basin 66

Figure 3.1: Map and sampling locality of Station M1 in Aarhus Bay, Denmark 73
Figure 3.2: Porosity and POC models of Aarhus Bay sediment core 77
Figure 3.3: Modeled rate profiles (SRR, MOR, and H_2SOR) 88
Figure 3.4: Modeled and measured concentration profiles of aqueous and solid phase species . . 88
Figure 3.5: Model fits of Aarhus Bay species, and tests of fractionation factor inputs 92
Figure 3.6: Triple isotope plot of SO_4^{2-}, H_2S, and FeS_2 95
Figure 3.7: Comparison of $^{34}\varepsilon_{SR}$ and $^{34}\varepsilon_{PY}$ 100

Figure 4.1: $\delta^{34}S$, $\Delta^{33}S$, $\Delta^{36}S$ values of Cretaceous and Cenozoic marine barite 111
Figure 4.2: Triple isotope ($\Delta^{33}S/\delta^{34}S$ and $\Delta^{36}S/\delta^{34}S$) plots of marine barite 112
Figure 4.3: Box and whisker plots ($\Delta^{33}S$ and $\Delta^{36}S$) of $\delta^{34}S$-binned data 115
Figure 4.4: $\Delta^{33}S/\Delta^{36}S$ plot of marine barite data 117
Figure 4.5: Box model $\Delta^{33}S$ test of sulfur cycle perturbation 121
Figure 4.6: Mixing model of evaporite dissolution 121

Figure A2.1: Location of coring site OST-2 within the Amazon Delta 143
Figure A2.2: Porewater SO_4 concentrations from OST-2 cores 2227 and 4121 145
Figure A2.3: Plot of $\delta^{34}S$ versus depth in cores 2227 and 4121 146
Figure A2.4: Triple isotope plot ($\delta^{34}S/\Delta^{33}S$) of pore water sulfate at 2227 and 4121 147

Figure A3.1: Establishing the isotopic composition of seawater sulfate 150
Figure A3.2: Pore water $\delta^{18}O$ profiles at high and low SRR 151
Figure A3.3: Model predictions for high and low rates of SRR 153

List of Tables

Table 1.1: Atomic abundance and atomic weight of the sulfur isotopes 5

Table 2.1: Boundary conditions of the baseline geochemical model for Alfonso Basin 28
Table 2.2: Physical parameters for the baseline model for Alfonso Basin 29
Table 2.3: Diffusion coefficients for pore water species 30
Table 2.4: Kinetic parameters for diagenetic equations 31
Table 2.5: Boundary conditions for three isotope sulfate diagenetic model 34
Table 2.6: Pore water data from Alfonso Basin 63

Table 3.1: Boundary condition of geochemical model for Aarhus Bay 78
Table 3.2: Physical parameters used in geochemical model 79
Table 3.3: Bulk diffusion coefficients for Aarhus Bay sediments 79
Table 3.4: Reactions considered in Aarhus Bay geochemical model 81
Table 3.5: Kinetic parameters and fractionation factors for diagenetic models 84
Table 3.6: Pore water and isotope data for Aarhus Bay Station M1 105

Table A1.1: Standard measurements of IAEA-S-1 at Harvard University 134
Table A1.2: Standard measurements of IAEA-S-2 at Harvard University 136
Table A1.3: Standard measurements of IAEA-S-3 at Harvard University 137
Table A1.4: Standard measurements of CDT versus 'HAR-1' at Harvard University 138
Table A1.5: Measurement of seawater sulfate (SW-SO_4) versus 'HAR-1' 139
Table A1.6: Inter-laboratory comparison of IAEA measurements on S-1 reference frame 140
Table A1.7: Sulfur isotopic composition of CDT and S-1 measurements at Harvard 141
Table A1.8: Sulfur isotopic compositions ($\Delta^{33}S$ and $\Delta^{36}S$ values) of IAEA-S-1 141
Table A1.9: Derivation of the sulfur isotopic composition of SW-SO_4 142

Table A2.1: Sampling, concentration, and isotope data of Amazon Delta pore waters 144

List of Equations

Equation 1.1: Definition of $\delta^{34}S$ with respect to VCDT . . . 3
Equation 1.2: Definition of $^{34}\alpha$ with respect to ^{34}R . . . 4
Equation 1.3: Definition of $^{33}\lambda$ . . . 4
Equation 1.4: Definition of $\Delta^{33}S$ with respect to ^{33}R and ^{34}R . . . 5
Equation 1.5: Definition of $\Delta^{36}S$ with respect to ^{36}R and ^{34}R . . . 5
Equation 1.6: Definition of $^{33}\lambda$ . . . 5
Equation 1.7: Definition of $^{36}\lambda$ . . . 5
Equation 1.8: Simplified sulfate reduction pathway . . . 6
Equation 1.9: Reactive transport equation . . . 12

Equation 2.1: Definition of $\delta^{34}S$ . . . 21
Equation 2.2: Definition of $\Delta^{33}S$ . . . 22
Equation 2.3: Definition of $^{33}\lambda$ with respect to α . . . 22
Equation 2.4: Derivation of $^{33}\alpha$ . . . 33
Equation 2.5: Definition of maximum csSRR . . . 46
Equation 2.6: Definition of minimum csSRR . . . 46
Equation 2.7: Steady-state reactive transport equation for an aqueous species . . . 56
Equation 2.8: Steady-state reactive transport equation for a solid-phase species . . . 56
Equations 2.9: Derivation of fractional abundances of G_n . . . 57
Equation 2.10: Reactive transport equation for G_n . . . 57
Equation 2.11: Derivation of remineralization rate GRR_{PW} . . . 57
Equations 2.12: Derivation of SRR_{PW} . . . 57
Equations 2.13: Derivation of methane production rate CH_4PR . . . 58
Equation 2.14: Isotope mass balance equation for $[SO_4^{2-}]$ . . . 58
Equations 2.15: Natural abundance ratios ^{33}F and ^{34}F . . . 58
Equations 2.15: Natural abundance ratios ^{33}F and ^{34}F . . . 59
Equations 2.16: Natural ratio ($^{33}F/^{34}F$) . . . 59
Equation 2.17: $[SO_4^{2-}]$ with respect to $[^{32}SO_4^{2-}]$ . . . 59
Equation 2.18: $[^{32}SO_4^{2-}]$ with respect to $[SO_4^{2-}]$ . . . 59
Equation 2.19: $[SO_4^{2-}]$ with respect to $[^{33}SO_4^{2-}]$ . . . 59
Equation 2.20: $[^{33}SO_4^{2-}]$ with respect to $[SO_4^{2-}]$ . . . 59
Equation 2.20: $[SO_4^{2-}]$ with respect to $[^{33}SO_4^{2-}]$ . . . 59
Equation 2.21: $[^{33}SO_4^{2-}]$ with respect to $[SO_4^{2-}]$ . . . 59
Equation 2.21: $[SO_4^{2-}]$ with respect to $[^{34}SO_4^{2-}]$ . . . 59
Equation 2.22: $[^{34}SO_4^{2-}]$ with respect to $[SO_4^{2-}]$ . . . 59
Equation 2.23: Lower boundary conditions for $[^{3x}SO_4^{2-}]$ . . . 60
Equation 2.24: Definition of $^{33}\lambda_{SR}$ . . . 60
Equation 2.25: Definition of ^{32}SRR . . . 61
Equation 2.26: Definition of ^{33}SRR . . . 61
Equation 2.27: Definition of ^{34}SRR . . . 61
Equation 2.28: ^{32}SRR with respect to ^{33}SRR . . . 61
Equation 2.29: ^{32}SRR with respect to ^{34}SRR . . . 61
Equation 2.30: Isotope mass balance of SRR . . . 61
Equation 2.31a: Derivation of ^{32}SRR with respect to α's and $[^{3X}SO_4^{2-}]$ . . . 61
Equation 2.31b: Derivation of ^{33}SRR with respect to α's and $[^{3X}SO_4^{2-}]$ . . . 61
Equation 2.31c: Derivation of ^{34}SRR with respect to α's and $[^{3X}SO_4^{2-}]$ . . . 61
Equation 2.32a: Derivation of ^{32}SRR with respect to α's and $[^{3X}SO_4^{2-}]$ . . . 62
Equation 2.32b: Derivation of ^{33}SRR with respect to α's and $[^{3X}SO_4^{2-}]$ . . . 62
Equation 2.32c: Derivation of ^{34}SRR with respect to α's and $[^{3X}SO_4^{2-}]$ . . . 62

Equation 4.1: Definition of $\Delta^{33}S$ 110
Equation 4.2: Definition of $\Delta^{36}S$ 110
Equation 4.3: Derivation of the sulfur mass balance of a single-box ocean 118
Equation 4.4: Derivation of the sulfur isotope mass-balance of seawater sulfate 118
Equation 4.5: Derivation of ^{33}R of seawater sulfate 119
Equation 4.6: Derivation of ^{34}R of seawater sulfate 119
Equation 4.7: Derivation of ^{33}R of seawater sulfate with respect to pyrite burial 119
Equation 4.8: Derivation of ^{34}R of seawater sulfate with respect to pyrite burial 119
Equation 4.9: $\delta^{33}S$ values derived from evaporite mixing 120
Equation 4.10: $\delta^{34}S$ values derived from evaporite mixing 120

Acknowledgements

First and foremost, I would like to express my gratitude for my advisor, Dave Johnston. Over the past twelve years, Dave has provided the guidance, both scientific and technical, to help me forge a path as a scientist. He taught me how to use my first mass spectrometer and the techniques of stable isotope geochemistry at the University of Maryland. He had enough confidence in my abilities to bring me on as his lab manager in 2010, and then as a graduate student a year later. Despite my occasionally free-wheeling approach to lab construction he gave me a great deal of financial and personal space for instrument development and graciously provided me with funding during my Ph.D. Thanks for all the great years, Dave. The next Santa Fe beers are on me.

I would also especially like to thank the members of my committee, Dan Schrag for his keen geochemical insights and for always pushing the scope of a good scientific question, and Ann Pearson, for her guidance, for sharing her encyclopedic knowledge of low-T isotope geochemistry, and technical writing advice. Faculty from other institutions also provided substantial help. Will Berelson from USC allowed me access to his sample archive and provided key insights on S/C cycling. Bob Aller from Stony Brook University graciously provided Amazon delta samples. Marc Alperin from UNC taught me the techniques of building reactive transport models and provided me with access to his Fortran code, carefully crafted and tested over 25 years. James Farquhar of the University of Maryland has been a mentor and friend for more than a decade, always lending technical, professional, and scientific advice. Boz Wing has also been an insightful mentor for a fledgling scientist, doggedly pursuing quantitative approaches to biogeochemical problems and pushing me to do the same.

Many colleagues and lab contemporaries have contributed directly or indirectly to this thesis over the years, providing advice, technical help, *eureka* moments, and sounding boards. Though there are too many to count, I'll try to express some of my thanks here. Ben Gill, Wil Leavitt, Jc Creveling, Scott Wankel, Erik Sperling, Alex Bradley, Renata, Esther and Tor led the initial J-lab charge, getting the instrumentation up and running and framing the research during those early years. Wil fostered the transition of the lab into a 'culturally' active place, microbially and otherwise, and made it a great place to be. Viv and Ben C. brought new research backgrounds and put up with my training protocols. Maya

and Greg brought cheer and endless enthusiasm for biogeochemistry, and Alan Rooney brought advice on Scotch selection. Emma Bertran brought comic relief via XKCD, Frasier ultimate Frisbee advice, and Anna joined me in the box-modeling trenches. Erin Beirne took the reins as lab manager, provided five years of great conversation and cooking tips, and took my unsolicited technical advice and frequent Simpsons references in stride. Thanks, Erin, for being a great friend and officemate.

The graduate student community at Harvard is a vibrant one, and I would be remiss to not mention some of my colleagues, including third floor groupies past and present: Itay, Kate, Sierra, Tom, Lauren, Scott, Katie, and Ploy. Pearson Lab folks provided friendship and chemostat discussion groups: Sarah H., Elise, and Hilary, and MacDonald lab folks provided mineral separation and outdoor adventure advice: Justin, Emmy, Blake, and Uyanga. Other members of the G1 class of 2011: Shannon, Joe, Jacky, Will, and Emily Estes, how far we've come.

Thanks go to department staff who have created a productive environment over the past six years and made all of our lives easier: Sabinna, Sarah Colgan, Chenoweth, Maryorie and Paul Kelley. A special thanks go to Mitra, Eric, and Bobby for always heeding my technical requests and drumming up spare parts and lab furniture from around campus. Roommates past and present brought great times, homebrew, foosball, and lifelong friendships: Yoel and Nancy, Nigel and Emily, Evan and Susie, and honorary roommate Martha Munoz. Rob Masek and the other scientists and artists at the Artisan's Asylum brought creative inspiration, and Krishanu Sankar and the members of Cambridge Running Club, grueling workouts and improved race performances.

Lastly, I would like to thank my family: Mom and Dad, for always encouraging my scientific, creative, and technical interests, my siblings and niece and nephew for providing welcome distractions, and especially my in-laws Michele and Chuck Rehberg, for graciously taking me in and providing a home-away-from-home. To my loving, genuine and caring wife, Julia, thank you for giving me the fortitude and strength to follow through, and for being a beacon of hope and affirmation in our two grad student household.

For my mother, an artist. For my father, a storyteller. For my late Uncle Brian, a craftsman.

CHAPTER 1

INTRODUCTION

1 INTRODUCTION

Understanding and quantifying biogeochemical sulfur cycling at its smallest analytically practical scale—marine sediments and their interstitial waters—is key to reconstructing the cycle's larger scale interaction with the carbon and iron cycles. Sulfur isotope geochemistry has historically provided the most powerful tool for understanding microbially mediated sedimentary S cycling, and in recent years, a renaissance in the analytical techniques of minor S isotope (^{33}S and ^{36}S) geochemistry has opened up a new avenue of research (Farquhar et al., 2000, Farquhar et al., 2003). The ensuing studies provided key insights into microbial metabolism and physiology (Fike et al., 2015; Bradley et al. 2015; Leavitt et al., 2014; Leavitt et al., 2013; Sim et al., 2011a; Sim et al., 2011b; Johnston et al., 2011; Zerkle et al., 2009; Johnston et al., 2008; Farquhar et al. 2008; Johnston et al., 2007; Johnston et al., 2005; Farquhar et al., 2003). While some of those studies have highlighted the potential of multiple S isotopes as a tool for reconstructing environmental S cycling, none have employed direct measurements to place those physiological and metabolic constraints into a broader geochemical context.

This thesis chronicles the methodological development of multiple S isotope measurements at Harvard University and provides the first quantitative study of how minor S isotope biosignatures are produced and diagenetically inherited in sedimentary systems. One dimensional reactive transport models of two geochemically well-characterized continental margin settings (Alfonso Basin, Gulf of California, and Aarhus Bay, Denmark) are presented and their isotope signatures placed in the context currently understood from microbial calibrations. Additionally, this thesis revisits a critical historical

(0-120 Ma) sulfate proxy record of marine barite (Paytan et al., 2004; Paytan et al., 1998) using minor isotope techniques, to place constraints on the magnitude of fluxes (*e.g.*, sedimentary pyrite burial) capable of influencing that isotope record on million year time scales. As a preface to the thesis, in this chapter I introduce sulfur isotope geochemistry and its use in reconstructing Earth's surface S cycle, detail the nomenclature used by the minor S isotope community, and provide a brief overview of the work to date in understanding microbial physiology and the role of S in marine sediment geochemistry. This provides the foundation from which the manuscripts that comprise this dissertation will draw.

1.1 EARTH'S SURFACE SULFUR CYCLE

Sulfur is the 15th most abundant element in the continental crust, representing ~0.042% by mass. Its multiple stable oxidation states allow for its deep role in the redox evolution of the Earth's surface. The burial of reduced sulfur as pyrite (FeS_2), in addition to reduced carbon burial allow for the net accumulation of O_2 in Earth's atmosphere on geologic timescales (Hayes and Waldbauer, 2006; Berner, 1982). On the other hand, the oxidative weathering of sulfides—including igneous and sedimentary pyrite, has produced the largest reservoir of S on the Earth's surface, as seawater sulfate (SO_4). At ~28 mmol/L, seawater sulfate constitutes ~$3.8x10^{19}$ moles S and carries more oxidative capacity than atmospheric O_2 (Hayes and Waldbauer, 2006).

Sulfate serves as a terminal electron acceptor for microbially mediated organic matter remineralization, and in marine sediments is responsible for >50% of total sedimentary particulate organic carbon (POC) oxidation (Jørgensen, 1982). Microbial sulfate reduction (MSR), a metabolism that couples the dissimilatory reduction of sulfate (*cf.* Bradley et al., 2011) to electron donor (organic carbon) oxidation produces hydrogen sulfide (H_2S). This biogenic sulfide is either lost to pyrite burial, or is alternatively reoxidized to sulfate in an intricate pathway of biologically and abiologically mediated reactions (Zopfi et al., 2004). Terminal sulfide loss via sedimentary pyrite represents the largest flux out of the seawater sulfate reservoir. Globally averaged estimates of sulfate reduction rates

(SRR) for marine sediments vary depending on the technique used, but range from ($1.1x10^{13}$ moles/yr to $7.5x10^{13}$ moles/yr) (*e.g.*, Jørgensen, 2006, Bowles et al., 2014), whereas pyrite burial estimates are an order of magnitude lower. This implies that a substantial portion of the sulfate reduced to sulfide *in situ* is reoxidized and escapes terminal burial. This oxidative sulfur cycling, and the consequently long residence time of sulfate in the oceans, carries deep implications for the isotope records used to understand and quantify the fluxes in the biogeochemical sulfur cycle, introduced and discussed below.

1.2 SULFUR ISOTOPE SYSTEMATICS

Sulfur has four stable isotopes (^{32}S, ^{33}S, ^{34}S, ^{36}S) with atomic masses and mole fractions as listed in Table 1.1 below (Audi and Wapstra, 1993; Ding et al., 2001; Coplen et al., 2002):

Isotope	**Atomic Mass[1]**	**Mole Fraction[2]**
^{32}S	31.972 070 73(15)	0.950 3957(90)
^{33}S	32.971 458 54(15)	0.007 4865(12)
^{34}S	33.967 866 87(14)	0.041 9719(87)
^{36}S	35.967 080 88(25)	0.000 1459(21)

Table 1.1: Atomic Masses and mole fractions of the four stable isotopes of sulfur, with an assumed composition of $\delta^{34}S = 0‰$. Information is as compiled in Coplen et al. (2002).
[1] Audi and Wapstra (1993)
[2] Ding et al., (2001)

Of the four stable isotopes, ^{32}S is the most abundant (95.04%), followed by ^{34}S (4.20%). The two less abundant of the four isotopes are frequently referred to as *minor isotopes*, and include ^{33}S (0.75%) and ^{36}S (0.015%). For analytical and historical reasons, the ^{32}S and ^{34}S are the most frequently measured, and reported as ($^{34}S/^{32}S$) ratios with respect to a standard (Vienna Canon Diablo Troilite, 'VCDT') using δ-notation:

$$\delta^{34}S = 1000 \times \left(\frac{\left(^{34}S/^{32}S\right)_{sample}}{\left(^{34}S/^{32}S\right)_{VCDT}} + 1 \right) \quad = \quad 1000 \times \left(\frac{R^{34}_{sample}}{R^{34}_{VCDT}} + 1 \right) \quad (‰) \tag{1.1}$$

where δ–values are reported in parts per thousand, or per mil (‰). The R^{34} is shorthand notation for an isotope abundance ratio (*e.g.*, $^{34}S/^{32}S$) and can be written with the other isotopes of sulfur in mind, in sum referred to as the *multiple* S isotopes.

1.2.1 MULTIPLE S ISOTOPE NOMENCLATURE

Although researchers initially measured all four stable isotopes more than fifty years ago for cosmochemical studies (Hulston and Thode, 1965a; Hulston and Thode, 1965b), it was thought that the variations in the abundance of ^{33}S and ^{36}S were predictable using accurate measurements of $\delta^{34}S$ values and quantum mechanical first principles. For example, consider a single-step (bio)chemical process imparting a fractionation (denoted by the fractionation factor α), which, for a dual isotope system, *e.g.*, for $^{34}S/^{32}S$:

$$A \xrightarrow{^{34}\alpha_{A-B}} B, \qquad ^{34}\alpha = \frac{R_A^{34}}{R_B^{34}} \tag{1.2}$$

Introducing a second isotope system ($^{33}S/^{32}S$), simple quantum mechanical characterizations of equilibrium processes detail that the relationship between the fractionation factors $^{33}\alpha$ and $^{34}\alpha$ can be described by a *mass fractionation law* (*cf*. Young et al., 2002):

$$^{33}\beta_{A-B} = \frac{ln(^{33}\alpha_{A-B})}{ln(^{34}\alpha_{A-B})} = \frac{\left(\frac{1}{m_{32}} - \frac{1}{m_{33}}\right)}{\left(\frac{1}{m_{32}} - \frac{1}{m_{34}}\right)} \tag{1.3}$$

Using atomic masses from Table 1.1 this *mass law* predicts a $^{33}\beta_{A\text{-}B} = 0.5159$ for high temperature equilibrium processes. Repeating for the remaining triple isotope system ($^{32}S/^{34}S/^{36}S$) yields a theoretical $^{36}\beta_{A\text{-}B} = 1.89$. Most natural processes (microbial, chemical) operating on the Earth's surface abide closely by these mass laws, and produce characteristic fractionation arrays (*e.g.*, $\delta^{33}S$ vs. $\delta^{34}S$) with a predictable correlation ($\delta^{33}S \sim 0.5\delta^{34}S$). Given this predictable fractionation array, and with the analytical complexity of the minor isotope measurements, sulfur isotope geochemistry for

most of the next 35 years (1965-2000) focused almost exclusively on natural variability in ($^{34}S/^{32}S$) ratios, excluding ^{33}S and ^{36}S.

The discovery of large *mass-independent* signatures in the Archean sulfur isotope record and the elucidation of the physical chemical processes that produce them (Farquhar et al. 2000; Farquhar et al., 2001; Farquhar and Wing, 2003) renewed interest in minor S isotope geochemistry. Subsequent measurements of ^{33}S and ^{36}S in biological samples (Farquhar et al., 2003) opened the door for the study of *mass-dependent* variability observed in microbiological samples. Studies of both mass-dependent and mass-independent S isotope fractionation emplace a reference frame that relies on the high-T equilibrium relationship (*e.g.*, Eq. 1.3) to quantify $\Delta^{33}S$ and $\Delta^{36}S$ values:

$$\Delta^{33}S_{A-B} = \delta^{33}S_{A-B} - 1000 \times \left(\left(\frac{\delta^{34}S_{A-B}}{1000} + 1\right)^{0.515} - 1\right) \quad = \quad 1000 \times \left(R^{33}_{A-B} - (R^{34}_{A-B})^{0.515}\right) \tag{1.4}$$

$$\Delta^{36}S_{A-B} = \delta^{36}S_{A-B} - 1000 \times \left(\left(\frac{\delta^{34}S_{A-B}}{1000} + 1\right)^{1.9} - 1\right) \quad = \quad 1000 \times \left(R^{36}_{A-B} - (R^{34}_{A-B})^{1.9}\right) \tag{1.5}$$

where $\Delta^{33}S_{A\text{-}B}$ and $\Delta^{36}S_{A\text{-}B}$ relate the isotopic compositions between two pools, A and B. Those values are frequently reported on a universal reference frame with VCDT defining $\delta^{34}S = 0$, $\Delta^{33}S = 0$, and $\Delta^{36}S = 0$, (*cf.* Wing and Farquhar, 2015; Ono et al., 2006). In reality, the isotopic relationship between any two analytical pools can be described using Eqns 1.4 and 1.5. In the case of positive $\Delta^{33}S$ and $\Delta^{36}S$ values, samples contain more ^{33}S and ^{36}S than described by high-T equilibrium, and vice versa. Additionally, it is possible to describe the relationship between two different pools (again A and B) using the values $^{33}\lambda_{A\text{-}B}$ and $^{36}\lambda_{A\text{-}B}$:

$$^{33}\lambda_{A-B} = \frac{ln(\delta^{33}S_A/1000 + 1) - ln(\delta^{33}S_B/1000 + 1)}{ln(\delta^{34}S_A/1000 + 1) - ln(\delta^{34}S_B/1000 + 1)} = \frac{ln(R^{33}_{A-B})}{ln(R^{34}_{A-B})} \tag{1.6}$$

$$^{36}\lambda_{A-B} = \frac{ln(\delta^{36}S_A/1000 + 1) - ln(\delta^{36}S_B/1000 + 1)}{ln(\delta^{34}S_A/1000 + 1) - ln(\delta^{34}S_B/1000 + 1)} = \frac{ln(R^{36}_{A-B})}{ln(R^{34}_{A-B})} \tag{1.7}$$

where these values approximate the slope of a line connecting the two compositional points A and B in a triple isotope reference frame. Two samples at equilibrium in this case would possess $^{33}\lambda_{A\text{-}B}$ and $^{36}\lambda_{A\text{-}B}$ values of 0.515 and 1.9, respectively. Deviations from those values, related to compositional variability, will also manifest as non-zero $\Delta^{33}S_{A\text{-}B}$ and $\Delta^{36}S_{A\text{-}B}$ values. This can be the result of mass-conservation (and mixing), both at the metabolic and geochemical levels (*cf*. Farquhar et al., 2007). The usage of this notation (Δ and λ values) is the primary means of describing the minor isotope fractionation characteristics detailed for microbial experiments.

1.2.2 MULTIPLE S ISOTOPE INSIGHTS INTO MICROBIAL METABOLISMS

Historically, researchers in low temperature S isotope biogeochemistry focused on understanding the factors controlling the fractionation capacity of a specific organism or metabolism, like microbial sulfate reduction. These experimental constraints are then used in drawing the connection to modern sediments to infer characteristics about environmental S cycling. The earliest research primarily considered MSR and its biochemical and isotopic characteristics (*e.g*., Rees et al., 1973; Kemp and Thode, 1968; Kaplan and Rittenberg, 1964; Peck, 1961; Peck, 1959; Harrison and Thode, 1958; Jones and Starkey, 1957). From that early work emerged a model (Rees et al., 1973) that considered dissimilatory sulfate reduction (DSR, the biochemical pathway of sulfate reducers) as a series of enzymatic steps to which individual ($^{34}S/^{32}S$) fractionation characteristics can be ascribed:

$$SO_4^{2-} \rightleftharpoons \boxed{SO_4^{2-} \rightleftharpoons APS \rightleftharpoons SO_3^{2-}} \rightarrow H_2S \tag{1.8}$$

where the reactants, intermediates, and products are sulfate (SO_4^{2-}), adenosine-5'-phosphosulfate (APS), sulfite (SO_3^{2-}) and hydrogen sulfide (H_2S) (modeled after Johnston, 2011; Bradley et al., 2011). Rees et al. (1973) initially prescribed empirically derived fractionation factors for the steps in the network (sulfate transport, APS activation, APS reduction, and sulfite reduction) to explain the *total* fractionation of the DSR pathway between sulfate and sulfide. The application of his steady state

isotope fractionation model, in concert with the recycling of S intermediates, was the first to aim to quantify the influence of S intermediate recycling on the fractionation magnitude of the DSR pathway. A subsequent study of organic-carbon limited continuous cultures of a laboratory sulfate reducer *Desulfovibrio desulfuricans* (Chambers and Trudinger, 1975) demonstrated that the S isotope fractionation also varies inversely as a function of the specific rate of sulfate reduction—S isotope fractionation is not fixed by individual biochemistry of a sulfate reducer, but is instead related to the rate of metabolism. Since specific rate is also related to the recycling of S-intermediates, those continuous culture experiments can be recognized as one of the earliest empirical validations of Rees' steady-state model.

In the late 1980's, researchers isolated a new energy metabolism coupled to the inorganic fermentation of inorganic sulfur compounds, (*e.g.*, sulfite, thiosulfate, and elemental sulfur).(Bak and Pfennig, 1987). An isolated organism produced both sulfate and sulfide from the fermentation of a single S compound of intermediate valence—carrying important implications for the interpretation of environmental S cycling where chemical oxidation of sulfide in the presence of O_2 and Fe^{3+} produces a vast array of S intermediates (*cf.* Zopfi et al., 2004). The discovery of additional types of microbial S disproportionation (MSD) (Thamdrup et al., 1993), and the isotopic characterization of those collective pathways (Habicht et al. 1998; Habicht et al., 1997) demonstrated that oxidative sulfur cycling plays a powerful role both in the geochemistry of modern marine sediments, and their S isotopic characteristics. Researchers extended that understanding of oxidative sulfur cycling to deep time records, and used the temporal range of variability in $\delta^{34}S$ proxy records to infer the history of the progressive oxygenation of Earth's surface (Canfield, 2004; Canfield et al., 1998; Canfield and Teske, 1996). The central issue in using $\delta^{34}S$-based records to infer the presence of a metabolism and its geochemical drivers, however, are the non-uniqueness of their signatures. Microbial sulfate reduction and microbial sulfur disproportionation each produce ^{34}S-enriched sulfate, and ^{34}S-depleted sulfides and only non-quantitative estimates of the contribution of each metabolism can be inferred.

With the re-emergence of minor isotope techniques in the early 2000's — in response to the discovery of mass-independent S isotope fractionation signatures in Archean (Farquhar et al., 2000) sedimentary sulfides — studies of purely mass-dependent systems (microbial, biochemical) showed that significant variations in $\Delta^{33}S$ ($\geq \pm 0.05‰$) and $\Delta^{36}S$ ($\geq \pm 0.2‰$) also exist. These variations, entirely within the analytical precision of SF_6-based techniques (Farquhar and Wing, 2003), expanded the understanding of S metabolisms. This is true both in terms of the network structure of MSR and MSD, as well as in the extension of those relationships to the geological sulfur isotope record (Johnston et al., 2008; Johnston et al., 2007; Ono et al., 2006; Johnston et al., 2005a; Johnston et al., 2005b; Farquhar et al., 2003). Furthermore, those studies showcased the benefits of including ^{33}S and ^{36}S measurements in microbial and geochemical studies because the precision of $\Delta^{33}S$ and $\Delta^{36}S$ measurements allowed for the distinction of MSR and MSD independent of $\delta^{34}S$ measurements alone. That research led to a series of studies highlighting the minor isotope characteristics of MSR in batch experiments (Leavitt et al., 2014; Sim et al., 2012; Sim et al., 2011a; Sim et al., 2011b), continuous culture experiments (Leavitt et al., 2013) and pure enzyme studies (Leavitt et al., 2015). Leavitt et al. (2013) provided evidence corroborating the results of Chambers and Trudinger (1975) that fractionation relationships—in this case both $^{34}\alpha_{SR}$ and $^{33}\lambda_{SR}$—are linked to the specific rate of sulfate-reduction. Low rates are correlated with large (>50‰) S isotope fractionation and $^{33}\lambda_{SR}$ approaching the thermodynamic limit of ~0.515, with a diminution of both at high specific rates. It is unknown whether this rate relationship holds in natural systems, and quantitatively how important that relationship is in controlling the S-isotope characteristics of marine sediments. This final question is one of the key targets of this dissertation.

1.2.3 ANALYTICAL METHODS FOR MULTIPLE S ISOTOPE GEOCHEMISTRY

The analytical methods for multiple S isotope geochemistry were established in the early 1960's for cosmochemical studies exploring the abundance of ^{33}S and ^{36}S in meteorites (Hulston and Thode, 1965a; Hulston and Thode, 1965b). These studies used fluorination chemistry to generate SF_6 as an

analyte gas. This is useful given that fluorine is mono-isotopic. In contrast to studies using common SO_2-based methods, which are largely only useful for ($^{34}S/^{32}S$) measurements, SF_6-based techniques have sufficient precision to be useful for studying mass-dependent variability in $\Delta^{33}S$ and $\Delta^{36}S$ due to the purity and physical chemical properties of the analyte, and the high mass resolution achievable by measuring SF_5^+ (m/z = 127, 128, 129, 131 for $^{32}SF_5^+$, $^{33}SF_5^+$, $^{34}SF_5^+$, $^{36}SF_5^+$). The difficulty lies in generating SF_6 from geologically relevant materials, requiring a fluorination agent, either bromine pentafluoride (BrF_5) or pure fluorine gas (F_2), and Ag_2S as the starting S compound. The introduction of methods for purifying F_2 gas aided the problem of dealing with contaminating gases like CF_4 and O_2 (Asprey, 1976). Further, the application of laser-based microanalytical techniques in fluorination also improved precision and sample throughput (Rumble et al., 1997). With developments in mass-spectrometry and purification chemistry, sulfur hexafluoride based methods for S isotope chemistry have improved precision on $\Delta^{33}S$ and $\Delta^{36}S$ measurements to the parts per million level (*cf*. Johnston et al., 2014; Ono et al., 2012), with σ-$\Delta^{33}S$ = 0.006‰, and σ-$\Delta^{36}S$ = 0.1‰ frequently reported. This high precision of quadruple S isotope variability is precisely the reason that the natural range of mass-dependent signatures (0.3‰ and 2.0‰, respectively), such as those detailed in this study, can be readily explored.

1.3 ROLE OF SULFUR IN EARLY DIAGENESIS OF MARINE SEDIMENTS

The high concentration of sulfate in the seawater (28 mmol/L), its role as a terminal electron acceptor for microbial metabolism, and the interaction of its reduced products (*e.g.*, H_2S) with reactive iron oxy(hydroxides) mean that sulfur has an integral part in the biogeochemistry of early diagenesis. A full description of that role is beyond the scope of this contribution, thus this section focuses on (i) the use of sulfate concentration profiles to infer aspects of organic matter degradation kinetics, and (ii) the use of S isotope distributions in marine sediments and interstitial waters to infer microbial activity.

1.3.1 SEDIMENTARY S/C CYCLING

Determination of *in situ* sulfate reduction rates with radiotracer ($^{35}SO_4^{2-}$) techniques have been used in concert with benthic dissolved oxygen concentrations to estimate the contribution of sulfate reduction to total organic carbon remineralization in marine sediments at greater than 50% (Jørgensen, 1982). Sulfate is a terminal electron acceptor for 'classic' organoclastic sulfate reduction, where the electron donors are generally short chain organic compounds (acetate, lactate, propionate), and anaerobic methane oxidation (AOM), where the electron donor is dissolved methane (CH_4) derived from methanogenic degradation of organic carbon under sulfate-limiting conditions (*cf.* Tarpgaard et al., 2011; Boetius et al., 2000). Although other terminal electron acceptors (NO_3^-, Fe^{3+}, Mn^{4+}) are responsible for some organic carbon remineralization in marginal sediments, it is thought that, on average, they contribute <10% to the total oxidant budget of shelf environments (Aller, 2014; Meister, et al., 2013). It is worth noting that the fraction of sedimentary organic carbon lost to sulfate reduction drops off significantly at water depths >1000 m, driven primarily by lower TOC contents of deep sea sediments and an increased role for oxic respiration.

Empirical and model studies of sulfate concentration profiles are employed frequently to infer organic carbon degradation kinetics in marine systems. With the mathematical formulations of Berner, 1980, studies validated the 'G' model of POC remineralization (Westrich and Berner, 1984). Here, G is a term describing the pool of reactive organic carbon in a sedimentary system that is subject to first-order decay kinetics. Multi-G models (Berner and Westrich, 1984) expanded this to include multiple 'G' pools that are binned by their reactivity, and share a single decay constant. These studies also recognized that *in situ* rates of sulfate reduction are also largely independent of sulfate concentration above ~1 mmol/kg, and likely even less than that threshold. Together these results implied that sulfate loss due to microbial sulfate reduction in sediments is independent of sulfate concentration and the kinetics of its consumption are driven almost exclusively by organic carbon reactivity. Subsequent research has updated the sulfate concentration thresholds to include different microbial physiologies, with different sulfate affinities, but the threshold is still estimated to be between 50-200 μmol/kg

(Bradley, 2015; Tarpgaard et al., 2011). The abundance and reactivity of sedimentary POC thus controls the sulfate concentration profile in marine sediments, and is the primary factor controlling the bulk rate of *in situ* sulfate reduction.

The organic carbon that escapes remineralization via sulfate reduction in marine sediments is available to be converted to methane deeper in the sediment column. Pore water methane is then free to diffuse towards the sediment water interface, and most is lost to AOM mediated by a microbial consortium with sulfate as an electron acceptor (*cf.* Alperin and Hoehler, 2010; Alperin and Hoehler, 2009; Boetius et al., 2000; Hoehler et al., 1994). The exact mechanism of AOM is unclear, but what is agreed upon is that AOM represents another significant loss pathway for sulfate within marine sediments. Estimates for the total fraction of sulfate consumed via AOM, as opposed to organoclastic sulfate reduction, vary widely (1-90%) and depend strongly on environment (*cf.* Jørgensen, 2010; Reeburgh, 2007).

1.3.2 REACTIVE TRANSPORT MODELING OF SEDIMENTARY SYSTEMS

Diagenetic modeling, a branch of reactive transport modeling in porous media, is the primary means of inferring *in situ* biogeochemical rate information in sedimentary systems. Complementing the analytically challenging, radiometric measurements that are frequently used, diagenetic modeling quantifies rates by reconciling concentration information with physical transport processes (diffusion and advection). Marine sediments are, by volume, mostly interstitial water and, except in cases of extreme sedimentation, aqueous diffusion represents the primary means of transport. The mathematical modeling of sediments and pore waters has been diligently described in several textbooks (Boudreau, 1997; Berner, 1980) and reams of scientific papers. Numerous software packages, such as PROFILE have been created for reactive transport modeling of sedimentary systems (*cf.* Berg et al., 1998). With that said, we provide only very brief overview of the models constructed and employed in this thesis.

Steady-state diagenetic modeling relies on the assumptions that (i) pore water concentrations of species/metabolites are not changing and (ii) boundary conditions, such as those inferred from the sediment water interface (SWI), also remain constant. Certainly this is not always true, and researchers have noted particular cases in dynamic physical regimes where sedimentation and pore water geochemistry are fundamentally out of steady-state. The Amazon Delta and regions near Papua New Guinea are now classic examples (*e.g.*, Aller et al., 2010). However, many, relatively quiescent continental margin sediments approximate steady-state conditions. For that case, a reactive transport equation frequently used (eq 1.9) modified from Boudreau (1997):

$$\underbrace{\varphi^2 D \frac{d^2 c_{pw}}{dx}}_{\text{diffusion}} + \underbrace{\left(3\varphi D \frac{d\varphi}{dx} - \frac{\omega_\infty \varphi_\infty}{\varphi}\right) \frac{dc_{pw}}{dx}}_{\text{advection}} + \underbrace{\Sigma R_{pw}}_{\text{reaction}} = 0 \qquad (1.9)$$

where c is a general pore water species, D is a the diffusivity, φ is the porosity, ω is the sedimentation rate, and R is the reactive production or loss of species c. The terms approximating the diffusion, advection and reaction are shown. In the non-steady case, eq. 1.9 equals ∂c/∂t, the depth-dependent change in concentration with time. All the terms in eq. 1.9, with the exception of the reaction term, are measured or known for a specific environment (diffusion terms are known for most species in seawater, as are their relationship to pressure, temperature, and salinity, and the sedimentation rate is usually known from site-specific radiometric assays). Thus, the primary goal of most diagenetic models is to infer the depth-dependent reaction term, and to reconcile it with measured or empirically calibrated biogeochemical rate information. Predictive models are occasionally used in the absence of any analytical information. In this thesis, we use variations of equation 1.9 to predict rate information, such as the sulfate reduction rate (SRR), the methane oxidation rate (MOR), and the pyrite precipitation rate (FeS_2FR), to understand the concentration data of two margin settings, and use an isotope-dependent modified version of equation 1.9 to understand S isotope distributions for the S-bearing species observed in those systems. Those S isotope-specific models have been constructed by

others researchers to explain isotope distributions (Dale et al., 2009; Donahue et al., 2008; Jørgensen, 1979), but have never explicitly included ^{33}S.

1.4 ISOTOPE RECORDS OF THE GLOBAL BIOGEOCHEMICAL S CYCLE

Our understanding of the global biogeochemical sulfur cycle in the late Cretaceous and Cenozoic has benefited from the construction of a time-calibrated $\delta^{34}S$ record of seawater sulfate from marine barite ($BaSO_4$) isolated from deep sea sediment cores. A pair of studies produced the $\delta^{34}S$ record of Cenozoic (0-65 Ma) seawater sulfate (Paytan et al., 1998) and the later Cretaceous (Paytan et al., 2004). In the light of substantial variability in the major ion composition of seawater, including sulfate, through the Phanerozoic (*e.g.,* Brennan et al., 2013; Lowenstein et al., 2003; Horita et al., 2002; Lowenstein et al., 2001), researchers have attempted to understand the changes in the biogeochemical S cycle by modeling the $\delta^{34}S$ excursions in this proxy record. Models have suggested major perturbations in the C cycle at the Paleocene-Eocene Thermal Maximum (PETM), and invoked massive changes in the pyrite and evaporitic sulfate burial fluxes in the Cretaceous (Wortmann et al., 2012; Halevy et al., 2012) to explain earlier isotopic excursions. Previous researchers suggest that the characteristic $\Delta^{33}S/\delta^{34}S$ isotope signatures associated with sulfate reduction—and indeed other microbial processes—are reflected in other Phanerozoic S isotope records (Wu et al., 2014; Wu et al., 2010), and have incorporated ^{33}S into global models of the S cycle. In this thesis, I present a similar analysis for the samples original presented in Paytan et al. (2004) and Paytan et al. (1998), re-evaluated to include $\Delta^{33}S$ and $\Delta^{36}S$ measurements.

1.5 SUMMARY OF THESIS CHAPTERS

In this thesis, I describe the implementation of multiple S isotope analytical techniques at Harvard University and the development of reactive transport diagenetic models to include ^{33}S. The thesis has three body chapters and three separate appendices. Chapter 2 describes the development of a pore water sulfate diagenetic model for an anoxic basin in the California-Mexico margin (Alfonso) that estimates sulfate reduction rates from pore water geochemical data, and uses laboratory-calibrated S isotope fractionation characteristics to understand the $\Delta^{33}S$ and $\delta^{34}S$ signatures observed in the multi-core pore water data. Chapter 3 is an extension of Chapter 2 that reconstructs the sedimentary S cycle of a shallow continental margin site (Aarhus Bay, Denmark) and extends the modeling techniques to include other sulfur species of interest, including sulfide and pyrite (solid phases). In Chapter 4, I revisit a historical marine sulfate $\delta^{34}S$ record and provide additional information with paired $\Delta^{33}S$ and $\Delta^{36}S$ records and conduct a simple sensitivity study to place limits on the biogeochemical fluxes (*e.g.,* sulfate weathering and pyrite burial) allowable within the range demonstrated by marine sulfate $\Delta^{33}S$ and $\Delta^{36}S$ values over 120 Ma. Further, Appendix 1 details measurements of IAEA standards and the calibration of VCDT and seawater sulfate $\delta^{34}S$, $\Delta^{33}S$, and $\Delta^{36}S$ values over approximately three years of analyses—one of the more rigorous calibrations of its kind. Appendix 2 describes the triple isotope signatures ($\delta^{34}S$ and $\Delta^{33}S$) for pore waters within the Amazon delta, and Appendix 3 is a published manuscript (Johnston et al., 2014) describing the rate limits that can be placed on microbial sulfate reduction within a water column oxygen minimum zone (OMZ). This thesis describes the utility of minor S isotope techniques in understanding and quantifying aspects of the sulfur cycle in modern sediments and in deep time, using a variety of analytical and modeling techniques.

1.6 REFERENCES

Aller, R.C., 2014, Sedimentary Diagenesis, Depositional Environments, and Benthic Fluxes, ed., Sedimentary Diagenesis, Depositional Environments, and Benthic Fluxes Treatise on Geochemistry, p. 293–334.

Aller, R.C., Madrid, V., Chistoserdov, A., Aller, J.Y., and Heilbrun, C. (2010) Unsteady diagenetic processes and sulfur biogeochemistry in tropical deltaic muds: Implications for oceanic isotope cycles and the sedimentary record. *Geochimica et Cosmochimica Acta* **74**, 4671–4692.

Alperin, M., and Hoehler, T. (2010) The ongoing mystery of sea-floor methane. *Science* **329**, 288–289.

Alperin, M.J., and Hoehler, T.M. (2009) Anaerobic methane oxidation by archaea/sulfate-reducing bacteria aggregates: 2. Isotopic constraints. *American Journal of Science* **309**, 958–984.

Asprey, L.B. (1976) The preparation of very pure fluorine gas. *Journal of Fluorine Chemistry* **7**, 359–361.

Audi, G., and Wapstra, A.H. (1995) The 1995 update to the atomic mass evaluation. *Nuclear Physics A* **595**, 409–480.

Bak, F., and Cypionka, H. (1987) A novel type of energy metabolism involving fermentation of inorganic sulphur compounds.

Berg, P., Risgaard-Petersen, N., and Rysgaard, S. (1998) Interpretation of measured concentration profiles in sediment pore water. *Limnology and Oceanography* **43**, 1500–1510.

Berner, R.A. (1982) Burial of organic carbon and pyrite sulfur in the modern ocean: its geochemical and environmental significance. *Am. J. Sci* **282**, 451–473.

Boetius, A., Ravenschlag, K., Schubert, C.J., Rickert, D., Widdel, F., Gieseke, A., Amann, R., Jørgensen, B.B., Witte, U., and Pfannkuche, O. (2000) A marine microbial consortium apparently mediating anaerobic oxidation of methane. *Nature* **407**, 623–626.

Boudreau, B.P., and Westrich, J.T. (1984) The dependence of bacterial sulfate reduction on sulfate concentration in marine sediments. *Geochimica et Cosmochimica Acta* **48**, 2503–2516.

Bowles, M.W., Mogollón, J.M., Kasten, S., Zabel, M., and Hinrichs, K.U. (2014) Global rates of marine sulfate reduction and implications for sub-sea-floor metabolic activities. *Science* **344**, 889–891.

Bradley, A.S., Leavitt, W.D., Schmidt, M., Knoll, A.H., Girguis, P.R., and Johnston, D.T. (2015) Patterns of sulfur isotope fractionation during Microbial Sulfate Reduction. *Geobiology* 1–11.

Bradley, A.S., Leavitt, W.D., and Johnston, D.T. (2011) Revisiting the dissimilatory sulfate reduction pathway. *Geobiology* **9**, 446–457.

Brennan, S.T., Lowenstein, T.K., and Cendon, D.I. (2013) The major-ion composition of Cenozoic seawater: The past 36 million years from fluid inclusions in marine halite. *American Journal of Science* **313**, 713–775.

Canfield, D.E. (2004) The evolution of the Earth surface sulfur reservoir. *American Journal of Science* **304**, 839–861.

Canfield, D.E. (1998) A new model for Proterozoic ocean chemistry. *Nature* **396**, 450–453.

Canfield, D.E., and Teske, A. (1996) Late Proterozoic rise in atmospheric oxygen concentration inferred from phylogenetic and sulphur-isotope studies. *Nature* **382**, 127–132.

Chambers, L.A., Trudinger, P.A., Smith, J.W., and Burns, M.S. (1975) Fractionation of sulfur isotopes by continuous cultures of Desulfovibrio desulfuricans. *Canadian Journal of Microbiology* **21**, 1602–1607.

Coplen, T.B., Hopple, J.A., Boehike, J.K., Peiser, H.S., and Rieder, S.E. (2002) Compilation of minimum and maximum isotope ratios of selected elements in naturally occurring terrestrial materials and reagents.

Dale, A.W., Brüchert, V., Alperin, M., and Regnier, P. (2009) An integrated sulfur isotope model for Namibian shelf sediments. *Geochimica et Cosmochimica Acta* **73**, 1924–1944.

Ding, T., Valkiers, S., Kipphardt, H., De Bievre, P., Taylor, P.D.P., Gonfiantini, R., and Krouse, R. (2001) Calibrated sulfur isotope abundance ratios of three IAEA sulfur isotope reference materials and V-CDT with a reassessment of the atomic weight of sulfur. *Geochimica et Cosmochimica Acta* **65**, 2433–2437.

Donahue, M.A., Werne, J.P., Meile, C., and Lyons, T.W. (2008) Modeling sulfur isotope fractionation and differential diffusion during sulfate reduction in sediments of the Cariaco Basin. *Geochimica et Cosmochimica Acta* **72**, 2287–2297.

Farquhar, J., Johnston, D.T., and Wing, B.A. (2007) Implications of conservation of mass effects on mass-dependent isotope fractionations: Influence of network structure on sulfur isotope phase space of dissimilatory sulfate reduction. *Geochimica et Cosmochimica Acta* **71**, 5862–5875.

Farquhar, J., Johnston, D.T., Wing, B.A., Habicht, K.S., Canfield, D.E., Airieau, S., and Thiemens, M.H. (2003) Multiple sulphur isotopic interpretations of biosynthetic pathways: implications for biological signatures in the sulphur isotope record. *Geobiology* **1**, 27–36.

Farquhar, J., and Wing, B.A. (2003) Multiple sulfur isotopes and the evolution of the atmosphere. *Earth and Planetary Science Letters* **213**, 1–13.

Fike, D.A., Bradley, A.S., and Rose, C.V. (2015) Rethinking the Ancient Sulfur Cycle. *Annu. Rev. Earth Planet. Sci.* **43**, 593–622.

Habicht, K.S., Canfield, D.E., and Rethmeier, J.O. (1998) Sulfur isotope fractionation during bacterial reduction and disproportionation of thiosulfate and sulfite. *Geochimica et Cosmochimica Acta* **62**, 2585–2595.

Habicht, K.S., and Canfield, D.E. (1997) Sulfur isotope fractionation during bacterial sulfate reduction in organic-rich sediments. *Geochimica et Cosmochimica Acta* **61**, 5351–5361.

Halevy, I., Peters, S.E., and Fischer, W.W. (2012) Sulfate burial constraints on the Phanerozoic sulfur cycle. *Science* **337**, 331–334.

Harrison, A.G., and Thode, H.G. (1958) Mechanism of the bacterial reduction of sulphate from isotope fractionation studies. *Transactions of the Faraday Society* **54**, 84–92.

Hayes, J.M., and Waldbauer, J.R. (2006) The carbon cycle and associated redox processes through time. *Philos Trans R Soc Lond B Biol Sci* **361**, 931–950.

Horita, J., Zimmermann, H., and Holland, H.D. (2002) Chemical evolution of seawater during the Phanerozoic: implications from the record of marine evaporites. *Geochimica et Cosmochimica Acta* **66**, 3733–3756.

Hulston, J.R., and Thode, H.G. (1965) Cosmic ray produced S36 and S33 in the metallic phase of iron

meteorites. *Journal of Geophysical Research* **70**, 4435–4442.

Hulston, J.R., and Thode, H.G. (1965) Variations in the S33, S34, and S36 contents of meteorites and their relation to chemical and nuclear effects. *Journal of Geophysical Research* **70**, 3475–3484.

Johnston, D.T. (2011) Multiple sulfur isotopes and the evolution of Earth's surface sulfur cycle. *Earth-Science Reviews* **106**, 161–183.

Johnston, D.T., Farquhar, J., Summons, R.E., Shen, Y., Kaufman, A.J., Masterson, A.L., and Canfield, D.E. (2008) Sulfur isotope biogeochemistry of the Proterozoic McArthur Basin. *Geochimica et Cosmochimica Acta* **72**, 4278–4290.

Johnston, D.T., Farquhar, J., and Canfield, D.E. (2007) Sulfur isotope insights into microbial sulfate reduction: When microbes meet models. *Geochimica et Cosmochimica Acta* **71**, 3929–3947.

Johnston, D.T., Farquhar, J., Wing, B.A., Kaufman, A.J., Canfield, D.E., and Habicht, K.S. (2005) Multiple sulfur isotope fractionations in biological systems: a case study with sulfate reducers and sulfur disproportionators. *American Journal of Science* **305**, 645–660.

Johnston, D.T., Gill, B.C., Masterson, A., Beirne, E., Casciotti, K.L., Knapp, A.N., and Berelson, W. (2014) Placing an upper limit on cryptic marine sulphur cycling. *Nature* **513**, 530–533.

Jones, G.E., and Starkey, R.L. (1957) Fractionation of stable isotopes of sulfur by microorganisms and their role in deposition of native sulfur. *Applied microbiology* **5**, 111.

Jørgensen„ B.B. (1979) A theoretical model of the stable sulfur isotope distribution in marine sediments. *Geochimica et Cosmochimica Acta* **43**, 363–374.

Jørgensen, B.B. (1982) Mineralization of organic matter in the sea bed—the role of sulphate reduction.

Jørgensen, B.B., and Kasten, S., 2006, Sulfur cycling and methane oxidation, eds., Marine geochemistry, p. 271–309.

Jørgensen, B.B., and Parkes, R.J. (2010) Role of sulfate reduction and methane production by organic carbon degradation in eutrophic fjord sediments (Limfjorden, Denmark). *Limnol. Oceanogr.* **55**, 1338–1352.

Kaplan, I.R., and Rittenberg, S.C. (1964) Microbiological fractionation of sulphur isotopes. *Journal of General Microbiology* **34**, 195–212.

Kemp, A.L.W., and Thode, H.G. (1968) The mechanism of the bacterial reduction of sulphate and of sulphite from isotope fractionation studies. *Geochimica et Cosmochimica Acta* **32**, 71–91.

Kurtz, A.C., Kump, L.R., Arthur, M.A., Zachos, J.C., and Paytan, A. (2003) Early Cenozoic decoupling of the global carbon and sulfur cycles: Paleogene C and S cycles. *Paleoceanography* **18**.

Leavitt, W.D., Bradley, A.S., Santos, A.A., Pereira, I.A., and Johnston, D.T. (2015) Sulfur Isotope Effects of Dissimilatory Sulfite Reductase. *Front Microbiol* **6**, 1392.

Leavitt, W.D., Cummins, R., Schmidt, M.L., Sim, M.S., Ono, S., Bradley, A.S., and Johnston, D.T. (2014) Multiple sulfur isotope signatures of sulfite and thiosulfate reduction by the model dissimilatory sulfate-reducer, Desulfovibrio alaskensis str. G20. *Front Microbiol* **5**, 591.

Leavitt, W.D., Halevy, I., Bradley, A.S., and Johnston, D.T. (2013) Influence of sulfate reduction rates on the Phanerozoic sulfur isotope record. *Proc Natl Acad Sci U S A* **110**, 11244–11249.

Lowenstein, T.K., Hardie, L.A., Timofeeff, M.N., and Demicco, R.V. (2003) Secular variation in

seawater chemistry and the origin of calcium chloride basinal brines. *Geology* **31**, 857–860.

Lowenstein, T.K., Timofeeff, M.N., Brennan, S.T., Hardie, L.A., and Demicco, R.V. (2001) Oscillations in Phanerozoic seawater chemistry: evidence from fluid inclusions. *Science* **294**, 1086–1088.

Meister, P., Liu, B., Ferdelman, T.G., Jørgensen, B.B., and Khalili, A. (2013) Control of sulphate and methane distributions in marine sediments by organic matter reactivity. *Geochimica et Cosmochimica Acta* **104**, 183–193.

Milucka, J., Ferdelman, T.G., Polerecky, L., Franzke, D., Wegener, G., Schmid, M., Lieberwirth, I., Wagner, M., Widdel, F., and Kuypers, M.M. (2012) Zero-valent sulphur is a key intermediate in marine methane oxidation. *Nature* **491**, 541–546.

Ono, S., Wing, B., Johnston, D., Farquhar, J., and Rumble, D. (2006) Mass-dependent fractionation of quadruple stable sulfur isotope system as a new tracer of sulfur biogeochemical cycles. *Geochimica et Cosmochimica Acta* **70**, 2238–2252.

Paytan, A., Kastner, M., Campbell, D., and Thiemens, M.H. (2004) Seawater sulfur isotope fluctuations in the Cretaceous. *Science* **304**, 1663–1665.

Paytan, A. (1998) Sulfur Isotopic Composition of Cenozoic Seawater Sulfate. *Science* **282**, 1459–1462.

Peck, H.D. (1959) The ATP-dependent reduction of sulfate with hydrogen in extracts of Desulfovibrio desulfuricans. *Proceedings of the National Academy of Sciences* **45**, 701–708.

Peck, H.D. (1961) Evidence for the reversibility of the reaction catalyzed by adenosine-5 phosphosulfate reductase. *Biochimica et biophysica acta* **49**, 621–624.

Reeburgh, W.S. (2007) Oceanic methane biogeochemistry. *Chem Rev* **107**, 486–513.

Rees, C.E. (1973) A steady-state model for sulphur isotope fractionation in bacterial reduction processes. *Geochimica et Cosmochimica Acta* **37**, 1141–1162.

Rumble, D., Farquhar, J., Young, E.D., and Christensen, C.P. (1997) In situ oxygen isotope analysis with an excimer laser using F 2 and BrF 5 reagents and O 2 gas as analyte. *Geochimica et Cosmochimica Acta* **61**, 4229–4234.

Sim, M.S., Ono, S., Donovan, K., Templer, S.P., and Bosak, T. (2011) Effect of electron donors on the fractionation of sulfur isotopes by a marine Desulfovibrio sp. *Geochimica et Cosmochimica Acta* **75**, 4244–4259.

Sim, M.S., Ono, S., and Hurtgen, M.T. (2015) Sulfur isotope evidence for low and fluctuating sulfate levels in the Late Devonian ocean and the potential link with the mass extinction event. *Earth and Planetary Science Letters* **419**, 52–62.

Sim, M.S., Bosak, T., and Ono, S. (2011) Large sulfur isotope fractionation does not require disproportionation. *Science* **333**, 74–77.

Sim, M.S., Ono, S., and Bosak, T. (2012) Effects of iron and nitrogen limitation on sulfur isotope fractionation during microbial sulfate reduction. *Appl Environ Microbiol* **78**, 8368–8376.

Tarpgaard, I.H., Røy, H., and Jørgensen, B.B. (2011) Concurrent low- and high-affinity sulfate reduction kinetics in marine sediment. *Geochimica et Cosmochimica Acta* **75**, 2997–3010.

Thamdrup, B., Finster, K., Hansen, J.W., and Bak, F. (1993) Bacterial disproportionation of elemental sulfur coupled to chemical reduction of iron or manganese. *Applied and environmental microbiology* **59**, 101–108.

Westrich, J.T., and Berner, R.A. (1984) The role of sedimentary organic matter in bacterial sulfate reduction: The G model tested. *Limnology and oceanography* **29**, 236–249.

Wing, B.A., and Farquhar, J. (2015) Sulfur isotope homogeneity of lunar mare basalts. *Geochimica et Cosmochimica Acta* **170**, 266–280.

Wortmann, U.G., and Paytan, A. (2012) Rapid variability of seawater chemistry over the past 130 million years. *Science* **337**, 334–336.

Wu, N., Farquhar, J., and Strauss, H. (2014) $\delta^{34}S$ and $\Delta^{33}S$ records of Paleozoic seawater sulfate based on the analysis of carbonate associated sulfate. *Earth and Planetary Science Letters* **399**, 44–51.

Wu, N., Farquhar, J., Strauss, H., Kim, S.-T., and Canfield, D.E. (2010) Evaluating the S-isotope fractionation associated with Phanerozoic pyrite burial. *Geochimica et Cosmochimica Acta* **74**, 2053–2071.

Young, E.D., Galy, A., and Nagahara, H. (2002) Kinetic and equilibrium mass-dependent isotope fractionation laws in nature and their geochemical and cosmochemical significance. *Geochimica et Cosmochimica Acta* **66**, 1095–1104.

Zerkle, A.L., Farquhar, J., Johnston, D.T., Cox, R.P., and Canfield, D.E. (2009) Fractionation of multiple sulfur isotopes during phototrophic oxidation of sulfide and elemental sulfur by a green sulfur bacterium.

Zopfi, J., Ferdelman, T.G., and Fossing, H. (2004) Distribution and fate of sulfur intermediates sulfite, tetrathionate, thiosulfate, and elemental sulfur in marine sediments. *Geological Society of America Special Papers* **379**, 97–116.

CHAPTER 2

A MULTIPLE SULFUR ISOTOPE DIAGENETIC MODEL FOR ANOXIC SEDIMENTS OF THE CALIFORNIA-MEXICO MARGIN: ALFONSO BASIN*

ABSTRACT

Recent studies targeting the metabolic, physiological, and biochemical controls of S isotope fractionation in microbial systems have drawn linkages between culture experiments and the sulfur isotope signatures observed in natural environments. Several of those studies have used newer techniques to explore the minor isotope (^{33}S and ^{36}S) variability in those systems, and also have attempted to place them in an ecophysiological context. Sparingly few have incorporated this newfound understanding of minor isotope behavior into natural systems (sediments, water columns) and none of them have refined existing isotope-dependent reactive transport models to explicitly include ^{33}S. In this study, we construct a three-isotope (^{32}S, ^{33}S, and ^{34}S) reactive transport model of pore water sulfate for a well-characterized sedimentary system within the California-Mexico Margin (Alfonso Basin) that aids in placing recent microbial studies into a natural context. The model first reproduces the bulk geochemical characteristics of the pore water—including [SO_4^{2-}], [CH_4], [DIC], and [Ca^{2+}]—and predicts bulk (non-isotope-specific and depth-dependent) rates of sulfate reduction. Next, the model uses those depth-dependent bulk rates, in combination with empirically calibrated fractionation factors, to explain the minor isotope characteristics of the core-top pore water SO_4^{2-}, including $\delta^{34}S$ and $\Delta^{33}S$ values. The down core, isotopic evolution of pore water sulfate requires a large fractionation associated with sulfate reduction ($^{34}\varepsilon_{SR}$ = 70±5‰) that appears to be independent of bulk rate. The minor isotope characteristics ($^{33}\lambda_{SR}$ = 0.5130±0.0005) are also independent of rate and

*A version of this chapter has been submitted to the *American Journal of Science* with co-authors Marc J. Alperin, William M. Berelson and David T. Johnston.

fall near the range expected from microbial calibrations, but differ from predictions from thermodynamic equilibrium. This raises key questions in relating the physiological state of marine microorganisms relative to their laboratory counterparts, as well as points toward exceedingly low metabolic rates in marine sediments.

2.1 INTRODUCTION

Microbial sulfate reduction (MSR) is quantitatively the most important remineralization pathway for organic matter in modern continental margin sediments (Jørgensen, 1982), and carries profound geochemical consequences for the environmental interpretation of biogeochemical cycling (Canfield, 2004). Sulfur isotope geochemistry is a primary analytical tool for tracking and quantifying the influence of MSR and other sulfur metabolic pathways in those environments. Several decades of research focused on understanding the S isotope biochemistry of MSR (Rees, 1973; Detmers et al., 2001; Canfield, 2001) and metabolisms such as microbial sulfur disproportionation (Bak and Pfenning, 1987; Canfield and Thamdrup, 1994; Thamdrup et al., 1994; Canfield and Teske, 1996; Finster et al., 1997; Habicht et al., 1998). Those studies concerned only the two isotope system of S ($^{34}S/^{32}S$) and largely used the magnitude of a fractionation ($^{34}\varepsilon$; see below for definition) as a diagnostic feature for distinguishing between different metabolisms.

With the application of multiple or *minor* S isotope ($^{33}S/^{32}S$ and $^{36}S/^{32}S$) systematics to microbial systems (Farquhar et al., 2003), researchers expanded the understanding of microbial metabolisms and S isotope fractionation behavior to include ^{33}S and ^{36}S. The physical chemistry of mass-dependent isotope fractionation has a solid theoretical foundation (Bigeleisen and Mayer, 1947; Young et al., 2002; Farquhar et al., 2003), and the application of such principles to biological systems highlighted the added level of interpretability that comes with exploring paired metrics such as $\delta^{34}S$, $\Delta^{33}S$, and $^{33}\lambda_{SR}$. The common nomenclature used to define these systematics is based on standard delta notation:

$$\delta^{34}S = 1000 \cdot \left[\frac{(^{34}S/^{32}S)_{samp}}{(^{34}S/^{32}S)_{VCDT}} - 1 \right] \tag{2.1}$$

that then gives rise to two minor isotope short-hands. The first is a deviation from a reference line in units of parts per thousand (or ‰):

$$\Delta^{33}S = \delta^{33}S - 1000 \cdot \left[\left[\frac{\delta^{34}S}{1000} + 1 \right]^{0.515} - 1 \right] \tag{2.2}$$

whereas the fractionation factors from a defined system can also be used to define an effective slope of a triple isotope relationship:

$$^{33}\lambda_{SR} = \frac{ln(^{33}\alpha_{SR})}{ln(^{34}\alpha_{SR})} \tag{2.3}$$

Together these terms serve as the means for cataloging variability in $^{33}S/^{32}S$, $^{34}S/^{32}S$ and $^{36}S/^{32}S$.

Variability in $\Delta^{33}S$ values, paired with an understanding of how mass is conserved at the cellular scale, demonstrated that the signatures of MSR and sulfur disproportionation are potentially unique. This feature led to minor S isotopes being used to understand S cycling in ancient systems (Johnston et al., 2005a; Johnston et al., 2005b; Johnston et al., 2008). Subsequent studies have further characterized those multiple S isotope signatures in microbial experiments (Johnston et al., 2007; Sim et al., 2011a; Sim et al. 2011b) and improved our understanding of the influence of rate (Leavitt et al., 2013) sulfate concentration (Bradley et al., 2015) and enzyme effects (Leavitt et al., 2015) in the ultimate expression of multiple S isotope biosignatures. Due to the overwhelming importance of MSR in the historical S isotope record (*e.g.,* Strauss et al., 1999), multiple S isotope studies have also tried to interpret these mass dependent $\Delta^{33}S$ signatures in proxy records (Johnston et al., 2008; Wu et al., 2010; Wu et al., 2015; Sim et al., 2015; Masterson et al., 2016). The variability in the $\Delta^{33}S$ record is clearly connected to microbial metabolism, but the proper quantification of the connection between laboratory calibrations of microbial ($\delta^{34}S$ and $\Delta^{33}S$) signatures depends on placing those isotopic systematics into a diagenetic context. Such has been done for the ($^{34}S/^{32}S$) system, but has never been explicit done to include the minor isotopes.

Diagenetic reactive transport modeling is the primary means for reconstructing rates of low temperature (including microbial biogeochemistry) from the concentrations of pore water and solid phase species in continental margin sediments. The mathematical framework underlying the modeling has long been established (Berner, 1980; Boudreau, 1997), and models of increasing complexity are continuing to be constructed (*cf*. Arndt et al., 2013). Such models have been used to understand organic matter degradation kinetics (Aller, 2014), methane biogeochemistry (*e.g*., Alperin et al., 1994), and S cycling (Berner, 1964; Jørgensen, 1979; Aller and Blair, 1996, Aller et al., 2010). Sometimes bulk geochemical rates serve as model inputs, but more often biogeochemical rates, ascertained from concentration profiles, are the desired model output (Bowles et al., 2014). A small cadre of studies have constructed such models for the S isotope system, beginning with the seminal study of Jørgensen (1979), and later to the deep biosphere (Wortmann et al., 2001), and Cariaco Basin (Donahue et al., 2008). The only attempt to apply a multiple S isotope diagenetic model to a sedimentary system, Mangrove Lake, Bermuda (Pellerin et al., 2015), used pore water sulfate concentration and isotope information alone to construct the model. Needed is a more comprehensive diagenetic study that interprets sulfate concentration profiles in parallel with those of other geochemical species (organic matter, CH_4, DIC) to improve the quantification of biogeochemically important rates like sulfate reduction and anaerobic methane oxidation. In concert with multiple S isotope information, this next generation of model will allow for a better understanding of the connection between microbial signatures—where rates are generally well understood—and natural systems.

In this study we target pore water data and samples from an anoxic basin in the California-Mexico margin—Alfonso Basin to reconstruct sedimentary S cycling and to understand the implications for interpreting minor S isotope ($\Delta^{33}S_{SO4}$) pore water sulfate profiles. The anoxic-silled basins of the California-Mexico margin are an ideal place to study S cycling due to their low bottom water O_2 content (<5μM), laminated sediments, and high POC content (>5%). Alfonso Basin in particular has been well-studied (Berelson et al., 2005; Gonzalez-Yajimovich et al., 2007; Staines-

Urias et al., 2015). Sediment and pore water data previously sampled and measured (Berelson et al., 2005) during the CalMex campaign of 2001 include POC, $[SO_4^{2}]$, $[CH_4]$, [DIC], and $[Ca^{2+}]$, and form the basis for our model, which includes organic matter degradation kinetics, sulfate reduction, methanogenesis, anaerobic methane oxidation, and authigenic carbonate precipitation. The essential output of that bulk model is a *net* sulfate reduction rate (SRR) that is used as a model input for running an isotope-specific reactive transport model for the isotopologues of interest ($^{32}SO_4^{2-}$, $^{33}SO_4^{2-}$, $^{34}SO_4^{2-}$). We ignore $^{36}SO_4^{2-}$ because of its very low abundance (<0.02%). The model inputs include fractionation factors associated with sulfate reduction—$^{33}\alpha_{SR}$ and $^{34}\alpha_{SR}$—and the model outputs

Figure 2.1

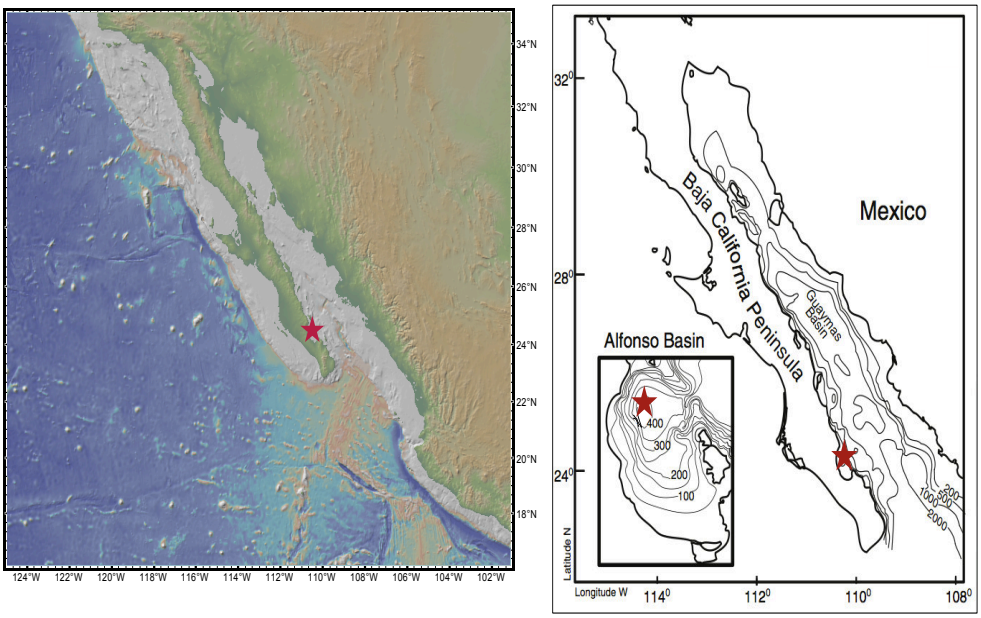

Figure 2.1: Map showing the sampling locality within Alfonso Basin for the cores studied herein. The cores were sampled at approximately 408 m water column depth, at latitude of 24°38.18' (N) and longitude of 110°36.06' (W) in November 2001. Separate cores (multi cores and gravity cores) were retrieved, and archived sulfate provided the material for analysis in this study. The details of the cruise, and the sampling were originally published in Berelson et al. (2005). The left panel provides the location of Alfonso Basin, and the right panel, a modified version of that appearing in Staines-Urias, et al. (2015), provides the details of the bathymetry of the California-Mexico margin.

include pore water sulfate $\delta^{34}S$ and $\Delta^{33}S$ profiles/gradients. The results demonstrate that it is possible to extract S isotope fractionation behavior from a sediment column, and to use pore water $\Delta^{33}S$ and $\delta^{34}S$ profiles to extrapolate microbial calibrations to natural environments where biogeochemical rates are largely unconstrained.

2.2 ALFONSO BASIN SAMPLING AND ANALYTICAL METHODS

2.2.1 CORING AND PORE WATER SAMPLING

Coring and pore water sampling of Alfonso Basin took place during the CalMex cruise of October and November 2001. That particular sampling cruise processed sediment cores from numerous sites along the California and Mexican Margin (Berelson et al., 2005). We have focused on Alfonso Basin and briefly describe the sample site characteristics and pore water sampling protocols. Although there is some temporal variability, in general, bottom water oxygen concentrations are less than 5 μM, and sediments are laminated, indicating long-term bottom water anoxia. Alfonso Basin, station 15 (24° 38.18', 110° 36.06) lies off the coast of La Paz (Baja Mexico) and was sampled at a water depth of 408 m (see Fig. 2.1). Sample coring was done with a combination of a multicorer, and via gravity coring. Cores with a well-preserved sediment-water interface were utilized for whole-core squeezing to extract pore waters to define gradients in the upper few centimeters. Additional multicores from each station were sectioned in an anoxic glove bag. Sections were alternatingly sectioned for methane (CH_4) and dissolved SO_4^{2-}, Ca^{2+}, TCO_2, NH_4^+, and silica. Methane was sampled and analyzed as described in Sansone et al. (2004), as revisited in Berelson et al. (2005). Pore water was filtered and stored in glass syringes for DIC analysis and bottled for the remaining constituents. See the appendix for all of the pore water and isotope data used for this model study.

2.2.2 SULFUR ISOTOPE ANALYSES

Frozen, unacidified pore waters from the CalMex (2001) cruise were shipped to the laboratory for Stable Isotope Geobiology at Harvard University in 2014 for further sample preparation and isotope analyses. Thawed pore water samples were acidified with 1N HCl to a pH of ~2.5, and to each sample (ranging in volume from 0.25 mL to 3.0 mL) 500 μL of a concentrated solution of barium chloride (1M $BaCl_2$) was added in order to precipitate sulfate as $BaSO_4$. Barium sulfate precipitates were rinsed several times with deionized water and dried for a minimum of 12 hours for $\delta^{34}S_{SO4}$ analyses. Isotope analyses for $\delta^{34}S_{SO4}$ were done directly on $BaSO_4$ precipitates at the Harvard University using continuous flow IRMS. Samples for $\delta^{34}S_{SO4}$ were performed with CF-IRMS and analyzed as SO_2. Online combustion utilizing a V_2O_5 catalyst at 500°C was performed with a Costech EA, mated to the Delta V. Reproducibility was estimated from repeat analyses of IAEA-S-1, S-2, S-3, as well as NBS-127, to be better than ±0.2‰ (1σ).

For minor isotope measurements ($\Delta^{33}S_{SO4}$), samples were first chemically converted to Ag_2S by reductive distillation with a mixture of hydriodic acid (HI), hypophosphorous (H_3PO_4) and hydrochloric acid (HCl) at ~90°C for 3 hours (Forrest and Newman, 1978). The reactors were purged with N_2 and product H_2S was captured as ZnS and converted to Ag_2S by cation exchange with $AgNO_3$. Samples were rinsed with ~100 mL of millipore water, 15 mL of 1M NH_4OH, an additional ~100 mL of Millipore water, and dried in a 90°C oven overnight. Powdered Ag_2S samples were fluorinated at 300°C in a F_2 atmosphere at 10X stoichiometric excess. Product SF_6 was cryogenically and chromatographically purified and analyzed on a Thermo Finnigan 253 in Dual Inlet mode. Analyses of repeat standards of IAEA-S-1, S-2, S-3, yield a reproducibility of ±0.2‰ and ±0.006‰ for $\delta^{34}S$ and $\Delta^{33}S$, respectively. Samples are reported versus VCDT, calibrated from the long-term running average of IAEA-S-1 versus the working standard gas at Harvard University.

2.3 MODEL CONSTRUCTION

2.3.1 MODEL ARCHITECTURE AND OPERATION

All reactive-transport models used in this study are steady-state finite-difference models, and were coded and run in Fortran 77 to a specified depth (*i.e.* model domain length, L). The baseline geochemical model that reproduces the bulk pore water profiles consists of two parts (i) An organic carbon degradation model that produces a remineralization rate profile (GRR), and (ii) a reactive transport model that calculates depth-dependent reaction rates, such as organoclastic sulfate reduction, methanogenesis, and anaerobic methane oxidation and solves that boundary value problem to reproduce the pore water profiles of $[SO_4^{2-}]$, $[CH_4]$, DIC, and $[Ca^{2+}]$. Key outputs of the model are the depth-dependent rate profiles, such as sulfate reduction rate (SRR) and anaerobic methane oxidation rate. The output SRR, in concert with the $[SO_4^{2-}]$ boundary conditions, and isotope information is then used to run the isotope-specific reactive transport model that computes independent rates (*e.g.*, ^{32}SRR, ^{33}SRR, and ^{34}SRR), as well as isotope ($\delta^{34}S$ and $\Delta^{33}S$) profiles that can be used to fit the measured data. Discussed below are the more explicit details of the model construction (boundary conditions, diffusion coefficients, kinetics parameters) that were used to run each of the models.

2.3.2 BULK PORE WATER GEOCHEMICAL ('G', SO_4^{2-}, CH_4, DIC, Ca^{2+}) MODEL

2.3.2.1 POROSITY

Porosity (ϕ), or the fraction of whole sediment volume occupied by pore water, was measured at the time of pore water sampling of the multi and gravity cores. The extracted porosity follows a characteristic, exponential decay function with steady-state compaction (see Fig 2.2a). The model fit is used throughout the domain and everywhere it appears in the reactive transport equations.

2.3.2.2 PORE WATER BOUNDARY CONDITIONS

Although a bottom water sample was not retrieved in this study, other work (Gonzalez-Yajimovich et al., 2007) have estimated the bottom water salinity to be S = 35 psu. These data were used to estimate

the upper boundary concentration conditions for $[SO_4^{2-}]$ = 28.93 mM and $[Ca^{2+}]$ = 10.2 mM. The upper boundary conditions for $[CH_4]$ and DIC were as determined in Sansone et al., (2004). In all model runs, the upper boundary conditions for the five species were constant (Dirichlet) concentrations ([C]), and the lower boundaries were Neumann (d[C]/dx = 0) gradients. Boundary conditions for all species used in the baseline geochemical model, including POC, and described in more detail below, are shown in Table 2.1.

Table 2.1

Solute	Concentration (mmol/L)	Source
SO_4^{2-}	28.93	I†
CH_4	0.00025	L[1]
DIC	2.35	L[2]
Ca^{2+}	10.53	I†

Solid	Concentration (%)	Source
POC	7.79	L[3]
POC_∞	2.24	C
G	5.55	C

Solid	Flux (mmol cm^{-2} y^{-1})	Source
G_1	0.990	C
G_2	4.170	C
G_3	4.760	C

†Determined from a salinity of S = 35.
[1]Sansone, and others (2004)
[2]Berelson, and others (2005)
[3]Silverberg, and others (2014)

Table 2.1: **Boundary Conditions of the Baseline Geochemical Model**
Solid phase and pore water concentration boundary conditions for the baseline geochemical model. In this table and the remaining tables, the Source terms refer to L = Literature, I = calculated from other model conditions, and C = Model parameterization.

Table 2.2: Physical parameters used in the baseline model

Symbol	Description	Value	Units	Source
z	Water depth	408	m	L[1]
T	Bottom water temperature	9	°C	L[2]
S	Bottom water salinity	35	-	L[1]
L	Length of model domain	3000	cm	C
ϕ_o	Porosity at sediment surface	0.945	-	C
ϕ_∞	Porosity below zone of compaction	0.835	-	C
β	Porosity attenuation coefficient	0.0147	cm^{-1}	C
ρ_{SM}	Dry sediment density	2.65	$g\ cm^{-3}$	L[1]
F_{SM}	Mass accumulation rate	14.9	$mg\ cm^{-2}\ y^{-1}$	L[1]

[1] Gonzalez-Yajimovich, et al. (2007)
[2] Berelson, et al. (2005)

2.3.2.3 PHYSICAL PARAMETERS AND DIFFUSION COEFFICIENTS

There are a number of physical parameters that are critical to the analysis. For instance, model inputs for the baseline simulation are physical parameters, such as the size of the model domain (L = 3000 cm), below which compaction is negligible, and rates are largely constant. Water depth, z = 408 m, temperature, T= 9C, and salinity, S = 35 were all specified and are used to compute the diffusion coefficients, which are influenced by the physical chemical characteristics of seawater (see Tables 2.2 and 2.3). Sediment density, ρ_{SM} = 2.65 g/cm^3 and the mass accumulation rate F_{SM} = 0.0149 g/cm^2 are also necessary to properly compute the coefficients in the diffusion and advection terms of the reactive transport equations. Mass accumulation rate is critical in determining the flux of POC into the model domain since it parameterized as a weight %.

Table 2.3: Diffusion coefficients

	25°C, 0 psu, 0 m[1]	9°C, 35 psu, 408 m[2]
D_{SO4}	$10.7x10^{-6}$	$6.5x10^{-6}$
D_{CH4}	$16.7x10^{-6}$	$10.1x10^{-6}$
D_{DIC}	CO_2: $19.7x10^{-6}$	CO_2: $11.7x10^{-6}$ (α_o = 2.92%)[3]
	HCO_3^-: $11.9x10^{-6}$	HCO_3^-: $7.23x10^{-6}$ (α_1 = 95.26%)[3]
	CO_3^{2-}: $9.31x10^{-6}$	CO_3^{2-}: $5.65x10^{-6}$ (α_2 = 1.82%)[3]
		DIC: $7.33x10^{-6}$[4]
D_{Ca}	$8.08x10^{-6}$	$4.91x10^{-6}$

[1] Boudreau (1997)
[2] Corrected to in situ temperature, salinity, and pressure used in the Stokes-Einstein equation.
[3] α values calculated at in situ temperature, salinity, and pressure (assumed pH 7.5) using csys (Zeebe and Wolf-Gladrow, 2001).
[4] $D_{DIC} = \alpha_o D_{CO2} + \alpha_1 D_{HCO3} + \alpha_2 D_{CO3}$

2.3.2.4 ORGANIC CARBON DEGRADATION

Organic carbon remineralization is parameterized using a '3G' model (Dale et al., 2009; Westrich and Berner, 1984). In this formulation, particulate organic carbon (POC) deposited at the sediment water interface is divided into four fractions, an unreactive fraction, the concentration of which remains constant throughout the model domain (POC_∞), and three fractions (G_1, G_2, and G_3) with decreasing reactivity towards remineralization. The relative contributions of each fraction to the total reactive carbon pool are adjustable as model inputs. The solution to the 3G model was solved as a first order decay model for each fraction of G, and the remineralization rate normalized to reflect the pore water concentration of C remineralized—thus GRR_{pw} is determined in units of μmol $cm^{-3}d^{-1}$ (see Appendix for a more elaborate description of the calculation of GRR). The remineralization rate constants, $k_1 > k_2 > k_3$, were adjustable as model inputs. Of course, the reactive fractions G_n do not resemble actual carbon compounds, but are a simplified means of modulating the rate kinetics of the whole model—since all other rates, including SRR and anaerobic methane oxidation (AOM) are calculated from GRR, the concentration profiles are most easily adjusted by changing the fraction of each G_n and their remineralization rate constants.

Table 2.4

Parameter	Description	Value	Unit	Source
k_1	Reactivity of POC pool G_1	0.0100	y^{-1}	C
k_2	Reactivity of POC pool G_2	0.0010	y^{-1}	C
k_3	Reactivity of POC pool G_3	0.0001	y^{-1}	C
f_1	Fraction of reactive POC pool as G_1	0.100	-	C
f_2	Fraction of reactive POC pool as G_2	0.420	-	C
k_{AOM}	Rate constant for methane oxidation	0.250	yr^{-1}	C
$[SO_4^{2-}]^*$	Threshold concentration for sulfate uptake	0.200	mM	L[1]
$[Ca^{2+}]^*$	Threshold concentration for calcium	5.0	mM	C
k_{CaCO3}	Rate constant for calcite precipitation	0.030	mM y^{-1}	L
K_{ADS}	Equilibrium adsorption coefficient for Ca^{2+}	1.6	$cm^3\ g^{-1}$	L[2]
$K'_{sp,calcite}$	Solubility product for calcite	$4.92x10^{-7}$	M^2	L[3]
XS	Oxidation state of organic matter	-0.7		L[4]

[1] Habicht, et al.(2002)
[2] Li and Gregory (1974)
[3] Zeebe and Wolf-Gladrow (2001)
[4] Alperin, et al. (1994)

2.3.2.5 SULFATE REDUCTION RATE, METHANOGENESIS, AND CH_4 OXIDATION

The bulk model assumes that organic carbon is degraded via only two pathways: organoclastic sulfate reduction and methanogenesis. Thus, aerobic oxidation, which is minimal in an anoxic basin like Alfonso, is neglected. Dissimilatory Fe reduction is also excluded. Quantifying the sulfate reduction rate, SRR, with respect to GRR requires knowledge of the oxidation state of organic matter (XS) as it influences the stoichiometry of remineralization (C/S). Moreover, the mathematical constraints of the diagenetic model require parameterizing sulfate limitation (to dampen rates at low sulfate thresholds) for SRR, and require a similar parameterization of sulfate inhibition for methanogenesis. These are accomplished with the error function (erfc), a smoothed version of a step function that dials down rates when sulfate concentrations reach the threshold ($[SO_4^{2-}]^*$) of limitation and inhibition. Here the thresholds are shared for both limitation –in the case of sulfate reduction—and inhibition—in the case

of methanogenesis, and is prescribed as $[SO_4^{2-}]^* = 200$ μM. That limit is one of several estimated from sulfate affinity measurements (Tarpgaard et al., 2011) and also from isotope fractionation characteristics in MSR cultures (Habicht and Canfield, 2002). The incorporation of this parameterization into the reaction terms is detailed more clearly in the Appendix, but the most important consequence of this input is to prevent the occurrence of *negative* rates—mathematically feasible, but entirely unphysical, and a classical problem in early diagenetic modeling (Boudreau and Westrich, 1984; Boudreau, 1997). Rate constants also appearing in the model (see Table 2.4) are that for anaerobic methane oxidation k_{MO}, and the kinetic and equilibrium constants associated with $CaCO_3$ precipitation and $Ca^{2=}$ adsorption.

2.3.2.6 DIC PRODUCTION AND $CaCO_3$ PRECIPITATION

To have a more realistic and complete carbon cycle, we include dissolved inorganic carbon and $CaCO_3$ precipitation in the model, we have included them as a feasibility check. DIC production rates are directly linked to GRR and methane oxidation, and the $CaCO_3$ precipitation rate is expressed as a function of the saturation state of $CaCO_3$. Since a substantial fraction of DIC and pore water Ca^{2+} is lost to $CaCO_3$, including these rates is necessary to reproduce the DIC and $[Ca^{2+}]$ pore water profiles, and can be used as a feasibility check on DIC production via GRR and methane oxidation.

2.3.2.7 BASELINE PORE WATER GEOCHEMICAL MODEL OUTPUTS

The details of the diagenetic equations and model run details are fully elaborated upon in the appendix. The principal output of the model, in addition to POC, $[SO_4^{2-}]$, $[CH_4]$, DIC, and $[Ca^{2+}]$, is the sulfate reduction rate, which included sulfate consumed via organoclastic sulfate reduction and methane oxidation, into one term, SRR. While is theoretically possible to calculate the *isotope-specific* rates of sulfate reduction (^{32}SRR, ^{33}SRR, and ^{34}SRR) and incorporate them into the same model, it is far more straightforward to use the output *bulk* sulfate reduction rates, by definition SRR = ^{32}SRR

+^{33}SRR +^{34}SRR, as the model input for a separate isotope model that considers only the sulfate isotopologues $^{32}SO_4^{2-}$, $^{33}SO_4^{2-}$, and $^{34}SO_4^{2-}$, considered in the following section.

2.3.3 TRIPLE ISOTOP(OLOGU)E MODEL FOR SO_4^{2-} ($^{32}SO_4^{2-}$, $^{33}SO_4^{2-}$, $^{34}SO_4^{2-}$)

Researchers have previously approached the problem of calculating isotope-specific rates from the total rate, both for sulfur (Jørgensen, 1979) and carbon (Alperin and Hoehler, 2009). As expected, it requires (i) the natural abundance ratio of the two or more isotopes in a known material, usually a standard, (ii) knowledge of the isotopic composition of the starting reservoir or boundary condition, and (iii) the fractionation factors (α) for the particular microbial processes involved in order to calculate their abundance as a reaction proceeds. The formulation is fairly simple for two isotope systems, but algebraically more complex with three or more isotopes to consider. The derivation of the isotope-specific boundary conditions for [$^{32}SO_4^{2-}$], [$^{33}SO_4^{2-}$], and [$^{34}SO_4^{2-}$], as functions of $\delta^{34}S$ and $\Delta^{33}S$ values, as well as the isotope-specific reaction terms with respect to SRR and the fractionation factors ($^{34}\alpha_{SR}$ and $^{33}\alpha_{SR}$) are shown in the Appendix. The actual concentrations of $^{32}SO_4^{2-}$, $^{33}SO_4^{2-}$, and $^{34}SO_4^{2-}$, used as upper boundary conditions in the isotope model are shown in Table 2.5. As in the baseline geochemical model, all lower boundary conditions for the isotope model are Neumann conditions (*i.e.* constant gradient conditions (d[$^{3X}SO_4^{2-}$]/dx).

2.3.3.1 FRACTIONATION FACTORS—$^{34}\alpha_{SR}$ AND $^{33}\alpha_{SR}$ VIA $^{33}\lambda_{SR}$

As with other S isotope reactive transport models (Aller et al., 2010; Dale et al., 2009; Jørgensen, 1979), the input fractionation factors, the literal ratio of isotope-specific rate constants for a particular biogeochemical process, are an important component of quantifying the rates for individual species (*e.g.*, ^{32}SRR, ^{33}SRR, ^{34}SRR) with respect to bulk rate. In the case of each isotope model run, the input values include $^{34}\alpha_{SR}$ and $^{33}\lambda_{SR}$—$^{33}\alpha_{SR}$ is calculated via:

$$^{33}\alpha_{SR} = \left(^{34}\alpha_{SR}\right)^{^{33}\lambda_{SR}} \tag{2.4}$$

in keeping with previous determinations (*cf.* Young et al., 2002). The computation of the individual rates ^{32}SRR, ^{33}SRR, and ^{34}SRR is shown in Appendix, demonstrating that the accurate determination of each depends on SRR, $[^{32}SO_4^{2-}]$, $[^{33}SO_4^{2-}]$, $[^{34}SO_4^{2-}]$, $^{33}\alpha_{SR}$, and $^{34}\alpha_{SR}$. The isotope-specific diagenetic model considers all species independently, but they are mathematically linked through their reaction terms.

Table 2.5

Solute	Value	Units	Source
SO_4^{2-}	28.93	mM	L[1]
Composition			
$\delta^{34}S$	21.150	‰	L[2]
$\Delta^{33}S$	0.0475	‰	L[2]
Ratio			
$^{33}R_{VCDT}$	0.00787726	-	L[3]
$^{34}R_{VCDT}$	0.04416264	-	L[3]
Species			
$^{32}SO_4^{2-}$	27.472	mM	C[4]
$^{33}SO_4^{2-}$	0.218	mM	C[4]
$^{34}SO_4^{2-}$	1.239	mM	C[4]

[1] Gonzalez-Yajimovich (2007)
[2] Johnston et al. (2014)
[3] Coplen et al. (2002)
[4] Calculations are shown in Appendix

2.3.3.2 MODEL OUTPUT

The model output produces depth-dependent concentrations of $[^{32}SO_4^{2-}]$, $[^{33}SO_4^{2-}]$ and $[^{34}SO_4^{2-}]$, used in concert with the natural abundance ratios to compute the isotope profiles $\delta^{34}S_{SO4}$, $\delta^{33}S_{SO4}$, and $\Delta^{33}S_{SO4}$. Although the bulk sulfate reduction rates are fixed, the sulfate isotopologue profiles are adjustable with $^{34}\alpha_{SR}$ and $^{33}\lambda_{SR}$ only, providing the means for ascertaining how their natural expression

in Alfonso Basin is reflected in pore water sulfate $\delta^{34}S$ and $\Delta^{33}S$ values. To be clear, the $^{34}\alpha_{SR}$ and $^{33}\lambda_{SR}$ values that are used to describe the pore water sulfate profile are comparable to the fractionations extracted from laboratory microbial studies.

2.4 RESULTS AND DISCUSSION

2.4.1 SEDIMENT GEOCHEMISTRY, ORGANIC CARBON (POC), AND MODEL FITS

Previously reported measurements of the weight % organic carbon (POC) suggests that the concentration decreases by several weight % from the core-top to a depth of ~300 cm. Gonzalez-Yajimovich (2004) quantified the weight % of the top 10 cm of Alfonso Basin sediments using the same New Horizon cores employed for this study, suggesting POC = 6.2±0.4 wt%, with the largest values measured at 6.85%. At 250-300 cm, those values have decreased to 3.3±0.2%. These measurements were also corroborated by Berelson et al. (2005). As suggested in Gonzalez-Yajimovich et al. (2007), there is evidence of seismically induced turbidity flow in Alfonso Basin, leading to non-steady state conditions of sedimentation—not surprising for a small marginal basin in the tectonically active Gulf of California. Despite this evidence for non-steady conditions, a simple linear loss model ($r^2 = 0.8$) for organic carbon implies ~1.0 wt% loss per 100 cm for the top 300 cm. The POC modeled in the reactive transport model (3G model) overestimates the concentration at shallow depths ($POC_o = 7.79\%$), but accurately reproduces the concentrations mid-depth. The upper boundary condition was derived from estimates of sinking POC fluxes from sediment trap data in Alfonso Basin (Silverberg et al., 2004).

The 3G model partitioned the 'reactive' organic matter into three different fractions, lumped by reactivity. Each fraction decays (independent mathematically) with first-order decay kinetics with decay constants k_1, k_2, and k_3 for G_1, G_2, and G_3, respectively. The values used for the first-order decay constants ($k_1 = 0.0100\ yr^{-1}$, $k_2 = 0.0010\ yr^{-1}$, and $k_3 = 0.0001\ yr^{-1}$) were chosen empirically, as were the respective fractions of G (f_1, f_2, $f_3 = 1 - f_1 - f_2$). The wt % of each fraction is displayed in Figure 2b, as is total wt% POC. It is worth noting that G_1 and G_2 are consumed almost entirely by

organoclastic sulfate reduction, and that a substantial fraction of G_3, the least reactive fraction of G, is lost via methanogenesis. The summed remineralization rates of the fractions G leads to GRR_{PW}, which decreases from ~2 μmol/cm^3 d^{-1} at the sediment water interface to ~0 at the lower boundary. The output rates for the rest of the model, including SRR, are mathematically linked to GRR via reaction stoichiometry. Since there is no direct proxy for remineralization rates, the kinetics were tuned by the [SO_4^{2-}] and [CH_4] profiles, discussed below.

2.4.2 PORE WATER SO_4^{2-}, [CH_4], AND DIC

The pore water sulfate concentration data in Alfonso Basin, combined gravity core and multicore data exhibits a distinctly linear profile (Berelson et al., 2005). Such profiles are typical of organic carbon rich-sediments, and are, to first order, linked to sedimentation rate (*cf.* Niewohner et al., 1998; Berner, 1978). As shown in Figure 2.4a (see Appendix for data), [SO_4^{2-}] decreases from 27.1±1.0 mM at 1 cm depth to 1.35 mM at ~230 cm depth. An additional measurement from deeper within the gravity core yields a larger concentration measurement, but this is within error of the gravimetrically determined data. Pore water sulfate decreases linearly from the sediment-water-interface to the sulfate-depletion of depth at ~230 cm. Pore water methane reaches concentrations >1 mM at depths greater than 180 cm, giving a sulfate methane transition zone from approximately 175-225 cm. The concentration of dissolved inorganic carbon, DIC, increases from ~3 mM at 1 cm depth approximately linearly to ~40 mM at 150 cm depth, where the slope changes and the concentration gradient decreases. Berelson et al. (2005) postulated that this change in slope is the result of the different reaction stoichiometries associated with organoclastic sulfate reduction and anaerobic methane oxidation. This, in concert with the precipitation of $CaCO_3$, likely explains the deep core behavior of pore water DIC.

Figure 2.2

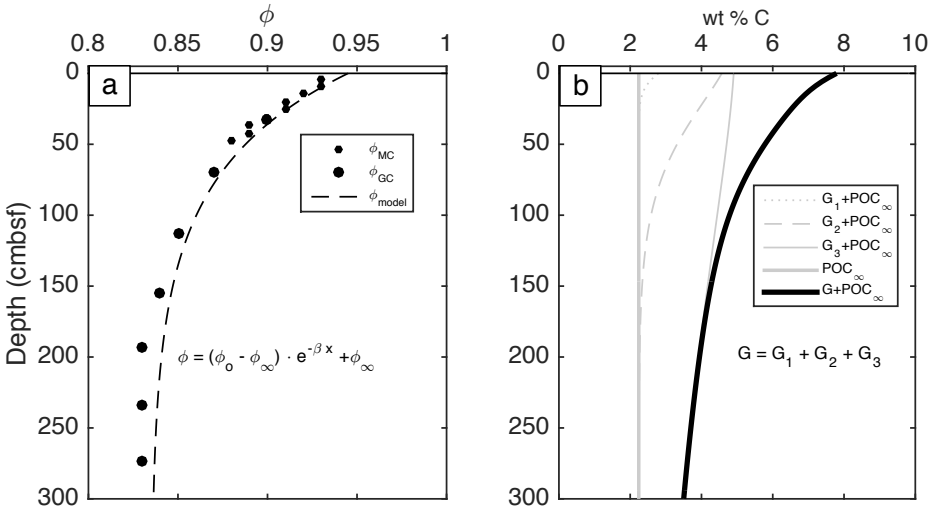

Figure 2.2: **(a)** Porosity (ϕ) data from the gravity (GC) and multicores (MC) used in this study, and originally published in Berelson, et al. (2005). The exponential fit to the porosity data is typical of continental margin sediments and is used to determine the porosity in the diagenetic models constructed here. **(b)** Model parameterization of organic carbon degradation kinetics. The '3G' model used here partitions the pool of reactive carbon (G) into three fractions with shared reactivity (G_1, G_2, G_3), where $k_1 > k_2 > k_3$. The respective sizes of the pools G_n are adjustable, as are the rate constants. POC_∞ is the fraction of organic matter completely resistant to degradation, and $G+POC_\infty$ implies the size (wt% C) of total organic carbon within the Alfonso Basin sediments.

2.4.3 MODELED RATE PROFILES: GRR AND SRR

The modeled organic carbon remineralization rate (GRR), and methane oxidation rate (CH_4OR) were used directly to calculate the sulfate reduction rate (see Fig. 2.3). As mentioned previously, an assumption in the baseline model is that all organic carbon is remineralized either via organoclastic sulfate reduction or methanogenesis. Since anaerobic methane oxidation also has only sulfate as a terminal electron acceptor—by inference, all organic carbon that is remineralized in the model domain is ultimately oxidized with sulfate. The reaction stoichiometries of sulfate reduction, specified here as (C:S) of 0.5875:1 and AOM of 1:1 determine the relationship between the rates of GRR, CH_4OR, and

SRR (see Fig. 2.3b). From the rate profiles, however, it is possible to estimate the fraction of POC that is remineralized via sulfate reduction (~70%) and AOM (~30%). These fractions agree reasonably with those estimated in Berelson et al. (2005), and are within the range determined for typical organic carbon-rich margin sediments. The output SRR, of course is the modulating factor for determining the sulfate concentration profile, and accurately reproduces the pore water data at depths <200 cm. Analytical data from deeper in the core is noisier, and the values > 2mM are likely a sampling artifact.

The column-integrated SRR, across the model domain, yields remineralization rates matching sulfate flux estimates of 400 mmol S/m^2 y^{-1}. As a check, Berelson et al., (2005) computed the DIC flux across the sediment-water interface in Alfonso Basin as ~660 mmol/m^2 y^{-1}, which, using the stoichiometry specified here equates to ~390 mmol S/m^2 y^{-1}. This is in agreement with our estimates.

Figure 2.3

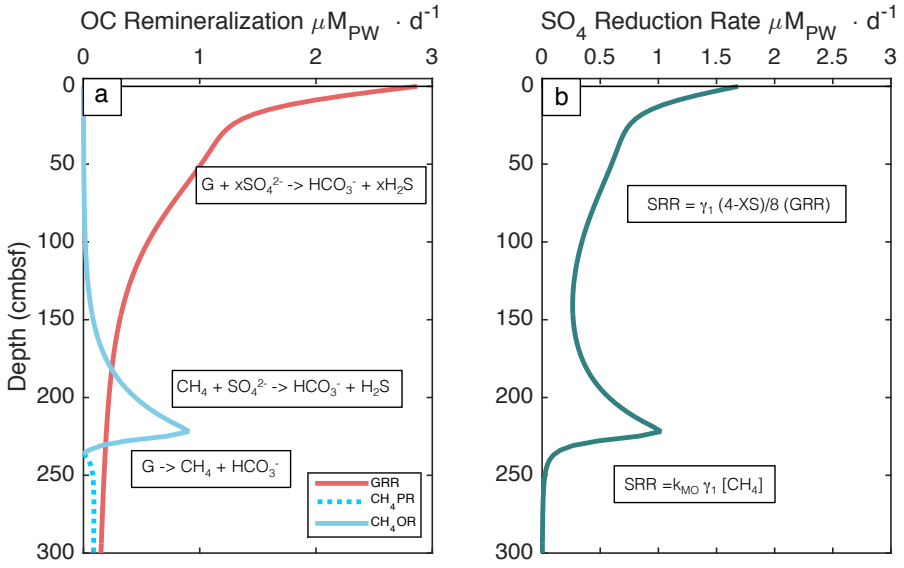

Figure 2.3: (a) Model output from the 3G POC degradation model that parameterizes the remineralization rate, GRR (μM_{PW} d^{-1}), the methane production rate CH_4PR, and the methane oxidation rate CH_4OR. The rates are the primary output of the 3G model, and are used to determine the sulfate reduction rate. **(b)** Modeled sulfate reduction rate, SRR (μM_{PW} d^{-1}), determined from the organic carbon remineralization and methane oxidation rates, as shown in (a). The different stoichiometries of oxidation (1:1 in the case of methane oxidation), control their contribution to SRR. In all cases, sulfate consumption is reduced in cases where sulfate is limiting (*e.g.* $[SO_4^{2-}] < [SO_4^{2-}]^*$).

There is very little actual rate data (*e.g.* ^{35}S-based) to corroborate our modeled rates, however the output $[SO_4^{2-}]$, $[CH_4]$ and DIC data realistically reflect the modeled rates.

Figure 2.4

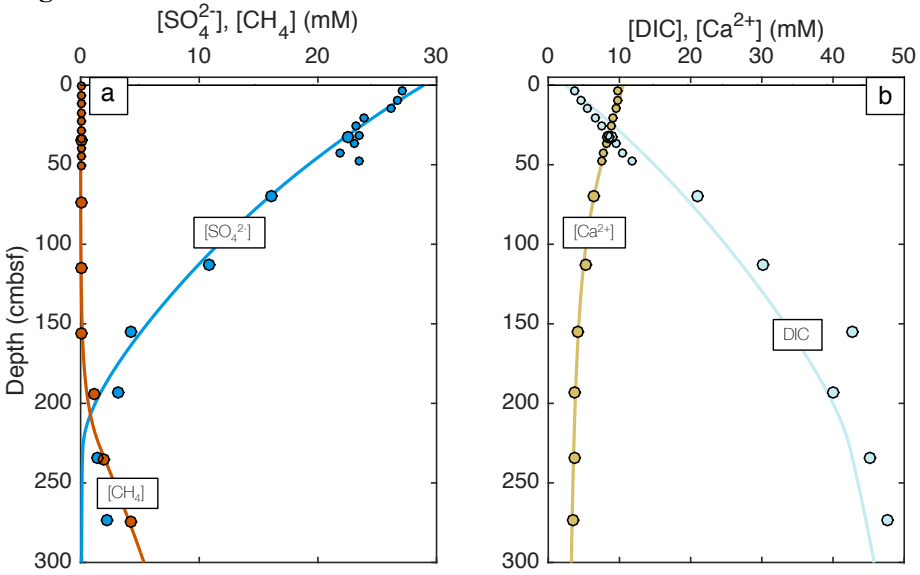

Figure 2.4: (a) Model concentration outputs and Alfonso pore water data for $[SO_4^{2-}]$ and $[CH_4]$. The smaller data points (core top) are multi-core samples, and the larger data points are gravity core samples. The model fits are produced by parameterizing SRR as a function of organic carbon remineralization (GRR). See Appendix for the details of the model construction. **(b)** Dissolved inorganic carbon (DIC) and pore water calcium ($Ca^{2=}$) concentrations and diagenetic model fits. The DIC profile is largely controlled by organic carbon remineralization, and Ca^{2+} is largely controlled by authigenic $CaCO_3$ precipitation.

2.4.4 SULFATE $\delta^{34}S$ AND $\Delta^{33}S$ PROFILES

The measured $\delta^{34}S$ for pore water sulfate increases with depth (see Figure 2.5) as is typical of margin sediments, reflecting the consumption of $^{32}SO_4^{2-}$ by microbial sulfate reduction in pore waters. We were materially limited for most of the samples deeper in the gravity core, but the pore water sulfate $\delta^{34}S$ values increase from seawater values $\delta^{34}S$ = 21.15±0.3‰ (Johnston et al., 2014) to 33.0‰ at approximately 48 cm depth, where $[SO_4^{2-}]$ has dropped to ~22 mM. Less intuitive is the increase in $\Delta^{33}S$ values with depth (see Figure 2.6), rising from near seawater values of 0.047±0.006‰ to 0.089±0.006‰ at 48 cm depth. A few other studies have observed similar behavior in pore waters (Pellerin et al., 2015; Johnston et al., 2008), and researchers demonstrated that closed-system reaction

of sulfate via MSR leads to similar behavior (increases in the values of both $\delta^{34}S$ and $\Delta^{33}S$) (Ono et al., 2006). Rayleigh distillation modeling of such systems shows that a similar trajectory is possible, and is a universal consequence of sulfate consumption with ${}^{34}\alpha_{SR}$ and ${}^{33}\lambda_{SR}$ values typical of MSR.

Figure 2.5

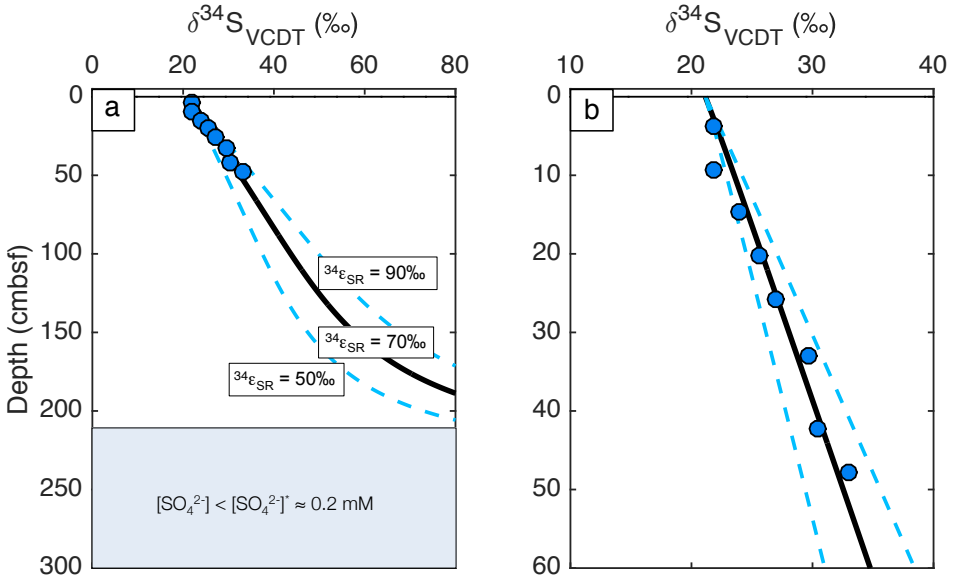

Figure 2.5: (a) Pore water $\delta^{34}S_{SO4}$ values with respect to depth, and corresponding model fits output by the triple isotope reactive transport model. The model uses bulk SRR as an input and recalculates isotope specific rates using fractionation factors (${}^{34}\alpha_{SR}$). The model fits here demonstrate that the best fit comes with a large applied fractionation associated with sulflate reduction (*e.g.* ${}^{34}\varepsilon_{SR}$ = 70‰). Other model fits demonstrate the range of possibilities in $\delta^{34}S$ gradients from different applied fractionation factors (${}^{34}\varepsilon_{SR}$ = 50 and 90‰). **(b)** Same data and models as in (a), but for the depth range covered by the multicore data. The analytical precision on $\delta^{34}S$ values including chemistry and measurement is ±0.3‰.

2.4.5 FRACTIONATION FACTORS (${}^{34}\alpha_{SR}$ AND ${}^{33}\lambda_{SR}$) AND OPEN-SYSTEM MODELING

A primary goal of this study is to determine if the rate – fractionation relationship observed in experimental studies is captured in marine sediments (Leavitt et al., 2013). Importantly, the isotopic model inputs were tunable in the values and down core behavior of ${}^{34}\varepsilon_{SR}$ and ${}^{33}\lambda_{SR}$, while still taking the SRR from the same bulk geochemical model. Recognizing that closed-system modeling of sulfate reduction yields an increase of both $\delta^{34}S$ and $\Delta^{33}S$ values, it is important to highlight that sedimentary

systems are open to diffusive and advective exchange with overlying seawater. First this means that the pore water $\delta^{34}S$ and $\Delta^{33}S$ signatures cannot be used directly to compute intrinsic environmental $^{34}\alpha_{SR}$ and $^{33}\lambda_{SR}$ values. The seminal study that highlighted the consequence of considering sediments as closed systems (Jørgensen, 1979) demonstrated that Rayleigh modeling of sedimentary systems leads to erroneous estimates of the fractionation factors of biogeochemical processes. Though the latter is still frequently used to infer information about biological isotope effects, we submit that only properly constructed reactive transport models can accurately predict information about biologically-mediated isotope effects when considered for open systems. The second key assumption that is explored with our approach is the requirement in a classic closed-system model that the fractionation factor be constant, as opposed to allowing for a depth-dependence to fractionation.

With this in mind, we used the S isotope reactive transport model to estimate the intrinsic fractionation factors required to reproduce the pore water $\delta^{34}S$ and $\Delta^{33}S$ values. As shown in Figs. 2.5 and 2.6, to reproduce the pore water $\delta^{34}S$ values requires a large intrinsic fractionation associated with sulfate reduction ($^{34}\alpha_{SR}$ = 1.070, $^{34}\varepsilon_{SR}$ = 70‰, r^2 = 0.96). For reference, the model $\delta^{34}S_{SO4}$ outputs resulting from $^{34}\varepsilon_{SR}$ = 50‰ (r^2 = 0.71) and 90‰ (r^2 = 0.78) are included as well. Model fits using 60‰ < $^{34}\varepsilon_{SR}$ <80‰ all give $r^2 > 0.90$, though it is important to remember that the depth range covered is only the top 50 cm. Repeating a similar exercise for $^{33}\lambda_{SR}$, a similar error estimate can be done to determine the best fit to the pore water $\Delta^{33}S$ data. For that case we run only models with fixed $^{34}\alpha_{SR}$ (= 1.070), as the $\delta^{34}S$ profile is independent of the errors in the $\Delta^{33}S$ profile estimations. The $^{33}\lambda_{SR}$ value that best produces the pore water $\Delta^{33}S$ data is $^{33}\lambda_{SR}$ = 0.5130 (r^2 = 0.85), shown in Fig 2.6. Other model $\Delta^{33}S$ outputs shown result from $^{33}\lambda_{SR}$ = 0.5110 (r^2 = 0.25) and $^{33}\lambda_{SR}$ = 0.515 (r^2 = 0.25). The implications of these paired fractionation factors/parameters in the light of such experiments is discussed in more detail in the following section, with a sensitivity of these fits (including $^{34}\varepsilon_{SR}$) presented in the Appendix.

Figure 2.6

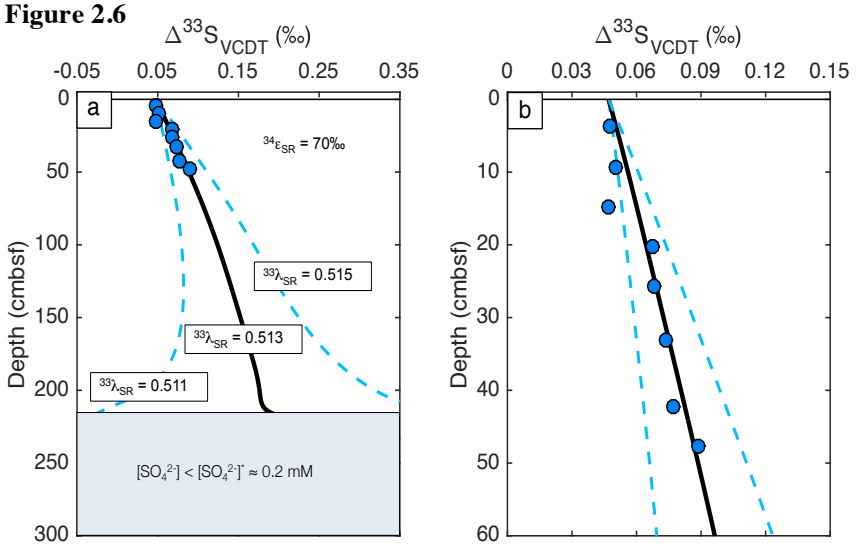

Figure 2.6: (a) Pore water $\Delta^{33}S_{SO4}$ values with respect to depth, and corresponding model fits output by the triple isotope reactive transport model. The model uses bulk SRR as an input and recalculates isotope specific rates using fractionation factors ($^{34}\alpha_{SR}$), and the 'exponent' $^{33}\lambda_{SR}$, which relates that two fractionation factors ($^{33}\alpha_{SR}$ and $^{34}\alpha_{SR}$). The model outputs shown here were run with a constant $^{34}\varepsilon_{SR}$ = 70‰, but variable $^{33}\lambda_{SR}$ values. A value of $^{33}\lambda_{SR}$ ~0.513 fits the data, and the other fits demonstrate the model $\Delta^{33}S$ gradients with $^{33}\lambda_{SR}$ values = 0.511 and 0.515). **(b)** Same data and models as in (a), but for the depth range covered by the multicore data. The measurement precision on $\delta^{34}S$ values is ±0.006‰.

Figure 2.7

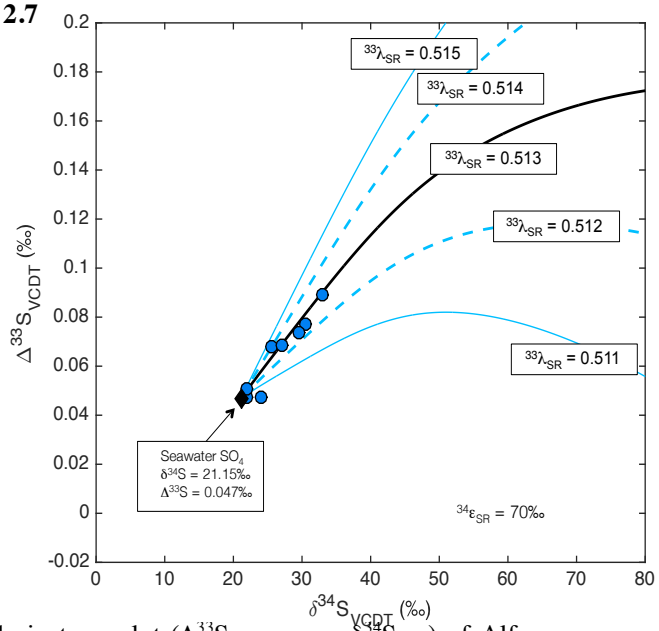

Figure 2.7: Triple isotope plot ($\Delta^{33}S_{SO4}$ versus $\delta^{34}S_{SO4}$) of Alfonso pore water sulfate that plots the model outputs from Fig 5 and 6 concurrently and shows the range provided by variable $^{33}\lambda_{SR}$ values. It is noteworthy that $^{33}\lambda_{SR}$ = 0.515—on the reference frame defined by $\Delta^{33}S$ has a high positive trajectory—and is the isotopic consequence of closed system loss of pore water sulfate via microbial sulfate reduction. For reference, the isotopic composition of seawater sulfate is ($\delta^{34}S_{SO4}$ = 21.15±0.3‰, $\Delta^{33}S_{SO4}$ = 0.0475‰).

2.4.6 ENVIRONMENTAL EXPRESSION OF S ISOTOPE EFFECTS AND IMPLICATIONS[1]

There are several environmental and sedimentary implications stemming from the interpretation of the diagenetic model built to explain the Alfonso Basin. For clarity, the isotopic consequence of the diagenetic model exercise results in an intrinsic fractionation for sulfate reduction of $^{34}\varepsilon_{SR}$ = 70‰ with an accompanying $^{33}\lambda_{SR}$ of 0.5130. Until recently, researchers postulated that the natural upper limit of sulfur isotope fractionation via MSR was limited to $^{34}\varepsilon_{SR} = \delta^{34}S_{SO4} - \delta^{34}S_{H2S} \sim 46‰$ (Johnston, 2011; Habicht and Canfield, 1997; Rees, 1973; Kemp and Thode, 1968; Peck, 1961; Peck, 1958). As a consequence, oxidative sulfur cycling was frequently invoked to explain environmental measurements of isotopic fractionation between sulfate and sulfides—either as H_2S or iron sulfides that exceeded this limit (Habicht et al., 1998; Habicht and Canfield, 1997). Not only did this carry consequences for studying S cycling in modern systems, it also carried deep implications for interpreting ancient S cycling through geological proxy records (*e.g.*, $BaSO_4$, $CaSO_4$, and sedimentary pyrite) (Canfield and Farquhar, 2009; Canfield, 2004; Canfield, 2001; Strauss, 1999; Canfield and Teske, 1996). Despite the lack of empirical evidence that sulfur isotope fractionations could exceed ~46‰, theoretical metabolic models suggested that it was possible (Johnston, 2011; Johnston et al., 2007; Brunner and Bernasconi, 2005). These models called up low-temperature thermodynamics, where calculations suggest sulfur isotope fractionation could even approach the low temperature limit (=70-80‰) at Earth's surface temperatures. More recent experimental work has since demonstrated that microbial fractionations can exceed the canonical 46‰ value, both in laboratory experiments with single cultures of sulfate reducers (Leavitt et al., 2013; Sim et al., 2011) and in environmental systems such a stratified lakes (Gomes et al., 2013; Canfield et al., 2010). An emerging picture highlights the importance of rates of sulfate reduction, modulated by temperature, and more particularly electron donor/carbon source (Leavitt et al., 2013; Sim et al., 2011) as playing a key role in setting the

[1] For completeness, we consider a full sensitivity analysis of different relationships between fractionation and SRR in the Appendix. Briefly, we explore three different dependencies. We examine an exponential relationship, like that seen in pure culture chemostat experiments, as well as a linear dependence of fractionation on SRR. Given the nature of the current data set, using a fixed fractionation value is the most conservative and defendable approach. As such, we explore this scenario in the main text. However, the exploration of the other scenarios is critical for advancing the usage of minor S isotopes in the future.

maximum $^{34}\varepsilon_{SR}$. Specific (*i.e.* biomass-normalized) rates of sulfate reduction are inversely correlated with the magnitude of an expressed isotope effect. Low metabolic rates (~fmol/cell per day) produce fractionations that exceed 50‰ and approach 70‰, and are a predictable consequence from theoretical isotope modeling studies that consider the influence of sulfate reducer biochemistry (Wing and Halevy, 2014). As it relates to the diagenetic model proposed here, we explore the potential for an exponential relationship in the appendix. That aside, all this recent research is converging on the idea that metabolic rate is the governing physiological parameter that controls the magnitude of S isotope fractionation in sulfate reducers, and until proven incorrect, the majority of environmental isotopic compositions can be accommodated by sulfate reduction alone. Moreover, if the modeled fractionation factor demonstrated in this study (=70‰), is shared broadly across environments, it would demonstrate that marine sediments—particularly those in anoxic basins where oxidative S cycling is quantitatively less important—also foster the type of environmental conditions that keep metabolic rates of *in situ* communities of sulfate reducers operating near their physiological limit. The result of this is an isotope fractionation bordering the thermodynamic prediction and elaborated upon below.

The calculated SRR changes as a function of depth. Considering only the top 250 cm of the sediment column where sulfate reduction is actively taking place, the maximum bulk sulfate reduction rate is at the core-top, SRR_{max} = 1.7x10^{-6} mol/(L·d), and the minimum is at the base of the sulfate reduction zone, at 250 cm, SRR_{min} = 0.027 x10^{-6} mol/(L·d). This offers an opportunity to further revisit the environmental manifestation of the rate – fractionation relationship. Importantly, this offers the first critical environmental test of this hypothesis. Recall that there is a coupled nature of $^{34}\varepsilon_{SR}$ and $^{33}\lambda_{SR}$, or more accurately $^{34}\alpha_{SR}$ and $^{33}\lambda_{SR}$, and from experimental work there exists a correlation between the allowable range of $^{33}\lambda_{SR}$ and $^{34}\varepsilon_{SR}$. That is, $^{33}\lambda$ is predictable for fractionating processes (e.g. metabolism) that carry a specific $^{34}\varepsilon_{SR}$. In the case of sulfate reduction, which we have considered exclusively here, the natural range of $^{34}\varepsilon_{SR}$ spans ~70‰ whereas the natural mass-dependent range in $^{33}\lambda_{SR}$ is 0.508-0.515 (Johnston et al., 2008; Leavitt et al., 2013). The coupled nature of $^{34}\varepsilon_{SR}$ and $^{33}\lambda_{SR}$

results in a positive correlation between the two parameters. To put another way, as $^{34}\varepsilon_{SR}$ increases towards the maximum thermodynamically predicted value, $^{33}\lambda_{SR}$ does so concomitantly, to a value of approximately 0.515 (the basis for the $\Delta^{33}S$ reference frame: Farquhar et al., 2003). In the diagenetic model treatment of Alfonso Basin, the two model input parameters - $^{34}\varepsilon_{SR}$ and $^{33}\lambda_{SR}$ - are functionally independent with a best fit of $^{34}\varepsilon_{SR}$ = 70‰ and $^{33}\lambda_{SR}$ = 0.5130. This can be directly compared to the $^{34}\varepsilon_{SR}$ - $^{33}\lambda_{SR}$ pairs from published experiments with sulfate reducers.

The expectation from thermodynamic predictions, and as realized in microbial experiments, is that with a $^{34}\varepsilon_{SR}$ near an equilibrium value, the $^{33}\lambda_{SR}$ should similarly approach an equilibrium value of 0.5145-0.515. The product 0.5130 from our treatment is thus unexpected. We take this as potentially speaking to a number of solutions. First, it is always possible that there is a fundamental difference in the behavior of MSR in marine sediments relative to our preferred laboratory cultures. This could be purely physiological or speak to the behavior of a mixed community of organisms in sediments, as opposed to the tuned monoculture in the laboratory. It is also possible that the environmental conditions – and thus physiological state – of the laboratory culture insufficiently mimics that of marine sediments. Finally, it is possible that the slight mismatch between model fits and equilibrium predictions could reflect contributions from other metabolic processes. This would not augment equilibrium predictions, but would allow for additional (and largely unknown) kinetic effects. In all of these cases, laboratory cultures are a first-step toward interpreting sedimentary data, but necessarily incomplete. Fortunately, these types of features are testable.

It is also important to acknowledge a limitation of the current data set. That is, given the requirements for our mass spectrometry, only the upper reaches of the core were accessible. Having access to pore water sulfate samples from the full length of the pore water sulfate column would certainly improve our understanding of the deep-core behavior of $\Delta^{33}S_{SO4}$ systematics. There is also the opportunity to extend this style of analysis to a more appropriate relation to experimental data, drawing in data on biomass loads and cell counts. Recall that these are bulk geochemical rates, which differ from the normalized rates extracted from experimental microbiology.

There are no measurements of live cell numbers from Alfonso basin sediments. However, estimates exist for the concentration of cells more generally in margin sediments, ranging from 10^6-10^{10} cells/cm^3 for the top 10 cm, decreasing with depth (John Parkes et al., 2014). We can use these general down core observations to provide an order-of-magnitude estimate of the cell specific reduction in Alfonso basin sediments. These estimates are based upon on our modeled rate profile, with $SRR_{max} = 1.7x10^{-9}$ mol/cm^{3}d and $SRR_{min} = 2.7x10^{-11}$ mol/cm^{3}d. These are then simply converted to cell-specific rates, following:

$$csSRR_{max} = \frac{SRR_{max}}{cell\#} \tag{2.5}$$

$$csSRR_{min} = \frac{SRR_{min}}{cell\#} \tag{2.6}$$

Over the range sulfate reduction rates measured for Alfonso Basin, we find that a reasonable estimate of cell-specific reduction rates of csSRR = $1.7x10^{-15}$ -$1.7x10^{-19}$ mol/cell*d is the upper limit for 10^{10} cells/cm^3, and $2.7x10^{-17}$ and $2.7x10^{-21}$ for 10^6 cells/cm^3. A noteworthy consequence of this calculation is that, despite the ~10^2 range in modeled bulk rates for this particular sediment column, the computed range of cell-specific sulfate reduction rates for Alfonso basin sediments are significantly below those generated in the laboratory calibration of Leavitt et al., (2013). Since the lowest rates in Leavitt et al. were characterized by sulfur isotope fractionations >50‰, it is reasonable to suggest that the natural sulfate reduction rates of microbial communities in Alfonso basin are slow enough to explain the large sulfur isotope fractionation as indicated by our modeled profile. This does not amend the mismatch in $^{33}\lambda_{SR}$, but does allow for a significant step toward bridging between experimental and environmental data. It further points to the common behavior MSR in marine sediments operating at exceedingly low metabolic rates – rates approaching chemical equilibrium.

2.4.7 THE UNIQUENESS OF ALFONSO BASIN SEDIMENTS

The analysis given above provides quantitative evidence for the contributions of microbial sulfate reduction and physical transport to an observed pore water sulfate profile. Much of this analysis, however, is tightly linked to the specific geochemical and sedimentological environment present in Alfonso Basin—leading to the question of how these results can be extended more broadly to other diagenetic environments. Sulfate concentration profiles from a wide range of different environments are present in the literature, and Alfonso basin is unexceptional in this sense. Further, there are numerous cases where the $\delta^{34}S_{SO4}$ values of pore water sulfate has been included. Much like that for sulfate concentrations, there is broad similarity between the down core behavior of $\delta^{34}S_{SO4}$ values and $[SO_4^{2-}]$. This has commonly been the motivation for using a closed-system, Rayleigh model to describe this isotopic behavior. However, as we note from above, transport is also a key feature in discerning a strictly microbial feature within marine pore water profiles - a distinction that was aided by the inclusion of $\Delta^{33}S_{SO4}$ measurements. Thus to begin to address the broader applicability of ^{33}S and the model presented above, we present pore water sulfate data ($\delta^{34}S_{SO4}$ and $\Delta^{33}S_{SO4}$) from three other California margin basins: Mazatlan, Santa Monica, and San Blas.

A full, Alfonso basin-like model treatment of these other data sets is outside the scope of this study, given that the requisite supporting data are unavailable. However, the uniqueness of the minor sulfur isotope signature identified in Alfonso basin sediment pore water can serve as a proxy for whether the Alfonso result is more broadly applicable. In Fig. 8, we present data from the other California margin basins. What is immediately clear is that there is a consistency between the Alfonso Basin profiles and the other California margin sites. That noted, there are also potential differences. It is first important to note that pore water sulfate measurements from the other basins cover a wide range of sulfate concentrations, always beginning with bottom waters as the boundary

condition, and carrying seawater sulfate values. Like the Alfonso Basin, as sulfate is reduced in other basinal sediments, the $\delta^{34}S_{SO4}$, and $\Delta^{33}S_{SO4}$ values increase. The overwhelming trend across all basins is a characteristic trajectory in $\delta^{34}S_{SO4}$-$\Delta^{33}S_{SO4}$ values. That noted, there is variability outside of analytical precision. The root of this variance is a target for further research as it could be related to any one of the various parameters that come to control the early diagenesis of sulfur. Fortunately, the general consistency among the observations leaves the inclusion of ^{33}S as a promising direction for further study.

Figure 2.8

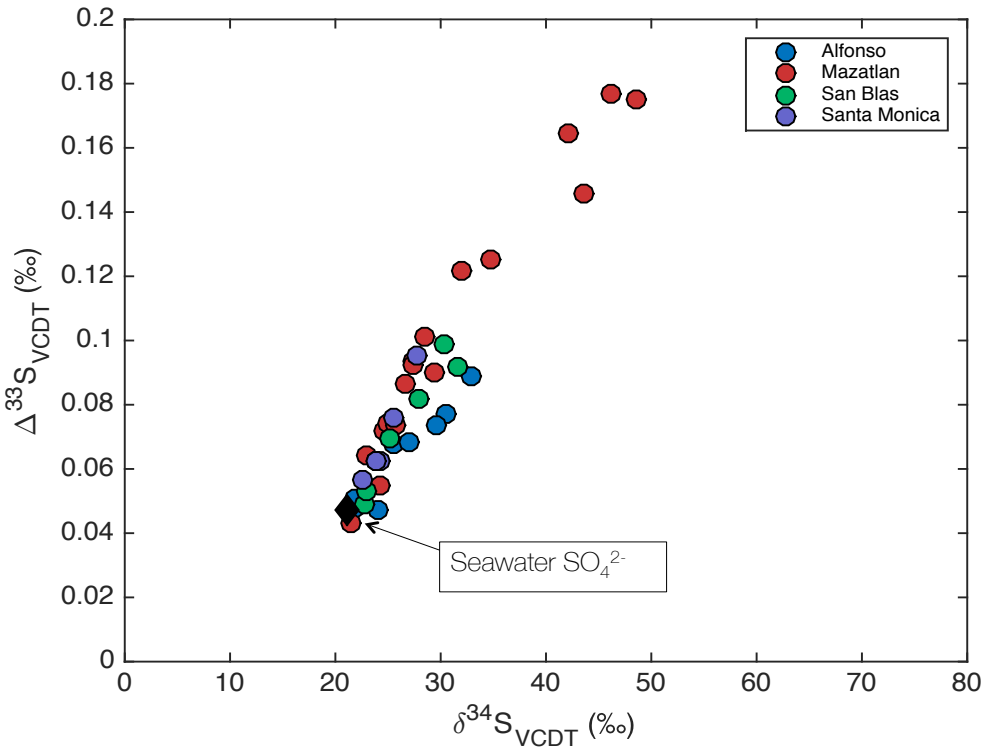

Figure 2.8: Triple isotope plot ($\Delta^{33}S_{SO4}$–$\delta^{34}S_{SO4}$) of pore water sulfate sampled during the CalMex (2001) cruise, with Alfonso, Mazatlan, Santa Monica, and San Blas Basins. All four basins are anoxic silled basins of the California-Mexican margin. The pore water sulfate displayed here is largely from the multicores sampled during that cruise, except for Mazatlan, which also includes gravity core sulfate. Seawater sulfate is included for reference ($\delta^{34}S_{SO4}$ = 21.15±0.15‰ and $\Delta^{33}S_{SO4}$ = 0.047±0.006‰).

2.5 CONCLUSIONS

Laboratory-based studies recently highlighted the dependence of metabolic rate of sulfate reduction on the magnitude of the product sulfur isotopic effect. In this study we examine whether isotope fractionation, as preserved in marine pore water sulfate, carries a memory effect of changes in microbial metabolic rates. In order to address this question, we analyzed a geochemically well-characterized core for the triple isotopic composition of pore water sulfate. We also formulated a reactive-transport diagenetic model for a sedimentary system in order to quantitatively understand the triple S isotope characteristics and its relationships to microbial calibrations of sulfur metabolisms. The model reproduces the profiles of the major pore water species, including [SO_4^{2-}], [CH_4], DIC, and Ca^{2+}, and generates realistic sulfate reduction and methane oxidation rate profiles that corroborate previously published data. The sulfate reduction rate profile is then used, in concert with fractionation parameters, to evaluate the intrinsic isotopic characteristics of sedimentary sulfate reduction required to reproduce the triple isotope behavior of pore water sulfate within Alfonso basin. From this we find a best-fit solution is where $^{34}\varepsilon_{SR}$ and $^{34}\lambda_{SR}$ are invariant with values of 70‰ and 0.5130 respectively. Put differently, no change in the intrinsic fractionation is necessary to account for the down core, evolving composition of sulfate. That noted, this result is constrained by the observational window presented herein, where we cover ~50 cm of depth, and 20% of sulfate removal. It is possible that in cases where a larger range is sampled, with the potential for greater changes in SRR, and/or a larger range in $\delta^{34}S$, such a relationship will be found. The model framework presented here is directly transferable to such as study.

We demonstrate that pore water isotope signatures are characteristic of environments with very low specific rates of sulfate reduction – despite the fact that Alfonso basin is an organic carbon-rich marginal setting. However, the triple isotope signatures ($\delta^{34}S$ /$\Delta^{33}S$) are still within the range of the predictions from laboratory calibrations of sulfate reducers, and no additional need for S cycling is required to produce the pore water $\Delta^{33}S_{SO4}$ profile. Despite the challenges in assessing a potential rate relationship to fractionation, what our treatment further reinforces that physical transport (advection

and diffusion) significantly contributes to observed isotopic behavior of pore water sulfate. The isotopic composition of pore water sulfate thus records more than biogeochemical processes and must be interpreted in the light of this finding. Future studies would benefit from whole core samples and more in-depth consideration of the triple isotope composition of other pore water and solid phase S species.

2.6 ACKNOWLEDGEMENTS

We thank Erin Beirne for laboratory assistance, Itay Halevy for thoughtful discussions, and the crew of New-Horizons for assistance with coring and sampling during the cruise of 2001. A.L.M. is funded through Harvard University through a Peirce Fellowship. This work is supported by an NSF instrument grant and NASA Astrobiology Institute to D.T.J.

2.7 REFERENCES

Aller, R.C., 2014, Sedimentary Diagenesis, Depositional Environments, and Benthic Fluxes, ed., Sedimentary Diagenesis, Depositional Environments, and Benthic Fluxes. Treatise on Geochemistry, p. 293–334.

Aller, R.C., Madrid, V., Chistoserdov, A., Aller, J.Y., and Heilbrun, C. (2010) Unsteady diagenetic processes and sulfur biogeochemistry in tropical deltaic muds: Implications for oceanic isotope cycles and the sedimentary record. *Geochimica et Cosmochimica Acta* **74**, 4671–4692.

Aller, R.C., and Blair, N.E. (1996) Sulfur diagenesis and burial on the Amazon shelf: major control by physical sedimentation processes. *Geo-Marine Letters* **16**, 3–10.

Alperin, M.J., Albert, D.B., and Martens, C.S. (1994) Seasonal variations in production and consumption rates of dissolved organic carbon in an organic-rich coastal sediment. *Geochimica et Cosmochimica Acta* **58**, 4909–4930.

Alperin, M.J., and Hoehler, T.M. (2009) Anaerobic methane oxidation by archaea/sulfate-reducing bacteria aggregates: 2. Isotopic constraints. *American Journal of Science* **309**, 958–984.

Arndt, S., Jørgensen, B.B., LaRowe, D.E., Middelburg, J.J., Pancost, R.D., and Regnier, P. (2013) Quantifying the degradation of organic matter in marine sediments: A review and synthesis. *Earth-Science Reviews* **123**, 53–86.

Bak, F., and Cypionka, H. (1987) A novel type of energy metabolism involving fermentation of inorganic sulphur compounds.

Berelson, W.M., Prokopenko, M., Sansone, F.J., Graham, A.W., McManus, J., and Bernhard, J.M. (2005) Anaerobic diagenesis of silica and carbon in continental margin sediments: Discrete zones of TCO_2 production. *Geochimica et Cosmochimica Acta* **69**, 4611–4629.

Berner, R.A. (1964) An idealized model of dissolved sulfate distribution in recent sediments. *Geochimica et Cosmochimica Acta* **28**, 1497–1503.

Berner, R.A. (1980) Early Diagenesis. pp. 256.

Berner, R.A. (1978) Sulfate reduction and the rate of deposition of marine sediments. *Earth and Planetary Science Letters* **37**, 492–498.

Bigeleisen, J., and Mayer, M.G. (1947) Calculation of Equilibrium Constants for Isotopic Exchange Reactions. *J. Chem. Phys.* **15**, 261.

Boudreau, B.P. (1996) Diagenetic Models and Their Implementation. pp 436.

Boudreau, B.P., and Westrich, J.T. (1984) The dependence of bacterial sulfate reduction on sulfate concentration in marine sediments. *Geochimica et Cosmochimica Acta* **48**, 2503–2516.

Bowles, M.W., Mogollón, J.M., Kasten, S., Zabel, M., and Hinrichs, K.U. (2014) Global rates of marine sulfate reduction and implications for sub-sea-floor metabolic activities. *Science* **344**, 889–891.

Bradley, A.S., Leavitt, W.D., Schmidt, M., Knoll, A.H., Girguis, P.R., and Johnston, D.T. (2015) Patterns of sulfur isotope fractionation during Microbial Sulfate Reduction. *Geobiology*, 1–11.

Brunner, B., and Bernasconi, S.M. (2005) A revised isotope fractionation model for dissimilatory sulfate reduction in sulfate reducing bacteria. *Geochimica et Cosmochimica Acta* **69**, 4759–4771.

Canfield, D.E. (2001) Biogeochemistry of sulfur isotopes. *Reviews in Mineralogy and Geochemistry* **43**, 607–636.

Canfield, D.E. (2004) The evolution of the Earth surface sulfur reservoir. *American Journal of Science* **304**, 839–861.

Canfield, D.E., and Farquhar, J. (2009) Animal evolution, bioturbation, and the sulfate concentration of the oceans. *Proceedings of the National Academy of Sciences* **106**, 8123–8127.

Canfield, D.E., Farquhar, J., and Zerkle, A.L. (2010) High isotope fractionations during sulfate reduction in a low-sulfate euxinic ocean analog. *Geology* **38**, 415–418.

Canfield, D.E., and Teske, A. (1996) Late Proterozoic rise in atmospheric oxygen concentration inferred from phylogenetic and sulphur-isotope studies. *Nature* **382**, 127–132.

Chambers, L.A., Trudinger, P.A., Smith, J.W., and Burns, M.S. (1975) Fractionation of sulfur isotopes by continuous cultures of Desulfovibrio desulfuricans. *Canadian Journal of Microbiology* **21**, 1602–1607.

Coplen, T.B., Hopple, J.A., Boehike, J.K., Peiser, H.S., and Rieder, S.E. (2002) Compilation of minimum and maximum isotope ratios of selected elements in naturally occurring terrestrial materials and reagents.

Dale, A.W., Brüchert, V., Alperin, M., and Regnier, P. (2009) An integrated sulfur isotope model for Namibian shelf sediments. *Geochimica et Cosmochimica Acta* **73**, 1924–1944.

Detmers, J., Brüchert, V., Habicht, K.S., and Kuever, J. (2001) Diversity of sulfur isotope fractionations by sulfate-reducing prokaryotes. *Appl Environ Microbiol* **67**, 888–894.

Donahue, M.A., Werne, J.P., Meile, C., and Lyons, T.W. (2008) Modeling sulfur isotope fractionation and differential diffusion during sulfate reduction in sediments of the Cariaco Basin. *Geochimica et Cosmochimica Acta* **72**, 2287–2297.

Farquhar, J., Canfield, D.E., Masterson, A., Bao, H., and Johnston, D. (2008) Sulfur and oxygen isotope study of sulfate reduction in experiments with natural populations from Fællestrand, Denmark. *Geochimica et Cosmochimica Acta* **72**, 2805–2821.

Farquhar, J., Johnston, D.T., Wing, B.A., Habicht, K.S., Canfield, D.E., Airieau, S., and Thiemens, M.H. (2003) Multiple sulphur isotopic interpretations of biosynthetic pathways: implications for biological signatures in the sulphur isotope record. *Geobiology* **1**, 27–36.

Finster, K., Liesack, W., and Thamdrup, B. (1998) Elemental sulfur and thiosulfate disproportionation by Desulfocapsa sulfoexigens sp. nov., a new anaerobic bacterium isolated from marine surface sediment. *Applied and Environmental Microbiology* **64**, 119–125.

Forrest, J., and Newman, L. (1977) Silver-110 microgram sulfate analysis for the short time resolution of ambient levels of sulfur aerosol. *Analytical Chemistry* **49**, 1579–1584.

Goldhaber, M.B., and Kaplan, I.R. (1980) Mechanisms of sulfur incorporation and isotope fractionation during early diagenesis in sediments of the Gulf of California. *Marine Chemistry* **9**, 95–143.

Gomes, M.L., and Hurtgen, M.T. (2013) Sulfur isotope systematics of a euxinic, low-sulfate lake: Evaluating the importance of the reservoir effect in modern and ancient oceans. *Geology* **41**, 663–666.

Gonzalez-Yajimovich, O.E., Gorsline, D.S., and Douglas, R.G. (2007) Frequency and sources of basin floor turbidites in alfonso basin, Gulf of California, Mexico: Products of slope failures. *Sedimentary*

Geology **199**, 91–105.

Gonzalez-Yajimovich (2004) Holocene sedimentation in the Gulf of California and its Climatic implications. Ph.D. thesis, pp 211.

Habicht, K.S., and Canfield, D.E. (2001) Isotope fractionation by sulfate-reducing natural populations and the isotopic composition of sulfide in marine sediments. *Geology* **29**, 555–558.

Habicht, K.S., and Canfield, D.E. (1997) Sulfur isotope fractionation during bacterial sulfate reduction in organic-rich sediments. *Geochimica et Cosmochimica Acta* **61**, 5351–5361.

Habicht, K.S., Canfield, D.E., and Rethmeier, J.O. (1998) Sulfur isotope fractionation during bacterial reduction and disproportionation of thiosulfate and sulfite. *Geochimica et Cosmochimica Acta* **62**, 2585–2595.

Habicht, K.S., Gade, M., Thamdrup, B., Berg, P., and Canfield, D.E. (2002) Calibration of sulfate levels in the Archean ocean. *Science* **298**, 2372–2374.

Johnston, D.T. (2011) Multiple sulfur isotopes and the evolution of Earth's surface sulfur cycle. *Earth-Science Reviews* **106**, 161–183.

Johnston, D.T., Farquhar, J., and Canfield, D.E. (2007) Sulfur isotope insights into microbial sulfate reduction: When microbes meet models. *Geochimica et Cosmochimica Acta* **71**, 3929–3947.

Johnston, D.T., Farquhar, J., Wing, B.A., Kaufman, A.J., Canfield, D.E., and Habicht, K.S. (2005) Multiple sulfur isotope fractionations in biological systems: a case study with sulfate reducers and sulfur disproportionators. *American Journal of Science* **305**, 645–660.

Johnston, D.T., Wing, B.A., Farquhar, J., Kaufman, A.J., Strauss, H., Lyons, T.W., Kah, L.C., and Canfield, D.E. (2005) Active microbial sulfur disproportionation in the Mesoproterozoic. *Science* **310**, 1477–1479.

Johnston, D.T., Farquhar, J., Habicht, K.S., and Canfield, D.E. (2008) Sulphur isotopes and the search for life: strategies for identifying sulphur metabolisms in the rock record and beyond. *Geobiology* **6**, 425–435.

Jørgensen, B.B. (1979) A theoretical model of the stable sulfur isotope distribution in marine sediments. *Geochimica et Cosmochimica Acta* **43**, 363–374.

Jørgensen, B.B. (1982) Mineralization of organic matter in the sea bed: the role of sulphate reduction. *Nature*. **296**, 643-645.

Kemp, A.L.W., and Thode, H.G. (1968) The mechanism of the bacterial reduction of sulphate and of sulphite from isotope fractionation studies. *Geochimica et Cosmochimica Acta* **32**, 71–91.

Leavitt, W.D., Bradley, A.S., Santos, A.A., Pereira, I.A., and Johnston, D.T. (2015) Sulfur Isotope Effects of Dissimilatory Sulfite Reductase. *Front Microbiol* **6**, 1392.

Leavitt, W.D., Halevy, I., Bradley, A.S., and Johnston, D.T. (2013) Influence of sulfate reduction rates on the Phanerozoic sulfur isotope record. *Proc Natl Acad Sci U S A* **110**, 11244–11249.

Li,Y-H and Gregory, S. (1974) Diffusion of ions in sea water and in deep-sea sediments. *Geochimica et Cosmochimica acta* **38**, 703–714.

Masterson, A.L., Wing, B.A., Paytan, A., Farquhar, J., and Johnston, D.T. (2016) The minor sulfur isotope composition of Cretaceous and Cenozoic seawater sulfate. *Paleoceanography*.

Niewöhner, C., Hensen, C., Kasten, S., Zabel, M., and Schulz, H.D. (1998) Deep sulfate reduction

completely mediated by anaerobic methane oxidation in sediments of the upwelling area off Namibia. *Geochimica et Cosmochimica Acta* **62**, 455–464.

Ono, S., Wing, B., Johnston, D., Farquhar, J., and Rumble, D. (2006) Mass-dependent fractionation of quadruple stable sulfur isotope system as a new tracer of sulfur biogeochemical cycles. *Geochimica et Cosmochimica Acta* **70**, 2238–2252.

Peck, H.D. (1961) Evidence for the reversibility of the reaction catalyzed by adenosine 5 - phosphosulfate reductase. *Biochimica et biophysica acta* **49**, 621–624.

Peck, H.D. (1959) The ATP-dependent reduction of sulfate with hydrogen in extracts of Desulfovibrio desulfuricans. *Proceedings of the National Academy of Sciences* **45**, 701–708.

Pellerin, A., Bui, T.H., Rough, M., Mucci, A., Canfield, D.E., and Wing, B.A. (2015) Mass-dependent sulfur isotope fractionation during reoxidative sulfur cycling: A case study from Mangrove Lake, Bermuda. *Geochimica et Cosmochimica Acta* **149**, 152-164.

Rees, C.E. (1973) A steady-state model for sulphur isotope fractionation in bacterial reduction processes. *Geochimica et Cosmochimica Acta* **37**, 1141–1162.

Sansone, F.J., Graham, A.W., and Berelson, W.M. (2004) Methane along the western Mexican margin. *Limnology and oceanography* **49**, 2242–2255.

Silverberg, N., Aguirre-Bahena, F., and Mucci, A. (2014) Time-series measurements of settling particulate matter in Alfonso Basin, La Paz Bay, southwestern Gulf of California. *Continental Shelf Research* **84**, 169–187.

Sim, M.S., Bosak, T., and Ono, S. (2011) Large sulfur isotope fractionation does not require disproportionation. *Science* **333**, 74–77.

Sim, M.S., Ono, S., and Bosak, T. (2012) Effects of iron and nitrogen limitation on sulfur isotope fractionation during microbial sulfate reduction. *Appl Environ Microbiol* **78**, 8368–8376.

Sim, M.S., Ono, S., and Hurtgen, M.T. (2015) Sulfur isotope evidence for low and fluctuating sulfate levels in the Late Devonian ocean and the potential link with the mass extinction event. *Earth and Planetary Science Letters* **419**, 52–62.

Staines-Urías, F., González-Yajimovich, O., and Beaufort, L. (2015) Reconstruction of past climate variability and ENSO-like fluctuations in the southern Gulf of California (Alfonso Basin) since the last glacial maximum. *Quaternary Research* **83**, 488–501.

Strauss, H. (1999) Geological evolution from isotope proxy signals--sulfur. *Chemical Geology* **161**, 89–101.

Tarpgaard, I.H., Røy, H., and Jørgensen, B.B. (2011) Concurrent low- and high-affinity sulfate reduction kinetics in marine sediment. *Geochimica et Cosmochimica Acta* **75**, 2997–3010.

Thamdrup, B., Finster, K., Hansen, J.W., and Bak, F. (1993) Bacterial disproportionation of elemental sulfur coupled to chemical reduction of iron or manganese. *Applied and environmental microbiology* **59**, 101–108.

Ullman, W.J., and Aller, R.C. (1982) Diffusion coefficients in nearshore marine sediments. *Limnology and Oceanography* **27**, 552–556.

Wortmann, U.G., Bernasconi, S.M., and Bottcher, M.E. (2001) Hypersulfidic deep biosphere indicates extreme sulfur isotope fractionation during single-step microbial sulfate reduction. *Geology* **29**, 647–650.

Westrich, J.T., and Berner, R.A. (1984) The role of sedimentary organic matter in bacterial sulfate reduction: The G model tested. *Limnology and oceanography* **29**, 236–249.

Wortmann, U.G., Bernasconi, S.M., and Bottcher, M.E. (2001) Hypersulfidic deep biosphere indicates extreme sulfur isotope fractionation during single-step microbial sulfate reduction. *Geology* **29**, 647–650.

Wu, N., Farquhar, J., and Fike, D.A. (2015) Ediacaran sulfur cycle: Insights from sulfur isotope measurements ($\Delta^{33}S$ and $\delta^{34}S$) on paired sulfate–pyrite in the Huqf Supergroup of Oman. *Geochimica et Cosmochimica Acta* **164**, 352–364.

Wu, N., Farquhar, J., Strauss, H., Kim, S.-T., and Canfield, D.E. (2010) Evaluating the S-isotope fractionation associated with Phanerozoic pyrite burial. *Geochimica et Cosmochimica Acta* **74**, 2053–2071.

Young, E.D., Galy, A., and Nagahara, H. (2002) Kinetic and equilibrium mass-dependent isotope fractionation laws in nature and their geochemical and cosmochemical significance. *Geochimica et Cosmochimica Acta* **66**, 1095–1104.

Zeebe, R.E., and Wolf-Gladrow, D. (2001) CO_2 in Seawater: Equilibrium, Kinetics, Isotopes, Volume 65 (Elsevier Oceanography Series). pp. 360.

2.8 APPENDIX

2.8.1 DERIVATION OF THE TERMS GRR AND SRR IN THE BULK GEOCHEMICAL (RTM)

Diagenetic reactive transport models have been extensively applied over the past 50 years (*cf*. Berner, 1964), and have been the subject of numerous papers. The mathematics behind them have also been fleshed out in two textbooks that are still the standard references on the subject (Berner, 1980; Boudreau, 1997). We apply a few of the formulations here to derive the equations used in the bulk geochemical model, and to demonstrate how rates are calculated from the concentrations of pore water species.

Using a combination of finite difference methods, and well-known relationship that defines tortuosity –the mean path of a solute through a porous medium, ($D_S = \phi^{-2}D$, see Ullman and Aller, 1982), the steady-state reactive transport equation for a solute c in a porous medium is defined as:

$$\varphi^2 D \frac{d^2 c_{pw}}{dx} + \left(3\varphi D \frac{d\varphi}{dx} - \frac{\omega_\infty \varphi_\infty}{\varphi} \right) \frac{dc_{pw}}{dx} + \Sigma R_{pw} = 0 \tag{2.7}$$

Where ϕ is the depth-dependent porosity, D is the bulk sediment diffusion coefficient, c_{pw} is the concentration of the species in pore water, ϕ_∞ and ω_∞ are the porosity and sedimentation rate at infinite depth—the lower depth boundary. The term ΣR_{PW} is sum of all the reaction terms influencing the pore water concentration of c. For solid phase components, the terms are simplified due to a lack of diffusion, and the steady state equation becomes:

$$\frac{\omega_\infty \varphi_\infty}{\varphi} \frac{dc_{ds}}{dx} + \Sigma R_{ds} = 0 \tag{2.8}$$

In this case c_{ds} is the concentration of the species in the dry sediment. To parameterize OC remineralization, we employ a '3G' model, consisting of three 'reactive' POC fractions that are binned by reactivity, and share a unique remineralization constant (*e.g.*, k_1, k_2, k_3). As model inputs, f_1 and f_2 are the fractions of G_1, and G_2 in the total reactive pool G, and thus the concentrations of G_1, G_2, and G_3 are determined as follows:

$$G_1 = f_1 \cdot G \tag{2.9a}$$

$$G_2 = f_2 \cdot G \tag{2.9b}$$

$$G_3 = (1 - f_1 - f_2) \cdot G \tag{2.9c}$$

The fractions of G_1, G_2, and G_3 are computed in this way, are used to set the upper boundary conditions for the model. The determination for the organic carbon remineralization rate—termed GRR, with respect to pore water, is derived from the Runge-Kutta finite-difference method for each of the reactive fractions (n =1,2,3):

$$\frac{dG_n}{dx} = -k_n \frac{G_n(1-\varphi)}{\omega_\infty(1-\varphi_\infty)} \tag{2.10}$$

$$GRR_{pw} = (k_1 G_1 + k_2 G_2 + k_3 G_3)\left(\frac{\rho_{sm}(1-\varphi)}{0.0012 \cdot \varphi}\right) \tag{2.11}$$

The term GRR_{pw} has units of μmol/cm^3/d, whereas all of the fractions G are as wt%, hence the normalizing term.In the bulk model, GRR_{pw} is computed first, and is conical rate that is used to determine the sulfate reduction rate (SRR), and methane production rate (CH_4PR). Implicit in this calculation is that all organic carbon remineralization taking place at depths where sulfate concentrations exceed a prescribed threshold ($[SO_4^{2-}] > [SO_4^{2-}]^*$) takes place via sulfate reduction (*i.e.* no aerobic remineralization, no ferric iron reduction, etc.). At any depth where $[SO_4^{2-}] < [SO_4^{2-}]^*$, remineralization takes place via methanogenesis. SRR also takes into account SO_4^{2-} consumed via methane oxidation (AOM). The calculation of SRR and GRR are demonstrated below:

$$SRR_{pw} = \gamma_1 \left[\left(\frac{4 - XS}{8}\right) \cdot GRR_{pw} + k_{MO}[CH_4]\right] \tag{2.12a}$$

Where:

$$\gamma_1 = 0.5\left[1 + erfc\left[\frac{[SO_4^{2-}] - [SO_4^{2-}]^*}{0.05}\right]\right] \tag{2.12b}$$

Is the function that modulates SRR in the presence of sulfate limitation (*i.e.* to parameterize Monod kinetics). The term XS is the oxidation state of organic matter (Alperin et al., 1994). The rate of methanogenesis CH_4PR is thus:

$$CH_4PR = \gamma_2 \cdot \left[\left(\frac{4 - XS}{8} \right) \cdot GRR_{pw} \right] \tag{2.13a}$$

Where:

$$\gamma_2 = 0.5 \left[1 - erfc \left[\frac{[SO_4^{2-}] - [SO_4^{2-}]^*}{0.05} \right] \right] \tag{2.13b}$$

This function γ_2 has a similar purpose, but modulates the rates of methanogenesis due to sulfate inhibition about the prescribed sulfate threshold $[SO_4^{2-}]^*$. These two rates (SRR and CH_4PR) are employed in the finite difference diagenetic model that solves for the concentrations of $[SO_4^{2-}]$ and $[CH_4]$. The model for Ca^{2+}, DIC is run separately, with the controlling rates (DIC production, $CaCO_3$ precipitation).

2.8.2 DERIVATION OF UPPER BOUNDARY CONDITIONS FOR $[^{32}SO_4^{2-}]$, $[^{33}SO_4^{2-}]$, AND $[^{34}SO_4^{2-}]$ FROM $\delta^{34}S_{SO4}$, AND $\Delta^{33}S_{SO4}$ VALUES OF SEAWATER SO_4

For the case where $[^{36}SO_4^{2-}]$ is excluded from consideration, $[SO_4^{2-}]$ is the sum of the constituent species $[^{32}SO_4^{2-}]$, $[^{33}SO_4^{2-}]$, and $[^{34}SO_4^{2-}]$, as below in Eq. (2.14)

$$[SO_4^{2-}] = [^{32}SO_4^{2-}] + [^{33}SO_4^{2-}] + [^{34}SO_4^{2-}] \tag{2.14}$$

The terms ^{33}F and ^{34}F refer to the ratio of the species $[^{33}SO_4^{2-}]$ and $[^{34}SO_4^{2-}]$ with respect to $[^{32}SO_4^{2-}]$, with $^{33}R_{std} = 0.00787726$, and $^{34}R_{std} = 0.04416264$ referring to the natural abundance ratios (Coplen et al., 2002).

$$^{33}F = \frac{[^{33}SO_4^{2-}]}{[^{32}SO_4^{2-}]} = \left[\frac{\delta^{33}S_{SO_4}}{1000} + 1 \right] \cdot {}^{33}\mathfrak{R}_{std} \tag{2.15a}$$

$$^{34}F = \frac{[^{34}SO_4^{2-}]}{[^{32}SO_4^{2-}]} = \left[\frac{\delta^{34}S_{SO_4}}{1000} + 1 \right] \cdot {}^{34}\mathfrak{R}_{std} \tag{2.15b}$$

$$\frac{^{33}F}{^{34}F} = \frac{[^{34}SO_4^{2-}]}{[^{33}SO_4^{2-}]} \tag{2.16}$$

Equations 2.16, in combination with 2.15, can be used to calculate the abundance/concentration of each of the species [$^{32}SO_4^{2-}$], [$^{33}SO_4^{2-}$], and [$^{34}SO_4^{2-}$], with respect to the bulk SO_4^{2-} concentration at the upper boundary condition, by algebraic manipulation, *e.g.* for [$^{32}SO_4^{2-}$]:

$$[SO_4^{2-}] = [^{32}SO_4^{2-}] + [^{32}SO_4^{2-}]\,^{33}F + [^{32}SO_4^{2-}]\,^{34}F = [^{32}SO_4^{2-}]\left(1 + {}^{33}F + {}^{34}F\right) \tag{2.17}$$

$$[^{32}SO_4^{2-}] = [SO_4^{2-}]\left[\frac{1}{1 + {}^{33}F + {}^{34}F}\right] \tag{2.18}$$

And for [$^{33}SO_4^{2-}$]:

$$[SO_4^{2-}] = \frac{[^{33}SO_4^{2-}]}{^{33}F} + [^{33}SO_4^{2-}] + \frac{[^{33}SO_4^{2-}]\,^{34}F}{^{33}F} = [^{33}SO_4^{2-}]\left(\frac{1}{^{33}F} + 1 + \frac{^{34}F}{^{33}F}\right) \tag{2.19}$$

$$[^{33}SO_4^{2-}] = [SO_4^{2-}]\left[\frac{1}{^{33}F} + 1 + \frac{^{34}F}{^{33}F}\right]^{-1} = [SO_4^{2-}]\left[\frac{^{33}F}{1 + {}^{33}F + {}^{34}F}\right] \tag{2.20}$$

And finally for [$^{34}SO_4^{2-}$]:

$$[SO_4^{2-}] = \frac{[^{34}SO_4^{2-}]}{^{34}F} + [^{34}SO_4^{2-}]\,\frac{^{33}F}{^{34}F} + [^{34}SO_4^{2-}] = \left[^{34}SO_4^{2-}\right]\left[\frac{1}{^{34}F} + \frac{^{33}F}{^{34}F} + 1\right] \tag{2.21}$$

$$[^{32}SO_4^{2-}] = \left[SO_4^{2-}\right]\left[\frac{1}{^{34}F} + \frac{^{33}F}{^{34}F} + 1\right]^{-1} = [SO_4^{2-}]\left[\frac{^{34}F}{1 + {}^{33}F + {}^{34}F}\right] \tag{2.22}$$

In principal, this method can be used to derive the concentrations of the individual species anywhere within the domain of the reactive transport model, but only truly serves where the isotope ratios (*e.g.*

$\delta^{34}S_{SO4}$, $\delta^{33}S_{SO4}$ and $\Delta^{33}S_{SO4}$) are satisfactorily known. The isotope model computes the concentrations of the species independently, but they are linked through the reaction terms ^{32}SRR, ^{33}SRR, and ^{34}SRR, which depend upon the constitutive fractionation factors ($^{33}\alpha_{SR}$ and $^{34}\alpha_{SR}$, linked by $^{33}\lambda_{SR}$). The derivation of these isotope-dependent rate terms is shown in the following section.

2.8.3 LOWER BOUNDARY CONDITIONS FOR [$^{32}SO_4^{2-}$], [$^{33}SO_4^{2-}$], AND [$^{34}SO_4^{2-}$]

In principal, it is possible to prescribe the lower boundary conditions for the species[$^{32}SO_4^{2-}$], [$^{33}SO_4^{2-}$], and [$^{34}SO_4^{2-}$] using isotope values, and thereby concentrations, *e.g.*, Dirichlet boundary conditions. However, since the isotopic composition of sulfate is unknown at depth, prescribing such values gives spurious results. In all cases, the model is run with Neumann boundary conditions, such that the isotopic composition is unchanging at depth, but without a specified composition:

$$\frac{d[^{32}SO_4^{2-}]_{x=L}}{dx} = 0, \quad \frac{d[^{33}SO_4^{2-}]_{x=L}}{dx} = 0, \quad \frac{d[^{34}SO_4^{2-}]_{x=L}}{dx} = 0 \tag{2.23}$$

2.8.4 DERIVATION OF ISOTOPE (^{32}S, ^{33}S, AND ^{34}S) SPECIFIC RATE TERMS ^{32}SRR, ^{33}SRR, AND ^{34}SRR, AND CONSTRUCTION OF THE STEADY-STATE DIAGENETIC EQUATIONS

The determination of isotope-specific rates for the sulfur system has been detailed before for the two-isotope system (^{32}S and ^{34}S) (Jørgensen, 1979; Dale et al., 2009), and by similarity, it can be shown for the three-isotope system (^{32}S, ^{33}S, and ^{34}S). The algebraic solution shares some similarities with those for the two isotope system, but naturally depends on two fractionation factors $^{33}\alpha_{SR}$ and $^{34}\alpha_{SR}$, which we have described in this paper as being mathematically linked via $^{33}\lambda_{SR}$:

$$^{33}\lambda_{SR} = \frac{ln(^{33}\alpha_{SR})}{ln(^{34}\alpha_{SR})} \tag{2.24}$$

The isotope-specific rates ^{32}SRR, ^{33}SRR, and ^{34}SRR depend on the concentrations of [$^{32}SO_4^{2-}$], [$^{32}SO_4^{2-}$], and [$^{34}SO_4^{2-}$], but also on the rate constants $^{32}k_{SR}$, $^{33}k_{SR}$, and $^{34}k_{SR}$:

$$^{32}SRR = {}^{32}k_{SR} \cdot [{}^{32}SO_4^{2-}] \tag{2.25}$$

$$^{33}SRR = {}^{33}k_{SR} \cdot [{}^{33}SO_4^{2-}] \tag{2.26}$$

$$^{34}SRR = {}^{34}k_{SR} \cdot [{}^{34}SO_4^{2-}] \tag{2.27}$$

Intrinsic within the rate constants are the fractionations associated with sulfate reductions, and the fractionation factors are simply the ratios of those rate constants. This allows for the expression of the isotope-specific rate constants as functions of each other, linked via the fractionation factors:

$$^{33}\alpha_{SR} = \frac{\frac{^{32}SRR}{[^{32}SO_4^{2-}]}}{\frac{^{33}SRR}{[^{33}SO_4^{2-}]}} \quad \Rightarrow \quad {}^{32}SRR = {}^{33}SRR\,\frac{^{33}\alpha_{SR}\left[^{32}SO_4^{2-}\right]}{[^{33}SO_4^{2-}]} \tag{2.28}$$

$$^{34}\alpha_{SR} = \frac{\frac{^{32}SRR}{[^{32}SO_4^{2-}]}}{\frac{^{34}SRR}{[^{34}SO_4^{2-}]}} \quad \Rightarrow \quad {}^{32}SRR = {}^{34}SRR\,\frac{^{34}\alpha_{SR}\left[^{32}SO_4^{2-}\right]}{[^{34}SO_4^{2-}]} \tag{2.29}$$

Recalling that the bulk sulfate reduction rate is simply the sum of the isotope-specific rates the equations for the isotope-specific rates can be solved as functions of the bulk rate, the isotopologue concentrations, and the fractionation factors:

$$SRR = {}^{32}SRR + {}^{33}SRR + {}^{34}SRR \tag{2.30}$$

$$^{32}SRR = SRR\left[\frac{^{33}\alpha_{SR}\,{}^{34}\alpha_{SR}[^{32}SO_4^{2-}]}{^{33}\alpha_{SR}\,{}^{34}\alpha_{SR}[^{32}SO_4^{2-}] + {}^{34}\alpha_{SR}[^{33}SO_4^{2-}] + {}^{33}\alpha_{SR}[^{34}SO_4^{2-}]}\right] \tag{2.31a}$$

$$^{33}SRR = SRR\left[\frac{^{34}\alpha_{SR}[^{33}SO_4^{2-}]}{^{33}\alpha_{SR}\,{}^{34}\alpha_{SR}[^{32}SO_4^{2-}] + {}^{34}\alpha_{SR}[^{33}SO_4^{2-}] + {}^{33}\alpha_{SR}[^{34}SO_4^{2-}]}\right] \tag{2.31b}$$

$$^{34}SRR = SRR\left[\frac{^{33}\alpha_{SR}[^{34}SO_4^{2-}]}{^{33}\alpha_{SR}\,{}^{34}\alpha_{SR}[^{32}SO_4^{2-}] + {}^{34}\alpha_{SR}[^{33}SO_4^{2-}] + {}^{33}\alpha_{SR}[^{34}SO_4^{2-}]}\right] \tag{2.31c}$$

It is these rate determinations that appear in the final steady-state diagenetic equations for the isotope RTM. By analogy to those described for the bulk geochemical model, they can be written as in equations 2.32a-c:

$$\varphi^2 D_o^{SO_4} \frac{d^2[^{32}SO_4^{2-}]}{dx^2} + \left(3\varphi D_o^{SO_4} \frac{d\varphi}{dx} - \frac{\omega_\infty \varphi_\infty}{\varphi}\right) \frac{d[^{32}SO_4^{2-}]}{dx} - {}^{32}SRR = 0 \tag{2.32a}$$

$$\varphi^2 D_o^{SO_4} \frac{d^2[^{33}SO_4^{2-}]}{dx^2} + \left(3\varphi D_o^{SO_4} \frac{d\varphi}{dx} - \frac{\omega_\infty \varphi_\infty}{\varphi}\right) \frac{d[^{33}SO_4^{2-}]}{dx} - {}^{33}SRR = 0 \tag{2.32b}$$

$$\varphi^2 D_o^{SO_4} \frac{d^2[^{34}SO_4^{2-}]}{dx^2} + \left(3\varphi D_o^{SO_4} \frac{d\varphi}{dx} - \frac{\omega_\infty \varphi_\infty}{\varphi}\right) \frac{d[^{34}SO_4^{2-}]}{dx} - {}^{34}SRR = 0 \tag{2.32c}$$

These equations are then solved using the same method as for the bulk geochemical model.

Table 2.6: Pore water data from Berelson et al. (2005) and isotope data generated in this study

Multicore ID	Depth (cm)	porosity (ϕ)	$[SO_4^{2-}]$ (mM	DIC (mM)	$Ca^{2=}$ (mM)	Depth CH_4 (cm)	$[CH_4]$ (mM)	$\delta^{34}S_{SO4}$ (SO_2) (‰)	$\delta^{34}S_{SO4}$ (SF_6) (‰)	$\Delta^{33}S_{SO4}$ (SF_6) (‰)
MC1	1	0.93	27.1	3.661	9.7	1	0.00047	21.7	21.9	0.0476
MC2	9.25	0.93	26.65	4.543	9.83	6.5	0.00138	22.7	21.9	0.0506
MC3	14.75	0.92	26.19	5.568	9.47	12	0.002225	23.9	24.0	0.0471
MC4	20.25	0.91	23.94	6.562	9.14	17.5	0.00278	25.7	25.6	0.0677
MC5	25.75	0.91	23.26	7.558	8.8	23	0.00376	26.6	27.0	0.0684
MC6	31.25	0.9	23.48	8.321	-	28.5	0.004625	-	-	-
MC7	36.75	0.89	23.03	9.449	8.12	34	0.005035	29.2	-	-
MC8	42.25	0.89	21.9	10.485	7.78	39.5	0.00647	31.5	30.5	0.0770
MC9	47.75	0.88	23.48	11.748	7.62	45	0.00689	33	33.0	0.0890
Gravity Core ID	Depth (cm)	porosity (ϕ)	$[SO_4^{2-}]$ (mM	DIC (mM)	$Ca^{2=}$ (mM)	Depth CH_4 (cm)	$[CH_4]$ (mM)	$\delta^{34}S_{SO4}$ (SO_2) (‰)	$\delta^{34}S_{SO4}$ (SF_6) (‰)	$\Delta^{33}S_{SO4}$ (SF_6) (‰)
GC1	33	0.9	22.58	8.767	8.36	34.5	0.00501	-	29.6	0.0738
GC2	70	0.87	16.03	20.9	6.45	73.5	0.0152	-	-	-
GC3	113	0.85	10.84	30.08	5.33	114.5	0.0222	-	-	-
GC4	155	0.84	4.29	42.76	4.21	156.5	0.0873	-	-	-
GC5	193	0.83	3.16	39.99	3.69	194.5	1.172	-	-	
GC6	234	0.83	1.35	45.22	3.76	235.5	1.950	-	-	-
GC7	273	0.83	2.26	47.75	3.46	274.5	4.235	-	-	-

Table 2.6: Pore water geochemical and isotopic data from Alfonso Basin (CalMex Station 15) used in this study. Core samples were retrieved in October and November of 2001 during the California-Mexico margin (CalMex) cruise. Multi-cores (MC) and gravity cores (GC) were retrieved. Shallow multi-core (0-50 cm) MC1-MC9 were sectioned at higher intervals that deeper gravity core (GC1-GC7) samples. With the exception of the isotope data, all geochemical data were reported previously in Berelson et al. (2005). Data missing here either had an error in sampling, or there was insufficient material for measurement.

The dependence of fractionation on rate

We tested three different depth dependences of fractionation: a constant fractionation (main text), a linear dependence of fractionation on SRR, and finally an exponential dependence on SRR – more like that seen in pure culture studies (Leavitt and others 2013). Each of the scenarios results in a different $^{33}\alpha$ and $^{34}\alpha$ applied at variable depths within the model domain, and results in depth-variable ^{32}SRR, ^{33}SRR, and ^{34}SRR. In all cases, isotope mass balance was conserved and checked such that SRR = ^{32}SRR + ^{33}SRR + ^{34}SRR.

Each of these different model solutions carries a different prescription between SRR and isotope fractionation. In the first scenario, we explored a linear dependence of $^{34}\varepsilon_{SR}$ on rate (at SRR_{max}, $^{34}\varepsilon_{SR} \approx {}^{34}\varepsilon_{max}$ and vice versa). Here we used the same regressed values as determined in Leavitt and others (2013):

$$^{34}\varepsilon_{SR} = \frac{-39.3}{SRR_{max} - SRR_{min}} SRR + 56.5$$

Next, we have parameterized the exponential connection between SRR and $^{34}\varepsilon_{SR}$ using the model values from Leavitt and others (2013), where $^{34}\varepsilon_{min}$ = 17.2±1.3‰ and $^{34}\varepsilon_{max}$ = 56.5±2.6‰. We have used an attenuation coefficient of $^{34}\beta$ = 10, and thus the equation can be written as:

$$^{34}\varepsilon_{SR} = 39.3e^{-10(SRR - SRR_{min})} + 17.2$$

Finally, we consider a constant value for $^{34}\varepsilon_{SR}$ with depth, or a fractionation that is rate independent over the range of values covered in the Alfonso sediments. This last case is carried forward in the main text.

A comparison the modeled fractionation factors, the whole core isotope model profile model profile demonstrates the isotopic behavior of each of the different scenarios. From this, we can highlight several key points. For both the linear and exponential cases, where the fractionation factor is a function of rate, a maximum fractionation factor of $^{34}\varepsilon_{max}$ = 56‰ is insufficient to capture the

behavior of the pore water sulfate $\delta^{34}S_{SO4}$ values. Although the $^{34}\varepsilon_{max}$ and $^{34}\varepsilon_{min}$ are the same in both cases, and values of $^{34}\varepsilon_{max}$ converge at depths where SRR decays to zero. The modeled isotope gradient in the exponential case is shallower than in the linear case because $^{34}\varepsilon_{SR}$ increases more slowly. Furthermore, the modeled $\delta^{34}S_{SO4}$ profiles largely do not reflect the structure of the $^{34}\varepsilon_{SR}$ input profile, reflecting the consequence of diffusive/advective transport of $^{32}SO_4^{2-}$, $^{33}SO_4^{2-}$ and $^{34}SO_4^{2-}$.

In all cases (exponential, linear, and constant), the sulfate $\delta^{34}S_{SO4}$ profile gradients are approximately linear with respect to depth down to 150 cm, where $[SO_4^{2-}] \approx 5$ mM. Utilizing different $^{34}\varepsilon_{min}$, fit to the highest SRR at shallow depths, ranging from $^{34}\varepsilon_{min}$ = (20‰-50‰), that same linear behavior in the sulfate isotope gradient is observed. Although a small change in the slope of $\delta^{34}S_{SO4}$ versus depth is observed, the chosen value of $^{34}\varepsilon_{max}$ has a much stronger influence on the sulfate isotope gradient than does $^{34}\varepsilon_{min}$. It is, of course, possible to model the $\delta^{34}S_{SO4}$ gradient with $^{34}\varepsilon_{max} >$ 70‰, in both the linear and the exponential case. The profile behavior is largely insensitive to the chosen $^{34}\varepsilon_{min}$ when $^{34}\varepsilon_{max}$ is large (> 70%). Despite the fact that there is pronounced structure in $^{34}\varepsilon_{SR}$ associated with the sulfate depletion depth, there is comparatively little influence on the resultant $\delta^{34}S_{SO4}$ profile. In the case where $^{34}\varepsilon_{SR}$ is held constant, independent of SRR, and by inference, depth, the best model fit to the isotope profile is produced when $^{34}\varepsilon_{SR}$ = 70‰. The model $\delta^{34}S_{SO4}$ gradient is also linear with respect to depth until ~150cm, when the sulfate concentration profile also begins to approach the sulfate depletion depth. All $^{34}\varepsilon_{SR}$ input values into the model where $^{34}\varepsilon_{SR} <$ 60‰ produce a $\delta^{34}S_{SO4}$ gradient that is too shallow, all input $^{34}\varepsilon_{SR} >$ 80‰ produce a $\delta^{34}S_{SO4}$ gradient that is too large to accurately reproduce the measured pore water sulfate samples within Alfonso Basin. Although the constant $^{34}\varepsilon_{SR}$ scenario was tested simply as an end member case, we acknowledge that it provides the best fit with the least number of assumptions—the most conservative approach) to the $\delta^{34}S_{SO4}$ values an accurately reproduces the pore water $\delta^{34}S_{SO4}$ gradient in the top 50 cm. A scenario that parameterized the connection between $^{34}\varepsilon_{SR}$ and SRR is not necessary. Further, it is critical to acknowledge that the physical transport of sulfate (diffusive and advective) results in the loss of information about the fractionation behavior at the reaction level.

Figure 2.9

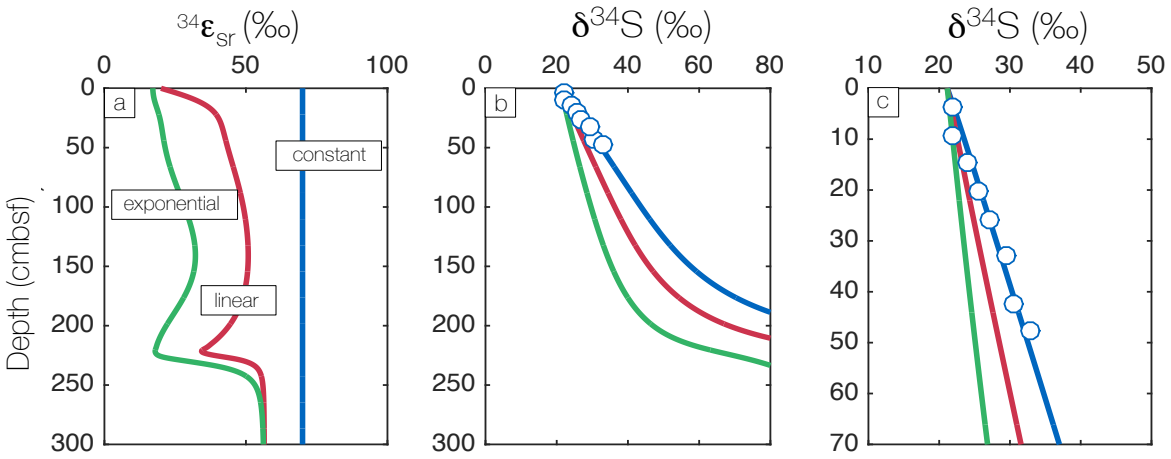

Figure 2.9: Isotope model fits ($\delta^{34}S_{SO4}$ vs. depth) for different parameterization scenarios (constant $^{34}\varepsilon_{SR}$, linear dependence of $^{34}\varepsilon_{SR}$ on SRR, and exponential dependence of $^{34}\varepsilon_{SR}$ on SRR). The panels demonstrate **(a)** the input $^{34}\varepsilon_{SR}$ as a function of depth, as determined from the different parameterization scenario **(b)** the model $\delta^{34}S_{SO4}$ profile fit for each of the scenarios in (a), plotted with the multi-core $\delta^{34}S_{SO4}$ Alfonso Basin data throughout the entire model domain sampled by the gravity core **(c)**, the $\delta^{34}S_{SO4}$ for the top 70 cm, the region sampled by the multicore.

In a similar fashion to that outlined above, it is possible to demonstrate a series of model fits to the pore water sulfate $\Delta^{33}S_{SO4}$ values. Noting that the variability in $\Delta^{33}S_{SO4}$ values are modest over the measured range (increasing from near seawater sulfate values at the SWI of 0.047±0.006‰ to 0.086±0.006‰ at 47 cm depth), Importantly, only minute variability in $^{33}l_{SR}$ is required to produce substantial changes in the trajectory of $\Delta^{33}S_{SO4}$ versus depth. Demonstrating a sensitivity test, Fig. A4.2 exhibits the influence of variable, rate-independent $^{33}\lambda_{SR}$ on the output pore water sulfate $\Delta^{33}S_{SO4}$. While not all of these values are physically reasonable given the $^{34}\varepsilon_{SR}$, several features are notable. First, increasing $^{33}\lambda_{SR}$ with constant $^{34}\varepsilon_{SR}$ produces a more rapid increase in the $\Delta^{33}S_{SO4}$ model output. This is an expected result, as $^{33}\lambda_{SR}$ relates the fractionation factors $^{33}\alpha_{SR}$ and $^{34}\alpha_{SR}$, larger values of $^{33}\lambda_{SR}$ produce a relatively larger enrichment in ^{33}S. Secondly, despite the fact that $\Delta^{33}S$ is calculated within the reference frame $^{33}\lambda = 0.515$, values of $^{33}\lambda_{SR} > 0.510$ are sufficient to produce a positive

trajectory in triple isotope space ($\delta^{34}S_{SO4}$-$\Delta^{33}S_{SO4}$). It is possible that closed system behavior, such as that observed in pore waters can partially explain this trajectory. Thirdly, with the application of both constant $^{34}\varepsilon_{SR}$ and $^{33}\lambda_{SR}$, non-linear trajectories are observed in the triple isotope composition of pore water sulfate. Whereas simple, Rayleigh-like models of sulfate in closed systems demonstrate linear arrays, the model trajectories for a diagenetic model like that constructed here are more complex.

CHAPTER 3

A MULTIPLE SULFUR ISOTOPE DIAGENETIC MODEL FOR AARHUS BAY: RECONCILING MEASUREMENTS WITH REACTIVE TRANSPORT*

ABSTRACT

Multiple sulfur isotope calibrations of microbial biosignatures enable the unique diagnosis of S-based metabolic processes: sulfate reduction, disproportionation, and sulfide oxidation. All three carry distinct geochemical consequences for S cycling in modern systems, and are particularly powerful for paleoenvironmental interpretations. To hone those interpretations and to further develop a quantitative context for understanding early diagenetic sulfur cycling, we constructed a multiple S isotope reactive transport model for the sediments of a geochemically well-characterized system (Aarhus Bay, Denmark). The model reconciles pore water and solid phase concentration profiles of the major species associated with Fe/S/C cycling, and provides for the incorporation of multiple S isotope systematics to predict the isotope profiles of the major S species, including pore water sulfate, sulfide and pyrite. We note that very large fractionations associated with sulfate reduction ($^{34}\varepsilon_{sr}$ = 70‰) are required to reproduce the observed pore water profiles, and we reconcile these fractionations with low temperature theoretical predictions for isotope equilibrium fractionation. The $\Delta^{33}S$ values of sulfate increase at shallow depths within the Aarhus Bay core, and decrease with sulfate <10 mM. Values ($\Delta^{33}S$) for sulfide decrease nearly monotonically towards seawater sulfate values near the zone of sulfate depletion. Pyrite $\Delta^{33}S$ values are nearly uniform downcore (0.170±0.010‰) despite a ~10‰ enrichment in surface versus deep pyrite $\delta^{34}S$ values. Sulfate reduction is the most important process controlling S isotope pore water distributions, and little contribution from oxidative S cycling is required despite the oxygenated conditions of Aarhus Bay sediments. Further, sulfate reduction

*A version of this chapter is in preparation for submission to *Geochimica et Cosmochimica Acta* with coauthors Marc J. Alperin, Gail A. Arnold, William M. Berelson, and David T. Johnston

demonstrates large fractionations typically not expected for shallow, organic rich continental margin systems.

3.1 INTRODUCTION

Microbial sulfate reduction (MSR) is a ubiquitous and quantitatively important anaerobic C-remineralization pathway in modern continental margin sediments (*e.g.*, Jørgensen, 1982). In addition to classic organoclastic sulfate reduction, sedimentary sulfur cycling is further involved in the oxidation of pore water CH_4 via anaerobic methane oxidation (AOM) (*e.g.,* Boetius et al. 2000; Knittel and Boetius, 2009; Milucka et al. 2012). This sedimentary biogeochemical linkage between the S and C cycle is thus globally important in determining rates of sediment metabolisms, and consequently rates of C burial within anoxic sediments (*e.g.,* Bowles et al. 2014; Meister et al., 2013). Certain sulfur (S) metabolisms, including both sulfate reduction and sulfur disproportionation, have different geochemical roles and occupy different environmental niches depending on substrate, specific S compound present (SO_4^{2-}, H_2S, S_0, $S_2O_3^{2-}$), and oxidant (O_2, Fe^{3+}) availability (*cf.* Canfield, 2001); diagnosing the individual contributions of these and other metabolisms is important for understanding how sedimentary S cycling is intertwined with other diagenetic reactions. Sulfur isotopes (^{32}S-^{34}S) are an important diagnostic tool for understanding the presence, activity, and rates of MSR and sulfur disproportionation (MSD) in marine sediments (*cf.* Habicht and Canfield, 2001). Isotopic approaches are also heavily involved in reconstructing S cycling within both modern sediments (Jørgensen, 1979), and in the establishment of proxy records used to understand S cycling in deep time (Canfield, 2004; Canfield and Farquhar, 2009). Unfortunately, the overlap of characterized fractionations (*i.e.* the $^{34}S/^{32}S$ effect generated by MSR and MSD) for particular processes represents a complication in diagnosing the contributions of each to sedimentary S isotope reservoir.

More recently, the use of minor (^{33}S and ^{36}S) S isotopes has been applied to understanding the contributions of juxtaposed metabolisms (Johnston et al., 2005; Johnston et al., 2007; Leavitt et al., 2013) and promises to aide in interpreting the sedimentary S cycle. Few studies, however, have

incorporated minor isotope systematics into diagenetic reactive transport models (RTMs) (Masterson et al., submitted; Pellerin et al., 2015), and none are constructed to explicitly incorporate all S species of interest. Such RTMs, steady-state and otherwise, will provide the framework for determining how minor sulfur biosignatures, characterized in pure culture experiments, are produced and diagenetically inherited in different sedimentary packages and environmental regimes. Therefore, it is critical to develop these models and apply them in geochemically and sedimentologically well-characterized systems (Aarhus Bay, Denmark).

To date, studies targeting the diagenetic reconstruction of S cycling have focused on (i) predicting the influence of sedimentary organic carbon (also known as particulate organic carbon, or POC) mineralization rates on sulfate profiles (Berner, 1964; Westrich and Berner, 1984, Masterson et al., submitted), (ii) understanding how depth-dependent variability in fractionation behavior (*e.g.* $^{34}\alpha_{MSR}$) influences sulfate and sulfide isotope ($\delta^{34}S_{SO4}$, $\delta^{34}S_{H2S}$) depth-profiles in the light of physical transport (Jørgensen, 1979; Masterson et al, submitted), and (iii) reconciling those fractionation characteristics with laboratory calibrations of pure culture microbial experiments (Habicht and Canfield, 1997; Habicht et al. 1998; Habicht and Canfield, 2001; Wortmann et al. 2001; Habicht et al. 2002). Broadly, those studies suggest that organic matter composition and reactivity has a strong influence on sulfate concentration profiles (Berelson et al., 2005). These reaction kinetics are further modulated by the particular diagenetic regime, meaning the balance between diffusion/advection, which relate to features like sedimentation rate, and the geochemical reactions themselves. All these processes then come to influences the S isotope characteristics or pore water and solid phase S-bearing species in early diagenetic marine systems. Still, the unresolved goal is to build a robust, quantitative bridge between the observed fractionation behavior and the isotope fractionations produced in well-constrained laboratory experiments. Previous attempts to champion this goal are hindered by the overlapping (*i.e.* non-unique) fractionation behavior for processes such as sulfate reduction and sulfur disproportionation. In essence, it is difficult to quantitatively separate the contribution from these metabolisms with the classic isotope system of $^{34}S/^{32}S$.

Here again we look to the incorporation of minor sulfur isotope (^{33}S and ^{36}S) to help resolve these challenges. In detail, the inclusion of ^{33}S calls upon a finer understanding of the mass-dependent isotopic behavior that more accurately diagnoses (i) the activity of sulfate reducers and disproportionators (Johnston et al., 2005) and provides (ii) a co-varying relationship between $^{34}\varepsilon_{MSR}$ and $^{33}\lambda_{MSR}$ that is potentially a more accurate proxy for the variability in the natural rates of sulfate reduction (Leavitt et al., 2013). Those minor isotope signatures, typically measured and presented using triple isotope notation (*e.g.* $\delta^{34}S$-$\Delta^{33}S$) have only sparingly been applied to studies of modern sediments (Johnston et al., 2008; Strauss et al. 2012; Pellerin et al., 2015; Masterson et al., submitted). Only the latter two studies attempted to provide a model framework for the evaluation of S isotope fractionation in this light, and only the last of these actually accounted for other biogeochemically important (C, Fe, Ca) cycles.

The simplest approach that can be employed to evaluate the minor isotope behavior of S in sedimentary systems and that satisfies the mass-balance requirements of S/C/Fe is to construct a steady-state, finite difference, reactive transport model that parameterizes POC mineralization kinetics, resolves SO_4^{2-} and H_2S concentration profiles, and evaluates how fractionation behavior influences the pore water isotope signatures. In a first step toward this goal, Masterson et al. (submitted) expanded a complex diagenetic model, which included a carbon, iron and calcium cycle, to include the ^{33}S behavior in pore water sulfate. Sulfate profiles are often seen as a proxy for the integrated behavior of S cycling in sediments, and as such, that study targeted sediment pore water from California margin sediments. However, using these types of rigorous investigations as a roadmap for paleoenvironmental reconstructions suffers from a nearly absent geological record of seawater sulfate, notwithstanding adequate pore water sulfate records. As such, geological reconstructions lean heavily on solid phase metal sulfide records (*i.e.* pyrite). The incorporation of solid phase (FeS and FeS_2) chemistry is therefore needed in diagenetic model reconstructions, and further allows for a more complete S isotope mass balance. Only a few studies have done this synchronously (*e.g.,* Dale et al., 2009; Aller et al., 2010), and none incorporate ^{33}S. To this end, we provide high-precision

measurements ($\sigma-\delta^{34}S$ = 0.2‰ and $\sigma-\Delta^{33}S$ = 0.006‰) of the major sulfur species from a gravity core taken at station M1 in Aarhus Bay, Denmark. We present these data alongside additional aqueous phase (CH_4) and solid phase (POC, Fe) metadata and use those results to feed a new, expanded diagenetic isotope model. Together these results will speak to the relationship between metabolic rates of sulfate reduction and the manifestation of an isotopic signal, and equally as important, what exact biogeochemical information is captured in the geologically interpretable pyrite record from early diagenetic environments.

3.1.1 ISOTOPE NOTATION

Throughout this work we use isotope ratios ($^{3x}R = {}^{3x}r/{}^{32}r$) as a means to define isotopic fractionation between reservoirs, here A and B. This is most simply characterized via a fractionation factor, where $^{3x}\alpha_{A\text{-}B} = {}^{3x}R_A/{}^{3x}R_B$ and x equals 3 or 4. This is then translated to standard delta notation ($\delta^{3x}S = (({}^{3x}R_{sample}/{}^{3x}R_{std} - 1) * 1000)$), or when A and B are known, the isotopic offset can be captured via a $^{34}\varepsilon$ value, which is calculated as $({}^{3x}\alpha_{A\text{-}B} - 1) * 1000$. Thus, when placing an isotopic composition on an absolute scale, often referenced to VCDT, a $\delta^{3x}S$ value is preferred. When comparing compositions within a data set or isolating a fractionation effect, we present the data as an $^{3x}\varepsilon$ value. For the minor isotopes, we can use the difference between a thermodynamic prediction and the measured composition: $\Delta^{33}S = \delta^{33}S - 1000((1+\delta^{34}S/1000)^{0.515} - 1)$, or through measuring the slope of a line loosely connecting $\delta^{33}S$ and $\delta^{34}S$, which is noted as $^{33}\lambda$. More technically, $^{33}\lambda$ is defined as $\ln({}^{33}\alpha_{A\text{-}B})/\ln({}^{36}\alpha_{A\text{-}B})$. In determining the isotopic fractionation associated with a specific process—even if that process is constituted by a number of steps—$^{33}\lambda$ is helpful and provides a $\delta^{34}S$ independent measure of fractionation. Importantly, the error associated with $^{33}\lambda$ is largely, and non-linearly, dependent on the $\delta^{34}S$.

3.2 AARHUS BAY SAMPLING AND ANALYTICAL METHODS

3.2.1 SITE CHARACTERISTICS AND GEOCHEMISTRY

Aarhus Bay is a partially enclosed embayment on the eastern side of the Jutland peninsula (see Figure 3.1), at the transition between the Baltic and the North seas. Studies suggest that the sediments consist of glacial till overlain by ~10 m of Holocene mud (Holmkvist et al., 2011). The region has been studied using seismic techniques to determine the depth and presence of subsurface CH_4 gas (Jensen and Bennike, 2008), and the depth to the zone of sulfate depletion—or sulfate methane transition zone (SMTZ). These characteristics have been heavily documented at two study stations (M1 and M5) (Dale et al., 2008). Further, Station M1 in Aarhus Bay (56°07.0580′N and 10°20.8650′E) – the study site for this work - is the site of regular coring, is relatively accessible at 15 m water depth, and the general geochemistry is well-documented by the METROL project and in subsequent research cruises (Fossing et al., 2004).

Figure 3.1

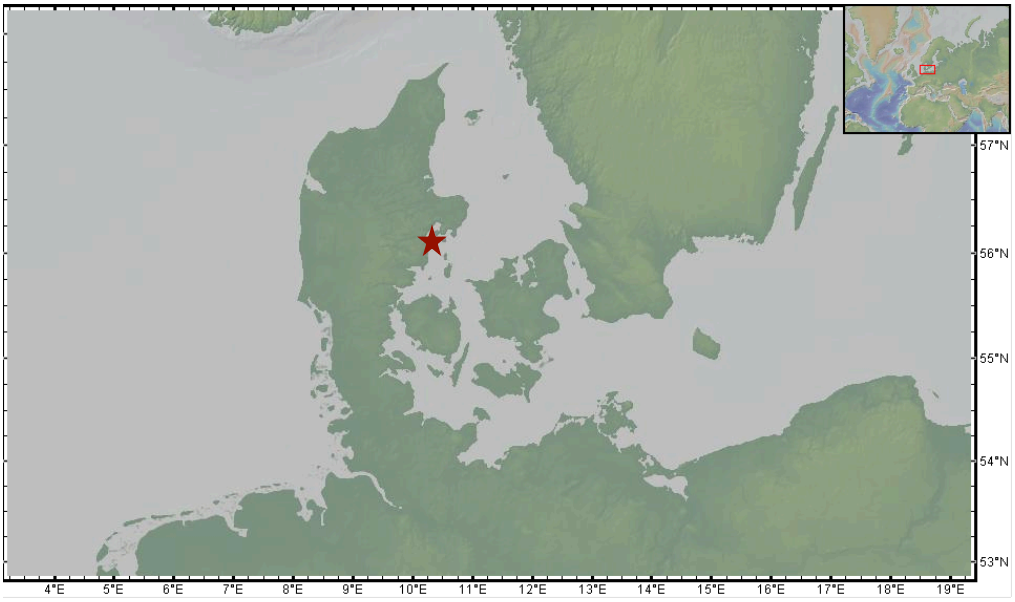

Figure 3.1: Map showing the sampling locality in Aarhus Bay, Denmark for the gravity core employed in this study. The cores were sampled at station 'M1' 56°07.0580 N and 10°20.8650 E in May, 2013, in a water depth of approximately 15 m on the *RV Tyra*. The cores samples employed in this study are those from the 'spring' core published in Brunner et al., (2016).

3.2.2 CORING AND PORE WATER SAMPLING

The cores used in this study were collected in May 2013 on a sampling campaign aboard the RV *Tyra* as a part of a larger sampling expedition (Brunner et al., 2016). Gravity cores were taken with a 12 cm steel barrel with a PVC core liner, and with a final sampled depth of ~220 cm. Upon collection, cores were taken to Aarhus University and processed in 4°C cold rooms. The cores were sectioned and pore water extracted anoxically in a pore water squeezer. The first ~5 mL of pore water were discarded and the remainder collected in N_2-purged 100 mL serum bottles with 1mL of 20% zinc acetate to capture pore water sulfide. Pore waters were split and separate analyses were done for sulfide concentrations and sulfate concentration by gravimetric determination. Separately, sulfate and chloride were determined by ion chromatography. Sulfide, precipitated as ZnS, was cation-exchanged with $AgNO_3$ to convert to Ag_2S and filtered for S isotope analyses. To the leachate was then added a saturated solution (1.3 M) of $BaCl_2$ to precipitate $BaSO_4$, which was then filtered and dried for S isotope analyses.

3.2.3 SULFUR ISOTOPE ANALYSES

Additional splits of $BaSO_4$ and Ag_2S pore water splits were sent to the Harvard University Laboratory for Stable Isotope Geobiology for multiple S isotope analyses. Barium sulfate was further washed in millipore H_2O, and dried in a 90°C oven. Both Ag_2S and $BaSO_4$ were prescreened for $\delta^{34}S$ using continuous flow IRMS, analyzed as SO_2. Samples were combusted online using V_2O_5 as a catalyst in a Costech EA, mated to a Thermo-Fisher Delta V. Reproducibility is estimated from IAEA standard measurements (S-1, S-2, S-3, and NBS-127) to be better than ±0.2‰ (1σ).

Pyrite was extracted from solid phase sediment samples (dried and powdered) using a modified technique from Canfield et al. (1986). Extracted H_2S was captured as ZnS and converted to Ag_2S, which was further cleaned and dried at 90°C for S isotope analyses. The distillation procedure also checked for the presence of acid-volatile sulfur (AVS) and zero-valent sulfur, but no quantifiable

amount was found in any of the sediment samples. Pyrite Ag_2S, extracted in duplicate, was analyzed for $\delta^{34}S$ values using the EA method, and a portion was also saved for multiple S isotope analysis.

Pore water sulfate (as $BaSO_4$) samples for multiple S isotope measurements ($\Delta^{33}S$) were first chemically converted to Ag_2S by reductive distillation with a mixture of hydriodic acid (HI), hypophosphorous (H_3PO_4) and hydrochloric acid (HCl) at ~90°C for 3 hours (Forrest and Newman, 1978). The N_2-purged reactors were connected to a series of acid traps and zinc acetate capture vials that precipitated evolved H_2S as ZnS. Cation-converted Ag_2S samples were rinsed with ~300 mL of Millipore water, and ~15mL of 1M NH_4OH to remove trace silver ions, and dried overnight in a 90°C oven. Powdered Ag_2S samples were fluorinated at 300°C in a F_2 atmosphere at 10X stoichiometric excess. Product SF_6 was cryogenically and chromatographically purified and analyzed on a Thermo Finnigan 253 in Dual Inlet mode. Analyses of repeat standards of IAEA-S1, S-2, and S-3 yield a reproducibility of ±0.2‰ and ±0.006‰ for $\delta^{34}S$ and $\Delta^{33}S$, respectively (see Appendix A1 for compiled standard data). Samples are reported versus VCDT, calibrated from the long-term running average of IAEA-S-1 versus the working standard gas at Harvard University.

3.3 MODEL CONSTRUCTION

3.3.1 MODEL ARCHITECTURE AND OPERATION

The reactive-transport models constructed for this study are steady-state finite difference models designed and run in Fortran 77. A baseline geochemical model was constructed to describe the depth distribution of the major pore water and solid phase chemical species—including organic carbon (POC), sulfate (SO_4^{2-}), methane (CH_4), dissolved inorganic carbon (DIC), sulfide (H_2S), reactive iron ('FeOOH'), elemental sulfur (S^0), and the iron sulfides (FeS and FeS_2). Organic carbon remineralization was used to 'drive' the other major biogeochemical reactions, with the assumption that sulfate reduction and methanogenesis are the major loss pathways for reactive POC. The major reactions incorporated into the model include sulfate reduction (SR), methane oxidation (MO), chemical sulfide oxidation (H_2SO), sulfur disproportionation (S^0D), FeS precipitation (FeSP) and pyrite formation (FeS_2F). The depth-dependent bulk rates of each reflect the reconciliation of the concentration profiles of all of the

major pore water and solid phase species and were the major output of the bulk geochemical model. These rates were then used as inputs for the isotope-dependent reactive transport model that produces the isotope profiles of the major S-bearing species, including $\delta^{34}S_{SO4}$, $\Delta^{33}S_{SO4}$, $\delta^{34}S_{H2S}$, $\Delta^{33}S_{H2S}$, $\delta^{34}S_{FeS}$, and $\delta^{34}S_{FeS2}$. Discussed below are the details of the model construction, including boundary conditions, diffusion coefficients, physical parameters, kinetic parameters, and isotope-dependent boundary conditions.

3.3.2 GEOCHEMICAL (POC, CH_4, SO_4^{2-}, H_2S, S^0, FeS, FeS_2, DIC) MODEL

3.3.2.1 POROSITY

Following in the convention of previous authors (*cf.* Boudreau et al., 1997), we have assumed that porosity follows an exponential decay function that implicitly assumes steady-state compaction of sediment across the model domain. Whole sediment porosity was not measured at the time of sampling for these particular cores in May 2013, but was measured by mass loss upon drying on a separate gravity core a month later. With porosity (ϕ) being the fraction of whole sediment volume constituted by pore water, the model fit and the porosity (ϕ = 0-1) are shown in figure 3.2a. That parameterized model fit is used in all of the reactive transport equations where ϕ appears.

3.3.2.2 BOUNDARY CONDITIONS FOR PORE WATER (CH_4, SO_4^{2-}, H_2S, Fe^{2+}) SPECIES

Aarhus Bay is a brackish body of water at the transition of the Baltic to the North Sea, and the salinity is known to fluctuate seasonally (Dale et al., 2008). With that in mind, the concentrations of the major conservative species are lower than typical for open ocean conditions. A bottom water sample was not taken at the time of sampling, so we have used a salinity (S = 30) to ascertain the concentration of SO_4^{2-} at the sediment water interface (SWI) ($[SO_4^{2-}]$ = 24.797 mmol/L). The upper boundary conditions for the pore water species were set given the concentrations at the shallowest interval measured (~6 cm) or if not measurable, approximating zero and close to the 'threshold' concentrations for the reactions. All of the boundary conditions used are shown in Table 3.1.

3.3.2.3 SOLID PHASE (POC,'G', Fe^{3+}, S^0, FeS, FeS_2) BOUNDARY CONDITIONS

Sediments in Aarhus Bay—at Station M1 and elsewhere—are relatively rich in organic carbon, with repeated cores at M1 yielding POC between 3-4 wt% (Holmkvist et al., 2011, Dale et al., 2008). In our steady-state model, we prescribed the concentration of 'unreactive' organic matter, hereafter POC_∞ to values approximating that at the lower limit of the model domain (= 2.5%). The flux of reactive organic matter, G', is a parameterized model input that is reconciled with the sulfate and methane concentration profiles. The details of how this is performed are discussed below, but nevertheless the concentration of reactive organic carbon is set at the upper boundary at 3.5 wt%. The total flux of the reactive organic carbon is then determined by this fixed concentration, and by the mass accumulation rate of solid matter to the sediment-water interface.

The boundary conditions for the remainder of the solid phases (Fe^{3+} as 'FeOOH', S^0, FeS, FeS_2) with the exception of the latter, we prescribed using model parameterizations. Both S^0 and acid volatile

Figure 3.2

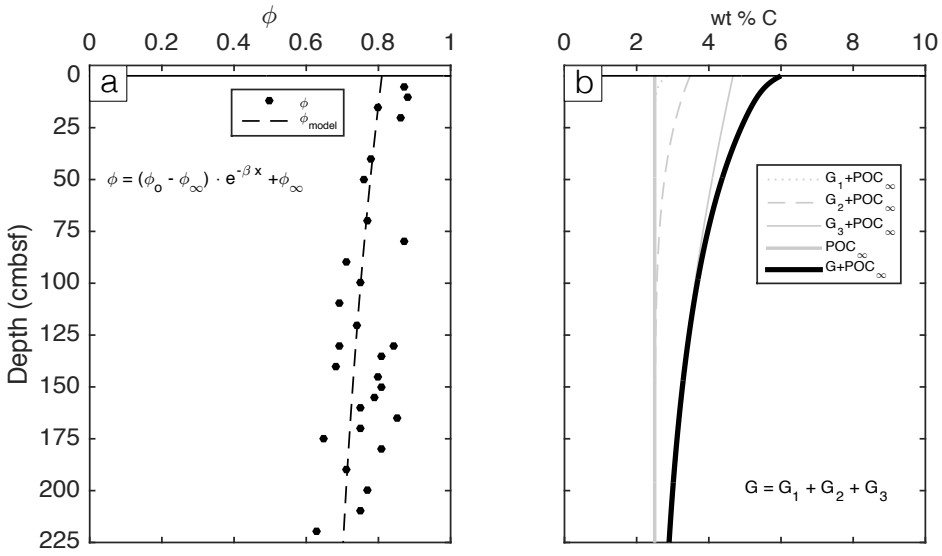

Figure 3.2: (a) Porosity (ϕ) data from a gravity core taken station M1 in Aarhus Bay-separately from the core used in this study. The exponential fit to the porosity data is used in the diagenetic models constructed here, and the values are corroborated by those used in Dale et al., (2008). **(b)** Model parameterization of POC degradation kinetics using a 3G model. The weight percent of each in addition to the unremineralized fraction is shown.

sulfur were below the limit of detection in all of the solid sediment samples (< 10 μmol/mg), but the upper boundary conditions were set to appropriately initialize the model scenario. The concentration of FeS_2 was set by the concentration (in wt% Fe) in the shallowest sediment interval measured (0.05%).

Table 3.1: Boundary conditions for geochemical model

Solute	Concentration (mmol/L)	Source
SO_4^{2-}	24.797	L[1]
H_2S	0.100	C
CH_4	0.00001	C
DIC	2.3	C
Fe^{2+}	0.001	C
Ca^{2+}	10.3	C
Solid	**Concentration (%)**	**Source**
POC	6.0	C
POC_∞	2.5	C
G	3.5	C
FeOOH	2.0	C
S^0	0.001	C
FeS	0.6	C
FeS_2	0.05	C

Table 3.1 Boundary conditions of the geochemical model
Solid phase and pore water concentration boundary conditions for the baseline geochemical model. In this table and the remaining tables, the Source terms refer to L = Literature, I = calculated from other model conditions, and C = Model parameterization.
[1] Dale et al., (2008)

3.3.2.4 PHYSICAL PARAMETERS AND DIFFUSION COEFFICIENTS

Several physical parameters are used in the reactive transport model construction for Aarhus Bay. Temperature and salinity are required for the determination of bulk diffusion coefficients of the pore water species, the size of the model domain (L = 1000 cm) is prescribed such that all the constitutive reactions approximate zero at the base of the model domain. The dry sediment density (ρ_{SM} = 2.50 g/cm^3) and the steady-state mass accumulation rate (F_{SM} = 0.02 mg/cm^2 y^{-1})—ascertained from ^{14}C

Table 3.2

Symbol	Description	Value	Units	Source
z	Water depth	15	m	L[1]
T	Bottom water temperature	8	°C	L[1]
S	Bottom water salinity	30	-	L[1]
L	Length of model domain	1000	cm	C
ϕ_o	Porosity at sediment surface	0.8096	-	C
ϕ_∞	Porosity below zone of compaction	0.6187	-	C
β	Porosity attenuation coefficient	0.00367	cm^{-1}	C
ρ_{SM}	Dry sediment density	2.50	$g\ cm^{-3}$	L[1]
F_{SM}	Mass accumulation rate	0.02	$mg\ cm^{-2}\ y^{-1}$	L[1]

Table 3.2: Physical parameters used in baseline geochemical model for Aarhus Bay
[1] Dale et al., (2008)

Table 3.3: Bulk diffusivities for Aarhus Bay sediments

Bulk diffusion coefficient	Computed[1] for 8°C, 30 psu, 15 m (cm^2/y)
D_{SO4}	200.63
D_{H2S}	396.09
D_{CH4}	313.72
D_{Fe}	134.34
D_{DIC}	216.27

Table 3.3: Diffusion coefficients for pore water species
[1] Computed from values in Schulz (2006)

abundance in mollusk shells (Dale et al., 2008), are terms required for computing solid phase fluxes of (POC), Fe^{3+}, FeS, and FeS_2 at the top of the model domain. The bulk diffusion coefficients (diffusivities) of the pore water species, including SO_4^{2-}, CH_4, H_2S, Fe^{2+}, and DIC were calculated for a bottom water temperature of 8ºC, using the values from Schulz (2006), and are listed in Table 3.3.

3.3.2.5 POC DEGRADATION KINETICS

As with the majority of other early-diagenetic reactive transport models, organic carbon degradation is the modulating reaction driving the rates of other biogeochemical processes. This is directly the case for sulfate reduction and methanogenesis, and indirectly for anaerobic methane oxidation, sulfide oxidation,

sulfur disproportionation and iron sulfide precipitation. With that in mind, we followed on what other researchers have done and parameterized organic carbon remineralization using a multi-G model (Dale et al., 2009; Westrich and Berner, 1984) that partitions organic carbon into different pools by reactivity. With the hypothetical but empirically validated approach, particulate organic carbon, with its prescribed flux at the sediment water interface, is divided into four fractions, including an unreactive fraction (POC_∞) and three fractions (G_1, G_2, and G_3) with decreasing reactivity towards remineralization (*e.g.*, $k_1 > k_2 > k_3$). The rate constants k and the fractional abundance of each pool G is adjustable in the model—with the final output determined as a pore-water normalized depth-dependent remineralization rate, hereafter deemed GRR_{PW}. Each fraction G displays a first-order loss profile with respect to depth, and GRR_{PW} is the cumulative reactive loss of organic carbon. The profiles of each fraction (G_1, G_2, G_3, and POC_∞) are shown in Figure 3.2b, and the rate constants k_1, k_2, k_3, and fractional abundances of each pool are catalogued in Table 3.5, alongside the other rate and equilibrium constants considered in the model.

3.3.2.6 BULK GEOCHEMICAL RATES AND KINETICS

All other reactions considered in the reactive transport model are linked to GRR via the stoichiometry of remineralization, and the biogeochemical kinetic thresholds required for a reaction to proceed (*i.e.* sulfate threshold required to limit sulfate reduction and methane oxidation and sulfate limitation of anaerobic methane oxidation). We have followed what others have done and use the error function to mathematically curtail these reaction rates near the thresholds. This has been demonstrated as a reasonable way to incorporate Monod-style kinetics into the reaction terms with a continuous function that does not cause issues in the solutions to the second-order differential equations. Some of these thresholds (K_{SO4}) have been demonstrated empirically (Bradley et al., 2016; Tarpgaard et al., 2011; Habicht et al., 2002) and others have been constrained by the model at low concentrations (K_{FeOOH}) to guard against the appearance of negative concentrations—mathematically reasonable but physically untenable.

Table 3.4

	Reaction	Rate Expression
GRR	$G_1 + G_2 + G_3 \rightarrow \Sigma CO_2$	$k_1 G_1 + k_2 G_2 + k_3 G_3 \cdot f_C$ $f_C = \rho_{SM}\left(\frac{1-\varphi}{\varphi}\right)\left(\frac{1}{0.0012}\right)$
SRR	$POC + \frac{1}{2} SO_4^{2-} \rightarrow \frac{1}{2} H_2S + \Sigma CO_2$	$GRR \cdot \left(\frac{4-XS}{8}\right) \cdot \gamma_1$ $\gamma_1 = 1$ if $\left[SO_4^{2-}\right] > K_{SO_4}$ 0 if $\left[SO_4^{2-}\right] < K_{SO_4}$
CH_4PR	$POC \rightarrow \frac{1}{2} CH_4 + \frac{1}{2} \Sigma CO_2$	$GRR \cdot \left(\frac{4-XS}{8}\right) \cdot \gamma_2$ $\gamma_2 = 1$ if $\left[SO_4^{2-}\right] < K_{SO_4}$ 0 if $\left[SO_4^{2-}\right] > K_{SO_4}$
MOR	$CH_4 + SO_4^{2-} \rightarrow H_2S + \Sigma CO_2 + 4H_2O$	$k_{MO}\left[CH_4\right] \cdot \gamma_1$ $\gamma_1 = 1$ if $\left[SO_4^{2-}\right] > K_{SO_4}$ 0 if $\left[SO_4^{2-}\right] < K_{SO_4}$
H_2SOR	$2Fe(OH)_3 + H_2S \rightarrow S^0 + Fe^{2+} + 6H_2O$	$k_{H_2SO}\left[Fe(OH)_3\right]\left[H_2S\right]^{0.5} \cdot \gamma_{H_2S} \cdot \gamma_{Fe(OH)_3} \cdot f_{Fe}$ $\gamma_{H_2S} = 1$ if $\left[H_2S\right] > K_{H_2S}$ $= 0$ if $\left[H_2S\right] < K_{H_2S}$ $\gamma_{Fe(OH)_3} = 1$ if $\left[Fe(OH)_3\right] > K_{Fe(OH)_3}$ $= 0$ if $\left[Fe(OH)_3\right] < K_{Fe(OH)_3}$ $f_{Fe} = \rho_{SM}\left(\frac{1-\varphi}{\varphi}\right)\left(\frac{1}{0.00556}\right)$
SoDR	$S^0 + H_2O \rightarrow \frac{3}{4} H_2S + \frac{1}{4} SO_4^{2-}$	$k_{SoD}\left[S_o\right] \cdot \gamma_{S_o} \cdot f_S$ $\gamma_{S_o} = 1$ if $\left[S_o\right] > K_{S_o}$ 0 if $\left[S_o\right] < K_{S_o}$ $f_S = \rho_{SM}\left(\frac{1-\varphi}{\varphi}\right)\left(\frac{1}{0.00321}\right)$

Table 3.4 (*continued)*

FeSPR	$Fe^{2+} + HS^- \rightarrow FeS$	$k_{FeSP}(\Omega_{FeS} - 1)$ $\Omega_{FeS} = \frac{[Fe^{2+}][HS^-]}{10^{-pH}K'_{FeS}}$ $[HS^-] = [H_2S]\left(\alpha^1_{H_2S}pH^2 + \alpha^2_{H_2S}pH + \alpha^3_{H_2S}\right)$
FeS_2FR	$FeS + H_2S \rightarrow FeS_2 + H_2$	$k_{FeS_2F}[FeS][H_2S] \cdot \gamma_{FeS} \cdot \gamma_{H_2S} \cdot f_{Fe}$ $\gamma_{FeS} = 1$ if $[FeS] > K_{FeS}$ $= 0$ if $[FeS] < K_{FeS}$
DICPR		$\gamma_1 \cdot (GRR + k_{MO}[CH_4]) + \gamma_2 \cdot \left(\frac{4 + XS}{8}\right)$

Table 3.4: Reactions considered in the geochemical model for Aarhus Bay sediments. Reactions as written do not explicitly take into account organic matter oxidation state (XS), though it is considered in the rate expressions. All rate expression terms with the exception of POC degradation have a term γ which modulates the rates of a particular reaction for below a prescribed concentration threshold (*e.g.*, *$[SO_4^{2-}]^*$*)—effectively parameterizing Monod or Blackman kinetics (Dale et al., 2009).

It is worth noting that the model assumes that all POC degradation takes place via sulfate reduction and methanogenesis, with the latter the principal loss pathway of the least reactive pool ('G_3'). For the purposes of testing the isotope model, we also treat the two diagenetic loss pathways of sulfate as distinct. The organoclastic sulfate reduction rate, hereafter SRR, is linked to GRR by the stoichiometry of remineralization and the oxidation state of organic matter (Alperin et al., 1994). The anaerobic methane oxidation rate, hereafter MOR, is ascertained from the stoichiometry of AOM (C/S =1), but is limited at concentrations substantially exceeding the threshold ($[SO_4^{2-}] >> [SO_4^{2-}]^*$). Although both reactions consume sulfate, they are treated separately to allow for potentially different intrinsic isotope fractionation characteristics (Jørgensen et al., 2006).

Simplifying the oxidation kinetics of sulfide, we have only considered the chemical oxidation of HS^- by ferric iron Fe^{3+}, and have not explicitly considered aerobic oxidation or biologically mediated oxidation. We also neglected ferric iron reduction as a source of ferrous iron to pore waters, and consider the only source as sulfide-mediated reduction of ferric iron. The oxidation kinetics of sulfide have been studied extensively, and we use reaction kinetics that are half-order with respect to sulfide

and first order with respect to ferric iron (*e.g.*, $H_2SOR = k_{H2SO}[H_2S]^{0.5}[FeOOH]$) (*cf.* Poulton et al., 2004). In this scenario, zero valent sulfur (S^0) is the only oxidation product, and sulfur disproportionation the only reactive fate of S^0. Acid volatile sulfur (nominally FeS) is the product of ferrous iron sulfidization and pyrite FeS_2 is the product of the reaction of FeS with H_2S—the only pyrite synthesis pathway considered. The rate outputs of the baseline model scenario, at least that consider S-bearing reactants and products, serve as model inputs for the isotope-specific reactive transport model, the construction of which is considered below.

Table 3.5

Parameter	Description	Value	Unit	Source
k_1	Reactivity of POC pool G_1	0.01000	y^{-1}	C
k_2	Reactivity of POC pool G_2	0.00100	y^{-1}	C
k_3	Reactivity of POC pool G_3	0.00024	y^{-1}	C
k_{MO}	Rate constant for methane oxidation	1.0000	y^{-1}	C
k_{H2SO}	Rate constant for chemical sulfide oxidation	0.00003	$mM^{-0.5}\ y^{-1}$	C
k_{SD}	Rate constant for S^0 disproportionation	0.0100	y^{-1}	L^1
k_{FeSP}	Rate constant for FeS precipitation	0.00001	$mM\ y^{-1}$	L^2
k_{FeS2F}	Rate constant for pyrite formation	0.0100	$mM^{-1}\ y^{-1}$	C
$[SO_4^{2-}]^*$	Threshold concentration for $[SO_4^{2-}]$	0.200	mmol/L	L^3
$[H_2S]^*$	Threshold concentration for $[H_2S]$	0.150	mmol/L	C
$[FeOOH]^*$	Threshold concentration for [FeOOH]	0.100	%	C
Fractionation factor inputs				
$^{34}\varepsilon_{SR}$	Fractionation factor for sulfate reduction	70	‰	C
$^{33}\lambda_{SR}$	Lambda for sulfate reduction	0.513		C
$^{34}\varepsilon_{MO}$	Fractionation factor for methane oxidation via sulfate	70	‰	C
$^{33}\lambda_{MO}$	Lambda for methane oxidation	0.513		C
$^{34}\varepsilon_{H2SO}$	Fractionation factor for sulfide oxidation with Fe^{3+}	-5	‰	C
$^{33}\lambda_{H2SO}$	Lambda for sulfide oxidation	0.515		C
$^{34}\varepsilon_{SoDSO4}$	Fractionation factor for disproportionation of S^0 to SO_4^{2-}	0	‰	C
$^{33}\lambda_{SoDSO4}$	Lambda for disproportionation of S^0 to SO_4^{2-}	0.515		C
$^{34}\varepsilon_{SoDH2S}$	Fractionation factor for disproportionation of S^0 to H_2S	0	‰	C
$^{33}\lambda_{SoDH2S}$	Lambda for disproportionation of S^0 to H_2S	0.515		C
$^{34}\varepsilon_{FeSP}$	Fractionation factor for FeS precipitation	0	‰	C
$^{33}\lambda_{FeSP}$	Lambda for FeS precipitation	0.515		C
$^{34}\varepsilon_{FeS2F}$	Fractionation factor for FeS_2 precipitation	0	‰	C
$^{33}\lambda_{FeS2F}$	Lambda for FeS_2 precipitation	0.515		C

Table 3.5: Kinetic parameters for the bulk geochemical and fractionation factor inputs for the isotope reactive transport model.

3.4 RESULTS AND DISCUSSION

The central goal of this work is to blend the interpretation of the pore water concentration profiles of Aarhus Bay, the modeled rates extracted, and the paired isotopic data. In the light of constructing this reactive transport model, a secondary goal is to quantify the intrinsic isotope fractionations necessary to generate the observed isotope profiles. These fractionations, noted below as $^{34}\varepsilon$ and $^{33}\lambda$ are then relatable to a real catalogue of how microorganisms generate fractionation—experimental data sets from both continuous and batch pure cultures of with known metabolic functions (sulfate reduction, disproportionation, etc.).

Dissimilatory sulfate reduction rests at the core of early diagenetic reactions within marine sediments like Aarhus Bay. Sulfate loss to organoclastic and methanotrophic oxidation leaves pore water sulfate ^{34}S enriched downcore, and recent work has focused on interpreting those profiles (Masterson et al., submitted; Pellerin et al., 2015). Although powerful on its own, the complementary sulfur pools in marine sediments offer added insight in the bulk biogeochemical activity as well as building a bridge to aid in interpreting geological signatures. In what follows, we expand the scope of previous work to include models for aqueous sulfide and solid phase metal sulfides. We focus on the fractionations associated with sulfate reduction, and then move to systematically test the role of other fractionation pathways present in the system. Furthermore, we highlight additional features that can be tested with new approaches to diagenetic modeling of sulfur isotopes in marine systems.

3.4.1 SEDIMENT AND PORE WATER GEOCHEMISTRY

Several biogeochemical studies of Aarhus Bay sediments have measured the weight percent organic carbon in the top 3-5 m of the sediment column. All suggest that at Station M1 the sediments are organic rich and methanic, with 3-5 wt% POC. Holmkvist et al. (2011) measured 2-3 wt% in the top 2 m, decreasing at the sediments transition into brackish marine unit. Our results for the core taken in May 2013 indicate sediment with 3.1±0.4 wt % POC, *increasing* slightly downcore to ~4 wt% at 140 cm depth. Although this is evidence of non-steady state conditions—or possibly lateral transport of sedimentary material at M1, we suggest that the diagenetic/diffusive timescale for the domain

represented by our model makes the fitting of the POC depth profile less important than the fitting of the pore water species. Nevertheless, the 3G model used partitioned reactive organic matter into three fractions (G_1, G_2, G_3)—and the values used for the first order decay constants (k_1 = 0.0100 y^{-1}, k_2 = 0.0010 y^{-1}, and k_3 = 0.00024 y^{-1}) were chosen empirically in order to effectively reproduce the sulfate and methane concentration profiles.

The pore water chemistry also resembles that exhibited in other studies that have sampled station M1 (Dale et al., 2008; Holmkvist et al., 2011). The pore water sulfate concentration, $[SO_4^{2-}] \approx$ 25 mmol/L in the shallowest depth intervals, is that expected for site with a slightly brackish salinity. Pore water sulfate concentrations decrease to < 1 mmol/L at a depth of ~150 cm. Other studies have demonstrated similar sulfate depletion depths (SDD) (Holmkvist et al., 2011), however there is variability of the SDD within station M1 from core to core (±80 cm), and perhaps even seasonally associated with temperature-dependent variations in methane biogeochemical cycling (Dale et al., 2008). Dissolved pore water methane remains below ~ 0.1 mmol/L at depths shallower than 170 cm, but rises to ~0.4 mmol/L deeper than 200 cm. The only solid phase S species detected in the M1 sediment samples was 'chromium-reducible sulfide' or pyrite sulfur. Extractions done on the frozen sediment cores yielded no acid volatile sulfur or zero valent sulfur species. Pyrite (FeS_2) is the primary stable S phase, and its concentration—in wt% Fe per gram of dry sediment weight—increases from 0.1% to ~1.0% at ~150 cm depth. Total acid and chromium extractable reactive iron is relatively constant over the same interval (1.5±0.1%).

3.4.2 DEPTH—RATE AND DEPTH—CONCENTRATION PROFILES

Through the parameterization of the organic carbon remineralization rate, and the additional reactions considered in table 3.4, all other downcore rates are resolved in the baseline simulation. These include the organoclastic sulfate reduction rate (SRR), the methane oxidation rate (MOR), the chemical sulfide oxidation rate (H_2SOR), the sulfur disproportionation rate (SoDR), and the iron sulfide and pyrite precipitation rates ($FeSPR/FeS_2FR$). The depth profile of SRR (Figure 3.4) demonstrates that most sulfate is lost to organoclastic sulfate reduction, of that, a substantial fraction is consumed in the

top ~50 cm of the profile. Additional sulfate is consumed via AOM between ~130 and 170 cmbsf. The column integrated SRR and MOR suggest fractional contributions to sulfate consumption of ~80% and 20%, respectively. This MOR fraction (~20%) has been suggested by additional modeling studies (Holmkvist et al., 2011) of Aarhus Bay pore waters. From the other rate profiles (H_2SOR and SoDR), only a small fraction of sulfide that is produced *in situ* is oxidized and disproportionated downcore, largely reflecting ferric oxide limitation. Our estimate for the total fraction of H_2S oxidized relative to that produced is on the order of 10%, whereas the majority of the sulfide is precipitated as FeS and incorporated into pyrite. The remaining sulfide is available for oxidation via alternative oxidants (like O_2 and NO_3^-). Even neglecting these sulfide sinks, what is clear is that the canonical estimates of >90% of biogenic sulfide reoxidized (*cf*. Jørgensen, 1982) are gross overestimates for depositional environments like Aarhus Bay.

The baseline model generates reactions rates that satisfy the concentration profiles of the major early diagenetic species. Most importantly, this includes the sulfur-bearing species of interest: [SO_4^{2-}], [H_2S], and FeS_2. Some of the remaining species were not measured in this study (Ca^{2+}, and DIC) but were nonetheless included to maintain the model architecture. The determined sulfate depletion depth of approximately ~150-160 cm matches the concentration, and is within the range of other studies at station M1 (Holmkvist et al., 2011; Dale et al., 2008). The methane profile (modeled) is slightly overestimated in our simulation—we did not expressly include methane gas ebullition which influences sampling at depth and results in aqueous concentrations lower than predicted, and is a common analytical problem pervasive in the methane literature.

Figure 3.3

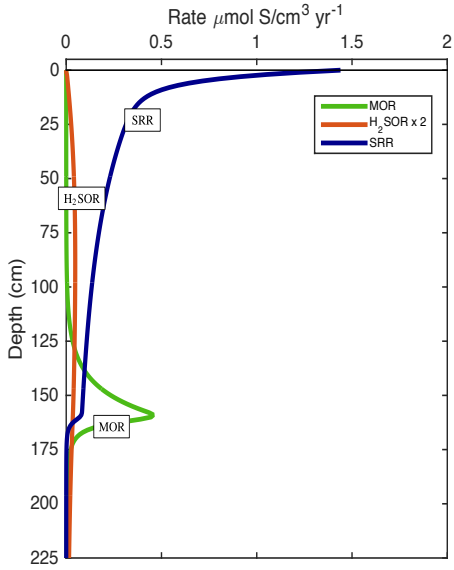

Figure 3.3: Modeled rate profiles for the major reactions influencing the concentration of sulfur species within the diagenetic model, including the sulfate reduction rate (SRR), methane oxidation rate (MOR), and sulfide oxidation rate (H_2SOR). The rate of disproportionation (k_{SoDR} >> k_{H2SOR}) closely approximates the sulfide oxidation rate, limiting the accumulation of zero valent sulfur (S^0).

Figure 3.4

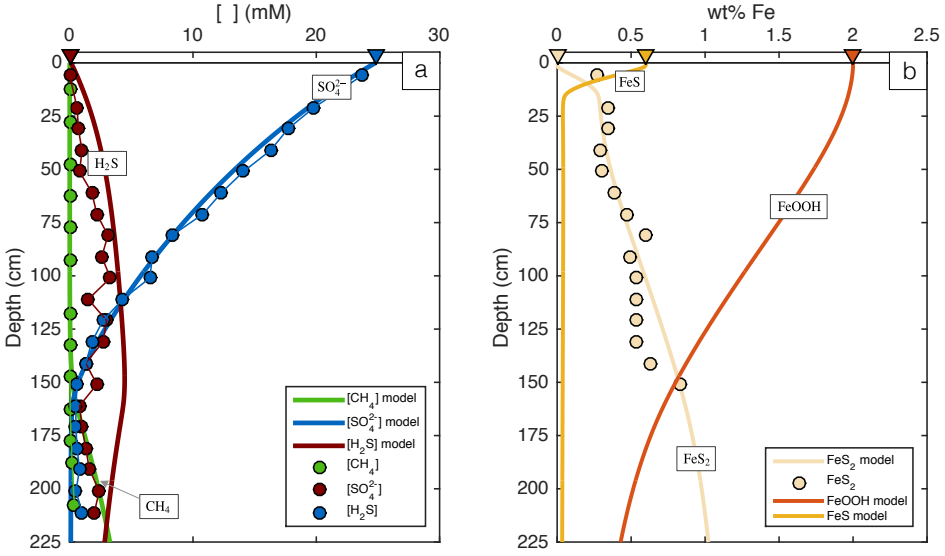

Figure 3.4: (a) Model concentration outputs and Aarhus bay sediment pore water data for $[SO_4^{2-}]$, $[H_2S]$, and $[CH_4]$. Heavy lines are reactive transport model outputs, and circles are from core samples taken at Station M1. **(b)** Model FeS_2 data, and pyrite (in wt % Fe per gram d.w.t.) for Aarhus bay sediments. The model outputs for other Fe species, including FeS ('acid volatile sulfur') and ferric oxide (binned as FeOOH) are included for reference.

3.4.3 ISOTOPE DYNAMICS—$^{34}\varepsilon_{SR}$ AND $\delta^{34}S$ MODEL FITS

The inclusion of multiple S isotopes ($\delta^{34}S$ and $\Delta^{33}S$) into a fully articulated diagenetic model allows for an entirely new suite of biogeochemical information. This is most simply approached via a discussion of the 'best-fit' fractionation parameters ($^{34}\varepsilon_{SR}$, $^{34}\varepsilon_{MO}$, $^{34}\varepsilon_{H2SO}$) and the sensitivity of the output model profiles ($\delta^{34}S_{SO4}$, $\delta^{34}S_{H2S}$, and $\delta^{34}S_{FeS2}$) to those parameters. These synthetic model data can then be merged with known isotope systematics and fit into a broader understanding of the sedimentary S cycle in Aarhus Bay and beyond.

The measured $\delta^{34}S$ values of pore water sulfate increase from $\delta^{34}S \sim 27‰$ at 6 cm to ~80‰ near the sulfate depletion depth at 150 cm. Similarly, the $\delta^{34}S$ values of pore water sulfide increase from -39.8‰ at 6 cm to 15.6‰ at 150 cm. The $\delta^{34}S$ isotope profiles of both sulfate and sulfide follow a strikingly linear pattern with depth, with a near constant coeval offset of $\delta^{34}S_{SO4} - \delta^{34}S_{H2S} = 66\pm2‰$. This is archetypal behavior for sulfate and sulfide in marine sediments. Such little variability in the slope of the $\delta^{34}S$-depth profiles leads to the necessity of a depth- (and thus rate-) independent fractionation factor for sulfate reduction. This is the same conclusion derived from studies of California margin sediments (Masterson et al., submitted), where different relationships between rate and fractionation were explored more thoroughly. With this in mind, we employed the S isotope reactive transport model to predict the intrinsic fractionation factors associated with each biogeochemical process (beyond just sulfate reduction), and to ultimately fit the $\delta^{34}S$ profiles of the three major species. Figure 3.5 demonstrates the sensitivity of these isotope profiles to variations in those fractionation factors for sulfate reduction (a), methane oxidation (b), sulfide oxidation (c), and sulfur disproportionation (d).

The isotope-specific model allows for the physical transport of each species, and we consider the 'fit' of the prescribed fractionation factors to each profile separately. Figure 3.5a demonstrates the results of several model fits from prescribed fractionation factors for sulfate reduction ($^{34}\varepsilon_{SR}$ = 50-90‰). The best 'fit' fractionation factor for the $\delta^{34}S_{SO4}$ profile is 70‰, a value at the high end of laboratory calibrations for microbial calibrations (Leavitt et al., 2013; Sim et al., 2011a; Johnston,

2011; Johnston et al., 2007), but in keeping with theoretical predictions from low temperature thermodynamics (Wing and Halevy, 2014). Such a value has been modeled before for a hypersaline, hypersulfidic system (Wortmann et al., 2001), and in the meromictic euxinic Lago di Cadagno (Canfield et al., 2010a), and is equal to the value recently inferred for the pore waters of Alfonso Basin (Masterson et al., submitted). Other applied fractionation factors within the reactive transport model predict a $\delta^{34}S_{SO4}$ gradient that is too shallow ($^{34}\varepsilon_{SR}$ = 50‰) or too steep ($^{34}\varepsilon_{SR}$ = 90‰). As mentioned previously, there is no apparent need for $^{34}\varepsilon_{SR}$ to be depth-dependent in order to explain the sulfate isotope profile. Far and away, the isotopic composition of pore water sulfate and sulfide reflects the signature of microbial sulfate reduction. However, since the two species are free to diffuse independently, the direct offset between the measured isotope profiles of sulfate and sulfide do not reflect the intrinsic fractionation factor $^{34}\alpha_{SR}$ (or $^{34}\varepsilon_{SR}$) associated with sulfate reduction—a major result from this work.

The $\delta^{34}S_{H2S}$ profile gradient is very similar to that for $\delta^{34}S_{SO4}$ ($\delta^{34}S_{SO4}$ - $\delta^{34}S_{H2S}$ = 66±2‰), but the $\delta^{34}S$ values are also set by physical transport, with $D_{H2S} > D_{SO4}$. Using the fractionation factors tested—also shown in Fig. 3.5a, an $^{34}\varepsilon_{SR}$ value (= 70‰) accurately predicts the $\delta^{34}S_{H2S}$ values at depths >120 cm, but predicts values more ^{34}S-enriched (5-10‰) at shallow depths. This enrichment appears to be independent of the choice of boundary condition ($\delta^{34}S_{x=0}$) and largely independent of the diffusion coefficient as well. It appears that values $^{34}\varepsilon_{SR}$ > 80‰ provide an improved fit to the upper core data, but we suggest, and discuss below, several alternative possibilities for this slight misfit. It is worth noting that the $\delta^{34}S_{SO4}$ of pore water sulfate displays continual enrichment at concentrations <1 mmol/L (likely a product of the model output, sulfate concentrations < 1 mmol/L are analytically challenging to measure using multiple S isotopes techniques), whereas the $\delta^{34}S_{H2S}$ values reach a constant value (= 16±1‰) at depth, independent of the choice of fractionation factor. Likely, this value reflects complete consumption of sulfate with an initial composition reflecting that of seawater ($\delta^{34}S_{SO4}$ = 21.15‰) and the isotope gradient ($\delta^{34}S_{H2S}$) reflects the diffusional profile between sulfide produced by microbial sulfate reduction at the surface, and that produced by the near-complete

consumption of pore water sulfate at depth. Perhaps most importantly from a geochemical perspective, the isotopic composition of pyrite (FeS_2) displays far less variability downcore than $\delta^{34}S_{SO4}$ and $\delta^{34}S_{H2S}$, indicating that the large majority of pyrite formation takes place near the sediment surface. Quantitatively, much less pyrite formation takes places at depth. It the solid phase species can be approximated from steady-state conditions, then the gravimetric FeS_2 data would suggest that ~30-40% of pyrite is formed within the top 20 cm of the sediment column. Again assuming the system is in steady state, then the shallow gradient in the isotopic composition of pyrite ($\delta^{34}S_{FeS2}$) from core top to core bottom of ~10‰ reflects the gradual inheritance of ^{34}S-enriched H_2S from $^{34}SO_4^{2-}$ enriched pore waters. This is all also in keeping with the iron source for pyritization, which is in the solid phase and delivered to the top of the sediment column.

It is worth noting and discussed in more detail below the type of signature preserved in the geologically observable fraction of the early diagenetic environment. That is, the oft-applied $^{34}\varepsilon_{PY}$ (= 1000 ($^{34}R_{SWS}/^{34}R_{PY}$ -1)), or the isotope 'fractionation' between seawater sulfate and pyrite in shallow sediments is between 50-60‰ despite an intrinsic sulfate reduction fractionation of 70‰. Also exhibited in Figure 3.5a, the input fractionation factors ($^{34}\varepsilon_{SR}$) carry little consequence for the isotopic composition of pyrite sulfur, even when varied (50-90‰). The information behind this mismatch, and more importantly what it means for future interpretation of geologically preserved sedimentary environments, is explored later in this contribution.

To summarize, the modeled fractionation factor $^{34}\varepsilon_{SR}$ (=70‰) reproduces the sulfate $\delta^{34}S_{SO4}$ gradient, and also adequately reproduces the $\delta^{34}S_{FeS2}$ isotope profile. A reasonable fit for $\delta^{34}S_{H2S}$ values can be observed at depths >120 cm, but $^{34}\varepsilon_{SR}$ =70‰ does not capture the behavior of shallow pore water sulfide. We discuss this further with respect to Fe chemistry in section 3.4, but first discuss the influence of additional biogeochemical processes on the pore water and solid phase isotope distributions in Aarhus Bay.

Figure 3.5

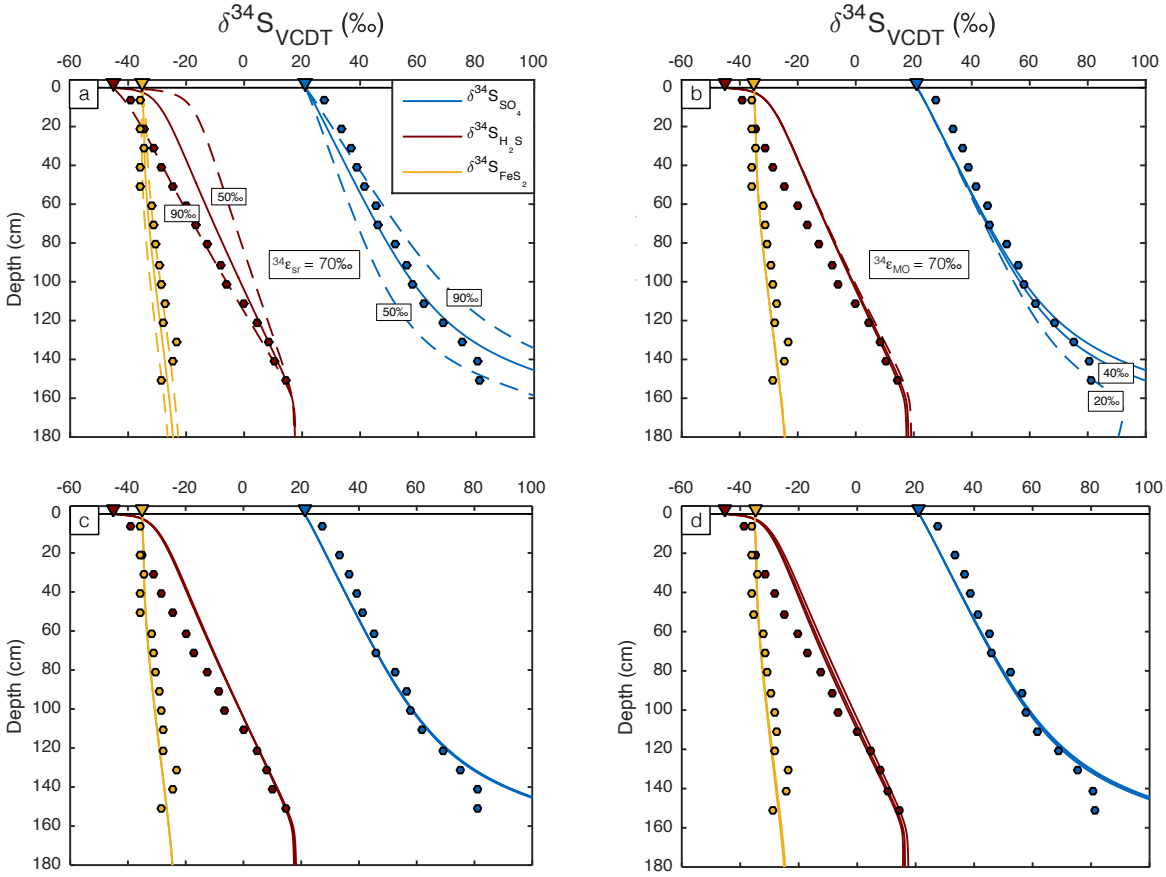

Figure 3.5: Model fits ($\delta^{34}S$) of Aarhus Bay pore water and solid phase S species, including SO_4^{2-}, H_2S, and FeS_2. The four panels demonstrate the results of testing a baseline case with variable **(a)** Fractionation associated with sulfate reduction $^{34}\varepsilon_{SR}$ **(b)** Methane oxidation $^{34}\varepsilon_{MO}$ **(c)** Chemical sulfide oxidation $^{34}\varepsilon_{H2SO}$ and **(d)** Sulfur disproportionation $^{34}\varepsilon_{SoDSO4}/^{34}\varepsilon_{SoDH2S}$. The most pronounced influence of the isotope profiles results from the variation in $^{34}\varepsilon_{SR}$ values.

3.4.4 INFLUENCE OF METHANE OXIDATION, SULFIDE OXIDATION AND DISPROPORTIONATION ON S ISOTOPE GEOCHEMISTRY OF AARHUS BAY SEDIMENTS

The S isotope community frequently calls upon additional biogeochemical S processes to explain the isotope records in deep time (Canfield and Farquhar, 2009; Canfield, 2004; Canfield and Teske, 1996) and draws analogies to those processes observed in modern sediments (Habicht and Canfield, et al., 2001; Habicht and Canfield, 1998; Habicht and Canfield, 1997). Oxidative S cycling—such as sulfur

disproportionation and chemical sulfide oxidation can complicate S isotope interpretations in two ways. First, they provide additional, and frequently non-unique, isotope fractionations associated with their specific biochemistries. Next, these alternative pathways catalyze sulfate recycling and allow for multi-stepped oxidation-reduction reactions that create additive isotope effects. Sulfur disproportionation, which is the inorganic fermentation of species like S^0, SO_3^{2-}, and $S_2O_3^{2-}$ to SO_4^{2-} and H_2S, has in particular been targeted as a likely explanation for large S isotope fractionations observed in modern marine sediments (Habicht and Canfield, 2001; Habicht and Canfield, 1997). Chemical and biological sulfide oxidation, with O_2 and NO_3^- as terminal electron acceptors or oxidants has also been invoked as means of explaining small, but not insignificant (5-30‰) S isotope effects (Dale et al., 2009; Fry et al., 1986).

As a means of testing the isotopic importance of each of these individual processes to the $\delta^{34}S$ distributions in Aarhus Bay sediments and pore waters (including the potentially for unique behavior during AOM), we systematically varied the input fractionation parameters ($^{34}\varepsilon_{MO}$, $^{34}\varepsilon_{H2SO}$, $^{34}\varepsilon_{SoDSO4}$, $^{34}\varepsilon_{SoDH2S}$) from the base model scenario (Table 3.5, $^{34}\varepsilon_{SR}$ = 70‰, $^{34}\varepsilon_{MO}$ = 70‰, $^{34}\varepsilon_{H2SO}$ = -5‰, $^{34}\varepsilon_{SoDSO4}$ = 0‰, $^{34}\varepsilon_{SoDH2S}$ = 0‰). The results of this sensitivity analysis are displayed as Figure 3.5b-d. Although there is no biogeochemical reason to suspect that AOM carries a different S isotope effect than organoclastic sulfate reduction, the isotope model allows for the two processes to be parameterized separately in order to characterize the influence on deep pore water sulfate $\delta^{34}S_{SO4}$ values. With ~20% of SO_4 lost to AOM, and the large majority below ~130 cm, a fractionation factor of $^{34}\varepsilon_{MO} < {}^{34}\varepsilon_{SR}$ would lead to a shallower $\delta^{34}S_{SO4}$ gradient within the vicinity of the sulfate depletion depth. Several model profiles are shown in 3.5b—with $^{34}\varepsilon_{MO}$ = 20‰-40‰, both sharing a shallower $\delta^{34}S_{SO4}$ gradient proportional to the prescribed fractionation factor. However, a comparison with the base case demonstrates that the effect of changing $^{34}\varepsilon_{MO}$ is small, and is not distinguishable from the base case $^{34}\varepsilon_{MO}$ at depths < 80 cm. Thus, although AOM constitutes ~20% of sulfate consumption within the whole core, the influence of its respective isotope characteristics on the final $\delta^{34}S_{SO4}$ is

minimal. There is no statistically significant influence on either the pore water (H_2S) or solid phase (FeS_2) sulfides.

The fractionation associated with sulfide oxidation is also important to explore. In varying $^{34}\varepsilon_{H2SO}$ and $^{34}\varepsilon_{SoDSO4}/^{34}\varepsilon_{SoDH2S}$ – in both cases tested allowing for fractionations of ±50‰, there is no statistically distinguishable influence on the pore water $\delta^{34}S_{SO4}$ and $\delta^{34}S_{H2S}$ or $\delta^{34}S_{FeS2}$ distributions. We note that ~10% of sulfide produced *in situ* is oxidized to S^0 and ultimately disproportionated to SO_4 and H_2S and those rates (H_2SOR and SoDR) are fairly uniformly distributed over the top ~100 cm. Nevertheless large isotope effects associated with oxidation ($^{34}\varepsilon_{H2SO} \approx \delta^{34}S_{S0} - \delta^{34}S_{H2S}$) and disproproportionation ($^{34}\varepsilon_{SoDH2S} \approx \delta^{34}S_{S0} - \delta^{34}S_{H2S}$, $^{34}\varepsilon_{SoDSO4} \approx \delta^{34}S_{S0} - \delta^{34}S_{SO4}$) exert minimal isotopic influence on the $\delta^{34}S_{SO4}$ and $\delta^{34}S_{H2S}$ profiles. This stands in stark contrast to the studies of marine sediment pore waters that required contributions from disproportionation to explain large magnitude isotope effects between coeval (depth) measurements of $\delta^{34}S_{SO4}$ and $\delta^{34}S_{H2S}$ values (Habicht and Canfield, 2001; Habicht and Canfield, 1997).

3.4.5 TRIPLE ISOTOPE (^{32}S, ^{33}S, ^{34}S) SIGNATURES

In the light of the $\delta^{34}S$ results, we explore the triple isotope ($\Delta^{33}S$ and $\delta^{34}S$) signatures of the pore water and solid phase samples. As shown in Figure 3.6, the $\Delta^{33}S$ values of pore water sulfate demonstrate an initial enrichment in $\Delta^{33}S$ values with depth and covary with the enrichment in $\delta^{34}S$ values. Such an enrichment in $\Delta^{33}S$ (~0.12±0.01‰) proceeds until ~60 cm depth ($\delta^{34}S_{SO4}$ = 60‰) before $\Delta^{33}S$ values begin to decline. A single measurement at ~150 cm displays $\Delta^{33}S$ = 0.073±0.006‰ with a $\delta^{34}S$ value of 81.4±0.2‰. Although the existing data sets are sparse, this is the first time that *declining* $\Delta^{33}S$ values are observed at a large fraction of sulfate consumption. All other pore water sulfate samples demonstrate continuous enrichment in ^{33}S with progressive sulfate loss (Masterson et al., submitted; Pellerin et al., 2015; Strauss et al., 2012). It is worth noting that entirely closed-system consumption of sulfate (*i.e.* Rayleigh-like behavior) displays a linear $\Delta^{33}S$ vs. $\delta^{34}S$ array that is related to the paired fractionation factors ($^{33}\alpha_{SR}$ and $^{34}\alpha_{SR}$, or $^{34}\alpha_{SR}$ and $^{33}\lambda_{SR}$). Deviation from that linear

behavior reflects open system behavior and mixing from other sources (Ono et al., 2006). Shallow pore water sulfide demonstrates $\Delta^{33}S$ values ^{33}S-enriched with respect to seawater sulfate ($\Delta^{33}S$ = 0.220±0.006‰ vs. $\Delta^{33}S$ = 0.0470.006‰ for seawater sulfate—pairing typical of systems where microbial sulfate reduction is dominant—and corresponding to $^{34}\varepsilon_{SR}$ ~ 60‰ and $^{33}\lambda_{SR}$ = 0.5120±0.0005 (Johnston, 2011; Johnston et al., 2007). The $\Delta^{33}S$ values of pore water H_2S display a near-monotonic drop in $\Delta^{33}S$ values with depth, toward the calibrated seawater sulfate value. As discussed previously, pore water sulfide $\delta^{34}S$ values follow are similar pattern, demonstrating a nearly linear ^{34}S enrichment with depth, and reaching a value of ~15‰ near the sulfate depletion zone at ~150 cm. The $\Delta^{33}S$ values of sedimentary pyrite display approximately uniform values, despite an enrichment in ^{34}S of approximately ~10‰ from 6 cm to 150 cm depth within the Aarhus Bay core. The average value of all sedimentary pyrite measured ($\Delta^{33}S$ = 0.170±0.009‰) indicates that pyrite possesses less ^{33}S than predicted from the composition of shallow pore water sulfide, and indicates one of three processes: either (i) the S contained within pyrite reflects the consequences of oxidative S cycling that have a large influence on $\Delta^{33}S$ values, but little influence on $\delta^{34}S$ values, or (ii) the composition of pyrite reflects multiple stages of mixing of sulfide and shallow pore water sulfide does not adequately capture the composition of solid phase S or (iii) the system is not in steady state, and the composition of pore water sulfide does not reflect the longer term history of pore water H_2S $\Delta^{33}S$ values. The first process (i) is less likely, although there is some evidence from microbial oxidation experiments that large ^{33}S effects are possible with sulfide oxidation (Zerkle et al., 2009). The latter two (ii and iii) are more likely: pyrite $\Delta^{33}S$ reflects multiple stages of mixing of pore water H_2S $\Delta^{33}S$, and the sulfide that is ultimately captured to form FeS_2 is not reflected by the sulfide 'snapshot' sampled at Station M1.

Figure 3.6

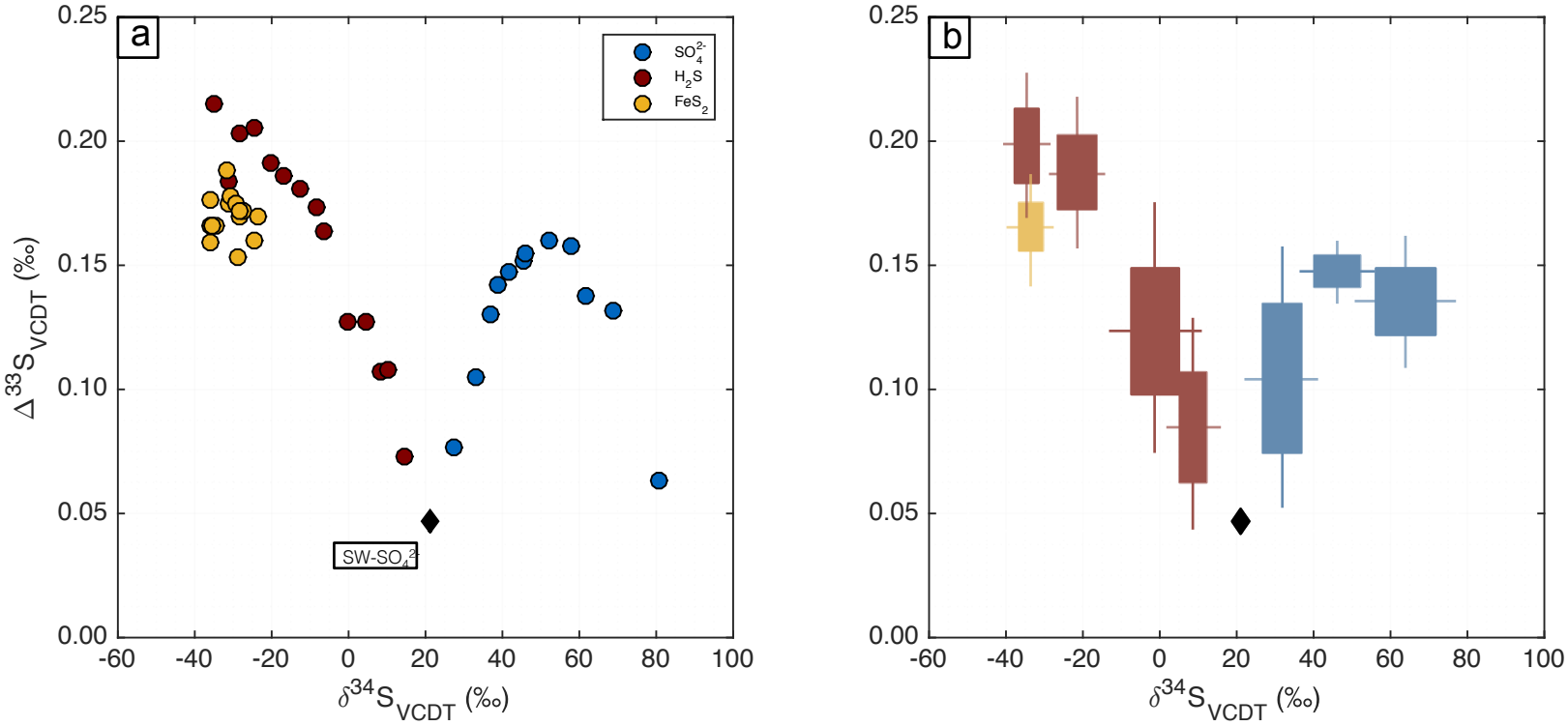

Figure 3.6: (a) Triple isotope plot ($\Delta^{33}S$ vs. $\delta^{34}S$) of Aarhus bay pore water species, including SO_4^{2-}, H_2S, and FeS_2, with the composition of seawater sulfate (SW-SO_4^{2-}) shown as a black diamond ($\delta^{34}S$ = 21.15‰ and $\Delta^{33}S$ = 0.047‰) (Johnston et al., 2014). All measurements have reproducibility of σ–$\delta^{34}S$ = 0.25‰ and σ–$\Delta^{33}S$ = 0.006‰. **(b)** Depth binned box plot of ranges of values ($\delta^{34}S$ and $\Delta^{33}S$) for S species. Sulfate bins include 6-41 cm, 51-91 cm, and >101 cm, where with sulfide bins including 6-41 cm, 51-91 cm, 101-131 cm, and > 141 cm). Bin for FeS_2 includes all depths and displays little variability in $\Delta^{33}S$ values. Solid boxes represent (1σ) variability in $\delta^{34}S$ and $\Delta^{33}S$ for that particular depth bin and whiskers represent (2σ).

3.4.6 FE AND OXIDATION CHEMISTRY

A few possibilities exist for reconciling the mismatch in the model output for sulfide $\delta^{34}S_{H2S}$ values and the measured coretop values. Recall that both the concavity and absolute value of the model prediction differ slightly from measured values in the upper reaches of the core. The most likely candidate mechanisms to amend this disparity relate to either oxidation and ferric iron sulfidization (Fe geochemistry), and/or the oxidation chemistry associated with bioturbation and biorrigation. We have parameterized Fe oxidation chemistry using a single reaction scheme ($H_2SOR = k_{H2SOR}[H_2S]^{0.5}[FeOOH]$), where [FeOOH] is an amorphous ferric iron(oxy)hydroxide. Iron (oxy)hydroxides are well known to have a range (~10^7) in their reactivities towards sulfide (Poulton et al., 2004; Poulton, 2003; Canfield et al., 1992; Canfield et al., 1989) that depends upon their crystallinity and surface area. Researchers have attempted to directly infer the reactivity of sedimentary iron oxides *in situ* in marine sediments (Haese et al., 1997; Canfield et al., 1992) using chemical and spectroscopic techniques—demonstrably, the rate of sulfide oxidation by ferric iron cannot be fully encapsulated by the rate term used in the baseline model. The model fit overpredicts sulfide concentrations at shallow depths (<75 cm) within Aarhus Bay sediments, and perhaps relatedly, the isotope model overpredicts the $\delta^{34}S_{H2S}$ at shallow depths as well. Further, we have not expressly included any bioturbation or bioirrigation in the baseline simulation, both of which can alter the diffusion regime of the upper reaches of the sediment. That said, there appears to be no evidence from the pore water data that bioirrigation influences the concentration profile, and this has been asserted by previous author (Dale et al., 2008).

3.4.7 ENVIRONMENTAL IMPLICATIONS OF $^{34}\varepsilon_{SR}$

Several recent studies of the environmental S isotope effects document apparent, large magnitude fractionations associated with sulfate reduction ($^{34}\varepsilon_{SR}$) in the water columns of euxinic systems (Gomes and Hurtgen, 2013; Canfield et al., 2010; Zerkle et al., 2009). A single study of a deep biosphere drill hole, encountering hypersaline, hypersulfidic (>10 mmol/L H_2S) sedimentary

conditions documented an isotopic fractionation between sulfate and sulfide of >65‰ (Wortmann et al., 2001). For environmental reasons, this study called on sulfate reduction alone to satisfy the large isotope effect. These environmental studies, in parallel to laboratory work illustrating the capacity of sulfate reduction to generate large isotope effects (Sim et al., 2011; Leavitt et al., 2013), hint at the potential for sulfate reduction to be dominating the entire environmental isotope signal, even at larger offsets between sulfate and sulfide. However, as we have demonstrated above, directly measuring the difference between sulfate and sulfide does not adequately (or faithfully) capture the $^{34}\varepsilon_{SR}$ (or $^{33}\lambda_{SR}$), but instead reflects biogeochemistry with the added effects of physical transport. What is required in order to isolate the biogeochemistry is a more rigorous approach that incorporates these physics.

Our analysis of Aarhus bay allows for the observed isotope signal to be broken out into its component parts. We find that when transport is removed, large intrinsic S isotope fractionations ($\gtrsim$ 70‰) are possible in a place like Aarhus Bay, an organic-rich shallow marine continental margin system where sulfate reduction rates are reasonably high. This is a similar predicted intrinsic sulfate reduction isotope effect as extracted from a modeling/data study continental margin sediments under >400 m of water (Masterson et al., submitted). These values are in keeping with recent theoretical studies that predicted the potential for $^{34}\varepsilon_{SR}$ = 70-80‰ at very low rates of sulfate reduction, characterized by a highly reversible sulfate reduction network (Wing and Halevy, 2014; Leavitt et al., 2013; Johnston et al., 2007; Brunner and Bernasconi, 2005). The modeled fractionation factors in this study provide an additional example to ground truth those theoretical predictions, and suggest that in marine sediments, $^{34}\varepsilon_{SR}$ values are almost invariably larger than those observed in laboratory cultures and most commonly in line with theoretical equilibrium predictions (see Farquhar et al., 2003; Johnston et al., 2007). This also means that there is no expressed requirement for a depth-dependent $^{34}\varepsilon_{SR}$ to explain the pore water data. The extension of this is that there appears to be negligible dependence of $^{34}\varepsilon_{SR}$ on organic matter, or more specifically, electron-donor (OM, CH_4) on controlling S isotope fractionation magnitude *in situ*. Finally, and equally as striking, our modeling demonstrates

that other biogeochemical processes, like sulfide oxidation and disproportionation, contribute little to the isotopic composition of pore water $\delta^{34}S$ distributions.

There is one additional level of discussion that is warranted given the data set and modeling presented herein. One goal of this work it to better understand how early diagenetic signals (i.e. biogeochemistry) are translated to the geological record. In turn, it is an open question what we can learn about *in situ* processes like rates of reactions and substrate delivery from these isotope records. The geological record does not capture or preserve pore water profiles, but instead records solid phase metal sulfide (i.e. pyrite) and sparingly seawater sulfate. For our study, this sulfate value is the boundary condition at the sediment water interface. We can then take the integrated picture of how geochemical and isotopic systematics down core come to reflect, or are related to the composition preserved in pyrite. In essence, the result is a simple one – the isotopic composition of pyrite is fixed near the sediment water interface. Thus, the down core systematics provides a rich record of modern biogeochemistry but will not be preserved geologically.

We can finally come to draw a final distinction between the effects of sulfate reduction as a metabolic process and remineralization catalyst, and broader isotopic records. As captured in Figure 3.7, we take both from this study and that of the Alfonso basin that the intrinsic isotope effect from sulfate reduction is near 70‰. This differs from the directly measured offset between pore water sulfate and aqueous sulfide – a commonly applied approach, by ~ 5‰. The offset is the result of diffusive and advective smoothing rather than oxidative metabolic processes. Equally as important, geological proxy records of the fractionation with respect to pyrite burial ($\delta^{34}S_{SO4} - \delta^{34}S_{py}$) would record a net fractionation 50-60‰, misinterpreting that of sulfate reduction. The next natural goal from this style of analysis is building a large scale, time dependent geochemical model that incorporates information like that reported here to make more use of the rich historical record of sedimentary pyrite.

Figure 3.7

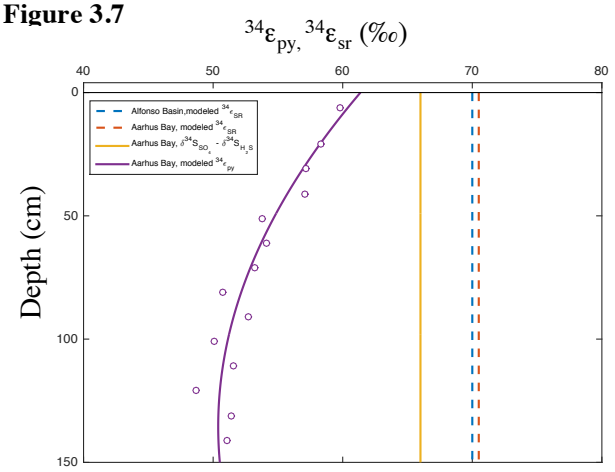

Figure 3.7: Modeled and measured fractionation factors for Aarhus Bay and Alfonso Basin (Masterson et al., submitted), and the values predicted from pyrite $\delta^{34}S$ values ($^{34}\varepsilon_{SR}$) and for the offset observed in pore water $\delta^{34}S$ values ($\delta^{34}S_{SO4} - \delta^{34}S_{H2S}$).

3.5 CONCLUSIONS

We have conducted an extensive survey of the geochemistry and isotope systematics of Aarhus Bay sediments and pore waters using multiple S isotope measurements in concert with a reactive transport model that (i) uses the concentrations of pore water species ($[SO_4^{2-}]$, $[CH_4]$, $[H_2S]$) to ascertain rates of biogeochemical processes like sulfate reduction, anaerobic methane oxidation and sulfur disproportionation, and (ii) prescribes fractionation characteristics ($^{34}\alpha$ and $^{33}\lambda$) to understand pore water $\delta^{34}S$ and $\Delta^{33}S$ values. The site and samples studied here demonstrate the following conclusions.

- All pore water $\delta^{34}S$ values can largely be explained by a *single*, depth and rate independent fractionation associated with sulfate reduction. That fractionation factor ($^{34}\varepsilon_{SR}$) is large (~70‰) and fits pore water $\delta^{34}S$ values quite well. The observed $^{33}\lambda_{SR}$ fits nicely with that expected for a mass-dependent fractionation and previous laboratory studies.

- Explaining the isotope systematics of Aarhus bay sediment and pore water is largely insensitive to additional S cycling processes like sulfur disproportionation and sulfide oxidation. Sensitivity analyses demonstrate that even if the intrinsic isotope effect associated with these metabolic processes is large, the overall isotopic characteristics preserved are those derived from sulfate reduction.
- The $\delta^{34}S$ isotope gradients reflect the influence of biogeochemical processing but also that of diffusive transport. It is possible that much of the isotopic information archived in sulfate is lost to the 'resetting' associated with physical transport.
- Pyrite $\delta^{34}S$ values reflect S isotope fractionations of slightly lower magnitude (= 50-60‰) than those predicted by the diagenetic modeling—reflecting the closed system effects associated with progressive down core pyrite precipitation.

These results are robust, and share many similarities with the results of Chapter 2 – a study of marine sediment deposited along the California – Mexico margin. As such, we suggest that these results can and should be applicable to the study and interpretation of other marginal marine sedimentary environments, both in the modern and throughout Earth history. For the later, the results noted above serve as a word of caution, calling attention to the need for careful evaluation of what geologically observable phases/minerals are being compared, and exactly what biogeochemical information phases/minerals will record.

That noted, there is still an opportunity to further expand the modeling captured here. Specifically, the complexities of Fe oxidation/reduction chemistry in early diagenetic environments is still coming to light and can be further incorporated. This should include similar studies to those noted here in environments with significantly different Fe:S ratios, and more variable POC loading in order to better cover the types of environments preserved throughout Earth history. Finally, the role of bioturbation, purposefully absent here (Dale et al., 2011), should be more rigorously handled in the future.

3.6 ACKNOWLEDGEMENTS

We acknowledge the crew of the *RV Tyra* for assistance with, and preparation for, core sampling, and Hans Røy and Bo Barker Jørgensen for graciously passing along samples, analytical information, and for helpful discussions.

3.7 REFERENCES

Aller, R.C., Madrid, V., Chistoserdov, A., Aller, J.Y., and Heilbrun, C. (2010) Unsteady diagenetic processes and sulfur biogeochemistry in tropical deltaic muds: Implications for oceanic isotope cycles and the sedimentary record. *Geochimica et Cosmochimica Acta* **74**, 4671–4692.

Berelson, W.M., Prokopenko, M., Sansone, F.J., Graham, A.W., McManus, J., and Bernhard, J.M. (2005) Anaerobic diagenesis of silica and carbon in continental margin sediments: Discrete zones of TCO_2 production. *Geochimica et Cosmochimica Acta* **69**, 4611–4629.

Berner, R.A. (1964) An idealized model of dissolved sulfate distribution in recent sediments. *Geochimica et Cosmochimica Acta* **28**, 1497–1503.

Boetius, A., Ravenschlag, K., Schubert, C.J., Rickert, D., Widdel, F., Gieseke, A., Amann, R., Jørgensen, B.B., Witte, U., and Pfannkuche, O. (2000) A marine microbial consortium apparently mediating anaerobic oxidation of methane. *Nature* **407**, 623–626.

Boudreau, B.P. (1996) Diagenetic models and their interpretation. Springer. 414 pp.

Bowles, M.W., Mogollón, J.M., Kasten, S., Zabel, M., and Hinrichs, K.U. (2014) Global rates of marine sulfate reduction and implications for sub-sea-floor metabolic activities. *Science* **344**, 889–891.

Bradley, A.S., Leavitt, W.D., Schmidt, M., Knoll, A.H., Girguis, P.R., and Johnston, D.T. (2015) Patterns of sulfur isotope fractionation during Microbial Sulfate Reduction. *Geobiology* 1–11.

Brunner, B., Arnold, G.L., Røy, H., Müller, I.A., and Jørgensen, B.B. (2016) Off Limits: Sulfate below the Sulfate-Methane Transition. *Front. Earth Sci.* **4**, 4.

Canfield, D.E. (2001) Biogeochemistry of sulfur isotopes. *Reviews in Mineralogy and Geochemistry* **43**, 607–636.

Canfield, D.E. (2004) The evolution of the Earth surface sulfur reservoir. *American Journal of Science* **304**, 839–861.

Canfield, D.E., and Farquhar, J. (2009) Animal evolution, bioturbation, and the sulfate concentration of the oceans. *Proceedings of the National Academy of Sciences* **106**, 8123–8127.

Canfield, D.E., Farquhar, J., and Zerkle, A.L. (2010) High isotope fractionations during sulfate reduction in a low-sulfate euxinic ocean analog. *Geology* **38**, 415–418.

Canfield, D.E., Raiswell, R., Westrich, J.T., Reaves, C.M., and Berner, R.A. (1986) The use of chromium reduction in the analysis of reduced inorganic sulfur in sediments and shales. *Chemical Geology* **54**, 149–155.

Dale, A.W., Brüchert, V., Alperin, M., and Regnier, P. (2009) An integrated sulfur isotope model for Namibian shelf sediments. *Geochimica et Cosmochimica Acta* **73**, 1924–1944.

Dale, A.W., Aguilera, D.R., Regnier, P., Fossing, H., Knab, N.J., and Jørgensen, B.B. (2008) Seasonal dynamics of the depth and rate of anaerobic oxidation of methane in Aarhus Bay (Denmark) ediments. *Journal of Marine Research* **66**, 127–155.

Forrest, J., and Newman, L. (1977) Silver-110 microgram sulfate analysis for the short time resolution of ambient levels of sulfur aerosol. *Analytical Chemistry* **49**, 1579–1584.

Fossing, H., Berg, P., Thamdrup, B., Rysgaard, S., Sorensen, H.M., and Nielsen, K., 2004, A model set-up for an oxygen and nutrient flux model for Aarhus Bay (Denmark).

Habicht, K.S., and Canfield, D.E. (1997) Sulfur isotope fractionation during bacterial sulfate reduction in organic-rich sediments. *Geochimica et Cosmochimica Acta* **61**, 5351–5361.

Habicht, K.S., and Canfield, D.E. (2001) Isotope fractionation by sulfate-reducing natural populations and the isotopic composition of sulfide in marine sediments. *Geology* **29**, 555–558.

Habicht, K.S., Canfield, D.E., and Rethmeier, J.O. (1998) Sulfur isotope fractionation during bacterial reduction and disproportionation of thiosulfate and sulfite. *Geochimica et Cosmochimica Acta* **62**, 2585–2595.

Habicht, K.S., Gade, M., Thamdrup, B., Berg, P., and Canfield, D.E. (2002) Calibration of sulfate levels in the Archean ocean. *Science* **298**, 2372–2374.

Holmkvist, L., Ferdelman, T.G., and Jørgensen, B.B. (2011) A cryptic sulfur cycle driven by iron in the methane zone of marine sediment (Aarhus Bay, Denmark). *Geochimica et Cosmochimica Acta* **75**, 3581–3599.

Jensen, J.B., and Bennike, O. (2009) Geological setting as background for methane distribution in Holocene mud deposits, Århus Bay, Denmark. *Continental Shelf Research* **29**, 775–784.

Johnston, D.T., Farquhar, J., Wing, B.A., Kaufman, A.J., Canfield, D.E., and Habicht, K.S. (2005) Multiple sulfur isotope fractionations in biological systems: a case study with sulfate reducers and sulfur disproportionators. *American Journal of Science* **305**, 645–660.

Johnston, D.T., Farquhar, J., and Canfield, D.E. (2007) Sulfur isotope insights into microbial sulfate reduction: When microbes meet models. *Geochimica et Cosmochimica Acta* **71**, 3929–3947.

Jørgensen, B.B. (1982) Mineralization of organic matter in the sea bed—the role of sulphate reduction. *Nature* **296**, 643–645.

Knittel, K., and Boetius, A. (2009) Anaerobic oxidation of methane: progress with an unknown process. *Annu Rev Microbiol* **63**, 311–334.

Leavitt, W.D., Halevy, I., Bradley, A.S., and Johnston, D.T. (2013) Influence of sulfate reduction rates on the Phanerozoic sulfur isotope record. *Proc Natl Acad Sci U S A* **110**, 11244–11249.

Meister, P., Liu, B., Ferdelman, T.G., Jørgensen, B.B., and Khalili, A. (2013) Control of sulphate and methane distributions in marine sediments by organic matter reactivity. *Geochimica et Cosmochimica Acta* **104**, 183–193.

Milucka, J., Ferdelman, T.G., Polerecky, L., Franzke, D., Wegener, G., Schmid, M., Lieberwirth, I., Wagner, M., Widdel, F., and Kuypers, M.M. (2012) Zero-valent sulphur is a key intermediate in marine methane oxidation. *Nature* **491**, 541–546.

Pellerin, A., Bui, T.H., Rough, M., Mucci, A., Canfield, D.E., and Wing, B.A. (2015) Mass-dependent sulfur isotope fractionation during reoxidative sulfur cycling: A case study from Mangrove Lake, Bermuda. *Geochimica et Cosmochimica Acta* **149**, 152–164.

Poulton, S.W., Krom, M.D., and Raiswell, R. (2004) A revised scheme for the reactivity of iron oxyhydr)oxide minerals towards dissolved sulfide. *Geochimica et Cosmochimica Acta* **68**, 3703–3715.

Strauss, H., Bast, R., Cording, A., Diekrup, D., Fugmann, A., Garbe-Schönberg, D., Lutter, A., Oeser, M., Rabe, K., and Reinke, D. (2012) Sulphur diagenesis in the sediments of the Kiel Bight, SW Baltic Sea, as reflected by multiple stable sulphur isotopes. *Isotopes in environmental and health studies* **48**, 166–179.

Tarpgaard, I.H., Røy, H., and Jørgensen, B.B. (2011) Concurrent low- and high-affinity sulfate reduction kinetics in marine sediment. *Geochimica et Cosmochimica Acta* **75**, 2997–3010.

Boudreau, B.P., and Westrich, J.T. (1984) The dependence of bacterial sulfate reduction on sulfate concentration in marine sediments. *Geochimica et Cosmochimica Acta* **48**, 2503–2516.

Wortmann, U.G., Bernasconi, S.M., and Bottcher, M.E. (2001) Hypersulfidic deep biosphere indicates extreme sulfur isotope fractionation during single-step microbial sulfate reduction. *Geology* **29**, 647–650.

Table 3.6

Mid-depth (cm)	$[SO_4^{2-}]$ (mM)	$[H_2S]$ (mM)	Wt %S	$\delta^{34}S_{SO4}$	$\Delta^{33}S_{SO4}$	$\delta^{34}S_{H2S}$	$\Delta^{33}S_{H2S}$	$\delta^{34}S_{CRS}$	$\Delta^{33}S_{CRS}$
6	23.7	0	0.22	27.6	0.077	-38.9	-	-36.48	0.166
21	19.8	0.6	0.36	33.3	0.105	-34.8	0.215	-35.13	0.159
31	17.7	0.7	0.37	36.9	0.130	-31.3	0.184	-34.13	0.166
41	16.3	1.0	0.47	39.0	0.142	-28.4	0.203	-34.09	0.176
51	14.1	0.8	0.4	41.5	0.147	-24.6	0.205	-31.00	0.166
61	12.3	1.8	0.33	45.5	0.152	-20.1	0.191	-31.27	0.188
71	10.8	2.2	0.52	46.1	0.155	-17	0.186	-30.46	0.175
81	8.3	3.1	0.75	52.2	0.160	-12.6	0.181	-28.22	0.178
91	6.7	2.6	0.34	56.2	-	-8.3	0.173	-29.97	0.175
101	6.5	3.3	0.37	57.8	0.158	-6.3	0.164	-27.59	0.170
111	4.3	1.5	0.48	61.9	0.138	-0.1	0.127	-28.96	0.172
121	2.7	3.0	0.52	68.9	0.132	4.5	0.127	-26.30	0.172
131	1.8	2.7	0.49	75.1	-	8.1	0.107	-28.80	0.170
141	1.3	1.3	0.72	80.8	0.063	10.3	0.108	-28.52	0.160
151	0.6	2.2	1.04	81.4	-	14.6	0.073	-27.72	0.153
161	0.5	0.8	-	-	-	-	-	-	-
171	0.5	1.0	-	-	-	-	-	-	-
181	0.6	1.3	-	-	-	-	-	-	-
191	0.8	1.6	-	-	-	-	-	-	-
201	0.5	2.4	-	-	-	-	-	-	-

Table 3.6: Pore water and S isotope data from core sampled at Station M1 in Aarhus Bay

CHAPTER 4

THE MINOR SULFUR ISOTOPE COMPOSITION OF CRETACEOUS AND CENOZOIC SEAWATER SULFATE*

ABSTRACT

The last 125 million years captures major changes in the chemical composition of the ocean and associated geochemical and biogeochemical cycling. The isotopic composition of seawater sulfate, as proxied in marine barite, is one of the more perplexing geochemical records through this interval. Numerous analytical and geochemical modeling approaches have targeted this record. Recently, measurement of the minor sulfur isotopes has provided unique insight into sulfur metabolisms and diagenetic sulfur cycling. In this study we extend the empirical isotope record of seawater sulfate to therefore include the two minor sulfur isotopes, ^{33}S and ^{36}S. These data record a distribution of values around averages of $\Delta^{33}S_{SO4}$ = 0.043±0.016‰ and $\Delta^{36}S_{SO4}$ = -0.39±0.15‰, which, regardless of $\delta^{34}S$-based binning strategy, are consistent with a single population of values throughout this interval. We demonstrate with simple box modeling that a substantial change in pyrite burial or evaporitic sulfate weathering can be accommodated within the range of our observed isotopic values.

*A version of this chapter was published as Masterson, A.L., Wing, B.A., Paytan, A., Farquhar, J., and Johnston, D.T. (2016) The minor sulfur isotope composition of Cretaceous and Cenozoic seawater sulfate. *Paleoceanography* 31, 1-10. doi: 10.1002/2016PA002945, Copyright Wiley and Sons.

4.1 INTRODUCTION

Reconstructing records of seawater sulfate and atmospheric oxygen are central to understanding Earth surface change over the last four billion years (Canfield, 2004; Hayes and Waldbauer, 2006). Through the Phanerozoic, where geological and geochemical records are more robust, more refined estimates of the concentration and isotopic composition of seawater sulfate are possible (Bergman et al., 2004; Berner and Canfield, 1989; Kampschulte and Strauss, 2004; Lowenstein et al., 2001; Paytan et al., 1998; Paytan et al., 2004). For instance, fluid inclusion records suggest large and bidirectional changes in sulfate concentrations over the Phanerozoic (Brennan et al., 2013; Horita et al., 2002; Lowenstein et al., 2003; Lowenstein et al., 2001). Further, isotopic records are also variable (Canfield and Farquhar, 2009; Kampschulte and Strauss, 2004), with the rate of change related to sulfate concentrations (Wortmann and Paytan, 2012). Matching isotopic and concentration records can, however, be challenging to interpret given the uncertainty associated with any given isotopic or concentration record. Fortunately, a high precision record is possible for the last 125 Ma-present via authigenic barite minerals extracted from deep-sea cores (Paytan et al., 1998; Paytan et al., 2004).

The isotopic composition of seawater sulfate is controlled by the same set of fluxes and mechanisms that establish and drive changes in seawater sulfate concentrations. The controls on both the concentration and isotopic composition of seawater sulfate are sulfate inputs to the ocean via oxidative weathering and evaporite dissolution, with delivery via rivers. These inputs are countered by sulfur removal through hydrothermal and sedimentary sulfide minerals, as well as sulfate mineral sinks (evaporites, anhydrite, and carbonate associated sulfate). Each of these input and output fluxes carry their own unique, time-dependent isotopic composition. The control on each is partly environmental, tectonic, and biological and each carries characteristic timescales for change. At present, however, the large marine sulfate reservoir (3.9×10^{19} moles) (Petsch and Berner, 1998) is buffered against modern perturbations given the long residence time of $\sim 10^7$ years (Claypool et al., 1980) and resultant well-mixed ocean isotopic composition (Johnston et al., 2014). However, this

noalways the case throughout earlier intervals of Earth history when sulfate concentrations my have been substantially lower.

It is within this framework, balancing inputs and outputs, that marine barite records have been interpreted. The composition of seawater sulfate as recorded in barite shows a distinctive and perplexing structure (Fig. 4.1) (Kurtz et al., 2003; Paytan et al., 2004; Paytan et al., 1998; Wortmann and Paytan, 2012). Namely the last 125 Ma is marked by a series of three relatively stable isotopic compositional period (120-100 Ma, 95-50 Ma, and 45-5Ma), separated by abrupt transitions (denoted by color scheme)

Notably, standard approaches thus require either a massive, punctuated changes in fluxes or intrinsic fractionations, an exceedingly small sulfate reservoir, or some combination of both. This is simply to satisfy the rate of isotopic change. Further, from first principles, changes in fluxes should manifest as an isotopic decay related to the size of the forcing, and modulated by the residence time of sulfate at that time. In originally interpreting these records, Paytan and colleagues rightfully evaluated possible biogeochemical and tectonic controls on marine sulfate (Paytan et al., 1998). A more mathematically driven C-S study (Kurtz et al., 2003) followed shortly thereafter and, similarly, demonstrated the changes necessary to the sulfur cycle in order to account for barite $\delta^{34}S$ records. Often, the driver of $\delta^{34}S$ changes is a major swing in pyrite burial in a low sulfate ocean. Ensuing studies moved away from pyrite burial and brought sulfate evaporite distributions to bear on the $\delta^{34}S$ record (Wortmann and Paytan 2012; Wortmann and Chernyavsky, 2007). For instance, massive evaporite deposition associated with the opening of the south Atlantic in the early Cretaceous (Hayes et al., 2006; Wortmann and Chernysavsky, 2007; Wortmann and Paytan, 2012) could serve as large and temporally punctuated sink for sulfate without imposing an extreme isotope effect. The substantial decrease in the standing stock of seawater sulfate, estimated to reach a minimum of ~2 mM, thus allows for the rapid (< 5 million years) changes preserved in $\delta^{34}S$ between 125 and 50 million years ago. As this hypothesis is framed, much of this gypsum is reintroduced to the ocean at ~45 Ma, again

an event that would not carry a significant point source of isotopic change in $\delta^{34}S$ of sulfate but impose a rapid change to the buffering capacity of the seawater sulfate reservoir.

In this study we present $\delta^{33}S$, $\delta^{34}S$, and $\delta^{36}S$ values of marine barite. These analyses are possible only through fluorination to SF_6, and in keeping with minor isotope literature (*e.g.*, Farquhar et al., 2003), we present these data as $\Delta^{33}S$ and $\Delta^{36}S$ values. The inclusion of minor sulfur isotope data allows for a sensitivity analysis on the mechanisms proposed to explain the published $\delta^{34}S$ barite record. Models outlined below explore perturbations to both pyrite burial and evaporite burial/weathering, each of which would carry a different multiple sulfur isotopic consequence for marine sulfate.

4.2 MATERIALS AND METHODS

The barite samples analyzed in this study are the same as those presented previously for the $\delta^{34}S$ composition (Paytan et al., 1998; Paytan et al., 2004). For that original work, barite minerals were chemically separated from core material and processed to convert barite to silver sulfide. This Ag_2S was generated prior to our study. Here, we fluorinated Ag_2S to generate SF_6 at both the University of Maryland and Harvard University. In both labs, an excess of F_2 is introduced to a reaction vessel containing the sample. The vessel is heated for approximately 8 hours to ensure a complete conversion of Ag_2S to SF_6. The product SF_6 is cleaned cryogenically and chromatographically prior to the introduction to a dual-inlet gas source mass-spectrometer (Thermo Scientific MAT 253). Analyte SF_6 is measured as SF_5^+ at m/e 127, 128, 129, 131. In both labs, full reproducibility of 1σ ($\Delta^{33}S$) and 1σ ($\Delta^{36}S$) is 0.008‰ and 0.2‰, respectively. We use a standard minor isotope notation to report variance in ^{33}S and ^{36}S. The variability is defined as a deviation from a prediction rooted in low-temperature thermodynamic equilibrium. This results in the following two expressions (Johnston et al., 2007; Johnston et al., 2011; Farquhar et al., 2003, Farquhar and Wing, 2003):

$$\Delta^{33}S = \delta^{33}S - 1000\left(\left(1+\delta^{34}S/1000\right)^{0.515} - 1\right) \quad (4.1)$$

$$\Delta^{36}S = \delta^{36}S - 1000\left(\left(1+\delta^{34}S/1000\right)^{1.9} - 1\right) \quad (4.2)$$

For these data, we assume a composition of VCDT, relative to IAEA-S-1 of -0.3‰, -0.107‰, and -0.5‰ for $\delta^{34}S$, $\Delta^{33}S$, and $\Delta^{36}S$, respectively.

4.3 RESULTS

The minor isotope records documented below were generated from the same silver sulfide samples-the product of sulfate reduction chemistry (Forrest and Newman, 1977) as reported on previously (Paytan et al., 1998; Paytan et al., 2004). This redundancy is used as a test of the higher precision methods. That is, the new $\delta^{34}S$ data record is tightly correlated (m = 1.000±0.023; b = 0.015±0.45‰) with published values (Paytan et al., 1998; Paytan et al., 2004). Here we add to the $\delta^{34}S$ compositions the $\Delta^{33}S$ and $\Delta^{36}S$ values (Fig. 4.1b, c). The mass-dependent nature of these records leaves the composition and variability of $\Delta^{33}S$ smaller than $\Delta^{36}S$ offset by a scaling factor that varies around 6.85 (*e.g.,* Ono et al., 2006a), depending on the particular mass law (Young et al., 2002; Miller et al., 2002). Contamination in ^{36}S is common, and as such, anomalously enriched $\Delta^{36}S$ values were vetted at the time of analysis. Viewed as an entire time series, the $\Delta^{33}S$ values vary around a mean of 0.043±0.016‰, 1σ) with no statistically significant trend through time (p = 0.3653; Fig. 4.2). A similar result is captured in $\Delta^{36}S$ values, where the mean is -0.37±0.14‰, 1σ) and p = 0.4717 for the 125 Ma record (Fig. 4.2). Notably the composition of the modern ocean is $\Delta^{33}S$ = 0.047‰ and $\Delta^{36}S$ = -0.50‰ and is noted as a black circle (with error) in Figures 4.1 and 4.2.

Figure 4.1

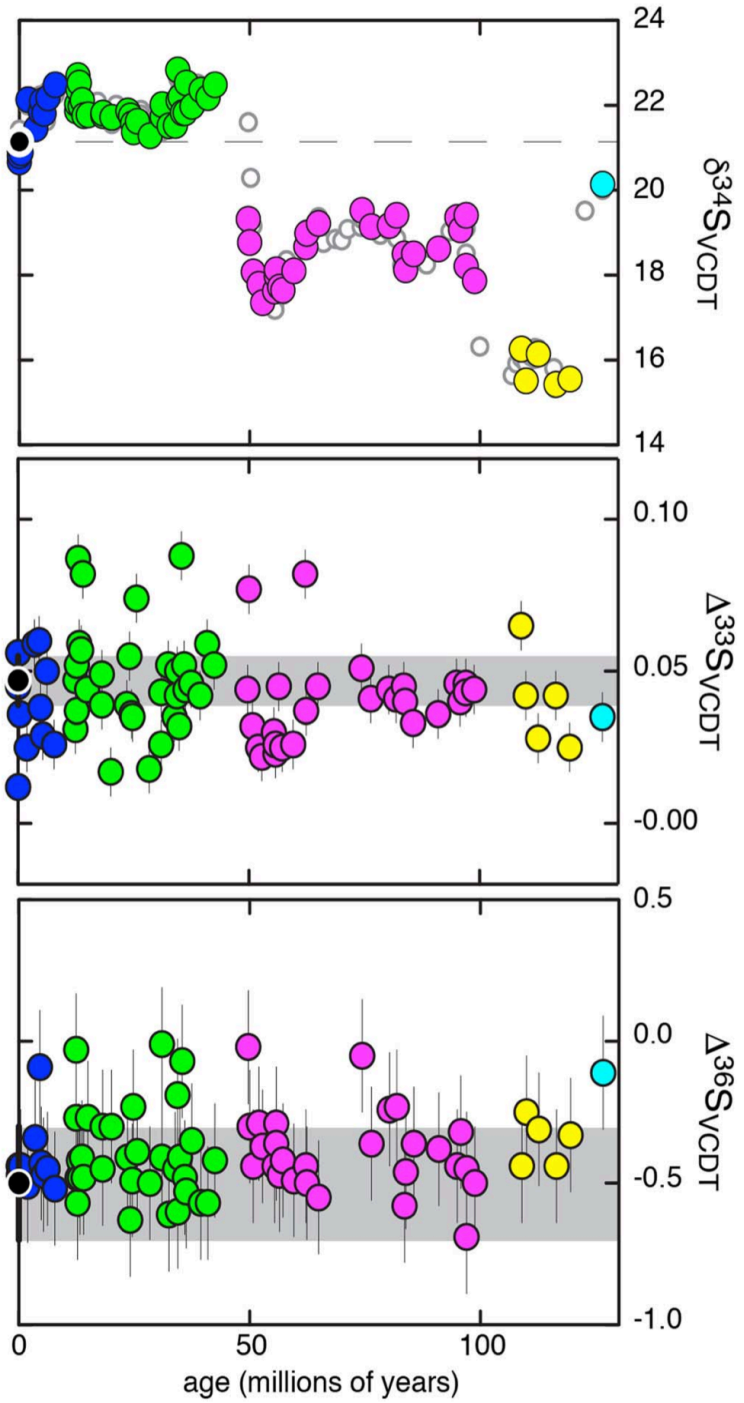

Figure 4.1: The barite record of (top) $\delta^{34}S$, (middle) $\Delta^{33}S$, and (bottom) $\Delta^{36}S$ versus time for the Cretaceous and Cenozoic. Samples in gray (background in Fig. 4.1, top) are previously published, whereas those in color represent this study. This color code is used throughout and based on the $\delta^{34}S$ compositions. Errors are 2σ. All data are placed upon a common V-CDT scale. Gray bar across each frame is the composition (and error) of the modern marine sulfate reservoir (Johnston et al., 2014; Tostevin et al. 2014).

Figure 4.2

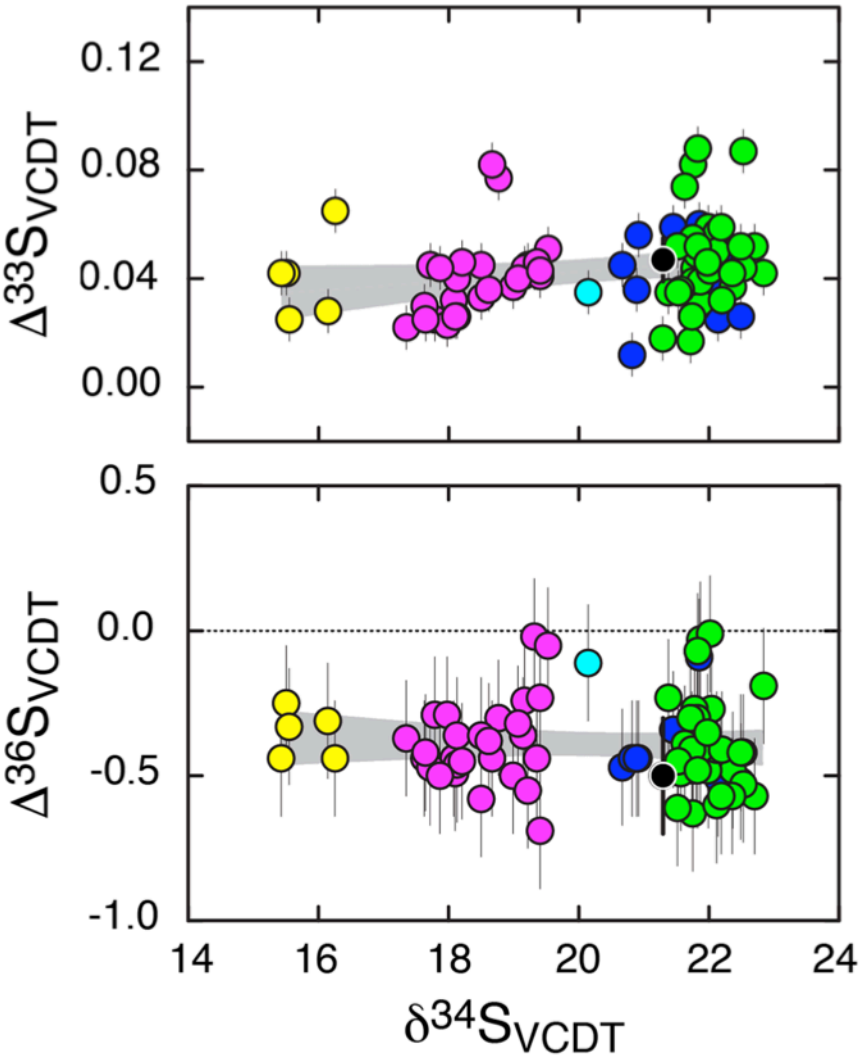

Figure 4.2: The $\delta^{34}S$ values versus $\Delta^{33}S$ and $\Delta^{36}S$ values for the samples presented in Fig. 4.1 (same color coding). Errors are 2σ. The regressions reflect a 95% confidence interval on the entire population.

4.4 DISCUSSION

The isotopic variability preserved within marine sulfate records over the last 125 million years can be explained by a combination of purely mass-dependent isotope effects, meaning that the isotopic fractionation mechanisms scale with the mass differences of the isotopes (Young et al., 2002; Miller, 2002) and mass conservation effects that arise from the mixing and unmixing of pools with different

isotopic compositions (*e.g.* Farquhar et al., 2007). This mass-dependence results in a $\delta^{33}S$ value that scales to $\delta^{34}S$ value offset by a factor that varies from 0.507 to 0.515, whereas the $\delta^{34}S$ value versus $\delta^{36}S$ value ratio fluctuates around 1.9 (Farquhar and Wing, 2003; Johnston, 2011). This covariance is defined as $^{33}\lambda$, which approximates the slope of a line on a three-isotope plot ($\delta^{33}S$ versus $\delta^{34}S$), or $\ln(^{33}\alpha/^{34}\alpha)$. The same expression can be cast for ^{36}S. Much of the variability within sulfur isotope records can be linked to biological activity and metabolic processes that induce fractionations within variable $^{3X}\lambda$ because of mixing and unmixing at the cellular level (Johnston et al., 2005a; Johnston et al., 2007; Farquhar et al., 2007; Farquhar et al., 2003). In many cases, these $^{3X}\lambda$ values manifest as resolvable $\Delta^{33}S$ values, providing a potential fingerprint of the processes that influenced a given measured composition (note that the magnitude of change in Δ values will vary as a function of the absolute change in $\delta^{3x}S$ values. Put differently, the specific $\delta^{33}S$-$\delta^{34}S$-$\delta^{36}S$ of seawater sulfate should reflect the amalgamation of the biological cycling within the S cycle over the mixing time of that reservoir. This approach holds true in interpreting modern marine sulfate (Tostevin et al., 2014; Johnston et al., 2014; Ono et al., 2012; Li et al., 2010), as it does in assessing paleo-environmental records (Johnston et al., 2005b, Wu et al., 2015; Wu et al., 2010; Sim et al., 2015). Given the larger signal/noise in $\Delta^{33}S$ records when compared to $\Delta^{36}S$ (a result of larger $\Delta^{36}S$ analytical error), mass-dependent studies generally focus on $\Delta^{33}S$ values. Thus although we include ^{36}S where necessary, much of the discussion and interpretation only considers ^{33}S systematics. Where this is done, it can be assumed that the inclusion of ^{36}S would result in the same conclusions

The largest isotopic effects measured within the sulfur cycle are microbial in origin. The two processes capable of generating large $\delta^{34}S$ effects, microbial sulfate reduction and sulfur disproportionation, produce highly resolvable $^{33}\lambda$ (Johnston et al., 2005a; Johnston et al., 2011) In the case of sulfate reduction, which is responsible for a majority of organic carbon remineralization in marine sediments (*e.g.*, Jørgensen et al., 1982) isotopic fractionation scales inversely as a function of metabolic rate (Leavitt et al., 2013) and results in $^{33}\lambda$ (values less than that predicted for thermodynamic equilibrium (~0.5145) (Johnston et al., 2007; Farquhar et al., 2003). At high rates, the $^{34}\varepsilon_{MSR}$ values are

generally small, approaching 17‰ (Goldhaber and Kaplan, 1975; Leavitt et al., 2013), with a $^{33}\lambda_{MSR}$ approaching 0.510. At low metabolic rates, much larger $^{34}\varepsilon_{MSR}$ and $^{33}\lambda_{MSR}$, are observed, often approaching thermodynamic equilibrium values of 70‰ and 0.5145 for $^{34}\varepsilon_{MSR}$ and $^{33}\lambda_{MSR}$, respectively (Farquhar and Wing, 2003; Johnston et al., 2007; Wing and Halevy, 2014). Much less is known about disproportionation, however existing data point to a wide range of possible $^{34}S/^{32}S$ fractionation effects, often scaling with both substrate (*e.g.,* Habicht et al., 1998) and metal availability (Bottcher and Thamdrup, 2001); here, metals serve to scavenge biogenic sulfide, keeping HS^- low and helping overall metabolic energetics. The net effect of disproportionation can however, be summarized as variable $^{34}\varepsilon_{MSR}$ with $^{33}\lambda_{MSR}$, always greater than 0.5145 (Johnston et al., 2005a). Importantly, this allows disproportionation to be resolved from effects associated with sulfate reduction, even where $^{34}\varepsilon$ values are similar (Johnston et al., 2005b). The final microbial process of note is sulfide oxidation, which imparts a small $^{34}S/^{32}S$ isotope effect (Fry et al., 1985; Fry et al., 1986; Zerkle et al., 2009) and a unique range of $^{33}\lambda$ values.

4.4.1 THE FIDELITY OF BARITE RECORDS

Barite harvested from marine sediments is inferred to capture the contemporaneous isotopic composition of seawater sulfate and has been validated for $\delta^{34}S$ records (Paytan et al., 1998). That is, core-top barite is statistically indistinguishable from modern water column sulfate. This was recently confirmed through a series of studies on modern seawater sulfate (Johnston et al., 2014; Tostevin et al., 2014; Wu et al. 2010; Ono et al., 2012), yielding a composition of $\delta^{34}S$ = 21.14±0.15‰, $\Delta^{33}S$ = 0.048±0.006‰, and $\Delta^{36}S$ = 0.5±0.20‰. In comparison, modern core-top barite reported here measure 20.81±0.2‰, 0.038±0.008‰, and -0.45±0.2‰, respectively, statistically indistinguishable from modern seawater sulfate. The correspondence in S isotope composition between seawater sulfate and core top barite is consistent with the suggested long residence time of sulfate and the use of marine barite as a proxy for the isotopic composition of seawater sulfate in the past.

Figure 4.3

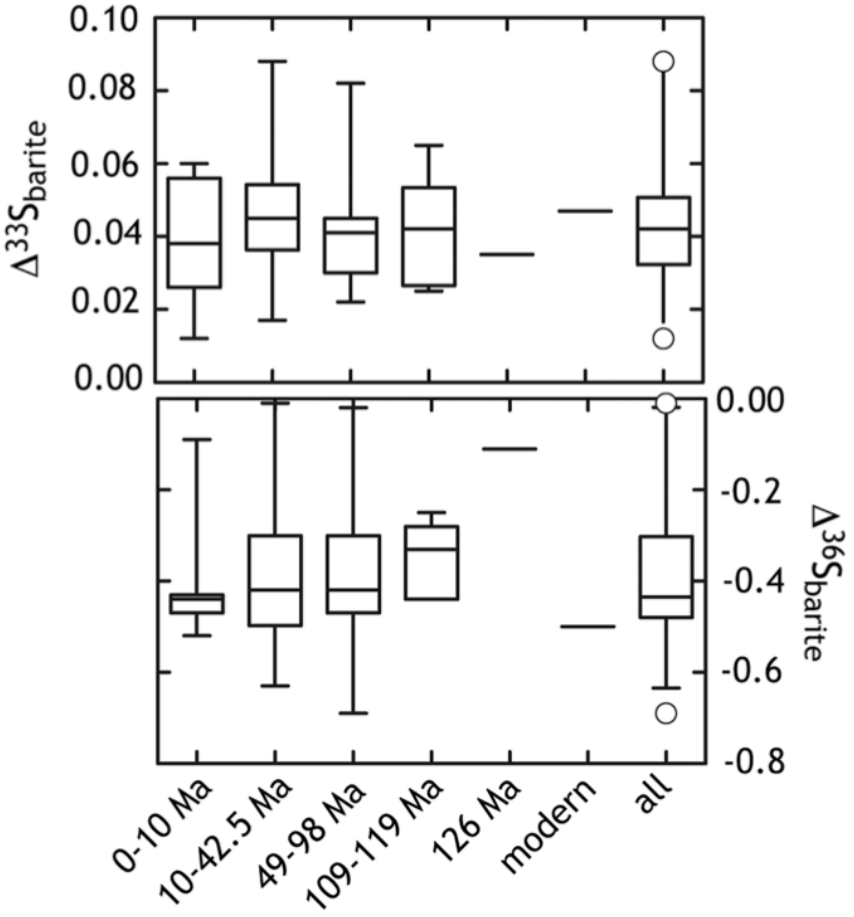

Figure 4.3: A box and whisker analysis of the different data populations. The errors reflect 95% confidence intervals on the population, with median values plotted as the center bars.

4.4.2 A 125 MILLION YEAR RECORD OF SEAWATER SULFATE

The interpretation of barite records can be approached with a number of different goals. First, when the data are coarsely binned according to the time domains displayed in Fig. 4.1 (see also Fig. 4.3) the entire 125 Ma data set is not normally distributed (according to a D'Agostino and Pearson normality test) in ^{33}S or ^{36}S. For ^{33}S, this may provide real insight into the nature of the variance, meaning that the mechanisms operating on the S cycle are more likely to enrich ^{33}S than deplete it, with the mean value reflecting some more robust steady state condition or compositional 'floor' (*i.e.*, a common state of the sulfur cycle represented by a lower $\Delta^{33}S$ value). However, the asymmetry in ^{36}S is possibly analytical.

As noted above, contamination on the m/z=131 where ^{36}S is measured as $^{36}SF_5^+$ will pull $\Delta^{36}S$ compositions toward more enriched values, which is the direction of the skew of the data. Of the more data-rich bins (the most recent three geological bins, with n = 11, 32 and 27), most of the data is, in fact, normally distributed for both $\Delta^{33}S$ values and $\Delta^{36}S$ values for a given time domain. This reinforces arguments made on an average composition of those bins. The exceptions are the 49-98 million year bin in $\Delta^{33}S$ values and the 0-10 million year bin in $\Delta^{36}S$ values. This is evident in the box and whisker analysis in Fig. 4.3 where the asymmetry is evident in the 95% confidence intervals.

Despite the nature of the distributions, Fig. 4.2 demonstrates the mass-dependence of the barite record and illustrates that little to no change in $\Delta^{33}S$ values and $\Delta^{36}S$ values accompanies the small (but resolvable) perturbations in the $\delta^{34}S$ record. As noted above, this is perhaps not unexpected, however does limit the available mechanisms that could be underpinning the $\delta^{34}S$ transitions. Recall that the nature of mass-dependent fractionation predicts that for any given change in $\delta^{34}S$ value, an accompanying magnitude of change in $\Delta^{33}S$ value and $\Delta^{36}S$ value is expected-the absolute change will be a function of both how far $^{33}\lambda$ values varies from the reference values of 0.515 and 1.9 that are used to define the values of $\Delta^{33}S$ and $\Delta^{36}S = 0$, and the magnitude of the change in $\delta^{34}S$ values. For example, the early Eocene transition is marked by a 4‰ change in $\delta^{34}S$, but an unresolvable signal in $\Delta^{33}S$ and $\Delta^{36}S$. If this event was triggered solely as a result of changes in sulfate reduction (setting all other factors aside for the moment) at a $^{33}\lambda = 0.510$ and $^{36}\lambda = 1.95$, then the associated changes in $\Delta^{33}S$ value and $\Delta^{36}S$ value would be roughly 0.02‰ and 0.2‰, respectively. As our measurement analytical uncertainty is similar in magnitude to the expected signal, actually 'seeing' this event in ^{33}S and ^{36}S would be near our analytically resolvable limit and thus unlikely. In order for a unique minor isotope effect to be discernible then, the $^{34}\varepsilon$ values would have to be larger, or the $^{33}\lambda$ and $^{36}\lambda$ values would have to deviate more significantly from the reference line value. Thus, it is perhaps not unexpected that no resolvable minor isotope signal exists associated with the early Eocene change in $\delta^{34}S$ record. The example presented here could also be viewed as a simple sensitivity analysis of the capacity for the minor sulfur isotopes to capture large, resolvable effect when viewed in light of the $\delta^{34}S$ variability

captured over the last 125 million years. Note that in a proper statistical analysis of the entire 125 million year time series, values of both $\Delta^{33}S$ and $\Delta^{36}S$ are unchanged (Figs. 4.1, middle and bottom, and Figs. 4.2-4.4). This places constraints on the type of changes undergone by the sulfur cycle over the last 125 Ma, and places limits on how changes in certain fluxes might be contributing to these records.

Figure 4.4

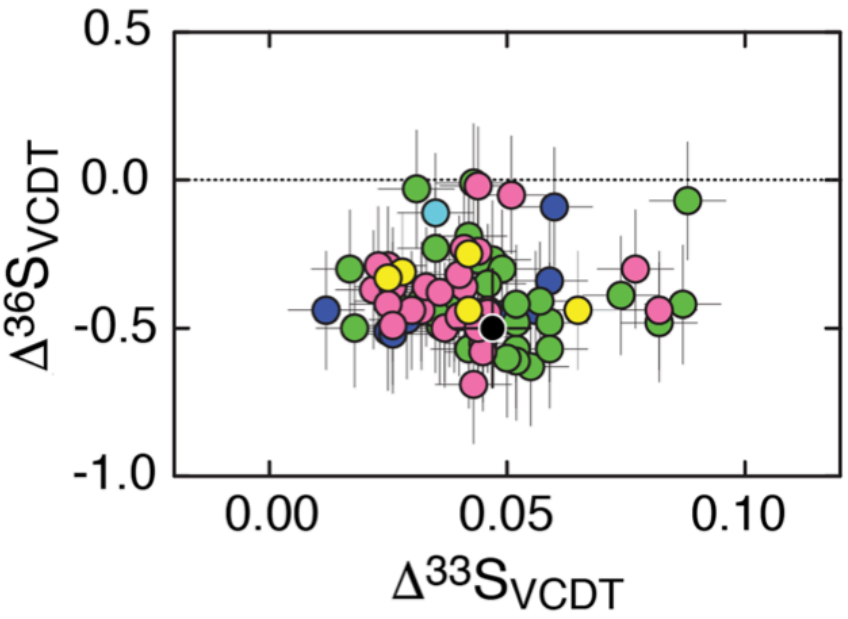

Figure 4.4: The barite record of (top) $\Delta^{33}S$ versus (bottom) $\Delta^{36}S$ versus time. The color coding is shared with Fig. 4.1, and errors are 2σ.

This treatment can be handled more rigorously. In traditionally interpreting $\delta^{34}S$ records, the fraction of sulfur leaving the oceans as pyrite (f_{py}) is commonly the metric of interest (Berner and Canfield, 1989; Canfield, 2004; Canfield and Farquhar, 2009). In such treatments, the microbial effects are often summarized as a single, constant fractionation factor ($^{34}\varepsilon$), so that the only variable is the fraction of burial (Kurtz et al., 2003; Halverson and Hurtgen, 2007). In much the same way, there are isotopic consequences in ^{33}S and ^{36}S that relate to how mass is partitioned within the marine sulfur cycle. The difference comes with the varying definitions of isotope notations. Mixing relationships are effectively linear in $\delta^{33}S$-$\delta^{34}S$-$\delta^{36}S$ relationships, but non-linear in $\Delta^{33}S$ and $\Delta^{36}S$ fractionation relationships (*cf.,* Farquhar et al., 2007; Johnston, 2011).

In order to test the sensitivity of the isotopic composition of sulfate, and specifically $\Delta^{33}S$ values, to the fluctuations that must relate to the changes preserved in the $\delta^{34}S$ record (*e.g.,* pyrite burial) we have constructed a pseudo steady-state box model. Using this simple approach, we test the capacity to induce a change in the $\Delta^{33}S$ values as a function of the companion $\delta^{34}S$ values. Recall that these effects are mass-dependent, so the change in both metrics is necessarily coupled. For this analysis, we arbitrarily chose a perturbation in the magnitude of pyrite burial. Following along the lines of similarly published models (*e.g.,* Kurtz et al., 2003), weathering rates are held constant, and pyrite burial rates are doubled over the course of one million years. The isotopic compositions ($\delta^{34}S$ and $\Delta^{33}S$ values) are held constant. For the weathering input, we have used $F_w = 1.5x10^{12}$ mol S/yr, and a constant flux of evaporite deposition of $F_{ev} = 1.05x10^{12}$ mol S/yr. Pyrite burial was initially held constant at $4.5x10^{11}$ mol S/yr, and doubled over 1.0 Myr to $9.0x10^{11}$ mol S/yr. Fractionation due to pyrite burial was also held constant at $^{34}\varepsilon_{py} = 35‰$ ($^{34}\alpha_{py} = 0.965$), independent of the variability within the burial flux. Finally, we have explored two different cases, with starting concentration of $[SO_4^{2-}] = 25.0$ mM and $[SO_4^{2-}] = 5.0$ mM. The concentration of sulfate was allowed to evolve accordingly. To introduce isotope systematics to the model, we have used isotope ratios directly, and utilized the trace-abundance approximation $^{32}F \equiv F$ (*e.g.,* Farquhar et al., 2007). In this case, the bulk mass-balance equations for a single box ocean can be written as:

$$\frac{dM_{OC}}{dt} = F_W - F_{EV} - F_{PY} \tag{4.3}$$

Where dM_o/dt is the rate of change in the concentration of seawater sulfate reservoir, F_W, F_{EV}, and F_{PY} are the weathering, evaporite deposition, and pyrite burial fluxes, respectively. The isotope mass balance equation (*e.g.,* for ^{34}S), can be written accordingly:

$$\frac{d}{dt}\left[M_{OC} \cdot {}^{34}R_{OC}\right] = F_W \cdot {}^{34}R_W - F_{EV} \cdot {}^{34}R_{EV} - F_{PY} \cdot {}^{34}R_{PY} \tag{4.4}$$

Expanding equation (4.4), incorporating equation (4.3) and assuming that $^{34}R_{EV} = {}^{34}R_{OC}$, yields the following non-steady state equations (4.5 and 4.6), in this case written for ^{33}S and ^{34}S:

$$\frac{d^{33}R_{OC}}{dt} = \frac{1}{M_{OC}}\left[F_W\left[{}^{33}R_W - {}^{33}R_{OC}\right] - F_{PY}\left[{}^{33}R_{PY} - {}^{33}R_{OC}\right]\right] \quad (4.5)$$

$$\frac{d^{34}R_{OC}}{dt} = \frac{1}{M_{OC}}\left[F_W\left[{}^{34}R_W - {}^{34}R_{OC}\right] - F_{PY}\left[{}^{34}R_{PY} - {}^{34}R_{OC}\right]\right] \quad (4.6)$$

Assuming that the fractionation associated pyrite deposition remains constant, the following substitution can be made:

$$\frac{d^{33}R_{OC}}{dt} = \frac{1}{M_{OC}}\left[F_W\left[{}^{33}R_W - {}^{33}R_{OC}\right] - F_{PY}\left[{}^{33}\alpha_{PY} - 1\right]\right] \quad (4.7)$$

$$\frac{d^{34}R_{OC}}{dt} = \frac{1}{M_{OC}}\left[F_W\left[{}^{34}R_W - {}^{34}R_{OC}\right] - F_{PY}\left[{}^{34}\alpha_{PY} - 1\right]\right] \quad (4.8)$$

Using a finite difference approach, equations (4.7) and (4.8) can thus be solved for the case where both M_{OC} and $^{3X}R_0$ are changing with time. Fig. 4.5 demonstrates the model output for the cases where $[SO_4^{2-}]_0$ = 5 and 25 mM. In both cases, a doubling of the pyrite burial flux for 1Myr (distributed as a Gaussian) produces positive excursions in the $\delta^{34}S$ value of the ocean form the initial value of $\delta^{34}S$ =15.2‰. As expected, the rate of increase varies inversely with the initial size of the sulfate reservoir. Notably, a new 'steady-state' value of $\delta^{34}S$ is not reached in the $[SO_4^{2-}]_0$ = 25 mM case due to the long residence time of sulfate in the ocean.

Introducing ^{33}S systematics, in both cases, a doubling of the pyrite burial flux yields subtle variations in the evolution of the $\delta^{34}S_{OC}$ values. Using $^{33}\lambda$ values representative of microbial sulfate reduction (*e.g.*, $^{33}\lambda$ = 0.512-0.514), the evolution of $\Delta^{33}S_{OC}$ positively correlated with the evolution of $\delta^{34}S_{OC}$, but the magnitude of the change from the initial value (set at $\Delta^{33}S$ = 0.047‰), though measurable, is small (±0.01‰). Thus, even with a large perturbation in $\delta^{34}S_{OC}$ associated with a

doubling of pyrite burial flux, the sensitivity of $\Delta^{33}S_{OC}$ to the same perturbation is small, and would be difficult to detect within the range of $\delta^{34}S_{OC}$ variability within the last 120 Ma (*e.g.,* $\delta^{34}S_{OC}$ = 15-22‰).

Along similar lines, it is possible to test the case where a substantial contribution from an evaporitic source (*e.g.,* Wortmann and Paytan, 2012) produces a perturbation in the isotopic composition of $\delta^{34}S_{OC}$ and $\Delta^{33}S_{OC}$ values. Although this can be incorporated into a steady-state model like the previous pyrite burial case, a mixture between two different isotopic end-member sources can be used to demonstrate the range of isotopic values that would result from the contribution of a large evaporitic source (*i.e.,* a simple mixing calculation). To do so, it is necessary to assume an evaporite composition, we suggest it falls within the range of isotopic values measured for barite within this study ($\delta^{34}S$ = 15-22‰, and $\Delta^{33}S$ = 0.02-0.08‰). The resulting mixture is a linear combination of the two isotopic sources, with f_{EV} as the fractional contribution of evaporitic sulfate to total seawater, and can be calculated as follows:

$$\delta^{33}S_{mix} = \delta^{33}S_{OC} \cdot \left(1 - f_{EV}\right) + f_{EV} \cdot \delta^{33}S_{EV} \tag{4.9}$$

$$\delta^{34}S_{mix} = \delta^{34}S_{OC} \cdot \left(1 - f_{EV}\right) + f_{EV} \cdot \delta^{34}S_{EV} \tag{4.10}$$

The $\delta^{34}S$ and $\Delta^{33}S$ values are, of course, functions, both of the end-member compositions and f_{EV}. Isotope mass-balance would then indicate that $\delta^{34}S$ and $\Delta^{33}S$ values must fall within the range prescribed by the two end-members. For example, mixing between seawater sulfate sharing the composition of modern sulfate $\delta^{34}S$ = 21.15‰ and $\Delta^{33}S$ = 0.047‰ and an evaporite source with $\delta^{34}S$ = 15‰ and $\Delta^{33}S$ = 0.02‰, gives the mixing relationship seen in Fig. 4.6. Simply, the mixture between seawater sulfate and an evaporitic source sharing isotopically similar $\Delta^{33}S$ values falls within the range of $\Delta^{33}S$ barite values measured here. Resolving a contribution from an evaporitic source using $\Delta^{33}S$

requires values statistically distinct from those inferred to exist from the composition of sulfate, at least through the latter half of the Phanerozoic.

Figure 4.5

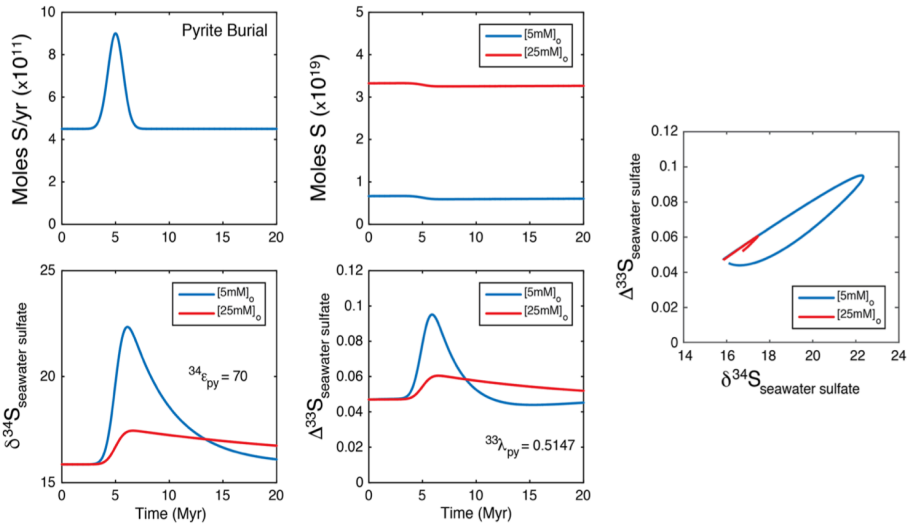

Figure 4.5: A simple one box sulfate model whereby the sensitivity of $\Delta^{33}S$ can be demonstrated, here as a function of changing pyrite burial over a 1 Myr period (top left). We model the change in pyrite burial as it propogates through (top right) the mass of seawater sulfate, (bottom left) the $\delta^{34}S$ composition of sulfate, and (bottom right) the $\Delta^{33}S$ composition of sulfate. Fractionation factors were derived from Farquhar et al. (2003).

Figure 4.6

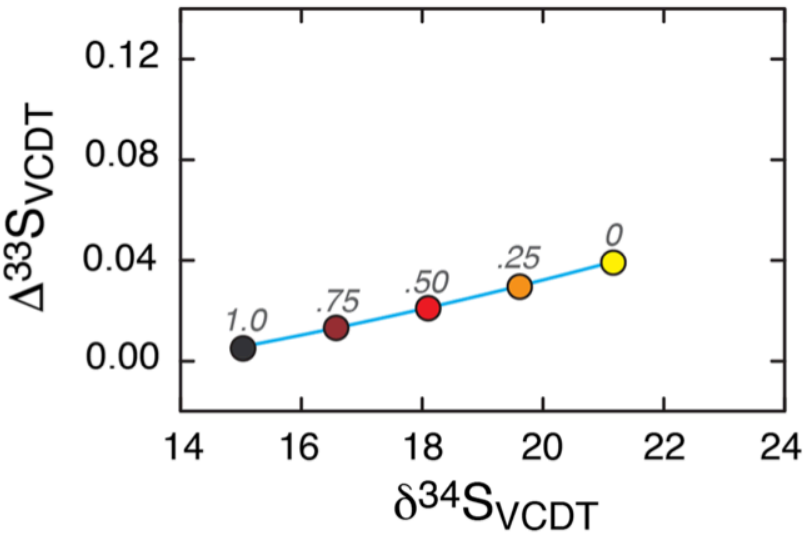

Figure 4.6: A simple mixing relationship demonstrating the consequences of reintroducing evaporitic sulfate back into the ocean.

4.5 CONCLUSIONS

The development of new isotopic systems and proxies is frequently followed by the critical generation of time series for those metrics. This study serves the role of providing a robust quantification of the minor sulfur isotope records of seawater sulfate of the late Cretaceous and Cenozoic. Pre-existing $\delta^{34}S$ records stand as one of the more under constrained of the major oceanographic chemical records. The new minor sulfur isotope data presented in this study record invariant $\Delta^{33}S$ and $\Delta^{36}S$ values associated with the swings of up to 5‰ in the $\delta^{34}S$ record. Models built to include the minor S isotopes can accommodate major changes in pyrite burial and sulfate inputs/outputs within the range of compositions measured. During intervals of Earth history with larger $\delta^{34}S$ perturbations in sulfate, $\Delta^{33}S$ and $\Delta^{36}S$ values should be more easily interpretable metrics (*e.g.,* Wu et al., 2015). In looking forward, perhaps improved minor isotope precisions, along with a closer association with $\delta^{18}O$ records (Turchyn and Schrag, 2004; Turchyn and Schrag, 2006), global models of sulfur cycling and sulfate reduction (*e.g.,* Bowles et al., 2014), and diagenetic modeling studies will further constrain the information held within sulfate records.

4.6 ACKNOWLEDGMENTS

We would like to thank ten years of conference goers for listening about and commenting on these data. We thank NSF EAR/IF (DTJ), NASA Exobiology (DTJ, JF, AM), NAI (DTJ, JF), NSF-OCE (AP), and NSF EAR (DTJ, JF). Erin Beirne, Ben Gill and many others are thanked for productive discussions.

4.7 REFERENCES

Bergman, N. M., T. M. Lenton, and A. J. Watson (2004), COPSE: A new model of biogeochemical cycling over Phanerozoic time, *Am. J. Sci.*, *304*(5), 397–437.

Berner, R. A., and D. E. Canfield (1989), A new model for atmospheric oxygen over Phanerozoic time, *Am. J. Sci.*, *289*(4), 333–361.

Bottcher, M. E., and B. Thamdrup (2001), Anaerobic sulfide oxidation and stable isotope fractionation associated with bacterial sulfur disproportionation in the presence of MnO_2, *Geochim. Cosmochim. Acta*, *65*, 1573–1581.

Bowles, M. W., J. M. Mogollón, S. Kasten, M. Zabel, and K.-U. U. Hinrichs (2014), Global rates of marine sulfate reduction and implications for sub-sea-floor metabolic activities., *Science*, *344*(6186), 889–891.

Brennan, S. T., T. K. Lowenstein, and D. I. Cendon (2013), The major-ion composition of Cenozoic seawater: The past 36 million years from fluid inclusions in marine halite, *Am. J. Sci.*, *313*(8), 713-775.

Canfield, D. E. (2004), The evolution of the Earth surface sulfur reservoir, *Am. J. Sci.*, *304*(10), 839–861.

Canfield, D. E., and J. Farquhar (2009), Animal evolution, bioturbation, and the sulfate concentration of the oceans, *Proc. Natl. Acad. Sci. U.S.A.*, *106*(20), 8123–8127.

Claypool, G. E., W. T. Holser, I. R. Kaplan, H. Sakai, and I. Zak (1980), The age curves of sulfur and oxygen isotopes in marine sulfate and their mutual interpretation, *Chem. Geol.*, *28*, 199–260.

Farquhar, J., and B. A. Wing (2003), Multiple sulfur isotopes and the evolution of the atmosphere, *Earth Planet. Sci. Lett.*, *213*(1–2), 1–13.

Farquhar, J., D. T. Johnston, B. A. Wing, K. S. Habicht, D. E. Canfield, S. Airieau, and M. H. Thiemens (2003), Multiple sulphur isotopic interpretations of biosynthetic pathways: Implications for biological signatures in the sulphur isotope record, *Geobiology*, *1*(1), 27–36.

Farquhar, J., D. T. Johnston, and B. A. Wing (2007), Implications of conservation of mass effects on mass-dependent isotope fractionations: Influence of network structure on sulfur isotope phase space of dissimilatory sulfate reduction, *Geochim. Cosmochim. Acta*, *71*(24), 5862 – 5875.

Forrest, J., and L. Newman (1977), Silver 110 microgram sulfate analysis for the short time resolution of ambient levels of sulfur aerosols, *Anal. Chem.*, *49*(11), 1579–1584.

Fry, B., H. Gest, and J. M. Hayes (1985), Isotope effects associated with the anaerobic oxidation of sulfite and thiosulfate by the photosynthetic bacterium, Chromatium vinosum, *FEMS Microbiol. Lett.*, *27*, 227–32.

Fry, B., J. Cox, H. Gest, and J. M. Hayes (1986), Discrimination between 34S and 32S during bacterial metabolism of inorganic sulfur compounds, *J. Bacteriol.*, *165*(1), 328–330.

Gill, B. C., T. W. Lyons, and M. R. Saltzman (2007), Parallel, high-resolution carbon and sulfur isotope records of the evolving Paleozoic marine sulfur reservoir, *Palaeogeogr. Palaeoclimatol. Palaeoecol.*,*256*(3–4), 156–173.

Goldhaber, M. B., and I. R. Kaplan (1975), Controls and consequences of sulfate reduction rates in recent marine sediments, *Soil Sci.*, *119*(1), 42–55.

Habicht, K. S., D. E. Canfield, and J. Rethmeier (1998), Sulfur isotope fractionation during bacterial reduction and disproportionation of thiosulfate and sulfite, *Geochim. Cosmochim. Acta*, *62*(15),

2585–2595.

Halevy, I., S. E. Peters, and W. W. Fischer (2012), Sulfate burial constraints on the Phanerozoic sulfur cycle, *Science*, *337*(6092), 331–334.

Halverson, G. P., and M. T. Hurtgen (2007), Ediacaran growth of the marine sulfate reservoir, *Earth Planet. Sci. Lett.*, *263*(1–2), 32–44.

Hay, W. W., A. Migdisov, A. N. Balukhovsky, C. N. Wold, S. Flögel, and E. Söding (2006), Evaporites and the salinity of the ocean during the Phanerozoic: Implications for climate, ocean circulation and life, *Palaeogeogr. Palaeoclimatol. Palaeoecol.*, *240*(1–2), 3–46.

Hayes, J. M., and J. R. Waldbauer (2006), The carbon cycle and associated redox processes through time, *Philos. Trans. R. Soc. B*, *361*(1470), 931 – 950.

Horita, J., H. Zimmermann, and H. Holland (2002), Chemical evolution of seawater during the Phanerozoic: Implications from the record of marine evaporites, *Geochim. Cosmochim. Acta*, *66*, 3733–3756.

Johnston, D. T. (2011), Multiple sulfur isotopes and the evolution of Earth's surface sulfur cycle, *Earth Sci. Rev.*, *106*, 161–183.

Johnston, D. T., J. Farquhar, B. A. Wing, A. J. Kaufman, D. E. Canfield, and K. S. Habicht (2005a), Multiple sulfur isotope fractionations in biological systems: A case study with sulfate reducers and sulfur disproportionators, *Am. J. Sci.*, *305*(6–8), 645–660.

Johnston, D. T., B. A. Wing, J. Farquhar, A. J. Kaufman, H. Strauss, T. W. Lyons, L. C. Kah, and D. E. Canfield (2005b), Active microbial sulfur disproportionation in the Mesoproterozoic, *Science*, *310*(5753), 1477–1479.

Johnston, D. T., J. Farquhar, and D. E. Canfield (2007), Sulfur isotope insights into microbial sulfate reduction: When microbes meet models, *Geochim. Cosmochim. Acta*, *71*(16), 3929–3947.

Johnston, D. T., B. C. Gill, A. Masterson, E. Beirne, K. L. Casciotti, A. N. Knapp, and W. Berelson (2014), Placing an upper limit on cryptic marine sulphur cycling, *Nature*, *513*(7519), 530–533.

Jørgensen, B.B. (1982), Mineralization of organic matter in the sea bed: The role of sulphate reduction, *Geochim. Cosmochim. Acta*, *106*, 161 – 183.

Kampschulte, A., and H. Strauss (2004), The sulfur isotopic evolution of Phanerozoic seawater based on the analysis of structurally substituted sulfate in carbonates, *Chem. Geol.*, *204*(3–4), 255–286.

Kurtz, A. C., L. R. Kump, M. A. Arthur, J. C. Zachos, and A. Paytan (2003), Early Cenozoic decoupling of the global carbon and sulfur cycles, *Paleoceanography*, *18*(4), 1090, doi:10.1029/2003PA000908.

Leavitt, W. D., I. Halevy, A. S. Bradley, and D. T. Johnston (2013), Influence of sulfate reduction rates on the Phanerozoic sulfur isotope record, *Proc. Natl. Acad. Sci. U.S.A.*, *110*, 11,244–11,249.

Li, X., W. P. Gilhooly, A. L. Zerkle, T. W. Lyons, J. Farquhar, J. P. Werne, R. Varela, and M. I. Scranton (2010), Stable sulfur isotopes in the water column of the Cariaco Basin, *Geochim. Cosmochim. Acta*, *74*(23), 6764–6778.

Lowenstein, T. K., M. N. Timofeeff, S. T. Brennan, L. A. Hardie, and R. V. Demicco (2001), Oscillations in Phanerozoic seawater chemistry: Evidence from fluid inclusions, *Science*, *294*(5544), 1086–1088.

Lowenstein, T. K., L. A. Hardie, M. N. Timofeeff, and R. V. Demicco (2003), Secular variation in seawater chemistry and the origin of calcium chloride basinal brines, *Geology*, *31*, 857–860.

Miller, M. F. (2002), Isotopic fractionation and the quantification of ^{17}O anomalies in the oxygen three isotope system: An appraisal and geochemical significance, *Geochim. Cosmochim. Acta*, *66*, 1881–1889.

Ono, S., B. Wing, D. Johnston, J. Farquhar, and D. Rumble (2006), Mass-dependent fractionation of quadruple stable sulfur isotope system as a new tracer of sulfur biogeochemical cycles, *Geochim. Cosmochim. Acta*, *70*(9), 2238–2252.

Ono, S., N. S. Keller, O. Rouxel, and J. C. Alt (2012), Sulfur-33 constraints on the origin of secondary pyrite in altered oceanic basement, *Geochim. Cosmochim. Acta*, *87*, 323–340.

Paytan, A., M. Kastner, D. Campbell, and M. H. Thiemens (1998), Sulfur isotopic composition of Cenozoic seawater sulfate, *Science*, *282*(5393), 1459 – 1462.

Paytan, A., M. Kastner, D. Campbell, and M. H. Thiemens (2004), Seawater sulfur isotope fluctuations in the Cretaceous, *Science*, *304*(5677), 1663 – 1665.

Petsch, S. T., and R. A. Berner (1998), Coupling the geochemical cycles of C, P, Fe, and S; the effect on atmospheric O_2 and the isotopic records of carbon and sulfur, *Am. J. Sci.*, *298*(3), 246–262.

Sim, M. S., S. Ono, and M. T. Hurtgen (2015), Sulfur isotope evidence for low and fluctuating sulfate levels in the Late Devonian ocean and the potential link with the mass extinction event, *Earth Planet. Sci. Lett.*, *419*, 52–62.

Tostevin, R., A. V. Turchyn, J. Farquhar, D. T. Johnston, D. L. Eldridge, J. K. B. Bishop, and M. McIlvin (2014), Multiple sulfur isotope constraints on the modern sulfur cycle, *Earth Planet. Sci. Lett.*, *396*, 14–21.

Turchyn, A. V., and D. P. Schrag (2004), Oxygen isotope constraints on the sulfur cycle over the past 10 million years, *Science*, *303*(5666), 2004 – 2007.

Turchyn, A. V., and D. P. Schrag (2006), Cenozoic evolution of the sulfur cycle: Insight from oxygen isotopes in marine sulfate, *Earth Planet. Sci. Lett.*, *241*(3–4), 763–779.

Wing, B. A., and I. Halevy (2014), Intracellular metabolite levels shape sulfur isotope fractionation during microbial sulfate respiration, *Proc. Natl. Acad. Sci. U.S.A.*, *111*, 18,116–18,125.

Wortmann, U. G., and B. M. Chernyavsky (2007), Effect of evaporite deposition on Early Cretaceous carbon and sulphur cycling, *Nature*, *446*(7136), 654–656.

Wortmann, U. G., and A. Paytan (2012), Rapid variability of seawater chemistry over the past 130 million years, *Science*, *337*(6092), 334–336.

Wu, N., J. Farquhar, H. Strauss, S. T. Kim, and D. E. Canfield (2010), Evaluating the S-isotope fractionation associated with Phanerozoic pyrite burial, *Geochim. Cosmochim. Acta*, *74*(7), 2053–2071.

Wu, N., J. Farquhar, and H. Strauss (2014), $\delta^{34}S$ and $\Delta^{33}S$ records of Paleozoic seawater sulfate based on the analysis of carbonate associated sulfate, *Geochim. Cosmochim. Acta*, *399*, 44–51.

Young, E. D., A. Galy, and H. Nagahara (2002), Kinetic and equilibrium mass-dependent isotope fractionation laws in nature and their geochemical and cosmochemical significance, *Geochim. Cosmochim. Acta*, *66*(6), 1095–1104.

Zerkle, A. L., J. Farquhar, D. T. Johnston, R. P. Cox, and D. E. Canfield (2009), Fractionation of multiple sulfur isotopes during phototrophic oxidation of sulfide and elemental sulfur by a green sulfur bacterium, *Geochim. Cosmochim. Acta*, *73*(2), 291–306.

CHAPTER 5

CONCLUSIONS AND FUTURE DIRECTIONS

The emerging field of multiple S isotope geochemistry has aimed to understand several questions in Earth history by providing a high precision analytical technique that (i) distinguishes between different sulfur metabolisms and (ii) provides a conservative tracer ($\Delta^{33}S$ and $\Delta^{36}S$ values) for tracking fluxes in the sulfur cycle at a variety of physical scales. To date, those results have corroborated those derived from $\delta^{34}S$ systematics, but they also provided additional analytical degrees of freedom that allow for finer scale resolution. This thesis originally aimed to place our newfound understanding of microbial physiology and metabolism into an environmental, specifically an early diagenetic context. The vast majority of sulfur cycling in the modern oxygenated oceans is confined to the organic-rich sediments of the continental margin. Though the nature of the *in situ* biogeochemical S cycle is complex, simplifying assumptions can be made, and those sediments can be treated as semi-enclosed diffusively supplied batch reactors. As such, the multiple S stable isotope signatures produced microbially can be quantitatively better understood when placed in a diagenetic reactive-transport context. The first two body chapters of this thesis (Chapters 2 and 3) explored the S cycle of modern sediments by building quantitative diagenetic models that reflect a more accurate C/S cycle, and reconcile the S isotope signatures observed in pore waters with those produced in laboratory calibrations. Chapter 4 revisits a historical seawater sulfate proxy record and places new constraints on the Cenozoic and Cretaceous S cycle within the limits allowed by $\Delta^{33}S_{SO4}$ and $\Delta^{36}S_{SO4}$ values. Finally, much of the work underpinning these calibrations was the development of methods for high precision minor S isotopes. Two key calibrations—the determination of the composition of international

standards and the characterization of modern seawater sulfate—are included in Appendix 1.Below I review the body chapters of this thesis and highlight the future directions that researchers in multiple S isotope geochemistry might endeavor to take.

In Chapter 2, we detailed the construction of a diagenetic model for the sediments of Alfonso Basin- an anoxic-silled basin of the California-Mexico margin. The model aimed to reproduce the pore water profiles of the major species [SO_4^{2-}], [CH_4], DIC, and [Ca^{2+}] with the expressed purpose of determining downcore changes in rates of both organoclastic sulfate reduction and anaerobic methane oxidation. Those bulk rates of sulfate consumption were then used as the backbone for constructing an isotope selective ([$^{32}SO_4^{2-}$], [$^{33}SO_4^{2-}$], and [$^{34}SO_4^{2-}$]) reactive transport model to which fractionation factors ($^{34}\alpha_{SR}$ and $^{33}\lambda_{SR}$) could be prescribed. As a first-order test of the rate-dependence of sulfate reduction (*e.g.,* Leavitt et al., 2013), we parameterized $^{34}\alpha_{SR}$ and $^{33}\lambda_{SR}$ directly as functions of rate—with a linear dependence and exponential dependence, in parallel to rate-independent values. Within the concentration ([SO_4^{2-}]) and isotope compositional ($\delta^{34}S_{SO4}$ and $\Delta^{33}S_{SO4}$) ranges, we found that no direct dependence of fractionation magnitude on rate is required to explain the values observed in pore water sulfate. Furthermore, a simple calculation demonstrated that, with the likely values expected for *in situ* specific rates of sulfate reduction, that the large, constant fractionation magnitude ($^{34}\varepsilon_{SR}$ ~70‰) required is within that expected from laboratory calculations. Put another way—the range in bulk rates of sulfate reduction observed in the model sediment profile are lower than the slowest rates observed for laboratory calibrations. Similarly, the $^{33}\lambda_{SR}$ that best describes the pore water profiles is near the thermodynamically predicted value for sulfate reduction, consistent with predictions from $^{34}\varepsilon_{SR}$. It is possible that the *in situ* fractionation magnitudes observed in most natural settings are larger than those observed experimentally because rates of sulfate reduction are substantially lower.

In Chapter 3, we extend our diagenetic model framework to include other S species important in S cycling of sedimentary systems, including SO_4^{2-}, H_2S, S^0, FeS, and FeS_2 for a model sediment system located in Aarhus Bay, Denmark. Similar to the model constructed for use in Chapter 2, this model expands the scope of the species considered to include active iron and sulfur oxidation

chemistry with the following reactions considered: sulfate reduction, anaerobic methane oxidation, chemical sulfide oxidation, sulfur disproportionation, iron sulfide precipitation, and pyrite formation. Though the reaction network is still far from complete, it describes a far more in-depth picture of Fe/S/C cycling as it appears in typical modern continental margin sediments. Analogous to chapter 2 as well, rates from the baseline geochemical model are also used to feed an isotope-specific (^{32}S, ^{33}S, and ^{34}S) RTM that aims to describe the pore water isotope signatures ($\delta^{34}S$ and $\Delta^{33}S$) observed. Given that a substantial portion of our understanding of the sulfur cycle is quantified using the pyrite $\delta^{34}S$ and $\Delta^{33}S$ proxy records (Canfield and Farquhar, 2009; Canfield et al., 2004; Strauss et al., 1999), understanding the linkage between microbially-produced multiple S isotope biosignatures and paired sulfate-pyrite values, reactive transport models that include such chemistry are critical to further disentangling the surface S cycle through such records. Consistent with the results of Chapter 2, the net fractionation factors extracted from this analysis suggest that sulfate reduction is characterized by very large $^{34}\varepsilon_{SR}$, again approaching the thermodynamic limit, and is apparently insensitive to rate at the SRR required to satisfy the Aarhus Bay pore water profiles, results that are also corroborated by $^{33}\lambda$ values, and their relationship to rate.

With a slightly different angle, Chapter 4 expands the scope of multiple S isotope studies from modern systems to a classic $\delta^{34}S$ marine barite record extracted from time-calibrated ocean drilling project (ODP) cores (*cf.* Paytan et al., 2004, Paytan et al., 1998). Marine barite, a proxy for seawater sulfate, is considered the most isotopically faithful representation of the composition of seawater sulfate, as it is precipitated directly from seawater. Other proxies, such as carbonate associated sulfate (CAS), rely on the structural incorporation of sulfate into another primary mineral (calcite and aragonite in that case) and are more susceptible to diagenetic alteration. The ~120 Ma $\delta^{34}S$ record from the two companion Paytan (1998 & 2004) studies has been used to reconstruct the Cretaceous and Cenozoic sulfur cycles using box modeling (Wortmann and Paytan, 2012; Halevy et al., 2012; Kurtz et al., 2003) and is key to quantifying the fluxes associated with major isotopic excursions in the composition of seawater sulfate. It is also the case that this $\delta^{34}S$ record reflects a

perplexing mass-balance problem for marine chemistry and alkalinity over the last 120 million years. Chapter 4 revisits this issue to provide $\Delta^{33}S$ and $\Delta^{36}S$ measurements from the same proxy record. Although the $\delta^{34}S$ values displays large excursions in the $\delta^{34}S$ values of seawater sulfate—ranging from 16-22‰ ($\delta^{34}S_{VCT}$), the $\Delta^{33}S$ and $\Delta^{36}S$ values over the same time frame exhibit a narrow distribution ($\Delta^{33}S = 0.043\pm0.016$‰ and $\Delta^{36}S = -0.39\pm0.15$‰). There is weak correlation with the $\delta^{34}S$ values throughout that interval, but a simple box model allows us to predict and place limits on the excursions allowed in $\Delta^{33}S$ and $\Delta^{36}S$ values from major perturbations to the sulfur cycle attributable to pyrite burial and evaporitic sulfate weathering. In essence, the minor sulfur isotope data do not uniquely diagnose the mechanism(s) underpinning the $\delta^{34}S$ change, however they do place limits on the mass fluxes that are allowable to explain the $\delta^{34}S$ excursions.

It is worth also elaborating upon the contributions within the appendices. These supplements reflect a substantial body of work, both in the development of multiple S isotope methods at Harvard University, and in their application to S cycling within the modern ocean. Appendix 1 catalogues the measurements of the isotope standards (IAEA-S-1, S-2, and S-3 and CDT), measured over two and a half years in the Laboratory for Stable Isotope Geobiology. The long term averages of those values ($\delta^{34}S$, $\Delta^{33}S$, and $\Delta^{36}S$) are shown alongside those generated in other labs actively measuring and reporting multiple S isotope data. This will serve as the calibration for all such measurements made in the Stable Isotope Geobiology Lab. Appendix 1 also demonstrates the characterization of the isotopic composition of seawater sulfate, an important value particularly for the diagenetic studies in this thesis. Those values for seawater sulfate were also corroborated by the measurements appearing in Appendix 3—a study aimed at quantifying the magnitude of the putative 'cryptic' sulfur cycling in oxygen minimum zones (*cf.* Canfield et al., 2010) through a careful isotopic evaluation of the $\delta^{18}O$, $\delta^{34}S$, and $\Delta^{33}S$ systematics of seawater extracted from ocean basin profiles from around the world. These sites include the Chilean margin, and the Namibian upwelling zone. This study was published as Johnston et al., (2014), and provides the most robust isotopic characterization of seawater sulfate to date.

In looking toward the future, we suggest several research directions that may benefit from the application of multiple S isotope techniques that range from studies in modern systems to those in deep time. Recent developments have pointed to the potential important of 'cryptic' sulfur cycling, both in oxygen minimum zones (OMZs) (Canfield et al., 2010) and *in situ* in sediments below the nominal sulfate depletion depth (Holmkvist et al., 2011). The latter carries important implications for our understanding of deep methane cycling, and the reactivity of deep buried ferric iron minerals. Although the concentrations of sulfate measured in this study, and purportedly that actively cycled, are low (~100 μmol/L), but new techniques using inductively coupled plasma mass spectrometry (ICP-MS) are being used to study S cycling down to such low concentrations (Crowe et al., 2014). Here, researchers are actively working to include ^{33}S measurements. Given the value that multiple S isotope measurements have in disentangling oxidative and reductive cycling, applying these new techniques to deep sedimentary systems seems a worthwhile enterprise.

A major research push in the S-isotope scientific community over the past twenty years has been to understand the contributions of oxidative sulfur cycling to the isotope records throughout geologic time. The temporal shift in the isotopic composition of preserved biogenic sulfides in the late Proterozoic was initially attributed to shifts in Earth's surface oxygenation, and requires the contributions of S metabolisms that oxidize and disproportionate sulfur and S intermediates (Canfield and Teske, 1996). The isotopic shifts in the sedimentary sulfide record (Canfield and Farquhar, 2009; Canfield, 2004) have continued to be interpreted in this light. More recent research highlights confounding interpretations that allow for the expression of large magnitude (>50‰) isotope fractionations that are possible from single step sulfate reduction demonstrated in laboratory and theoretical studies (Wing and Halevy, 2014; Leavitt et al., 2013; Sim et al., 2011) and environmentally (Crowe et al., 2014; Gomes and Hurtgen, 2013; Canfield et al., 2010). These studies do not require the presence of oxidative sulfur cycling to understand the magnitude of S isotope fractionations archived in biogenic sulfide records. They do not preclude the presence of disproportionation, but do not require it. The two diagenetic modeling studies in this thesis demonstrate that intrinsically large

(=70‰) S isotope fractionations associated with sulfate reduction are required to explain the pore water sulfate isotope values—both in $\delta^{34}S$ and $\Delta^{33}S$, without the need for oxidative sulfur cycling. This further complicates the necessity of oxidative cycling to amend geological $\delta^{34}S$ records. Mass-balance considerations certainly demonstrate that the large majority of biogenic sulfide produced in sediments escapes terminal burial as pyrite (Jørgensen, 1982), but it is not clear that that oxidative sulfur cycling leaves behind a substantial isotopic imprint. Further, the central conclusion from this thesis is that sulfate reduction generates an isotope effect in marine sediments that is near thermodynamic equilibrium at the derived sulfate reduction rates. This is corroborated via two environmentally distinct marine sediments. More quantitative diagenetic studies, like those performed in Chapters 2 and 3, will hopefully provide additional insights into the role of oxidative S cycling as it relates to S isotope proxy (barite and pyrite) records, and lay the groundwork for more quantitative approaches to studying the surface sulfur cycle in deep time.

REFERENCES

Canfield, D.E. (2004) The evolution of the Earth surface sulfur reservoir. *American Journal of Science* **304**, 839–861.

Canfield, D.E., and Teske, A. (1996) Late Proterozoic rise in atmospheric oxygen concentration inferred from phylogenetic and sulphur-isotope studies. *Nature* **382**, 127–132.

Canfield, D.E., and Farquhar, J. (2009) Animal evolution, bioturbation, and the sulfate concentration of the oceans. *Proceedings of the National Academy of Sciences* **106**, 8123–8127.

Canfield, D.E., Farquhar, J., and Zerkle, A.L. (2010) High isotope fractionations during sulfate reduction in a low-sulfate euxinic ocean analog. *Geology* **38**, 415–418.

Crowe, S.A., Paris, G., Katsev, S., Jones, C., Kim, S.T., Zerkle, A.L., Nomosatryo, S., Fowle, D.A., Adkins, J.F., Sessions, A.L., Farquhar, J., and Canfield, D.E. (2014) Sulfate was a trace constituent of Archean seawater. *Science* **346**, 735–739.

Gomes, M.L., and Hurtgen, M.T. (2013) Sulfur isotope systematics of a euxinic, low-sulfate lake: Evaluating the importance of the reservoir effect in modern and ancient oceans. *Geology* **41**, 663–666.

Halevy, I., Peters, S.E., and Fischer, W.W. (2012) Sulfate burial constraints on the Phanerozoic sulfur cycle. *Science* **337**, 331–334.

Holmkvist, L., Ferdelman, T.G., and Jørgensen, B.B. (2011) A cryptic sulfur cycle driven by iron in the methane zone of marine sediment (Aarhus Bay, Denmark). *Geochimica et Cosmochimica*

Acta **75**, 3581–3599.

Johnston, D.T., Gill, B.C., Masterson, A., Beirne, E., Casciotti, K.L., Knapp, A.N., and Berelson, W. (2014) Placing an upper limit on cryptic marine sulphur cycling. *Nature* **513**, 530–533.

Jørgensen, B.B. (1982) Mineralization of organic matter in the sea bed—the role of sulphate reduction. *Nature.*

Kurtz, A.C., Kump, L.R., Arthur, M.A., Zachos, J.C., and Paytan, A. (2003) Early Cenozoic decoupling of the global carbon and sulfur cycles: Paleogene C and S cycles. *Paleoceanography* **18**.

Leavitt, W.D., Halevy, I., Bradley, A.S., and Johnston, D.T. (2013) Influence of sulfate reduction rates on the Phanerozoic sulfur isotope record. *Proc Natl Acad Sci USA* **110**, 11244–11249.

Paytan, A., Kastner, M., Campbell D., Thiemens, MH (1998) Sulfur Isotopic Composition of Cenozoic Seawater Sulfate. *Science* **282**, 1459–1462.

Paytan, A., Kastner, M., Campbell, D., and Thiemens, M.H. (2004) Seawater sulfur isotope fluctuations in the Cretaceous. *Science* **304**, 1663–1665.

Sim, M.S., Bosak, T., and Ono, S. (2011) Large sulfur isotope fractionation does not require disproportionation. *Science* **333**, 74–77.

Strauss, H. (1999) Geological evolution from isotope proxy signals—sulfur. *Chemical Geology* **161**, 89–101.

Wing, B.A., and Halevy, I. (2014) Intracellular metabolite levels shape sulfur isotope fractionation during microbial sulfate respiration. *Proc Natl Acad Sci U S A* **111**, 18116–18125.

Wortmann, U.G., and Paytan, A. (2012) Rapid variability of seawater chemistry over the past 130 million years. *Science* **337**, 334–336.

APPENDIX A1

CALIBRATION OF MULTIPLE SULFUR ISOTOPE STANDARDS AT HARVARD UNIVERSITY

Several research labs regularly employ multiple sulfur isotope methodologies (University of Maryland, College Park, (UMd), the Geophysical Labs at the Carnegie Institute of Washington, (GL), University of California, San Diego, (UCSD), the Massachusetts Institute of Technology (MIT) and Harvard University (HU). To facilitate the inter-laboratory comparison of these measurements, the standard data, by analysts ALM and ECB, extracted over approximately three years, are included here. The IAEA international standards measured by fluorination (S-1, S-2, S-3), Cañon Diablo Troilite (CDT), and seawater sulfate samples, reductively converted (*cf.* Forrest and Newman, 1977) to Ag_2S are tabulated below. The latter samples, abbreviated SW-SO_4, have been published as a part of a broader study (Johnston et al., 2014), but are not 'true' standards. Due to the isotopic homogeneity of seawater sulfate (Rees et al., 1978), however, we assume that the sulfate in these samples is isotopically analogous to that extracted to form the 'true' seawater sulfate standard, NBS-127 (*cf.* Halas and Szaran, 2001).

For simplicity, the data are tabulated separately below, including IAEA-S-1 (Table A1.1), S-2 (Table A1.2), S-3 (Table A1.3), CDT measurements made at Harvard (Table A1.4), and measurements of SW-SO_4 (Table A1.5). Subsequent tables demonstrate the inter-laboratory comparison of IAEA measurements on the S-1 reference frame (Table A1.6), the calibration of V-CDT at Harvard University (Table A1.7) and the comparison of that calibration to other labs that employ SF_6 measurements (Table A1.8). Lastly, the multiple S isotopic composition of SW-SO_4 on the V-CDT reference frame is determined using the long-term measurements of IAEA-S-1 at Harvard, in concert with the $\Delta^{33}S$ and $\Delta^{36}S$ values derived from CDT measurements (Table A1.9). The values derived for SW-SO_4 of $\delta^{34}S$ = 21.34±0.30‰, $\Delta^{33}S$ = 0.049±0.006‰, and $\Delta^{36}S$ = -0.42±0.15‰ agree well with recent reports (Tostevin et al., 2014).

Table A1.1: Standard measurements of IAEA-S-1 at Harvard University versus 'HAR-1' SF_6

Analysis #	Standard	$\delta^{33}S$ (‰)	$\delta^{34}S$ (‰)	$\delta^{36}S$ (‰)	$\Delta^{33}S$ (‰)	$\Delta^{36}S$ (‰)
SF-484	IAEA-S-1	-8.309	-16.232	-31.72	0.083	-1.11
SF-545	IAEA-S-1	-8.239	-16.116	-31.70	0.093	-1.30
SF-577	IAEA-S-1	-8.090	-15.824	-31.29	0.091	-1.44
SF-615	IAEA-S-1	-8.247	-16.123	-31.73	0.089	-1.32
SF-657	IAEA-S-1	-8.219	-16.068	-31.65	0.089	-1.34
SF-658	IAEA-S-1	-8.186	-16.000	-31.28	0.087	-1.10
SF-659	IAEA-S-1	-8.204	-16.028	-31.52	0.083	-1.28
SF-660	IAEA-S-1	-8.240	-16.100	-31.49	0.085	-1.12
SF-859	IAEA-S-1	-8.155	-15.944	-31.83	0.088	-1.75
SF-863	IAEA-S-1	-8.103	-15.849	-31.72	0.091	-1.82
SF-882	IAEA-S-1	-8.271	-16.176	-32.33	0.093	-1.82
SF-893	IAEA-S-1	-8.074	-15.786	-31.57	0.087	-1.79
SF-943	IAEA-S-1	-8.188	-16.011	-32.08	0.090	-1.88
SF-948	IAEA-S-1	-8.222	-16.090	-31.92	0.097	-1.57
SF-956	IAEA-S-1	-8.155	-15.948	-31.95	0.090	-1.87
SF-980	IAEA-S-1	-8.213	-16.055	-31.92	0.088	-1.64
SF-996	IAEA-S-1	-8.159	-15.943	-31.91	0.083	-1.83
SF-1005	IAEA-S-1	-8.099	-15.838	-31.71	0.090	-1.83
SF-1023	IAEA-S-1	-8.006	-15.659	-31.29	0.090	-1.75
SF-1029	IAEA-S-1	-8.235	-16.099	-32.23	0.089	-1.86
SF-1053	IAEA-S-1	-8.159	-15.956	-31.86	0.090	-1.77
SF-1058	IAEA-S-1	-8.150	-15.943	-31.75	0.093	-1.68
SF-1068	IAEA-S-1	-8.232	-16.095	-31.92	0.089	-1.56
SF-1079	IAEA-S-1	-8.213	-16.077	-32.08	0.100	-1.75
SF-1080	IAEA-S-1	-8.319	-16.290	-32.53	0.104	-1.80
SF-1083	IAEA-S-1	-8.174	-15.999	-31.84	0.098	-1.66
SF-1084	IAEA-S-1	-8.317	-16.267	-32.07	0.094	-1.39
SF-1088	IAEA-S-1	-8.288	-16.216	-32.36	0.097	-1.77
SF-1089	IAEA-S-1	-8.260	-16.164	-32.32	0.098	-1.84
SF-1140	IAEA-S-1	-8.113	-15.846	-31.64	0.079	-1.75
SF-1144	IAEA-S-1	-8.299	-16.218	-32.37	0.086	-1.78
SF-1156	IAEA-S-1	-8.259	-16.139	-32.31	0.086	-1.87
SF-1183	IAEA-S-1	-8.339	-16.299	-32.54	0.089	-1.80
SF-1253	IAEA-S-1	-8.333	-16.297	-32.59	0.094	-1.86
SF-1297	IAEA-S-1	-8.134	-15.914	-31.90	0.093	-1.88
SF-1334	IAEA-S-1	-8.143	-15.928	-31.81	0.092	-1.77
SF-1358	IAEA-S-1	-8.172	-15.972	-32.00	0.086	-1.87
SF-1491	IAEA-S-1	-8.223	-16.077	-31.68	0.090	-1.35
SF-1501	IAEA-S-1	-8.171	-15.982	-31.77	0.092	-1.62
SF-1518	IAEA-S-1	-8.161	-15.943	-31.85	0.081	-1.78
SF-1561	IAEA-S-1	-8.489	-16.584	-32.53	0.086	-1.25
SF-1587	IAEA-S-1	-8.201	-16.014	-31.68	0.078	-1.48
SF-1596	IAEA-S-1	-8.170	-15.974	-32.02	0.089	-1.89
SF-1653	IAEA-S-1	-8.184	-16.009	-32.07	0.093	-1.87
SF-1660	IAEA-S-1	-8.154	-15.945	-31.90	0.090	-1.83
SF-1665	IAEA-S-1	-8.014	-15.673	-31.03	0.089	-1.46
SF-1687	IAEA-S-1	-7.941	-15.544	-30.57	0.095	-1.24
SF-1692	IAEA-S-1	-8.029	-15.712	-31.06	0.094	-1.42
SF-1692	IAEA-S-1	-8.029	-15.712	-31.06	0.094	-1.42

Table A1.1 (*continued)*

Analysis #	Standard	$\delta^{33}S$ (‰)	$\delta^{34}S$ (‰)	$\delta^{36}S$ (‰)	$\Delta^{33}S$ (‰)	$\Delta^{36}S$ (‰)
SF-1701	IAEA-S-1	-8.018	-15.683	-30.96	0.090	-1.37
SF-1702	IAEA-S-1	-7.968	-15.591	-30.80	0.092	-1.39
SF-1704	IAEA-S-1	-7.954	-15.560	-30.88	0.090	-1.52
SF-1706	IAEA-S-1	-7.929	-15.526	-30.72	0.098	-1.43
SF-1764	IAEA-S-1	-7.955	-15.563	-30.91	0.090	-1.54
SF-1766	IAEA-S-1	-8.063	-15.776	-31.16	0.093	-1.40
SF-1782	IAEA-S-1	-8.091	-15.838	-31.34	0.097	-1.46
SF-1802	IAEA-S-1	-8.068	-15.758	-31.28	0.079	-1.55
SF-1822	IAEA-S-1	-7.994	-15.645	-31.03	0.094	-1.51
SF-1840	IAEA-S-1	-8.042	-15.732	-31.24	0.091	-1.56
SF-1844	IAEA-S-1	-7.984	-15.617	-31.07	0.090	-1.61
SF-1846	IAEA-S-1	-7.983	-15.610	-31.05	0.087	-1.60
SF-2064	IAEA-S-1	-8.014	-15.682	-31.39	0.093	-1.81
SF-2069	IAEA-S-1	-8.036	-15.710	-30.88	0.079	-1.28
SF-2105	IAEA-S-1	-8.050	-15.745	-31.56	0.090	-1.85
SF-2114	IAEA-S-1	-8.019	-15.688	-31.06	0.092	-1.46
SF-2126	IAEA-S-1	-7.996	-15.641	-31.32	0.089	-1.81
SF-2144	IAEA-S-1	-8.053	-15.753	-31.41	0.091	-1.69
SF-2150	IAEA-S-1	-8.018	-15.688	-31.40	0.093	-1.80
SF-2166	IAEA-S-1	-7.994	-15.627	-31.33	0.085	-1.85
SF-2168	IAEA-S-1	-7.996	-15.635	-31.32	0.087	-1.82
Average (σ)	**IAEA-S-1**	**-8.14 (0.12)**	**-15.91 (0.23)**	**-31.6 (0.5)**	**0.090(0.005)**	**-1.62 (0.23)**

Table A1.2: Standard measurements of IAEA-S-2 at Harvard University versus 'HAR-1' SF_6

Analysis #	Standard	$\delta^{33}S$ (‰)	$\delta^{34}S$ (‰)	$\delta^{36}S$ (‰)	$\Delta^{33}S$ (‰)	$\Delta^{36}S$ (‰)
SF-493	IAEA-S-2	3.046	5.853	9.50	0.036	-1.65
SF-500	IAEA-S-2	3.196	6.160	10.17	0.028	-1.57
SF-524	IAEA-S-2	3.171	6.098	9.99	0.035	-1.63
SF-563	IAEA-S-2	3.325	6.401	11.66	0.033	-0.53
SF-625	IAEA-S-2	3.159	6.077	10.23	0.034	-1.35
SF-691	IAEA-S-2	3.054	5.876	10.88	0.032	-0.32
SF-778	IAEA-S-2	3.204	6.171	10.84	0.031	-0.92
SF-873	IAEA-S-2	3.240	6.240	10.46	0.031	-1.43
SF-950	IAEA-S-2	3.203	6.166	10.40	0.033	-1.35
SF-961	IAEA-S-2	3.170	6.094	9.99	0.036	-1.62
SF-973	IAEA-S-2	3.221	6.207	10.66	0.029	-1.17
SF-993	IAEA-S-2	3.254	6.254	10.26	0.038	-1.65
SF-1001	IAEA-S-2	3.270	6.289	10.36	0.036	-1.62
SF-1021	IAEA-S-2	3.284	6.334	10.68	0.027	-1.39
SF-1038	IAEA-S-2	3.321	6.398	10.59	0.031	-1.60
SF-1044	IAEA-S-2	3.263	6.289	10.42	0.029	-1.56
SF-1061	IAEA-S-2	2.978	5.734	9.43	0.030	-1.49
SF-1072	IAEA-S-2	3.254	6.267	10.33	0.032	-1.61
SF-1086	IAEA-S-2	3.104	5.961	9.81	0.039	-1.55
SF-1091	IAEA-S-2	3.057	5.861	9.52	0.043	-1.65
SF-1096	IAEA-S-2	2.926	5.596	8.95	0.048	-1.71
SF-1133	IAEA-S-2	3.213	6.178	10.33	0.036	-1.44
SF-1142	IAEA-S-2	3.156	6.082	10.16	0.028	-1.43
SF-1187	IAEA-S-2	3.140	6.049	10.08	0.030	-1.44
SF-1230	IAEA-S-2	3.039	5.852	9.56	0.029	-1.59
SF-1295	IAEA-S-2	3.227	6.228	11.19	0.024	-0.68
SF-1300	IAEA-S-2	3.300	6.356	10.40	0.032	-1.71
SF-1503	IAEA-S-2	3.105	5.997	10.01	0.021	-1.41
SF-1513	IAEA-S-2	3.208	6.181	10.18	0.029	-1.60
SF-1576	IAEA-S-2	3.166	6.099	10.14	0.030	-1.48
SF-1588	IAEA-S-2	3.458	6.651	10.94	0.038	-1.74
SF-1606	IAEA-S-2	3.235	6.228	10.29	0.032	-1.58
SF-1639	IAEA-S-2	3.411	6.574	11.31	0.031	-1.22
SF-1662	IAEA-S-2	3.207	6.164	10.13	0.037	-1.61
SF-1665	IAEA-S-2	3.290	6.335	11.48	0.033	-0.59
SF-1666	IAEA-S-2	3.277	6.301	11.49	0.037	-0.52
SF-1703	IAEA-S-2	3.414	6.564	11.25	0.039	-1.25
SF-1705	IAEA-S-2	3.458	6.644	11.32	0.042	-1.34
SF-1765	IAEA-S-2	3.398	6.537	11.27	0.037	-1.19
SF-1767	IAEA-S-2	3.354	6.470	10.95	0.027	-1.38
SF-1792	IAEA-S-2	3.223	6.204	10.46	0.033	-1.36
SF-1826	IAEA-S-2	3.380	6.507	11.27	0.034	-1.13
SF-1845	IAEA-S-2	3.511	6.734	11.40	0.049	-1.43
SF-1847	IAEA-S-2	3.255	6.233	10.54	0.050	-1.33
Average (σ)	**IAEA-S-2**	**3.23 (0.13)**	**6.22 (0.25)**	**10.5 (0.6)**	**0.034 (0.006)**	**-1.34 (0.36)**

Table A1.3: Standard measurements of IAEA-S-3 at Harvard University versus 'HAR-1' SF_6

Analysis #	Standard	$\delta^{33}S$ (‰)	$\delta^{34}S$ (‰)	$\delta^{36}S$ (‰)	$\Delta^{33}S$ (‰)	$\Delta^{36}S$ (‰)
SF-951	IAEA-S-3	-24.782	-47.692	-90.11	0.070	-1.44
SF-1082	IAEA-S-3	-24.847	-47.843	-90.25	0.085	-1.31
SF-1087	IAEA-S-3	-24.914	-47.947	-90.62	0.073	-1.49
SF-1092	IAEA-S-3	-24.846	-47.824	-90.47	0.076	-1.56
SF-1141	IAEA-S-3	-24.459	-47.089	-88.97	0.076	-1.40
SF-1504	IAEA-S-3	-24.827	-47.780	-90.09	0.072	-1.26
SF-1565	IAEA-S-3	-24.737	-47.605	-89.84	0.069	-1.33
SF-1649	IAEA-S-3	-24.391	-46.932	-88.70	0.060	-1.42
SF-1661	IAEA-S-3	-24.291	-46.743	-88.38	0.061	-1.44
SF-1664	IAEA-S-3	-24.599	-47.365	-88.87	0.081	-0.79
SF-1768	IAEA-S-3	-24.589	-47.327	-89.03	0.071	-1.02
SF-1770	IAEA-S-3	-24.589	-47.340	-89.08	0.078	-1.06
SF-2048	IAEA-S-3	-24.606	-47.350	-89.34	0.066	-1.30
SF-2058	IAEA-S-3	-24.652	-47.448	-89.58	0.072	-1.36
SF-2167	IAEA-S-3	-24.600	-47.347	-89.92	0.070	-1.88
SF-2169	IAEA-S-3	-24.573	-47.307	-89.71	0.077	-1.74
SF-2170	IAEA-S-3	-24.610	-47.358	-89.93	0.067	-1.87
SF-2181	IAEA-S-3	-24.589	-47.310	-89.66	0.062	-1.68
SF-2188	IAEA-S-3	-24.534	-47.239	-89.59	0.079	-1.75
Average (σ)	**IAEA-S-3**	**-24.63(0.16)**	**-47.41(0.31)**	**-89.6 (0.6)**	**0.072 (0.007)**	**-1.43 (0.29)**

Table A1.4: Standard measurements of CDT[a], versus 'HAR-1' SF_6 at Harvard University

Analysis #[b]	Standard	$\delta^{33}S$ (‰)	$\delta^{34}S$ (‰)	$\delta^{36}S$ (‰)	$\Delta^{33}S$ (‰)	$\Delta^{36}S$ (‰)
SF-1090	CDT (07)	-7.918	-15.265	-29.679	-0.027	-0.875
SF-1090	CDT (07)	-7.908	-15.262	-29.765	-0.019	-0.966
SF-1090	CDT (07)	-7.906	-15.268	-29.723	-0.014	-0.913
SF-1090	CDT (07)	-7.928	-15.280	-29.768	-0.029	-0.936
SF-1090	CDT (07)	-7.907	-15.278	-29.712	-0.009	-0.883
SF-1090	CDT (07)	-7.921	-15.277	-29.743	-0.024	-0.916
SF-1090	CDT (07)	-7.911	-15.279	-29.753	-0.013	-0.923
SF-1090	CDT (07)	-7.918	-15.265	-29.679	-0.027	-0.875
SF-1090	CDT (07)	-7.908	-15.262	-29.765	-0.019	-0.966
SF-1090	CDT (07)	-7.906	-15.268	-29.723	-0.014	-0.913
SF-1090	CDT (07)	-7.928	-15.280	-29.768	-0.029	-0.936
SF-1090	CDT (07)	-7.907	-15.278	-29.712	-0.009	-0.883
SF-1090	CDT (07)	-7.921	-15.277	-29.743	-0.024	-0.916
SF-1090	CDT (07)	-7.911	-15.279	-29.753	-0.013	-0.923
Average	**CDT (07)**	**-7.914**	**-15.273**	**-29.735**	**-0.019**	**-0.916**
(s)		**(0.008)**	**(0.007)**	**(0.032)**	**(0.008)**	**(0.031)**
SF-1094	CDT (07)	-8.155	-15.757	-30.820	-0.009	-1.094
SF-1094	CDT (07)	-8.145	-15.753	-30.743	-0.001	-1.025
SF-1094	CDT (07)	-8.156	-15.746	-30.648	-0.016	-0.943
SF-1094	CDT (07)	-8.155	-15.742	-30.766	-0.017	-1.068
SF-1094	CDT (07)	-8.149	-15.739	-30.764	-0.012	-1.072
SF-1094	CDT (07)	-8.147	-15.737	-30.720	-0.011	-1.032
SF-1094	CDT (07)	-8.148	-15.740	-30.711	-0.011	-1.017
Average	**CDT (07)**	**-8.151**	**-15.745**	**-30.739**	**-0.011**	**-1.036**
(s)		**(0.004)**	**(0.008)**	**(0.054)**	**(0.005)**	**(0.050)**

[a] CDT is shorthand for Cañon Diablo Troilite, an iron sulfide phase, extracted from Canyon Diablo Meteorite. It is a mineral that approximately shares the same S isotopic composition as the bulk Earth (e.g., Hulston and Thode, 1965). Subsequent studies demonstrated the isotopic heterogeneity in CDT sample splits, both in ^{34}S-abundance (Beaudoin et al. 1994) and that in minor isotope values $\Delta^{33}S$ and $\Delta^{36}S$ (Ono et al., 2006; Wing et al., 2015). By declaration, Vienna-CDT (V-CDT) is defined by the 'homogenous' Ag_2S standard IAEA-S-1, with a value defined as $\delta^{34}S = -0.3‰$ exactly (Coplen et al., 2002). Since CDT is heterogeneous in its isotope composition, this table serves only as reference frame to calibrate CDT measurements versus those made in, and reported by, other labs making SF_6 measurements (UMD, UCSD, GL, MIT). See Table A1.6.

[b] Contrasting with other tables in Appendix A1, this table reports individual measurement acquisitions of CDT (07), due to the importance of the measurement, and rarity of the remaining CDT standard. Averages are those of individual samples, and σ refers to the instrument error rather than total measurement (including preparation and extraction) error as in the other tables. The label (07) refers to the year the sample was converted from FeS to Ag_2S (2007), by Sang-Tae Kim, and packaged and distributed to other labs for analysis.

Table A1.5: Measurements of seawater sulfate ($SW\text{-}SO_4$)[a] versus 'HAR-1' at Harvard University

Analysis #[b]	Standard	$\delta^{33}S$ (‰)	$\delta^{34}S$ (‰)	$\delta^{36}S$ (‰)	$\Delta^{33}S$ (‰)	$\Delta^{36}S$ (‰)
SF-459	B1-11	2.694	5.163	8.781	0.038	-1.052
SF-465	P1-01	2.712	5.214	8.768	0.031	-1.162
SF-466	P1-03	2.675	5.126	8.065	0.038	-1.697
SF-468	P1-06	2.738	5.256	8.691	0.035	-1.319
SF-470	P1-07	2.555	4.900	8.051	0.034	-1.279
SF-475	P1-11	2.819	5.421	9.179	0.031	-1.146
SF-476	P1-13	2.839	5.463	9.178	0.029	-1.226
SF-477	P1-12	2.748	5.283	8.919	0.031	-1.143
SF-479	G1-04	2.536	4.855	8.260	0.038	-0.985
SF-481	G1-03	2.652	5.079	8.515	0.039	-1.158
SF-482	G1-06	2.649	5.068	8.079	0.042	-1.572
SF-483	G1-05	2.658	5.100	8.222	0.035	-1.491
SF-485	G1-07	2.919	5.626	9.179	0.025	-1.538
SF-486	G1-09	2.689	5.137	8.278	0.046	-1.505
SF-488	G1-10	2.857	5.493	9.079	0.032	-1.383
SF-489	G1-14	2.899	5.560	9.099	0.039	-1.491
SF-491	G1-12	2.900	5.540	9.602	0.051	-0.951
SF-492	G1-13	2.914	5.589	9.233	0.039	-1.412
SF-920	B1-01	2.786	5.347	8.671	0.036	-1.512
SF-921	B1-18	2.805	5.380	8.771	0.038	-1.476
SF-922	B1-02	2.751	5.274	8.578	0.038	-1.467
SF-923	B1-08	2.536	4.864	7.776	0.034	-1.486
SF-924	B1-07	3.104	5.991	10.007	0.023	-1.407
SF-927	B1-20	2.745	5.289	8.753	0.025	-1.320
SF-929	B1-22	2.826	5.436	9.214	0.030	-1.140
SF-1039	G2-11	2.798	5.371	8.623	0.035	-1.606
SF-1040	G2-01	2.918	5.617	9.202	0.029	-1.498
SF-1041	G2-08	2.549	4.890	7.870	0.034	-1.442
SF-1042	G2-04	2.576	4.942	7.943	0.034	-1.467
SF-1043	G2-12	2.897	5.577	9.083	0.029	-1.541
SF-1045	G2-16	2.646	5.077	8.182	0.035	-1.486
SF-1046	G2-23	2.950	5.671	9.315	0.033	-1.487
SF-1056	P1-15	3.017	5.801	9.431	0.033	-1.620
SF-1057	P1-17	2.927	5.632	9.086	0.031	-1.641
SF-1060	P1-18	2.902	5.578	9.136	0.033	-1.490
SF-1064	G2-02	2.877	5.527	8.963	0.034	-1.565
SF-1065	G2-06	3.168	6.104	10.140	0.029	-1.490
SF-1066	G2-03	3.063	5.902	9.804	0.028	-1.440
SF-1067	G2-05	2.972	5.727	9.549	0.027	-1.359
SF-1071	G2-09	3.031	5.830	9.545	0.033	-1.562
SF-1073	G2-10	2.791	5.395	8.997	0.016	-1.279
Average (σ)	**$SW\text{-}SO_4$**	**2.81 (0.16)**	**5.39 (0.32)**	**8.87 (0.60)**	**0.033 (0.006)**	**-1.39 (0.18)**

[a] Seawater sulfate (~28 mM) is the largest S reservoir on Earth. The long residence time of SO_4 (>10 Myr) compared with the circulation time of the oceans (~10^3 yrs) indicates that $SW\text{-}SO_4$ is isotopically homogeneous (Rees et al., 1978).

[b] The samples reported here were sampled on (Cruise, Name, Number), stored as $BaSO_4$ and were measured and reported in Johnston et al. (2014), with the analytical aid of Erin Beirne. $BaSO_4$ samples were subjected to reduction chemistry prior to analysis, contributing to total error.

Table A1.6: Inter-laboratory comparison of IAEA std measurements, on IAEA-S-1 reference frame[a,b]

Standard	$\delta^{33}S$ (‰)	$\delta^{34}S$ (‰)	$\delta^{36}S$ (‰)	$\Delta^{33}S$ (‰)	$\Delta^{36}S$ (‰)
UMd					
IAEA-S-1	0.00 (0.03)	0.00 (0.05)	0.0 (0.1)	0.000 (0.006)	0.0 (0.1)
IAEA-S-2	11.56 (0.04)	22.67 (0.08)	44.4 (0.2)	-0.054 (0.006)	0.9 (0.2)
IAEA-S-3	-16.74 (0.03)	-32.30 (0.07)	-60.7 (0.3)	-0.020 (0.007)	-0.4 (0.3)
GL					
IAEA-S-1	0.00 (0.25)	0.00 (0.49)	0.0 (0.9)	0.000 (0.003)	0.0 (0.1)
IAEA-S-2	11.66 (0.19)	22.86 (0.29)	44.4 (0.2)	-0.054 (0.006)	0.9 (0.2)
IAEA-S-3	-16.35 (0.25)	-31.47 (0.47)	-59.4 (0.7)	-0.015 (0.004)	-0.5 (0.3)
MIT					
IAEA-S-1	-	0.00 (0.26)	-	0.000 (0.007)	0.0 (0.1)
IAEA-S-2	-	22.54 (0.26)	-	-0.058 (0.005)	0.43 (0.05)
IAEA-S-3	-	-32.29 (0.26)	-	-0.017 (0.005)	-0.06 (0.05)
Harvard					
IAEA-S-1	**0.00 (0.12)**	**0.00 (0.23)**	**0.0 (0.5)**	**0.000 (0.005)**	**0.0 (0.2)**
IAEA-S-2	**11.46 (0.13)**	**22.48 (0.25)**	**43.5 (0.6)**	**-0.056 (0.006)**	**0.3 (0.4)**
IAEA-S-3	**-16.63 (0.16)**	**-32.01 (0.31)**	**-59.9 (0.6)**	**-0.018 (0.007)**	**0.1 (0.3)**

[a] Given the heterogeneity of CDT, we adopt the convention of Wing et al. (2015), and report the measurements of S-2 and S-3 on the S-1 reference frame to facilitate comparison. By definition, the values for IAEA-S-1 are $\delta^{33}S = \delta^{34}S = \delta^{36}S = 0.000‰$, as well as $\Delta^{33}S = \Delta^{36}S = 0.0‰$, and S-2 and S-3 are placed upon that reference frame.

[b] These data (UMd, GL, and MIT) were compiled and tabulated elsewhere in Wing et al. (2015), see Table 1. The analytical error in parentheses (σ) refers to the long-term measurement error of that standard in the individual lab.

Table A1.7: Sulfur isotopic composition of CDT and concurrent IAEA-S-1 measurements, measured versus 'HAR-1' at Harvard University[a]

Analysis #	Standard	$\delta^{33}S$ (‰)	$\delta^{34}S$ (‰)	$\delta^{36}S$ (‰)	$\Delta^{33}S$ (‰)	$\Delta^{36}S$ (‰)
SF-1079	IAEA-S-1	-8.213	-16.077	-32.079	0.0998	-1.75
SF-1080	IAEA-S-1	-8.319	-16.290	-32.528	0.1041	-1.80
SF-1083	IAEA-S-1	-8.174	-15.999	-31.839	0.0981	-1.66
SF-1084	IAEA-S-1	-8.317	-16.267	-32.074	0.0945	-1.39
SF-1088	IAEA-S-1	-8.288	-16.216	-32.355	0.0968	-1.77
SF-1089	IAEA-S-1	-8.260	-16.164	-32.325	0.0978	-1.84
SF-1093	IAEA-S-1	-8.282	-16.212	-32.379	0.1006	-1.80
SF-1095	IAEA-S-1	-8.206	-16.054	-32.188	0.0942	-1.91
Average (σ)	**IAEA-S-1**	**-8.257 (0.054)**	**-16.160 (0.106)**	**-32.221 (0.219)**	**0.0982 (0.0033)**	**-1.74 (0.16)**
SF-1090	CDT (07)	-7.914	-15.273	-29.735	-0.0193	-0.92
SF-1094	CDT (07)	-8.151	-15.745	-30.739	-0.0109	-1.04
Average (σ)	**CDT (07)**	**-8.032 (0.167)**	**-15.509 (0.334)**	**-30.237 (0.710)**	**-0.0151 (0.0060)**	**-0.98 (0.08)**

[a]To avoid long-term analytical artifacts, these samples were all measured concurrently, over the course of four days. The average composition of the IAEA-S-1 standards measured here deviates from the long-term averages by ($\delta^{34}S$ = -0.254‰, $\Delta^{33}S$ = 0.0082‰, and $\Delta^{36}S$ = -0.12‰), which are within the range of long-term reproducibility (1σ = 0.23‰, 0.005‰, and 0.23‰, respectively).

Table A1.8: Sulfur isotopic compositions ($\Delta^{33}S$ and $\Delta^{36}S$ values) of IAEA-S-1[a]

Laboratory	$\Delta^{33}S$ (‰)	σ-$\Delta^{33}S$ (‰)	$\Delta^{36}S$ (‰)	σ-$\Delta^{36}S$ (‰)
UCSD	0.0991	0.0085	-0.49	0.13
GL	0.1039	0.0087	-0.79	0.14
UMd	0.0858	0.0063	-0.85	0.20
HU	0.1133	0.0060	-0.76	0.16
	Weighted mean	SE on mean	Weighted mean	SE on mean
	0.1005	**0.0074**	**-0.7225**	**0.16**

[a] This table is extracted and modified from Wing et al. (2015), Table 3, with sources cited therein.

Table A1.9: Derivation of the sulfur isotopic composition of SW-SO_4

Standard	$\delta^{34}S$ (‰)	$\sigma-\delta^{34}S$ (‰)	$\Delta^{33}S$ (‰)	$\sigma-\Delta^{33}S$ (‰)	$\Delta^{36}S$ (‰)	$\sigma-\Delta^{36}S$ (‰)
Average versus HAR-1						
SW-SO_4	5.393	0.315	0.0335	0.006	-1.40	0.18
Average versus HAR-1						
IAEA-S-1	-15.911	0.229	0.0900	0.0047	-1.62	0.23
HAR-1 versus V-CDT[a]						
HAR-01	-15.615	-	-0.0151	0.0074	-0.98	0.16
SW-SO_4 versus V-CDT						
SW-SO_4	21.34	-	0.0486	-	-0.42	-

REFERENCES

Beaudoin, G., Taylor, B.E., Rumble, D.I.I.I., and Thiemens, M. (1994) Variations in the sulfur isotope composition of troilite from the Canon Diablo iron meteorite. *Geochimica et Cosmochimica Acta* **58**, 4253–4255.

Coplen, T.B., Hopple, J.A., Boehike, J.K., Peiser, H.S., and Rieder, S.E. (2002) Compilation of minimum and maximum isotope ratios of selected elements in naturally occurring terrestrial materials and reagents.

Forrest, J., and Newman, L. (1977) Silver-110 microgram sulfate analysis for the short time resolution of ambient levels of sulfur aerosol. *Analytical Chemistry* **49**, 1579–1584.

Johnston, D.T., Gill, B.C., Masterson, A., Beirne, E., Casciotti, K.L., Knapp, A.N., and Berelson, W. (2014) Placing an upper limit on cryptic marine sulphur cycling. *Nature* **513**, 530–533.

Halas, S., and Szaran, J. (2001) Improved thermal decomposition of sulfates to SO2 and mass spectrometric determination of d34S of IAEA SO-5, IAEA SO-6 and NBS-127 sulfate standards. *Rapid Commun. Mass Spectrom.* **15**, 1618–1620.

Hulston, J.R., and Thode, H.G. (1965) Variations in the S33, S34, and S36 contents of meteorites and their relation to chemical and nuclear effects. *Journal of Geophysical Research* **70**, 3475–3484.

Ono, S., Wing, B., Johnston, D., Farquhar, J., and Rumble, D. (2006) Mass-dependent fractionation of quadruple stable sulfur isotope system as a new tracer of sulfur biogeochemical cycles. *Geochimica et Cosmochimica Acta* **70**, 2238–2252.

Rees, C.E., Jenkins, W.J., and Monster, J. (1978) The sulphur isotopic composition of ocean water sulphate. *Geochimica et Cosmochimica Acta* **42**, 377–381.

Tostevin, R., Turchyn, A.V., Farquhar, J., Johnston, D.T., Eldridge, D.L., Bishop, J.K.B., and McIlvin, M. (2014) Multiple sulfur isotope constraints on the modern sulfur cycle. *Earth and Planetary Science Letters* **396**, 14–21.

Wing, B.A., and Farquhar, J. (2015) Sulfur isotope homogeneity of lunar mare basalts. *Geochimica et Cosmochimica Acta* **170**, 266–280.

APPENDIX A2

MINOR S ISOTOPE SIGNATURES OF PORE WATER SULFATE WITHIN AMAZON DELTA SEDIMENTS

The Amazon Delta is characterized by rapid deposition of terrigenous, iron-rich sediments (*cf*. Aller et al., 2010). The rate of deposition is so rapid, and the physical environment so dynamic that deltaic 'topset' of 2 meters is rapidly and frequently (<2 yrs) remobilized, transported, and deposited. The physical resuspension of that topset resets the local diagenetic regime, and results in the rapid re-oxidation of sulfur species in a non-steady manner. This oxidative sulfur chemistry is also coupled to the rapid oxidation of entrained organic matter. To explore the consequences of this sulfur chemistry on the minor isotope signatures of pore water SO_4, we analyzed archived samples taken during the sampling cruise in Aller et al. (1996), which were ultimately analyzed for $\delta^{34}S$ and $\delta^{18}O$ values, and reported in Aller et al. (2010). The sampling sites in 'Off-Shelf-Transect 2' (OST-2) are shown in Fig. A2.1 below.

Figure A2.1

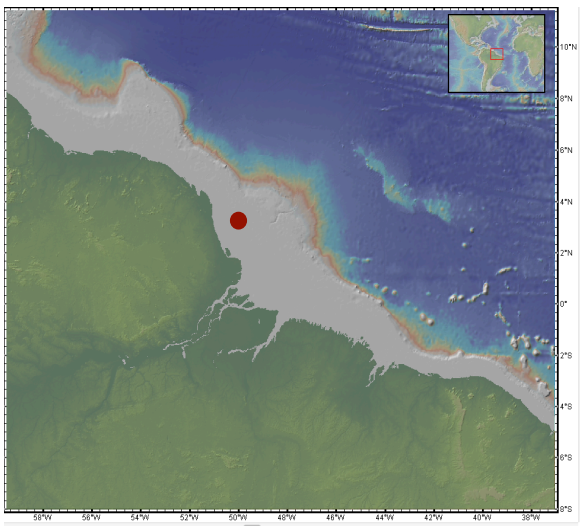

Figure A2.1: Location of coring site OST-2 within the Amazon Delta. OST-2 refers to 'Off-Shelf Transect-2' The details of sampling were first reported in Aller *et al*. (1996) and the initial isotope measurements were reported in Aller et al. (2010).

Two stations were sampled 2227 and 4121 on 2/23/1990 and 10/19/1991 during the rising and low stages of the Amazon River, respectively. The flow rate influences both the salinity of the overlying waters, as well as the general recycling of the delta topset. We analyzed archived $BaSO_4$ samples produced during both sampling cruises. They were prepared and analyzed as with the established methods of the other $BaSO_4$ samples in this thesis. The $\Delta^{33}S$ data, along with some of the other sampling metadata are shown below in Table A2.1:

Table A2.1

Station	Date	Depth Interval (cm)	Mid-depth (cm)	Pore water SO_4^{2-} (mM)	$\delta^{34}S$ –SO_4^{2} (‰)	$\Delta^{33}S$-SO_4^{2-} (‰)
OST-2	2/23/1990	0-10	5	27.3	21.3	0.035
KC2227		10-20	15	28.7	21.3	0.044
Rising		20-30	25	28.9	21.3	0.039
		30-40	35	28.5	21.3	0.038
		50-60	55	27.9	21.4	0.024
		70-80	75	28.2	23.0	0.064
		100-110	105	27.1	25.5	0.061
		130-140	135	24.8	29.7	0.063
		160-170	165	21.6	36.1	0.090
		190-200	195	17.4	44.9	0.121
		220-230	225	12.6	61.4	0.170
		250-260	255	9.5	77.0	0.220
OST-2	10/19/1991	0-10	5	29.8	21.1	0.041
KC4121		10-20	15	29.9	21.9	0.044
Low		20-30	25	27.5	23.0	0.040
		30-40	35	27.9	24.2	0.051
		40-50	45	26.7	26.1	0.062
		60-70	65	26.1	28.9	0.064
		80-90	85	24.3	31.5	0.072
		100-110	105	23.2	35.2	0.088
		120-130	125	20.2	40.7	0.104
		140-150	145	17.7	47.9	0.115
		160-170	165	14.3	57.8	0.154
		180-190	185	11.3	67.0	0.206

Table A2.1: Sampling, concentration, and S isotope data ($\delta^{34}S$ and $\Delta^{33}S$ values) for archived pore water samples from the Amazon Delta, Station OST-2. Two sampling trips were conducted at the rising and low flow rates of the Amazon River. Sulfur isotope values are reported on the V-CDT reference frame. For reference, SW-SO_4 replicates yield $\delta^{34}S$ = 21.35±0.3‰ and $\Delta^{33}S$ = 0.048±0.006‰ (Johnston et al., 2014).

In both cases, pore water [SO_4^{2-}] decreases with depth, as sulfate is drawn down in the underlying methanic zone (Aller et al. 2010), but the concentration profiles are typical of a non-steady state system where sulfate concentration is changing at any given depth (d{[SO_4^{2-}](z)}/dt > 0). Fig A2.2 below exhibits the concentration profiles of sulfate versus depth for the two sampled cores.

Figure A2.2

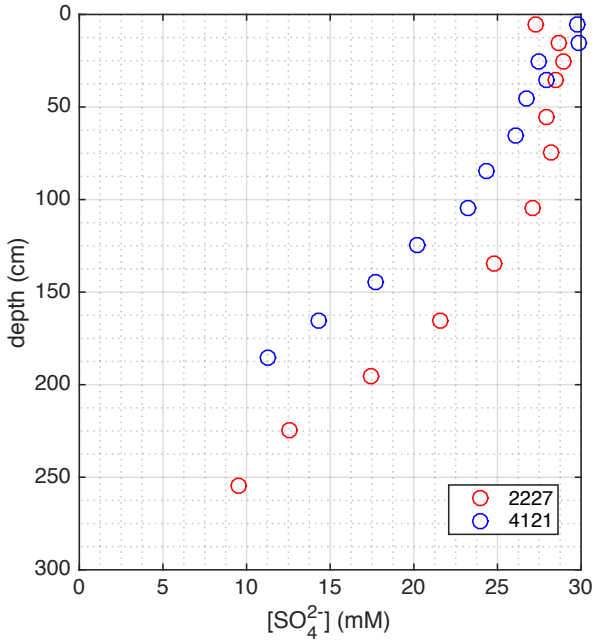

Figure A2.2: Pore water SO_4^{2-} concentrations from sampled cores 2227 and 4121. Core 2227 was sampled during the rising flow of of the Amazon River, and 4121 was sampled during low flow.

The consumption of pore water sulfate due to sulfate reduction (and anaerobic methane oxidation), carries a strong isotope effect $^{34}\varepsilon_{MSR}$ > 30‰, and results in the preferential loss of $^{32}SO_4^{2-}$, producing a strongly ^{34}S-enrichment in the residual sulfate. In both cores, there is a parallel increase in the δ^{34}S values with depth, rising to >60‰ with ~2/3 total sulfate loss, plotted below in Fig. A2.3.

Figure A2.3

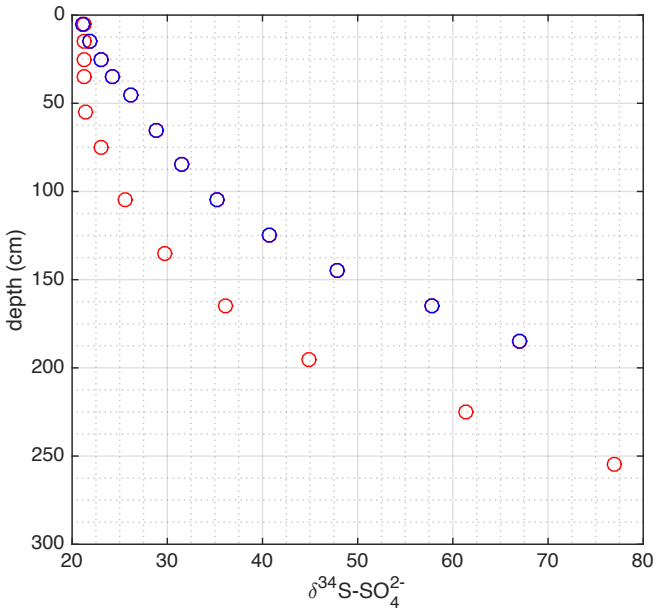

Figure A2.3: Plot of $\delta^{34}S\text{-}SO_4^{2-}$ values versus depth of the cores 2227 (red) and 4121 (blue). For reference, $SW\text{-}SO_4^{2-}$ is 21.15±0.3‰, and is the 'boundary condition' at 0 cm, the sediment water interface.

The consumption of pore water SO_4^{2-} is also associated with a dramatic increase in the $\Delta^{33}S\text{-}SO_4^{2-}$ values as well. The coupled nature of the fractionation parameters ($^{34}\alpha$ and $^{33}\lambda$), discussed elsewhere in this thesis form the basis for inferring microbial processes from $\delta^{34}S$ and $\Delta^{33}S$ values. The non-steady state nature of the diagenetic regimes make constructing reactive transport models more challenging. For the sake of completeness, however, the triple isotope plot ($\delta^{34}S/\Delta^{33}S$) is shown below.

Figure A3.3

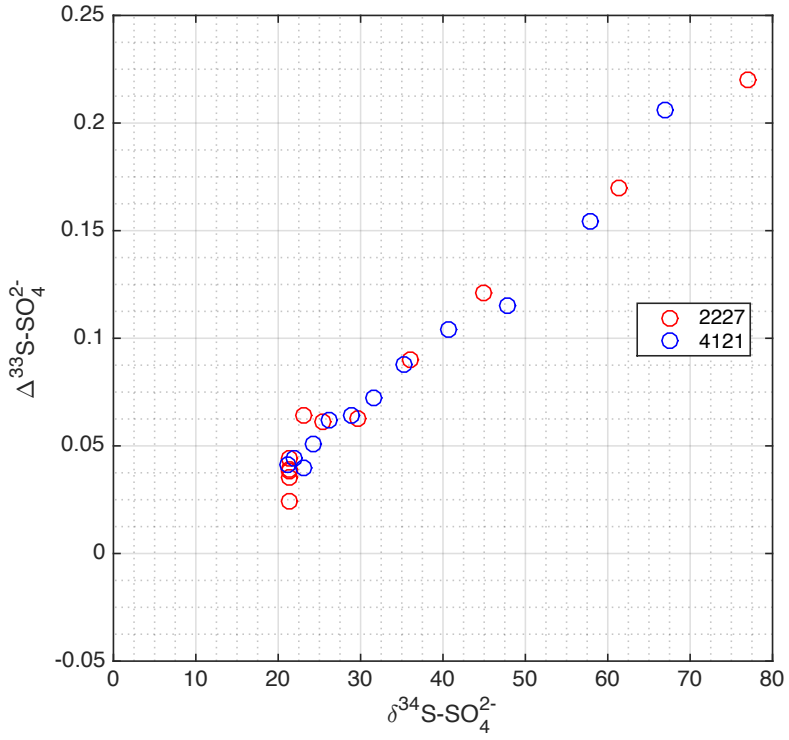

Figure A3.3: Triple isotope plot ($\Delta^{33}S$ vs. $\delta^{34}S$) of pore water sulfate in cores 2227 and 4121. The error associated with individual $\Delta^{33}S$ measurements is ±0.006‰ and for $\delta^{34}S$ approximately 0.3‰. For reference, the composition of SW-SO_4^{2-} is $\delta^{34}S$ = 21.15‰ and $\Delta^{33}S$ = 0.047‰ (Johnston et al., 2014).

REFERENCES

Aller, R.C., and Blair, N.E. (1996) Sulfur diagenesis and burial on the Amazon shelf: major control by physical sedimentation processes. *Geo-Marine Letters* **16**, 3–10.

Aller, R.C., Madrid, V., Chistoserdov, A., Aller, J.Y., and Heilbrun, C. (2010) Unsteady diagenetic processes and sulfur biogeochemistry in tropical deltaic muds: Implications for oceanic isotope cycles and the sedimentary record. *Geochimica et Cosmochimica Acta* **74**, 4671–4692.

Johnston, D.T., Gill, B.C., Masterson, A., Beirne, E., Casciotti, K.L., Knapp, A.N., and Berelson, W. (2014) Placing an upper limit on cryptic marine sulphur cycling. *Nature* **513**, 530–533.

APPENDIX A3

PLACING AN UPPER LIMIT ON CRYPTIC MARINE SULPHUR CYCLING*

A quantitative understanding of sources and sinks of fixed nitrogen in low-oxygen waters is required to explain the role of oxygen-minimum zones (OMZs) in controlling the fixed nitrogen inventory of the global ocean. Apparent imbalances in geochemical nitrogen budgets (Codispoti, 1995) have spurred numerous studies to measure the contributions of hetero- trophic and autotrophic N_2-producing metabolisms (denitrification and anaerobic ammonia oxidation, respectively) (Lam et al., 2009; Ward et al., 2009) Recently, 'cryptic' sulphur cycling was proposed as a partial solution to the fundamental biogeochemical problem of closing marine fixed-nitrogen budgets in intensely oxygen-deficient region (Canfield et al., 2010). The degree to which the cryptic sulphur cycle can fuel a loss of fixed nitrogen in the modern ocean requires the quantification of sulphur recycling in OMZ settings. Here we provide a new constraint for OMZ sulphate reduction based on isotopic profiles of oxygen ($^{18}O/^{16}O$) and sulphur ($^{33}S/^{32}S$, $^{34}S/^{32}S$) in seawater sulphate through oxygenated open-ocean and OMZ-bearing water columns. When coupled with observations and models of sulphate isotope dynamics and data-constrained model estimates of OMZ water-mass residence time, we find that previous estimates for sulphur- driven remineralization and loss of fixed nitrogen from the oceans are near the upper limit for what is possible given in situ sulphate isotope data.

---

*A version of this appendix was published as Johnston, D.T., Gill, B.C., Masterson, A., Beirne, E., Casciotti, K.L., Knapp, A.N., and Berelson, W. (2014) Placing an upper limit on cryptic marine sulphur cycling. *Nature* **513**, 530–533.

The ocean's budget of fixed nitrogen (primarily nitrate [NO_3^-], nitrite [NO_2^-] and ammonium [$NH_4^=$]) is predominantly controlled by the rates of biological dinitrogen (N_2) fixation and N_2 production by denitrification and anaerobic ammonia oxidation (anammox). Rates of anammox (converting NH_4^+ and NO_2^- to N_2) arguably compete with denitrification (reducing NO_3^- to N_2) for the NO_2^- used in N_2 production (Lam et al., 2009; Ward et al., 2009) although the flux of $NH_4^=$ supplied from the remineralization of organic matter by denitrification is in areas insufficient to fuel anammox. The role of the sulphur cycle was championed as a partial solution to the fundamental biogeochemical problem of closing marine fixed-nitrogen budgets in intensely oxygen-deficient regions, such as the Chilean OMZ (Canfield et al., 2010). The proposed involvement of sulphur cycling was aptly termed 'cryptic' for two reasons: first, the oxygen-deficient waters off the Chilean coast are devoid of free sulphide, H_2S—the terminal metabolic product of sulphate reduction—and, second, thermodynamic calculations favour respiration with oxidants such as NO_3^- over that of sulphate reduction. Evidence for cryptic sulphur cycling has come from microbial community analyses and shipboard incubations. Community-level pyrosequencing of DNA from waters within the Chilean OMZ indicated the presence of core sulphate reduction and sulphide oxidation genes. In addition, an array of sulphide-amended shipboard incubations demonstrated active sulphate reduction and sulphide oxidation in waters retrieved from the OMZ. Shipboard incubation experiments are a classic method of evaluating metabolic rates, and they underpin constraints on the nitrogen cycle as well (Lam et al., 2009; Ward et al., 2009). However, in nitrogen cycling, the rates measured by shipboard incubations have been substantiated by geochemical measurements and modeling (DeVries et al., 2013). The corrected sulphate reduction rates derived from *ex situ* incubation experiments (after accounting for sulphide oxidation) suggested that the cryptic sulphur cycle is responsible for up to 30% of the carbon remineralization within the Chilean OMZ and is therefore a substantial new source of NH_4^+ for anammox. If correct, these rates would be globally significant for marine elemental budgets.

Figure A3.1

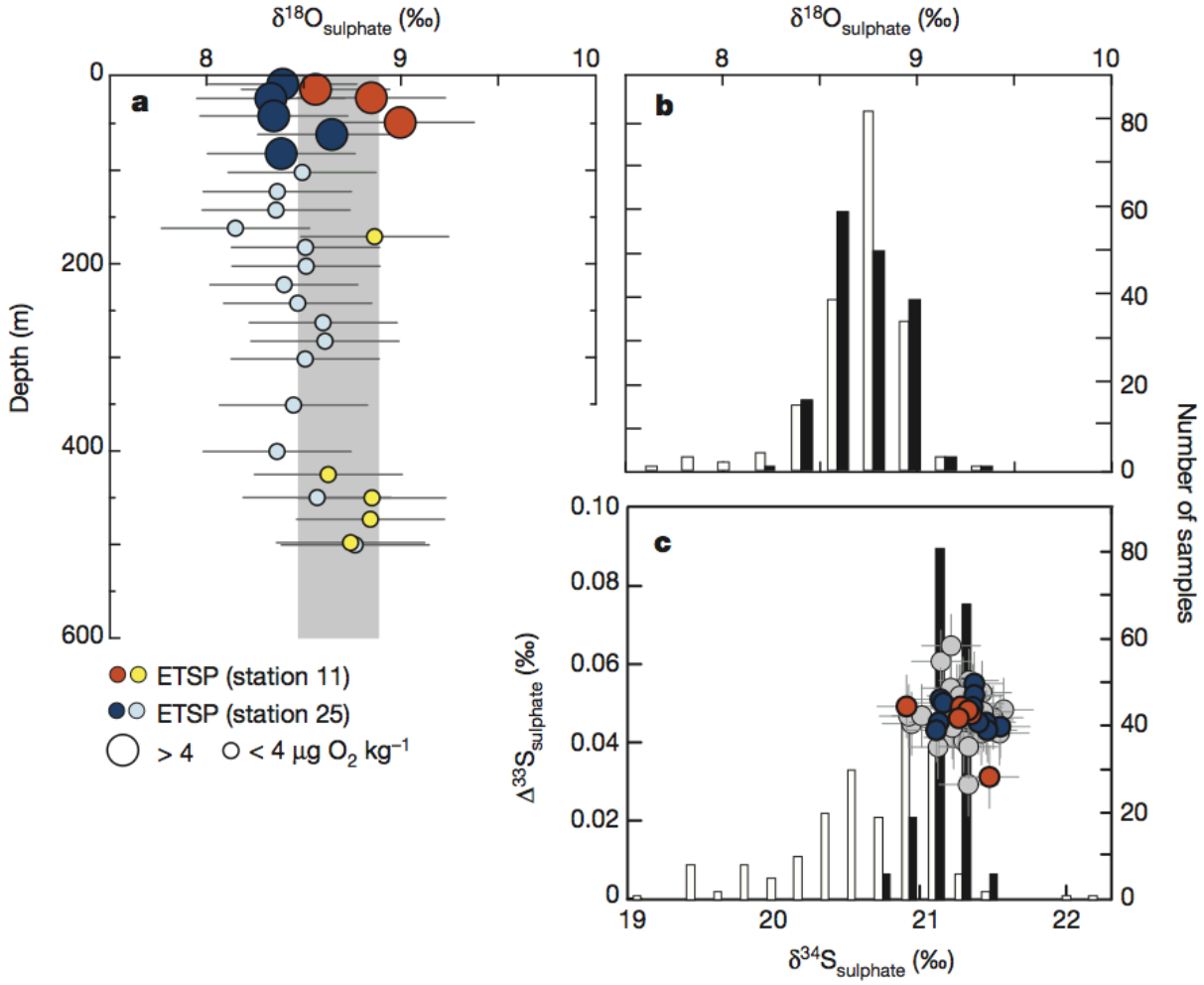

Figure A3.1: Establishing the isotopic composition of seawater sulphate (a) Water-column profiles of $\delta^{18}O_{sulphate}$ through two OMZ settings (ETSP stations 11 and 25) as a function of oxygen concentrations. Samples for this study are from the Bermuda Atlantic Time-series Study site, the Sampling and Analysis of Fe (SAFE) site, Eastern Tropical South Pacific stations 5, 6, 11 and 25, GEOTRACES stations 3-SS and 11, Angola upwelling station 18, and tropical South Atlantic station 1. Results are shown as means ±1σ **b, c,** Histograms of new (black) and published (white) $\delta^{18}O_{sulphate}$ data**. (b, c)** and $\Delta^{33}S$ values **(c)** for a larger suite of water-column profiles; this study further serves to establish the isotopic composition of seawater sulphate. Colours in c are same as in a (with grey samples from oxygenated water columns), all included with 1s errors. Note that published data sets did not sample OMZ environments. The histogram in c is from SO–SO_2-based analyses, whereas data points plotted are from SF6-based analyses (this study amends between SO_2 and SF_6 scales).

Figure A3.2

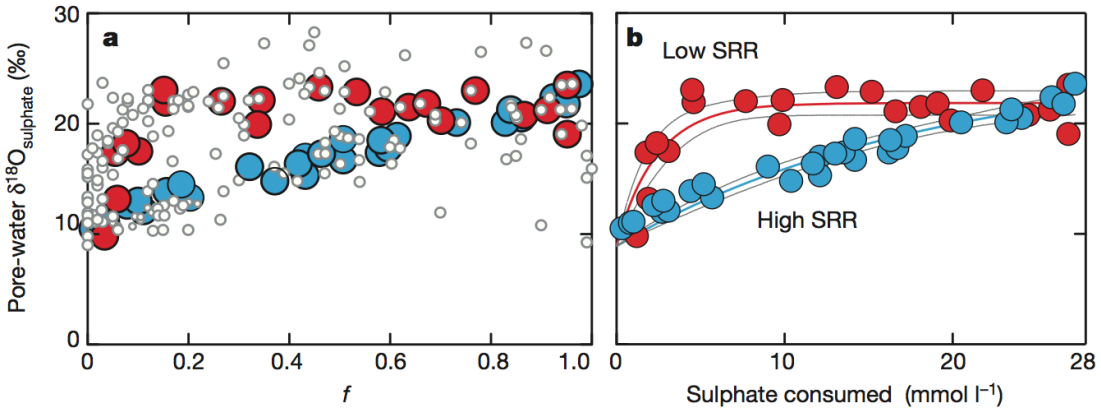

Figure A3.2: Pore-water $\delta^{18}O$ profiles. Two models were developed to quantify the isotopic response of sulphate reduction. They are derived from the compilation of 199 measurements of pore-water sulphate concentration and $\delta^{18}O_{sulphate}$ profiles (small white circles in **a**). To normalize the data to various bottom-water sulphate concentrations, we first plot them as a relative fraction of sulphate reduced (f). At the individual pore-water profile level, two types of down-core behaviour are present. A majority of the data show a strong nonlinearity (low relative rates of sulphate reduction), whereas a minority approach a more linear trend (very high rates of sulphate reduction) The red and blue data sets serve as an example of each. **b**, Model fits (and 95% confidence intervals) to these data. Our $\delta^{18}O_{s.c.}$ represents the isotopic composition at any given degree of sulphate consumed, so is analogous to that which is directly measurable in marine pore waters.

The impact of sulphur cycling can be directly tested through evaluating the stable isotope systematics of seawater sulphate. The O and S isotopic compositions of SO_4^{2-} are time-integrated recorders of biogeochemical processing. These isotope records preserve complementary, yet unique, information. Sulphate S isotopes primarily preserve the metabolic fingerprint of dissimilatory sulphate reduction, which commonly occurs in marine sediments and where the metabolite sulphide is depleted in heavy isotopes, leaving the residual sulphate enriched (Jørgensen, 1979). Further, the examination of ^{33}S provides additional leverage on biogeochemical activity, permitting differentiation between contributions from oxidative and reductive metabolisms (Johnston, 2011). Conversely, sulphate O isotopes are primarily controlled by equilibration between water and a redox intermediate, sulphite (Wankel et al., 2014). Sulphite has a central role in oxidation reactions but is also a requisite intermediate in reductive reactions. Microbial cycling there- fore results in the enrichment of 18O in

residual sulphate (that is, seawater sulphate). This O-isotope enrichment accompanies cycling even in the absence of net sulphate reduction (that is, intracellular recycling). Thus, the potential exists for a cryptic sulphur cycle to be recorded in the oxy- gen isotopic composition of sulphate within OMZs.

To investigate the significance of sulphur cycling in OMZs, we provide an isotopic characterization of modern seawater sulphate An accumulation of work dating back half a century (standardized herein) provides a context for evaluating these signals. Here we conducted a new, comprehensive characterization of S and O isotopes, including ^{33}S, in seawater sulphate from nearly 200 samples collected from ten different water-column profiles in the modern ocean. Taken together, we establish a strongly constrained average composition for seawater sulphate: $\delta^{18}O_{sulphate}$ = 8.67% (N = 60 0.21‰, 1σ), $\delta^{34}S_{sulphate}$ = 21.15% (N = 60, 0.15‰, 1σ), and $\Delta^{33}S_{sulphate}$ = 0.048‰ (N = 60, 0.006‰, 1σ). These samples range in dissolved oxygen and oxidized nitrogen concentrations ($[NO_3^-]$ $[NO_2^-]$) from essentially zero up to 250 and 45 mM, respectively. Two of these water columns (Eastern Tropical South Pacific (ETSP) stations 11 and 25) intersect regions experiencing significant oxygen depletion (as evident through the accumulation of nitrite, expression of an N deficit, and elevated $\delta^{15}N_{NO3}$ values.

Figure A3.3

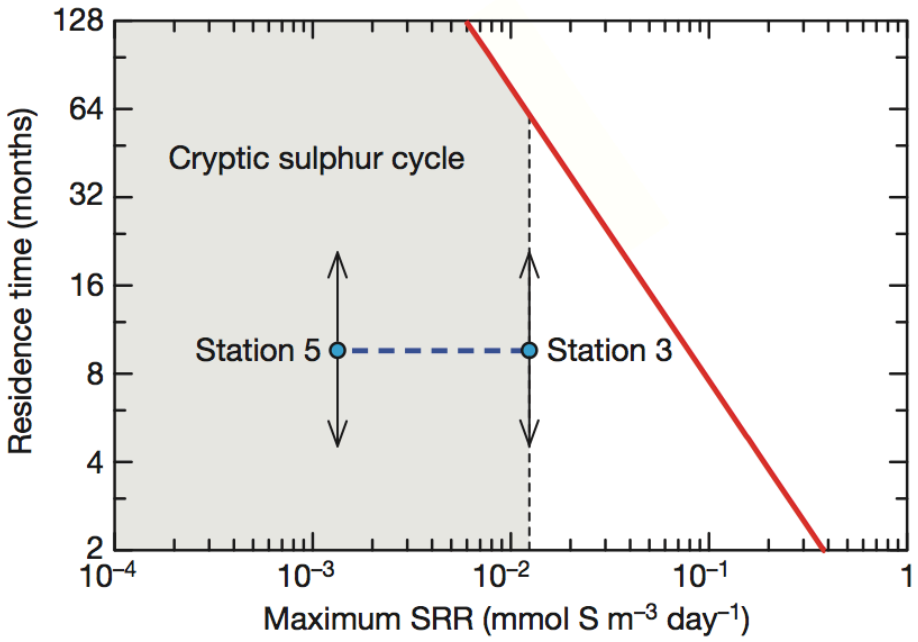

Figure A3.3: Model predictions for the maximum allowable rate of sulphate reduction. Predicted SRRs as a function of water mass residence time based on $\delta^{18}O_{sulphate}$ constraints. The line represents the minimum detectable SRR for a given t (using the low-SRR model), or a maximum possible rate that would not carry a resolvable $\delta^{18}O$ effect. Also included are the sulphate rate estimates from shipboard experiments at the Chilean upwelling, stations 3 and 5, without a prescribed residence time.

Studies of the marine sulphur cycle illustrate the long residence time and slow turnover of S and O in sulphate (10^7 and 10^6 years, respectively)(Turchyn and Schrag, 2004; Paytan et al., 2004), especially when placed in the context of much shorter oceanic mixing times (~1,000 years). It is therefore expected that both the S and O compositions of marine sulphate will be well mixed except in regions where biological cycling overcomes water mass circulation and mixing. Statistical analyses of our data show that OMZ samples are isotopically indistinguishable in $\delta^{18}O_{sulphate}$, $\delta^{34}S_{sulphate}$ and $\Delta^{33}S_{sulphate}$ from the global mean composition (95% confidence level; Fig A3.1. This homogeneity remains true whether comparing different depths and water masses within a single water-column

profile or comparing similar water depths from multiple profiles including OMZ-bearing and well-ventilated water masses.

The lack of a clear $\delta^{18}O_{sulphate}$ signal places direct constraints on the significance of a water-column sulphur cycle. A quantitative context derived from microbial (pure and mixed) culture experiments (Mizutani and Rafter, 1969; Fritz et al., 1989) and marine sediments (Aharon and Fu, 2000; Aharon and Fu, 2003; Turchyn et al., 2006; Wortmann et al., 2001; Wortmann et al., 2007) defines the expected isotopic change in $\delta^{18}O_{sulphate}$ as sulphate is cycled. Of the two, marine sedimentary pore waters may provide the most closely analogous system to an open-ocean water column and define a range of responses in $\delta^{18}O_{sulphate}$ as sulphate is consumed. However, both approaches (culture experiments and pore waters) yield essentially the same result. The reduction and cycling of sulphate always results in an enrichment in $\delta^{18}O_{sulphate}$, most often approaching ~25% (water = 0% versus Vienna Standard Mean Ocean Water (VSMOW); (Fig. A3.2) This holds true in the presence and absence of sulphide oxidation reactions (Farquhar et al., 2008; Mangalo et al. 2007). Thus, even in the absence of net sulphate reduction (that is, when reduction equals oxidation—the postulated cryptic sulphur cycle), sulphur cycling by sulphate-reducing bacteria in the water column should drive an increase in $\delta^{18}O_{sulphate}$. This characteristic $\delta^{18}O_{sulphate}$ response has been documented in nearly 200 pore water measurements in which both O isotopes and sulphate concentrations are available. In environments where sulphate reduction rates are low, such as those expected in the water column of an OMZ and commonly pre- served in sediment pore waters, a strong nonlinear increase in $\delta^{18}O_{sulphate}$ accompanies sulphate consumption (Antler et al, 2013). The best example of this behaviour is from diatomaceous sediments underlying the Angola–Benguela current (Fig A3.2)(Turchyn et al. 2006) Conversely, an almost linear increase in $\delta^{18}O_{sulphate}$ is associated with relatively high sulphate reduction rates, such as those captured in organic-rich sediments from the Gulf of Mexico (Fig A3.2) (Aharon and Fu, 2000). In this study we present these data as end-member responses and explore a variety of different forms of the fit (such as exponential, power and Michaelis–Menten) between $\delta^{18}O_{sulphate}$ and sulphate concentrations for the different sulphate reduction rates. We conservatively

choose a simple one-phase decay model (least-squares ordinary fit) to describe the data (Farquhar et al., 2008). We posit that quantifying the $\delta^{18}O_{sulphate}$ response to sulphate reduction permits the development of an *in situ* prediction for the integrated consequences of cryptic sulphur cycling. This prediction is a function of the vigour with which sulphate is processed, and if one considers that any parcel of water has a finite residence time within the OMZ (t, in days), this 'vigour' can be translated to a rate of sulphate reduction. Here we perform a set of simple calculations based on two features: first, the expected $\delta^{18}O_{sulphate}$ response (in per mille) to sulphate consumption (in millimolar), and second, the published residence times of water in the ETSP OMZ relative to mixing and advection (1–10 years)(DeVries et al., 2012; Kalvelage et al., 2013). The sharpness of this approach is primarily then limited by the precision of the isotopic measurement and estimates of t. Because no significant change in $\delta^{18}O_{sulphate}$ was observed in the OMZ relative to well-ventilated water masses, we ask the question: how large an isotopic excursion in $\delta^{18}O_{sulphate}$ could have been produced while remaining statistically unresolvable, and what rate of sulphate reduction does that correspond to? The capacity to identify a $\delta^{18}O_{sulphate}$ anomaly will be related to the average analytical uncertainty for any single measurement (better than 0.2‰) and the sample density (n) through the interval of interest. Further, each water column carries a unique mean, a normally distributed variance (of 0.13‰ (1σ)), and a standard error of (0.03‰) Because we are interested in an intra-water-column $\delta^{18}O_{sulphate}$ signal, we assign a value of 0.13‰ to the resolvable $\delta^{18}O_{sulphate}$ threshold signal, but note that our conclusions do not qualitatively change with the choice of a slightly larger or smaller value. Given the expected low overall rates of sulphate reduction in a water column and the rarity with which even marine-sediment pore-water $\delta^{18}O_{sulphate}$ data follow the 'high sulphate reduction rates (SRR)' trajectory, we take the 'low SRR' model from Fig. A3.2 as a guide (note that using the 'high SRR' model increases predictions of sulphate reduction rates about fivefold). Thus our prediction for the maximum sulphate reduction rates possible in the ETSP OMZs is between $6.4x10^{-2}$ and $6.4x10^{-3}$ mmol m^{-2} d at water mass residence times of 1 and 10 years, respectively (Fig. A3.3). These limits on in situ sulphate reduction rates overlap those experimentally extracted from the Chilean upwelling.

The cryptic nature of the sulphur cycle—that is, the absence of detectable water-column sulphide—requires that rates of chemoautotrophic sulphide oxidation match those of sulphate reduction in space and time. The putative rates of sulphate reduction in OMZ settings therefore carry important implications for our understanding of OMZ biogeochemistry. For example, the amount of nitrate consumption required to balance a sulphide oxidation rate of 1 mmol S m^{-2} d^{-1} could account for a large fraction of the estimated N loss from the ETSP5. If sulphide oxidation were coupled to complete denitrification (NO_3^{-1} to N_2), the oxidation of 1 mmol S m^{-2} d^{-1} would produce a flux of 0.8 mmol N_2 m^{-2} d^{-1}, or up to ~30% of estimates of total nitrate loss. In parallel, chemoautotrophic sulphide oxidation is indeed prevalent where free sulphide (from sedimentary sources) accumulates within coastal ETSP waters; however, in these settings sulphate reduction is spatially decoupled from the point of subsequent sulphur oxidation. Unlike conditions found in the ETSP: OMZ, the location of chemoautotrophic sulphide oxidation in coastal waters generally occurs at the interface between nitrate-reducing and sulphate-reducing waters (Lavik et al., 2009; Schunck et al., 2013). The occurrence of active sulphate reduction in the presence of nitrate and nitrite thus remains an intriguing puzzle. This puzzle may be in fact rectified through further work targeting the role of microenvironments within sinking particulate matter.

Although the predicted $\delta^{18}O_{sulphate}$ signal in the ETSP OMZ was at or just below detection with our current approach, the $\delta^{18}O$ effect predicted here is captured in other saline environments (for instance, Framvaren Fjord (Mandernack et al., 2003) and Blood Falls, Antarctica (Mukucki et al., 2009) and serves as an independent geochemical tool with which to track key biogeochemical processes in OMZ settings. Other direct tests, such as those for the N and O isotopes of nitrate and nitrite, provide independent estimates of the relative rates of nitrate and nitrite reduction (Casciotti et al., 2013) and detail the capacity of the nitrogen cycle to accommodate an oxidative sulphur cycle. If nitrate reduction is largely coupled to sulphide oxidation, then the isotope effect of nitrate reductase in those organisms (note that periplasmic nitrate reductase and respiratory nitrate reductase are present in many sulphur oxidizers and SUP05 (Walsh et al., 2009) will dictate the expressed slope of the $\delta^{15}N_{NO3}$

versus $\delta^{18}O_{NO3}$ signal that defines OMZ environments (Sigman et al., 2005). Finally, sulphide production in the ETSP OMZ, even if transient, might also be expected to serve as a sink for chalcophile trace elements; however, studies on elements such as cobalt and nickel show nutrient-like behaviour rather than inorganic scavenging (Saito et al., 2004). OMZ environments thus remain a biogeochemical conundrum in terms of closing mass-balance on key nutrient and major element cycles, especially fixed nitrogen. Solving this conundrum remains a critical challenge, given the importance of these settings in the overall chemical budget of the ocean; this is a role that only stands to increase as the climate of our planet warms.

REFERENCES

Aharon, P., and Fu, B. (2000) Microbial sulfate reduction rates and sulfur and oxygen isotope fractionations at oil and gas seeps in deepwater Gulf of Mexico. *Geochimica et Cosmochimica Acta* **64**, 233–246.

Aharon, P., and Fu, B. (2003) Sulfur and oxygen isotopes of coeval sulfate–sulfide in pore fluids of cold seep sediments with sharp redox gradients. *Chemical Geology* **195**, 201–218.

Antler, G., Turchyn, A.V., Rennie, V., Herut, B., and Sivan, O. (2013) Coupled sulfur and oxygen isotope insight into bacterial sulfate reduction in the natural environment. *Geochimica et Cosmochimica Acta* **118**, 98–117.

Canfield, D.E., Stewart, F.J., Thamdrup, B., De Brabandere, L., Dalsgaard, T., Delong, E.F., Revsbech, N.P., and Ulloa, O. (2010) A cryptic sulfur cycle in oxygen-minimum zone waters off the Chilean coast. *Science* **330**, 1375–1378.

Casciotti, K.L., Buchwald, C., and McIlvin, M. (2013) Implications of nitrate and nitrite isotopic measurements for the mechanisms of nitrogen cycling in the Peru oxygen deficient zone. *Deep Sea Research Part I: Oceanographic Research Papers* **80**, 78–93.

Codispoti, L.A. (1995) Is the ocean losing nitrate? *Nature* **376**, 724.

DeVries, T., Deutsch, C., Primeau, F., Chang, B., and Devol, A. (2012) Global rates of water-column denitrification derived from nitrogen gas measurements. *Nature Geosci* **5**, 547–550.

DeVries, T., Deutsch, C., Rafter, P.A., and Primeau, F. (2013) Marine denitrification rates determined from a global 3-D inverse model. *Biogeosciences* **10**, 2481–2496.

Farquhar, J., Canfield, D.E., Masterson, A., Bao, H., and Johnston, D. (2008) Sulfur and oxygen isotope study of sulfate reduction in experiments with natural populations from Fællestrand, Denmark. *Geochimica et Cosmochimica Acta* **72**, 2805–2821.

Fritz, P., Basharmal, G.M., Drimmie, R.J., Ibsen, J., and Qureshi, R.M. (1989) Oxygen isotope exchange between sulphate and water during bacterial reduction of sulphate. *Chemical Geology: Isotope Geoscience Section* **79**, 99–105.

Jørgensen, B.B. (1979) A theoretical model of the stable sulfur isotope distribution in marine sediments. *Geochimica et Cosmochimica Acta* **43**, 363–374.

Lam, P., Lavik, G., Jensen, M.M., van de Vossenberg, J., Schmid, M., Woebken, D., Gutierrez, D., Amann, R., Jetten, M.S.M., and Kuypers, M.M.M. (2009) Revising the nitrogen cycle in the Peruvian oxygen minimum zone. *Proceedings of the National Academy of Sciences* **106**, 4752–4757.

Lavik, G., Stührmann, T., Brüchert, V., Van der Plas, A., Mohrholz, V., Lam, P., Mussmann, M., Fuchs, B.M., Amann, R., Lass, U., and Kuypers, M.M. (2009) Detoxification of sulphidic African shelf waters by blooming chemolithotrophs. *Nature* **457**, 581–584.

Mandernack, K.W., Krouse, H.R., and Skei, J.M. (2003) A stable sulfur and oxygen isotopic investigation of sulfur cycling in an anoxic marine basin, Framvaren Fjord, Norway. *Chemical Geology* **195**, 181–200.

Mangalo, M., Meckenstock, R.U., Stichler, W., and Einsiedl, F. (2007) Stable isotope fractionation during bacterial sulfate reduction is controlled by reoxidation of intermediates. *Geochimica et Cosmochimica Acta* **71**, 4161–4171.

Mikucki, J.A., Pearson, A., Johnston, D.T., Turchyn, A.V., Farquhar, J., Schrag, D.P., Anbar, A.D., Priscu, J.C., and Lee, P.A. (2009) A Contemporary Microbially Maintained Subglacial Ferrous" Ocean". *Science* **324**, 397–400.

Paytan, A., Kastner, M., Campbell D., Thiemens, MH (1998) Sulfur Isotopic Composition of Cenozoic Seawater Sulfate. *Science* **282**, 1459–1462.

Saito, M.A., Moffett, J.W., and DiTullio, G.R. (2004) Cobalt and nickel in the Peru upwelling region: A major flux of labile cobalt utilized as a micronutrient. *Global Biogeochem. Cycles* **18**, 1-14.

Turchyn, A.V., and Schrag, D.P. (2004) Oxygen isotope constraints on the sulfur cycle over the past 10 million years. *Science* **303**, 2004–2007.

Turchyn, A.V., and Schrag, D.P. (2006) Cenozoic evolution of the sulfur cycle: Insight from oxygen isotopes in marine sulfate. *Earth and Planetary Science Letters* **241**, 763–779.

Turchyn, A.V., Sivan, O., and Schrag, D.P. (2006) Oxygen isotopic composition of sulfate in deep sea pore fluid: evidence for rapid sulfur cycling. *Geobiology* **4**, 191–201.

Walsh, D.A., Zaikova, E., Howes, C.G., Song, Y.C., Wright, J.J., Tringe, S.G., Tortell, P.D., and Hallam, S.J. (2009) Metagenome of a versatile chemolithoautotroph from expanding oceanic dead zones. *Science* **326**, 578–582.

Wankel, S.D., Bradley, A.S., Eldridge, D.L., and Johnston, D.T. (2014) Determination and application of the equilibrium oxygen isotope effect between water and sulfite. *Geochimica et Cosmochimica Acta* **125**, 694–711.

Ward, B.B., Devol, A.H., Rich, J.J., Chang, B.X., Bulow, S.E., Naik, H., Pratihary, A., and

ayakumar, A. (2009) Denitrification as the dominant nitrogen loss process in the Arabian Sea. *Nature* **461**, 78–81.

Wortmann, U.G., Bernasconi, S.M., and Bottcher, M.E. (2001) Hypersulfidic deep biosphere indicates extreme sulfur isotope fractionation during single-step microbial sulfate reduction. *Geology* **29**, 647–650.

Wortmann, U.G., Chernyavsky, B., Bernasconi, S.M., Brunner, B., Böttcher, M.E., and Swart, P.K. (2007) Oxygen isotope biogeochemistry of pore water sulfate in the deep biosphere: Dominance of isotope exchange reactions with ambient water during microbial sulfate reduction (ODP Site 1130). *Geochimica et Cosmochimica Acta* **71**, 4221–4232.